Diss. 2010 - 07
Juni

Surface characterisation and surface protection of Germanium detector crystals

Tobias Engert

(Dissertation University of Liverpool)

GSI Helmholtzzentrum für Schwerionenforschung GmbH
Planckstraße 1 · D-64291 Darmstadt · Germany
Postfach 11 05 52 · D-64220 Darmstadt · Germany

Surface characterisation and surface protection of Germanium detector crystals

Thesis submitted in accordance with the requirements of
the University of Liverpool for the degree of Doctor in Philosophy

by

Tobias Engert

Oliver Lodge Laboratory

June 2010

Abstract

Surface characterisation and surface protection
of Germanium detector crystals

Tobias Engert

Germanium-detectors are the most sensitive high-resolution γ detectors available and are the instrument in nuclear structure physics which allows important information about the structure of atomic nuclei to be obtained. The technology of High purity Germanium detectors is presented in [1]. However, conventional technology is more suited to standard commercial type of detectors rather then research type one's. The reported work is motivated by the need for a new mechanical treatment procedure within the manufacturing methods, in order to obtain better quality of the Germanium surfaces and increased cost-efficiency enabling complicated shapes to be produced.

Seven germanium crystals with different surface qualities due to varying mechanical treatment were employed for the characterisation and treatment evaluation. Five of them were fully processed to obtain working detectors. The crystals have a size of $8\times8\times10$ mm^3 and are fixed in special housings. These housings are optimized for all the different microscopes used as well as for a newly developed detector cryostat. The detector surfaces have been studied with an Electron Probe Micro Analyser and a Field Emission Scanning Microscope.

The two non-detector crystals have been designed only for the mechanical characterisation. One was only grinded while the other one was lapped in addition. This treatment status corresponds to the status of usual detectors before chemical processing. In these mechanical steps surfaces have been investigated with an Atomic Force Microscope and a Profiler.

Germanium treatment and shaping tests with a new ultrasonic grinding machine have been carried out and the results have shown very fine surface structures with tight surface parameters. This kind of sophisticated mechanical treatment allows also complicated shapes to be achieved. On the basis of these characterisation and ultrasonic treatment results the development of a novel type of planar Ge detector has started.
A further motivation of this work follows from the necessity to develop a new hermetic capsule unit with other manufacturing methods, better physical properties and in a cost-effective way. For this purpose, new processes have been selected and tested differently.

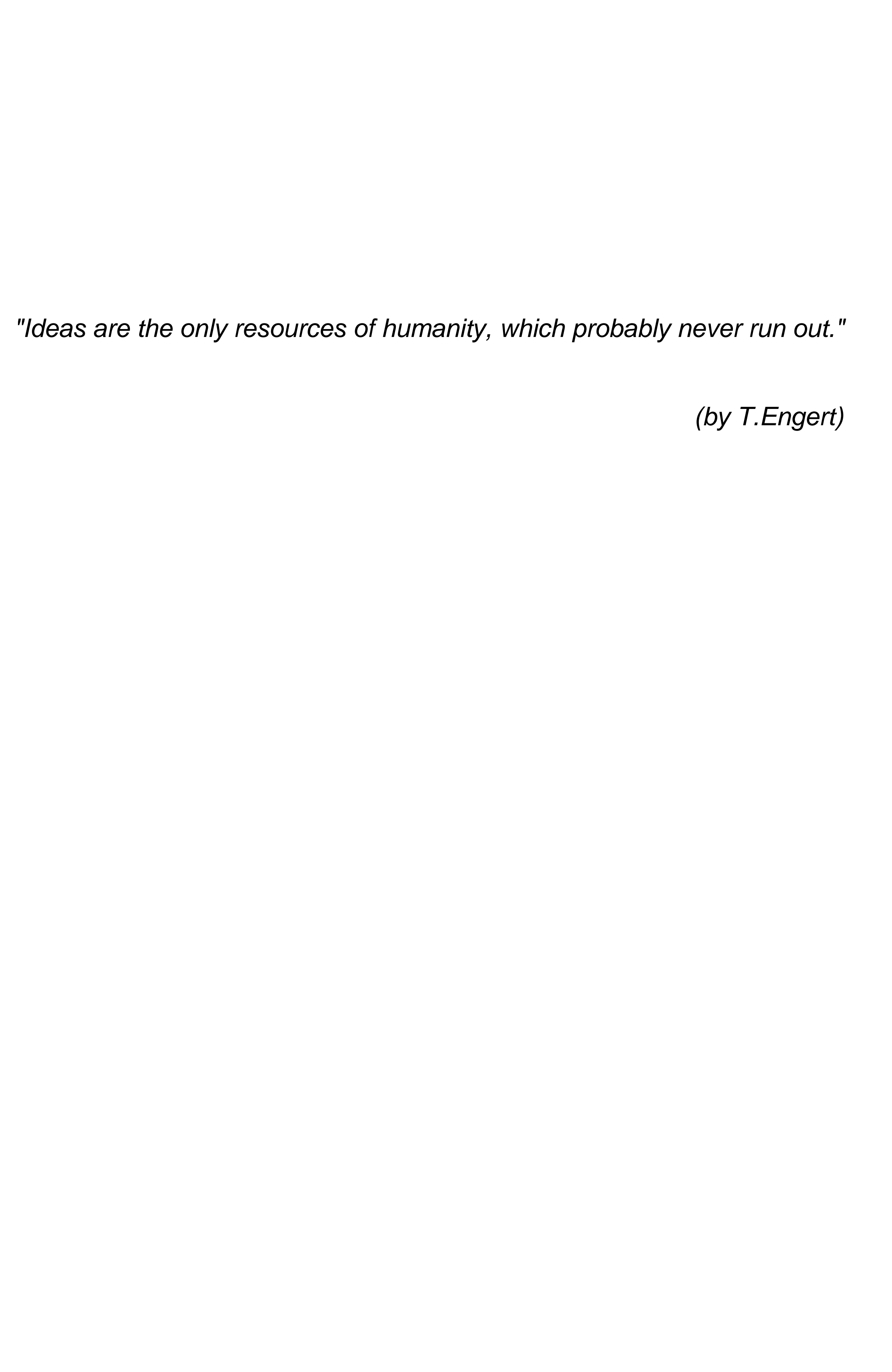

"Ideas are the only resources of humanity, which probably never run out."

(by T.Engert)

Acknowledgements

I would like to take this opportunity to thank all the people who supported me throughout my Ph.D.. I would like to thank the following people in particular:

> My supervisors Prof. P.J. Nolan and Dr. J. Gerl for giving me the opportunity to do a Ph.D. and for the invaluable support and guidance.

> My mentor Ivan Kojouharov, for his supervision and for all the help in the lab.

> I gratefully acknowledge Dr. habil H.J. Wollersheim for many discussions. I thank Namita Goel, Stephane Pietri, Frederic Ameil, Robert Hoischen, Cesar Domingo Pardo, Markus Kirk, Michael Maier and Henning Schaffner for their individual and friendly help.

> I want to address special thanks to all the other members of the nuclear spectroscopy and material research group at GSI for all the help and friendly working environment.

> Finally, I would like to thank my family for their continuous support throughout my Ph.D. work.

Thank you all very much.

Contents

CONTENTS i

1 Introduction 1

1.1 Detector geometry 15

1.2 The development of encapsulated detectors 17

1.3 Motivation 18

2 The basics of surface characterisation 21

2.1 Mechanical crystal processing 21

2.1.1 Principle of Grinding 22

2.1.2 Principle of Lapping 23

2.1.3 Principles of Ultrasonic Grinding 24

2.2 Defect layers as a result of mechanical crystal processing 25

2.2.1 Defect model 26

2.2.2 Characterisation of semiconductor surfaces 28

2.3 Basics of surface measurement 34

2.3.1 Orders of the form deviations 35

2.3.2 Roughness 37

2.3.3 Surface parameters 37

2.3.3.1 Maximum roughness depth *Rt* 38

2.3.3.2 Arithmetical mean deviation of the roughness profile *Ra* 39

2.3.3.3 Root mean square surface roughness value *Rq* 39

2.3.3.4 Average surface roughness *Rz* 40

2.3.3.5 Maximum peak to valley of waviness *Wt* 41

2.4 The applied measuring methods 41

2.4.1 Profilometer 42

2.4.2 Atomic Force Microscope (AFM) 43

2.4.3 Field Emission Scanning Electron Microscope (FESEM) 45

2.4.4 Electron Probe Micro Analyser (EMS) 47

3 Characterisation of Ge-detectors and crystals 48
3.1 Design and development methods of Ge-detectors and crystals........ 48
3.1.1 Current-voltage tests of the produced Ge-detectors..................... 51
3.1.2 Spectroscopic test of Ge-detectors 53
3.2 Characterisation of the surface morphology and topography............. 55
3.2.1 Profilometer 56
3.2.2 Atomic Force Microscope (AFM)... 59
3.2.3 The Electron Probe Micro Analyser (EPMA) 63
3.2.4 Field Emission Scanning Electron Microscope (FESEM)............. 69
3.3 Evaluation of the surface characterisation.. 72

4 Mechanical Ultrasonic-treatment.. 74
4.1 Ultrasonic-grinding experiment 74
4.2 Spectroscopic test of the germanium detector.................................. 79
4.3 Segmentation 81
4.3.1 Mechanically generated segmentation 81
4.3.2 Verification of the segmentation by profilometry 82
4.4 Evaluation of the ultrasonic grinding... 88

5 Capsule Unit 90
5.1 The encapsulated detectors 90
5.2 Encapsulation technology used for EUROBALL detectors 90
5.3 The new Encapsulation 92
5.3.1 Welding of the capsule with the lid 94
5.3.1.1 Welding experiments 95
5.3.1.1.1 Test capsules... 95
5.3.1.1.2 Measuring setup 98
5.3.1.2 Laser beam welding of the models 99
5.3.1.3 Results 100
5.3.1.4 Influence of heat during the welding operation 105
5.3.1.4.1 PT 100 measurements.. 105

5.3.1.4.2 Thermal imaging camera 107
5.3.1.5 Thermal stress 110
5.3.1.6 Evaluation of the capsule welding 111
5.3.2 Creation of the vacuum 112
5.3.2.1 Operating principle of the process 113
5.3.2.2 Experiment 115
5.3.2.3 Evaluation of the vacuum process 115
5.4 The getter element for maintaining the vacuum 116
5.4.1 The Getter configuration 117
5.4.2 Filter disc 118
5.4.3 Evaluation of the getter configuration 119

6 Conclusion and future work 120
6.1 Conclusion 120
6.2 Future work 122

7 Summary 124

8 Appendix 126

9 Publications 189

10 References 198

List of Figures

Figure 1: Band structure in insulators and semiconductors 2
Figure 2: Fermi function 4
Figure 3: In the n-doped region the electrons are located as free Charge carrier and in the p-doped region the holes are flexible. 6
Figure 4: At the barrier between the p- and n-doped regions a junction is generated 8
Figure 5: A p-n junction-charge electric field and potential distribution. Left: p-n junction with equal impurity concentration at the both sides. Right: p-n junction with heavily doped p-side and low doped n-side. 11
Figure 6: Different detector geometries 15
Figure 7: Detector technology 19
Figure 8: Schematic of the grinding method 23
Figure 9: Schematic of the lapping method 24
Figure 10: The combined treatment principle 25
Figure 11: Defect model 27
Figure 12: Example of mechanically produced scratches 29
Figure 13: Example of mechanically generated haze 29
Figure 14: Example of Edge chips 30
Figure 15: Microscopic contamination during the implementation and etching 31
Figure 16: Irregularities in thickness 31
Figure 17: Orange peel effect 32
Figure 18: Dimples of a Ge-crystal 33
Figure 19: Waves of the surface 33
Figure 20: Form deviation: 1st to 4th order 34
Figure 21: Metrologically detected surface 38
Figure 22: Roughness depth *Rt* 38
Figure 23: Arithmetical mean deviation of the roughness profile *Ra* 39

Figure 24: Root mean square surface roughness value *Rq* 40
Figure 25: Average surface roughness *Rz* 40
Figure 26: Waviness profile *Wt* 41
Figure 27: Functional principle of a profilometer 42
Figure 28: Functional principle of an Atomic Force Microscope (AFM) 44
Figure 29: The operating principle of the Field Emission Scanning Electron .. Microscope (FESEM) 46
Figure 30: The operating principle of an Electron Probe Micro Analyser (EPMA)...47
Figure 31: Basic structure of germanium probe detectors 49
Figure 32: Overview of developed Ge-detectors and crystals 50
Figure 33: Ge-detectors integrated in a cryostat 51
Figure 34: Current-voltage test..52
Figure 35: Example of the spectrum of detector B1 using ^{241}Am and ^{57}Co source 53
Figure 36: 2D parameter identification with a Profilometer 56
Figure 37: 3D surface using Profilometer 57
Figure 38: Lapped crystal B10 60
Figure 39: Grinded crystal B11..61
Figure 40: Ultrasonic-treated crystal B12 62
Figure 41: Ge-particles..64
Figure 42: Aluminium particles 66
Figure 43: Organic contamination (weak)...67
Figure 44: Organic contamination (strong) 68
Figure 45: The defect burst place detected with FESEM 71
Figure 46: Samples used for the ultrasonic grinding experiments 75
Figure 47: Quasi-planar geometry realised by ultrasonic grinding with Ge(Li) test crystal 76
Figure 48: Quasi-planar crystal after etching...77
Figure 49: High-purity germanium crystal..78

Figure 50: Current-voltage characteristic of the Quasi-planar detector produced by ultrasonic machining 79
Figure 51: Result of the spectroscopy test of the detector 80
Figure 52: Segmentation produced with ultrasonic grinding 82
Figure 53: Profilometry of the segmentation before etching 84
Figure 54: Profilometry of the segmentation after etching 87
Figure 55: Picture of the segmented crystal after the etching process 88
Figure 56: EUROBALL capsule-principle 92
Figure 57: Basic structure of AGATA germanium detectors 93
Figure 58: Capsule types 96
Figure 59: Sectional view of Model-type 2 97
Figure 60: Principle of the manufacturing process 98
Figure 61: Schematic representation of a measurement setup with PT100 sensors 99
Figure 62: Experimental setup 100
Figure 63: Welding micro crater 102
Figure 64: Principle of a leak test with a helium leak detector 103
Figure 65: Capsule model 1 with a double weld 103
Figure 66: Schematic diagram of the measurement setup 2 with the placement of the PT100 sensors 106
Figure 67: Graph of the PT100 sensors 1-8 of the measurement setup 2 . 107
Figure 68: Absorption image of the thermal camera in the temperature range of 24.4°C to 42.9°C before the welding process 108
Figure 69: Absorption image of thermal camera in the temperature range of 24.4°C to 42.9°C seven seconds after the welding process 108
Figure 70: Absorption image of the thermal camera in the temperature range of 56.6°C to 509°C during welding process 109
Figure 71: Absorption image of the thermal camera in the temperature range of 217°C to 711°C during welding process 110
Figure 72: Temperature diagram of the periodical heat test 110
Figure 73: Leak proof welded aluminium and copper pipes form 112

Figure 74: Temperature diagram of the periodical heat test 114
Figure 75: The lengths of the weld-area 116
Figure 76: Configuration of the getter element in the detector lid 117
Figure 77: Typical Heating Curves from a ST172/HIS/7-6/150C 118
Figure 78: Basic structure of the filter disk 119

List of Tables

Table 1: Acceptor elements of group III and donator elements of group IV relevant for Si and Ge diode detectors 4

Table 2: The two major p-n junction geometries and their properties. 10

Table 3: Properties of intrinsic Germanium 13

Table 4: The DIN 4670 36

Table 5: Overview of the processed Ge-detectors and crystals 50

Table 6: Overview of the measured resolution and used parameters of the detectors B1, B2, B5, B6 and B7 54

Table 7: Roughness parameters of Ge-Crystal B10 57

Table 8: Roughness parameters of Ge-Crystal B11 57

Table 9: Roughness parameters of Ge-Crystal B12 58

Table 10: Summary of the roughness parameters..................................... 58

Table 11: Summary of measured values with AFM 63

Table 12: Summarizes of the findings 70

Table 13: Specification of the capsule unit 94

Table 14: Type 1: Documentation of the experimental parameters 101

Table 15: Type 2: Documentation of the experimental parameters 104

Chapter 1

1. Introduction

Our understanding of the structure of atomic nuclei is based on the study of excited nuclear states and the transitions between them. Besides deexcitation by particle emission, γ-rays are usually emitted. Measuring the energy, angular momentum and polarization of these γ-rays by γ-spectroscopy is the most important tool to study the structure of the atomic nuclei. The continuous development of γ-ray spectrometers has permitted deeper and deeper insight in the structure of nuclear matter. For example, by replacing NaI(Tl)-detectors with germanium semiconductor detectors, a much improved energy resolution was obtained. Further optimisation of the detector and the crystals yielded better resolution and better detector response. The implementation of coincidence spectroscopy represented another milestone of γ-ray spectroscopy: This method significantly reduces uncorrelated background and thus allows for more rigid investigation of nuclear structure. A further reduction of uncorrelated background was achieved with the implementation of Anti-Compton-Shields (ACS) [NOL], [LIE], which suppress unwanted Compton scattering events.

Ge detectors are diodes operated in reverse-biasing. The operation of these detectors is based on the specific electrical character of semiconductors which is described by the *energy band atomic structure* of solids. The single crystal structure establishes allowed states of the electrons which are called *bands* and which are separated by forbidden energies gaps. The outer shell atomic electrons (or valence electrons) are confined in the *valence band* which correspond to low energy states of these electrons. If some of them obtain energy sufficient to leave the atoms, they occupy the band of the free electrons (still confined within the single crystal, but free to move across it due to fields or thermal diffusion) called *conduction band*. The conduction band electrons occupy high energy states and the energy states between both

bands are forbidden, since the electrons cannot occupy them. This is the band gap (or *gap*). Solids are categorized as insulators, semiconductors or metals depending on the particular band structure. If the gap width is more than 5 eV a solid behaves as insulator. Semiconductors typically have gaps of a few eV [KNO].

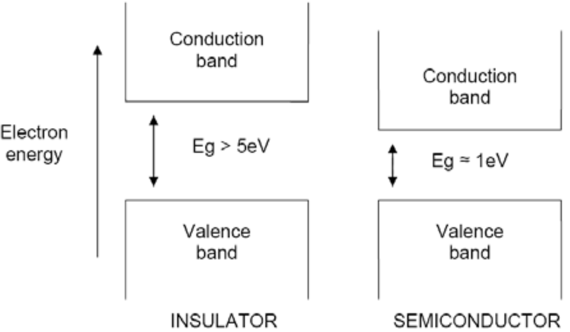

Figure 1: Band structure in insulators and semiconductors [KNO].

Semiconductors are classified in two major groups– *elementary* and compound semiconductors. Germanium and silicon belong to the elementary semiconductors, whereas for example CdZnTe (CZT), Hg_2I, GaAs belong to the compound semiconductors. Recently also organic semiconductors were synthesized [TNN] and [JCB].

When an electron obtains sufficient energy (by thermal excitation or radiation interactions) it can make a transition from the valence band to the conduction band. Thus in the valence band, due to the charge conservation rule, a “positive charge” which is called *hole* will appear. The specifics of the mobility of the negative charges, the electrons, and the positive charges, the holes, determine the electrical properties of the semiconductor.

In a completely pure semiconductor all the electrons in the conduction band and all the holes in the valence band are in equilibrium. In absence of ionizing

radiation the transitions between the bands would be caused by thermal excitation and such a material is called *intrinsic semiconductor*.

Each semiconductor, as any other solid, contains impurities which are due to imperfectness of the processing of the source material – purification and crystal growth. The purification process, due to the complexity of the chemical nature of the materials, causes always some minor amount of various elements (or even chemical associations) to remain embedded in the crystal lattice. Even if the purification is perfectly carried out, the crystal growth leads to defects and dislocations, generally described as crystal lattice imperfectness, and these two processes substantially change the behaviour of the semiconductor.

For example, if pentavalent element atoms remain in the crystal lattice of germanium, the excess electrons behave as free carriers thus filling the conductivity band with extra electrons. In the same fashion the trivalent element atoms incorporated in the crystal lattice cause unsaturated valences of the germanium atoms which can be also considered as hole. The energy states generated by pentavalent and trivalent impurities are close to the conduction and valence band respectively. Pentavalent impurities are Phosphorus (P), Arsenic (As) and Antimony (Sb) and trivalent ones are Boron (B), Gallium (Ga) and Indium (In). Some other elements which are not in groups III or V like Zink (Zn) also act as minor carrier impurities, generating energy states close to the conduction or valence bands.

Therefore, the elements which are generating excess electrons are known as n-type doping (*donors*) elements and the germanium doped with sufficient amount of such element is called *n-type germanium* (n-Ge). On the other hand, the elements which are generating excess holes are known as p-type doping elements (*acceptors*) and the germanium doped with such an element is known as *p-type germanium* (p-Ge). Typical concentration of the doping impurities of recent HPGe is 10^9 - 10^{11} at/cm^3. Indeed, germanium is the material which can be fabricated with highest material purity. Large-volume

crystals are produced with the Czochralski process [KNO]. The doping impurities of the semiconductors play an important role in determining the conductivity (and the related specific resistance) and the diode behaviour of the p-n transition. Table 1 describes the doping characteristics of the elements around Group 4 of the Periodic Table, where the elementary semiconductors as silicon and germanium are placed.

Table 1: Acceptor elements of group III and donator elements of group IV relevant for Si and Ge diode detectors.

Group	II	III	IV	V	VI
	Zn Cd	Al Ga In	Si Ge	N P As Sb	S Se Te

At any temperature which is not zero, an electron can obtain enough thermal energy to rise through the gap to the conduction band and to occupy one of the states which are there. The probability of occupation of the states in the conduction band is given by the Fermi function. In figure 2 is shown in principle the Fermi function for different temperatures: T4> T3> T2> T1> T0 = 0K.

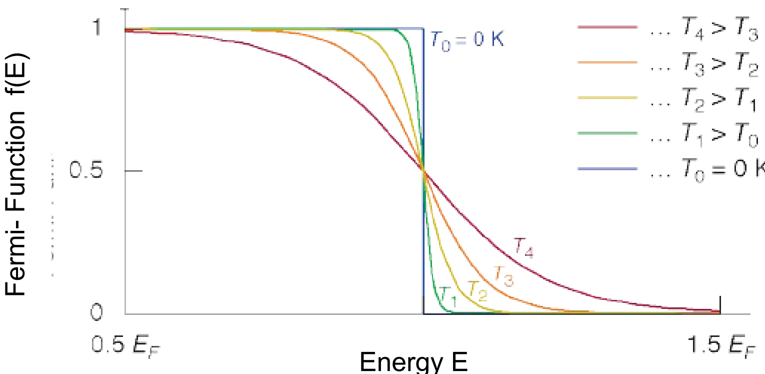

Figure 2: Fermi function [KRA].

The number n of free electrons can be calculated by multiplying the density of the states in the conduction band N(E) with the probability for occupation (or the Fermi function) F(E) and integrating from the lowest value of the conduction band to infinity [RFR]:

$$n = \int_{Ec=0}^{\infty} N(E)F(E)dE \qquad \textbf{(1.1)}$$

The Fermi function (in thermal equilibrium) can be expressed as

$$F(E) = \frac{1}{1 + e^{(E-E_F)} / kT} \qquad \textbf{(1.2)}$$

where E_F is the Fermi level, *k* the Boltzmann factor and T the temperature. Physically, the Fermi level is the chemical potential which is attributed to the electrons in the semiconductor. For an intrinsic semiconductor at temperature T=0 the Fermi level is the top of the occupied electron energy states, thus there is no electron with sufficient energy to rise above this level. At T>0 the Fermi level is placed in the middle of the gap. If the doping impurities are taken into account, E_F is shifted toward the conduction band (n-type) or valence band (p-type) since the donor and acceptor levels are close to the conduction band and the valence band respectively.

At zero temperature the valence band is filled with electrons and the conduction band is empty and the semiconductor behaves as an insulator. Partially occupied bands are important for the electrical character of semiconductors. The number of electrons in the conduction band which contribute to the transport is equivalent to the number of holes, in the valence band. The conductivity of an ideal semiconductor at T>0 is determined by the number of charge carriers in the bands and varies strongly with the temperature

$$n = 2(\frac{2\pi m_n kT}{h^2})^{3/2} e^{-(E_C - E_F)/kT} \quad (1.3) \qquad p = 2(\frac{2\pi m_p kT}{h^2})^{3/2} e^{-(E_F - E_V)/kT} \quad (1.4)$$

where m_n and m_p are the effective masses of the electrons and holes, E_C and E_V are the bottom of the conduction band and the top of the valence band and E_F is the Fermi level which is shown is Fig. 3 [KRA].

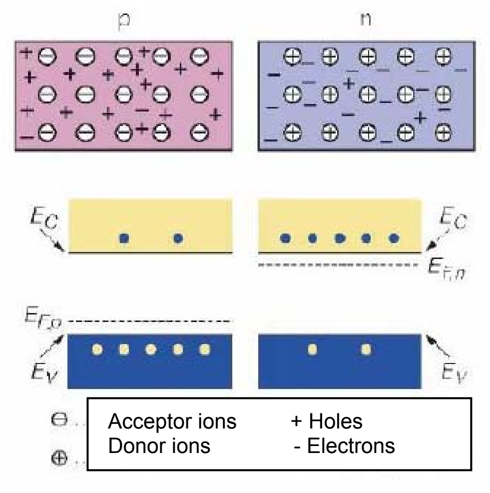

Figure 3: In the n-doped region the electrons are located as free charge carrier and in the p-doped region the holes are flexible [KRA].

If an electrical field is applied to the semiconductor, it affects the electrons and the holes leading to separation of opposite charges in opposite directions. The movement of these charges is determined by the electrical conductivity of the material. Let us assume an n-type material (n-Ge). In this case a certain number of free electrons, which are generated by the pentavalent atoms in addition to the electron-hole pair production as a result of thermal motion, will dominate the current. The contribution of the holes in the valence band is negligible, and these electrons are called majority carriers. The holes which are generated by the electron-hole pair production as a result of thermal motion are called minority carriers. Vice versa if p-type material is assumed, excess holes concentration in the valence band define

p-type majority carriers, while a small amount of electrons is majority carriers in the conduction band.

The electrical properties of a doped semiconductor material are determined by the majority charge carriers.

The free electrons and holes created by impurity atoms lie in the discrete energy levels created in the energy gap by the impurity atoms. In the case of n-type semiconductor these energy levels lie extremely close to the conduction band (e.g. the Boron levels in germanium are separated from the top of the valence band E_v by 10.8 meV and the Phosphorus levels are separated from the bottom of the conduction band E_c by 12.9 meV). Thus, the extra electron is easily excited into the conduction band, where it will enhance the conductivity of the semiconductor at room temperature. Similarly in the case of p-type semiconductor material the additional energy state is created close to the valence band. Electrons in the valence band are then easily excited into this extra level, leaving extra holes behind.

Semiconductors, whose conductivity is dominated by the impurity concentration, are called extrinsic semiconductors [LUT].

The most important phenomenon appears when two extrinsic semiconductors which have opposite doping are joined together - the p-n junction. The formation of a p-n junction creates a special zone at the interface between the two regions. Due to the difference of the Fermi levels on both sides of the junction the electrons and holes tend by thermal diffusion to align, leaving the p-side filled by electrons which compensate the holes there and the n-side filled by holes which compensate the electrons. This recombination of electrons and holes causes a charge build-up on both sides of the junction. This is shown in figure 3 and 4. This creates an electrical field gradient across the junction which eventually halts the diffusion process leaving a region of immobile space charge[1].

---

[1] *Strongly, this is valid if the generation current is neglected. In case of charge collection (thermally generated or due to ionizing radiation) the space charge varies slightly.*

Because of the electrical field there is a potential difference across the junction. This is known as the contact potential generally being of the order of 1V.

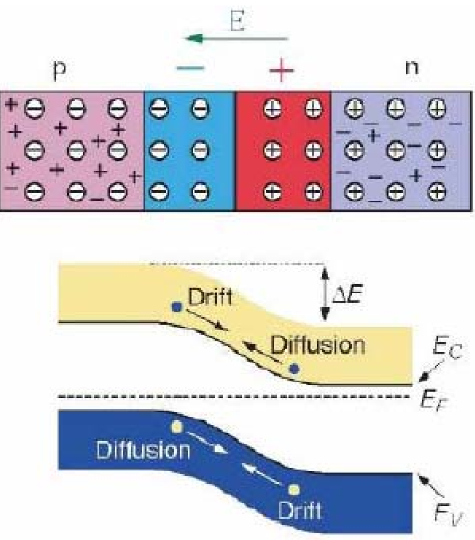

Figure 4: At the barrier between the p- and n-doped regions a junction is generated [KRA].

The zone in which the electric field is generated is free of charges (holes or electrons) and is known as depletion zone. If additional voltage is applied in direction of the built-in electric field it would remove even more charge carriers (due to their drift in the electric field, not thermal diffusion) from the both sides, thus increasing the depletion zone. In opposite direction the electric field would supply additional charge carriers, thus destroying the depletion zone, and above the value of the built-in field would cause electric current to flow.
The processes of charge separation and electric field generation are governed by the Poisson equation

$$\Delta \varphi = \frac{\rho(x, y, z)}{\varepsilon}, \tag{1.5}$$

where $\rho(x, y, z)$ is the space charge and $\varepsilon = \varepsilon_{Ge}\varepsilon_0$ is the dielectric constant ($\varepsilon_0 = 8.854 \cdot 10^{-12}\, F/m$ is the dielectric permittivity of vacuum and $\varepsilon_{Ge} = 16.6$ is the relative dielectric permittivity of germanium). The space charge $\rho(x, y, z) = e(N_d(x, y, z) - N_a(x, y, z))$ of donator N_d and acceptor N_a atoms depends of the special coordinates but is considered constant in the following to simplify the argument. At the boundaries of the semiconductor conditions defining the physics case are imposed, often these are the voltages, the normal and tangential component of the potential and symmetry conditions [LUT].

Since the depletion zone does not possess any free charges it may be considered as capacitor. The detector capacity is an important factor which limits the energy resolution. Table 2 shows the equations, boundary conditions, the solutions for the electric field, depletion voltage and detector capacity for the two major p-n junction (and detector) geometries – planar and coaxial (see also figure 6).

Table 2: The two major p-n junction geometries –coaxial and planar [KNO]. Also is given the boundary task describing the electric field of the detector- the differential equation and the boundary conditions. Important formula, following solving of the boundary task in planar and coaxial geometry- the electric field, depletion voltage and capacity of the detector, are presented.

	Planar	**Coaxial**
Detector Geometry	d, p+, i-n, n+, x $\rho = e(N_A - N_D)$	i-n, p+, n+, r, r_1, r_2 $\rho = e(N_A - N_D)$
Electric field differential Equation	$\frac{d^2\varphi}{dx^2} = -\frac{\rho}{\varepsilon}$	$\frac{d^2\varphi}{dr^2} + \frac{1}{r}\frac{d\varphi}{dr} = -\frac{\rho}{\varepsilon}$
Boundary Condition	$\varphi(d) - \varphi(0) = V$	$\varphi(r_2) - \varphi(r_1) = V$
Electric Field $\|E\|$	$\frac{V}{d} + \frac{\rho}{\varepsilon}(x - \frac{d}{2})$	$\frac{\rho}{2\varepsilon}.r + \frac{V - \frac{\rho}{4\varepsilon}(r_2^2 - r_1^2)}{r\ln(\frac{r_2}{r_1})}$
Depletion Voltage	$\frac{\rho d^2}{2\varepsilon}$	$\frac{\rho}{2\varepsilon}\left[r_1^2 \ln\left(\frac{r_2}{r_1}\right) - \frac{1}{2}\left(r_2^2 - r_1^2\right)\right]$
Capacity (at V_d)	$\frac{\varepsilon}{d}$ Per square unit	$\frac{2\pi\varepsilon}{\ln\left(\frac{r_2}{r_1}\right)}$ Per linear unit

The p-n junction with equal impurity concentration is essentially not met in the semiconductor detectors. The requirement for depleted (and sometimes large depleted) volume needs to applying of high purity material. However, in order to obtain sufficiently strong p-n junction, normally only an abstraction. Typically, only one of the contacts has strong doping concentration and in this case the depletion develops only in one direction. The comparison of both depletion processes is given in figure 5 [KNO].

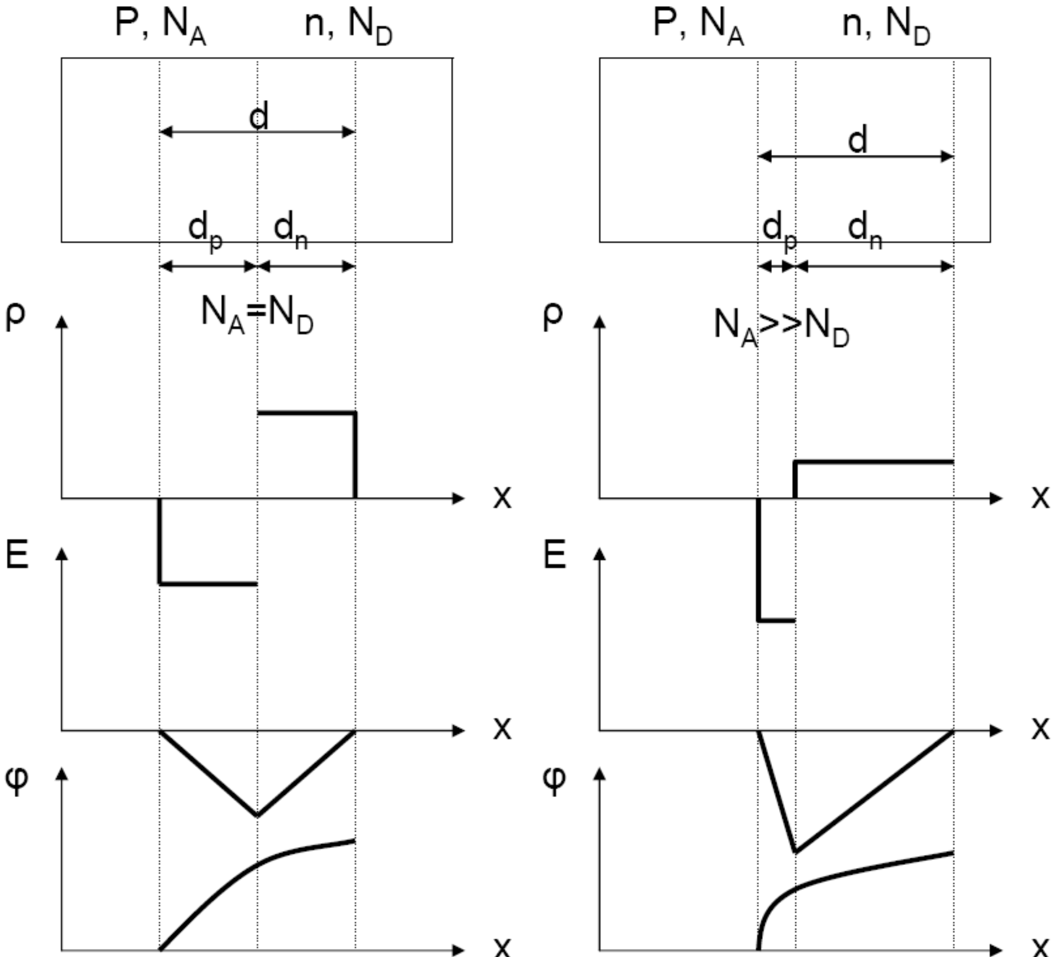

Figure 5: A p-n junction-charge electric field E and potential distribution φ. Left: p-n junction with equal impurity concentration N_A (acceptors) = N_D (donators) at both sides. Depletion depth d expands toward n and p- sides equally (d_n=d_p). Right: p-n junction with heavily doped p-side and low doped n-side NA>>ND. Depletion depth d expands predominantly toward n-side (d_n>>d_p) [KNO].

The thermally generated charge carriers in the depleted zone are removed by the electric field and this is the detector bulk current. For a typical p-n junction it is given by

$$J_{vol} \approx -e\frac{n_i}{\tau_g}\sqrt{\frac{2\varepsilon_0\varepsilon}{eN_D}V} \qquad \textbf{(1.6)}$$

where J_{vol} is the volume generated current per unit area, N_i is the intrinsic carrier concentration and τ_g is the carrier lifetime. The temperature dependence of the bulk current is hidden in the intrinsic charge carrier concentration and carrier lifetime. Taking into account this dependence the formula can be rewritten as

$$J_{vol} \propto T^2 e^{-E_g(T)/2kT} \qquad \textbf{(1.7)}$$

with E_g the band gap energy.

The total current of the detector is the sum of two currents – the bulk current and the surface current. The open surface between both contacts of a p-n junction is an area which is easily damaged by mechanical treatment and also contains adsorption impurities. They generate specific states which essentially lead to increased current and this current is difficult to predict. Too many factors must be taken into account – the treatment of the surface – polishing, lapping, etching, passivation etc. and the momentary condition of the surface due to the operation of the detector. Passivation of the surface greatly reduces the last effect, leaving the manufacturing issues to dominate. The mechanical treatment – cutting, grinding, polishing and lapping predetermine the properties of the open surface of the detector and thus has the major importance on the surface current.

To derive at a Ge diode which can be used as γ detector the bulk current needs to be minimized by cooling and the surface current by careful manufacturing. If the remaining current flow in the electrical field is sufficiently low, charge carriers generated by any interaction with ionizing redaction can

be distinguished from the current noise as a pulse signal. For HPGe this temperature is ≤ 100 K. Therefore liquid nitrogen with a boiling temperature of 77 K is often used as cooling agent.

If a γ- ray interacts with an electron in the intrinsic zone of the detector diode it transfers part or all of its energy to it. The most common processes are Compton, Photo and Pair effect [KNO] depending on the energy of the γ- ray. By interaction of this primary electron with further electrons an electron avalanche develops. The energy to create an energy hole pair is only 3 eV, therefore the number of electrons, respectively holes is large for the typical γ- ray energy range of 100 keV to 10 MeV leading to negligible statistical fluctuations. Table 3 shows the saturation mobility of the charge carries for high electrical fields. Taking into account typical electrode distances of few centimetres leads to a drift time of a few 100ns.

Table 3: Properties of intrinsic Germanium [KNO].

	Ge
Atomic number	32
Atomic weight	72.60
Density (300K); g/cm^3	5.32
Atoms/cm^3	4.41×10^{22}
Dielectric constant (relative to vacuum)	16
Forbidden energy gap (300K; eV)	0.665
Forbidden energy gap (0K; eV)	0.746
Intrinsic carrier density (300 K); cm^3	2.4×10^{13}
Electron mobility (77 K); cm^2/V • s	3.6×10^4
Hole mobility (77 K); cm^2/V • s	4.2×10^4
Energy per electron-hole pair (77K); eV	2.96

During their drift time the charge carriers induce an electrical signal at the electrodes. The signal strength is proportional to the transferred energy of the γ quantum.

1.1 Detector geometry

One of the main requirements of a germanium detector is the detection efficiency. Essential is the size of the active volume, because the absorption probability of a γ quant depends exponentially on the thickness of the absorber. Therefore, it is very important to achieve an expanded depletion zone when constructing a detector. In principle, there are two different germanium detector geometries, planar and coaxial. In a planar geometry the detector contacts are flat and parallel to each other. The disadvantage of this geometry is the relatively low active volume and the high leakage current on the non-contact sides.

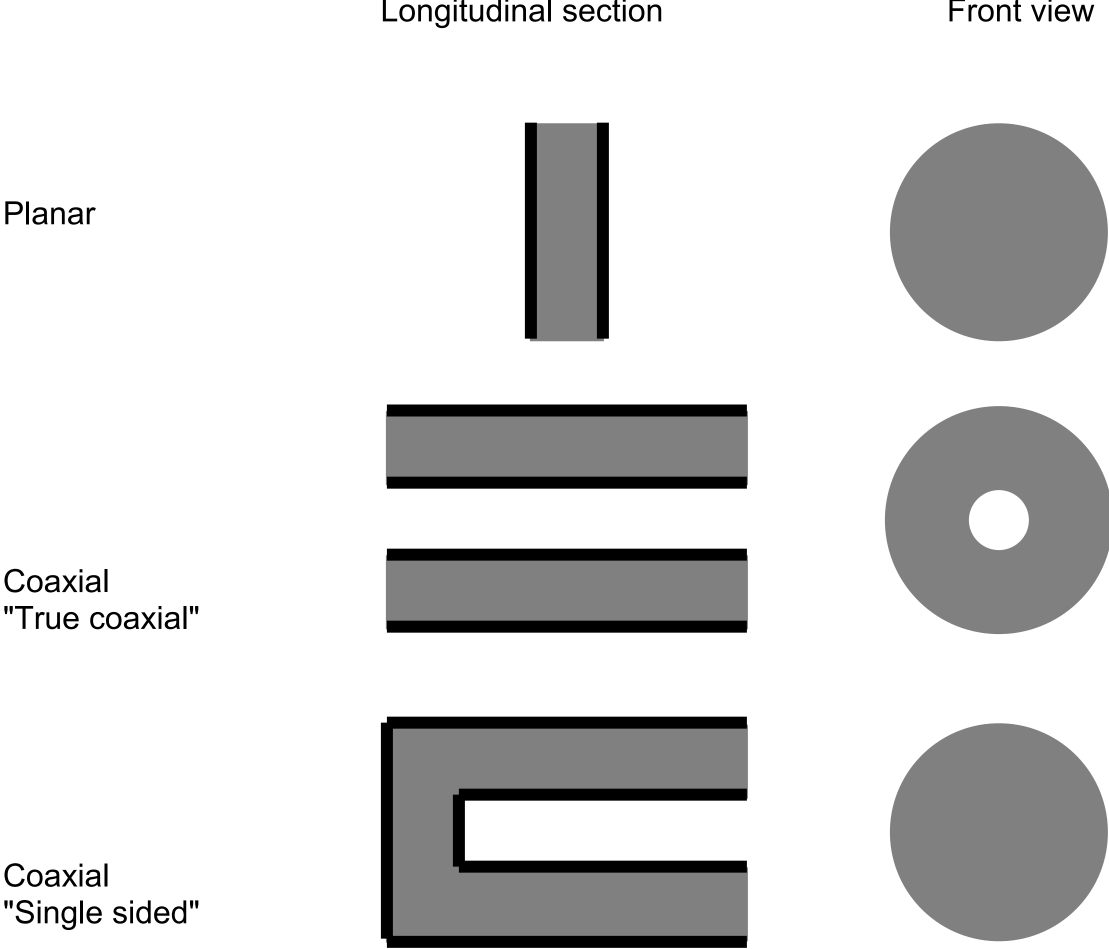

Figure 6: Different detector geometries [KNO]. Contacts are indicated by thick lines.

The coaxial type detector has two varieties – "true coaxial", which can be approximated by a thick wall tube (it has two open surfaces), and "closed coaxial" which can be approximated by a thick wall cup (it has one open surface). The coaxial hole typically measures about 4/5 of the total length of the crystal. For both coaxial cases, the active volume is much larger compared to the planar geometry. The voltage, which is creating the depletion zone, is dependent on the diameter of the crystal. The "true coaxial geometry" has the disadvantage of a higher leakage current at the non-contacted sides. The most common geometry is the single sided coaxial detector. With this geometry the largest active volume and the lowest leakage current can be achieved. Figure 6 shows the detector geometries. The contacting of the crystals is marked by thick lines.

In case of a coaxial detector the blocking contact is eventually at the outer cylindrical surface and the Ohmic contact at the inner cylindrical surface. This requirement comes from depletion voltage considerations. If the boundary task is solved for a geometry where the blocking contact is at the outer cylindrical surface, the additional energy needed to deplete volume layers going inwards is only slowly rising because the volumes to be depleted become radially. To the contrary a blocking contact on the inner surface, and thus depletion going outwards, needs much more energy to deplete the next layer because the volume is getting larger.

Due to the peculiarity of the solutions of the boundary tasks for planar and coaxial detector the depletion volume for a given voltage is smaller for the planars. Therefore, only the coaxial geometry is well suited for large volume germanium detectors.

High purity germanium crystals, which are used as detector material, are grown by the Czochralski method. The purification is done by the floating zone method in a pot [ORT]. Currently single crystals of HPGe can be fabricated approximately up to 10 cm diameter and 30 cm length. Due to the

processing technology the impurity concentration increases with the crystal radius and its length. To preserve good detector characteristics therefore the outer few mm are usually removed and cylinders of 10 to 14 cm length are cut at most.

1.2 The development of encapsulated detectors

As discussed in chapter 1.1 the volume at the largest Ge crystal used for detectors is limited to a few 100 cm^3. Therefore, in order to obtain significant coincidence yield in nuclear spectroscopy, a multitude of Ge-detectors as a system is needed. Developing such a complex detector system is a financial challenge to most research institutions and also their development capabilities. For this reason, collaborations for designing and building efficient γ-ray spectrometers have been established. More and more Ge-detector units with larger crystals were used in order to cover an as high percentage of the total solid angle around the target as possible. For this purpose the European collaboration EUROBALL and the US project GAMMASHERE have been established [CTT]. The aim of the EUROBALL collaboration was to build and operate a highly efficient γ-ray spectrometer based on Compton suppressed germanium detectors. Different criteria were used to compare the efficiency and the cost/benefit ratio of such a project. In Monte-Carlo simulations (e.g. [GER], [UTZ], [KUT]) the main parameters of the γ-ray spectrometer were determined for different detector concepts. The simulations and concept criteria indicated that only modernisation of detector technology could further increase the efficiency of such spectrometers. It followed the idea to realise a large Ge-volume with several Ge-crystals in one cryostat, and later to surround this Ge-block with an ACS. However, the integration of a finished single crystal into a cryostat is very critical and not always successful. An installation of several crystals would increase this risk. To realise this concept a new technology of detector building was required. This marked the beginning of an hermetic crystal enclosure, based on an idea of Jürgen

Eberth (IKP, Univ. Cologne). By hermetic encapsulation of the crystals, the Cluster detector [EBE], consisting of seven large-volume encapsulated Ge-detectors, has been realised. The encapsulation technology was developed and patented in collaboration with the KFA Juelich and the University of Cologne in conjunction with the manufacturer INTERTECHNIQUE (today CANBERRA Eurisys). This new concept proved successful since after more than 15 years of operation all the encapsulated detectors are still intact and have been used extensively in EUROBALL and until very recently in the RISING project [RIW] and [RIS].

1.3 Motivation

To realize HPGe germanium detectors, a variety of different technological processes are used. Some of these processes have been known for decades. By improvement of the semiconductor and detector technology more efficient and complicated detectors and detector structures have been developed. For example, several optimisations of the detector shape or crystal properties allowed better energy and time resolution.

Nuclear physics experiments are getting even more complicated. The nuclei of interest will be produced with enormously low cross sections, and to perform γ spectroscopy of such nuclei becomes a challenge. Not only the detector efficiency plays a role, but also other properties of the spectrometer are important – e.g. the Peak-to-Total ratio or the possibility of γ tracking and Imaging. To approach the goal of an “ideal spectrometer” one has to move toward more complicated and complex systems as tracking or imaging arrays. The challenge of the development is not only to *achieve the scientific goals* but also to make this *affordable*. Therefore, careful review and optimisation of the technological processes of detector manufacturing is necessary. In figure 7 the detector manufacturing process is presented, which is considered as guideline in this work [KOJ]. There are critical and important manufacturing

processes. Irreversible damage on the crystal can be generated during critical processes. The important processes add significantly to the functioning of the detector. Here an incorrect application or appearance of defects, allow a repetition of the process with the same crystal. The phase 1 to 3 of this flowchart shows systematically the development process for each type of germanium detector.

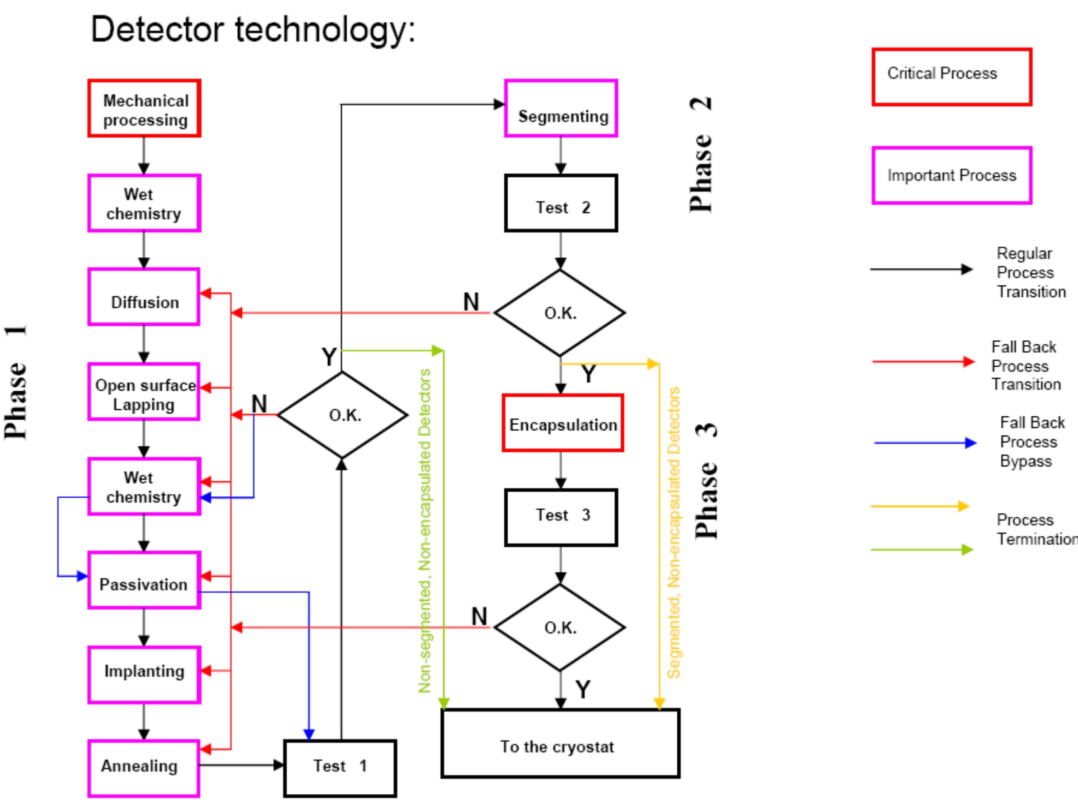

Figure 7: Detector technology [KOJ].

This work concentrates on the two critical processes of the detector manufacturing technology - the mechanical processing of crystals and the hermetic encapsulation of detectors. These processes are crucial for the manufacturing of modern HPGe detectors and therefore, their quality and reliability are particularly important. The detector shape usually is achieved by machining processes – cutting, grinding and lapping. The accuracy of any of them is not sufficient or is very difficult to be controlled, as well as the quality

of the surface. Detector geometries and their properties can be designed by computer modelling and simulation. However, by the classical manufacturing processes it may not be possible a particular shape to be produced with sufficient precision. Moreover, the risk to destroy or severely damage the expensive crystal is not negligible. Therefore in this work new methods for mechanical treatment and control of the surface and the shape of the crystal have been tried. Further attention has been paid on the mechanical segmentation of germanium detectors as a possible way to produce segmented lithium contacts. Machining inevitably affects the surface structure of a Ge crystal. Cracks, dislocations in the crystal lattice and other defects may occur. Furthermore, contaminating substances may be deposited on the surfaces. Any of these effects could be responsible for malfunction of the detector. Therefore avoiding or at least diagnosing it at the earliest is another important aspect to reduce the manufacturing cost of the detector. The study of germanium detector surfaces concentrated on the mechanical treatment impact on the crystal surface defects and the identification of the detector surface contamination which are generated during the manufacturing.

The encapsulation is the second critical process, which may lead to a complete loss of a detector. The classical method used so far for EUROBALL, MINIBALL and AGATA detectors relies on electron beam welding of a thin Al-capsule, containing the crystal, with a complex lid. Obviously this process is well under control, however, it is unacceptably expensive. Therefore in this work a more cost effective solution, based on the novel concept of Laser welding and an improved vacuum sealing has been studied.

Chapter 2

2. The basics of surface characterisation

In this chapter, some terms and general definitions are introduced for description and interpretation of a germanium surface and the measured data. At first, some basic principles of mechanical treatment of surfaces emphasizing on germanium crystals are presented and the syntax is specified to describe the geometry of the reconstructed surface. The focus of this chapter is the description of machining surface defects and their effects. The described measurement methods and their principles are also the basis for the further analysis of the results, which is presented in chapter 3.

2.1 Mechanical crystal processing

By mechanical crystal treatment the change of the body of the crystal through impact of mechanical forces is understood. These forces are introduced directly through the tools or with help of processing means, for example, loose grains of hard materials. Artificial effects, which are generated by the crystal treatment, are a form- or state change. For example, to shear off a semiconductor wafer of a compact crystal is considered a macroscopic form changing step. The separation planes undergo a state change through the treatment, in terms of surface characteristics as well as interferences of the surface volume sector.

On the one hand, mechanical crystal processing means the destruction of the monocrystalline structure. On the other hand, the formation and transformation of structure defects with respect to type, density and distribution in the mono crystal volume [HER].

For the most part, the mechanical crystal treatment consists of abrasive cutting (sawing), grinding and lapping. Accompanied cleaning of surfaces is

realised with deionised water and/or organic solvents and washing-up liquid in a cleaning system. Afterwards, the surface contaminations are removed in special cleaning steps. The next step is a treatment with chemical cleaning and polishing to remove semiconductor material. In case of germanium, for example, that is a short etching combined with the removal of a specific thick layer, so called defect layer. In the following chapters the principle of the manufacturing methods of grinding and lapping is introduced. In principle the difference between lapping and grinding is [ENG]:

- Grinding is cutting with bound grains
- Lapping is cutting with loose grains

In the following the principle of shaping methods for monocrystalline germanium surfaces are presented.

2.1.1 Principle of Grinding

The grinding treatment is a manufacturing process which uses a tool with undefined blade form. This means, the geometry of the abrasive grain, being the blade and the position of the cutting relative to the work piece are undefined. An abrasive tool is characterised by three phases: the abrasive grain, the bonding material and the pores.

In the grinding process, the blades are not constantly in action on the work piece surface and the cutting depth is low in relation to the size of an abrasive grain. Thus, the cuts (chips) are very small and in general are known as grinding dust. The cutting of chips from the surface depends on different factors, for example, the hardness and cutting ability, the toughness and mechanical, thermal and chemical resistance of the work piece [see. [DUB] and [HAM]]. In figure 8 is shown the principle of the grinding process. Typically grinding is used for the rough shaping of germanium. For germanium diamond, Silicon Carbide or Corundum (Aluminium Oxide) grains of about ~150 to ~300 µm are normally used.

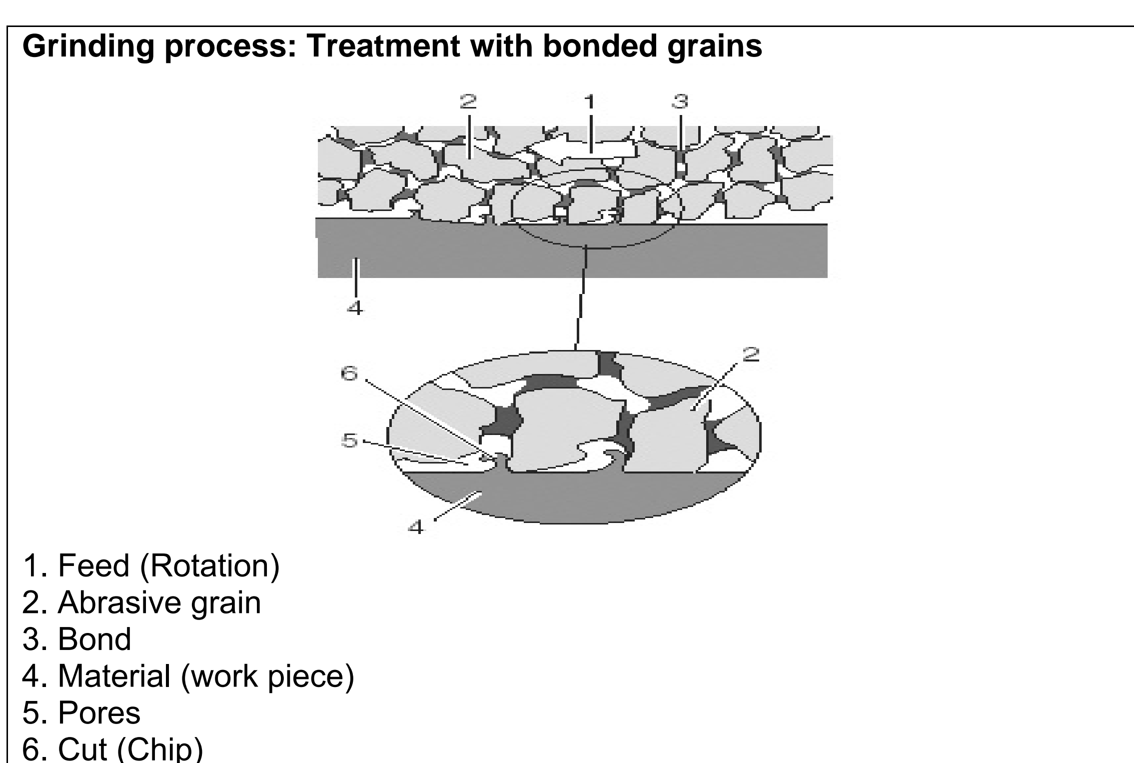

Figure 8: Schematic of the grinding method.

2.1.2 Principle of Lapping

According to [DUB], material is removed from a surface by the lapping process through rolling motion of loose grains. Thus, the lapping process is also a treatment with an undefined blade form. The loose grains are embedded in a paste or liquid which is situated between the surface and a lapping disc. Together with a rotation or feed of the lapping disc, the lapping process is generated on the surface. Figure 9 shows the principle of the lapping process. Normally lapping is employed as finish cutting in the mechanical process and diamond, Silicon Carbide or Corundum (Aluminium Oxide) grains of ≥10 µm are normally used. Typically surface layers of a few µm are removed by lapping.

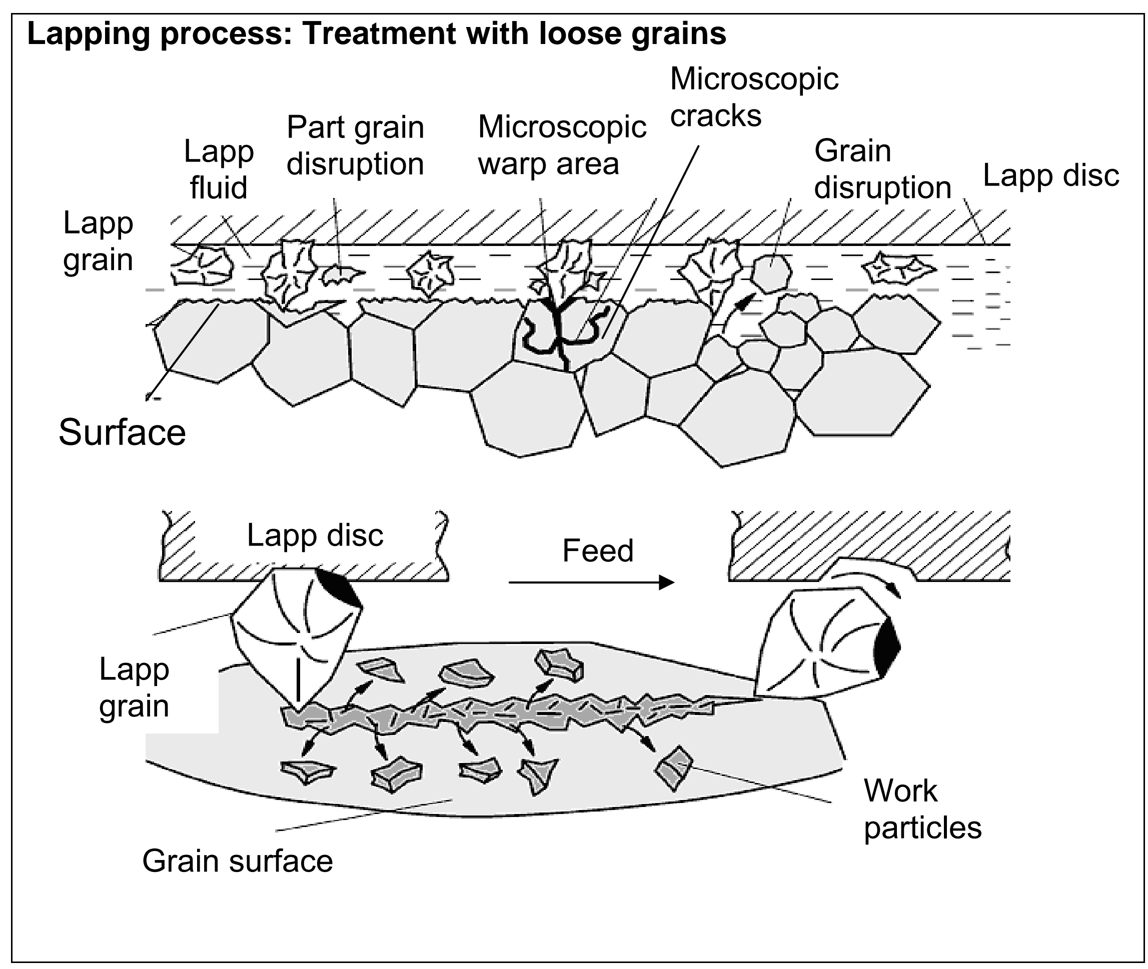

Figure 9: Schematic of the lapping method.

2.1.3 Principles of Ultrasonic-Grinding

Ultrasonic-Grinding is used in many industrial applications involving advanced materials. The use of a flexible, vibratory system for grinding, drilling and milling is the basis of this process. The principle is that in addition to the conventional grinding described in chapter 2.1.1 an oscillation of the tool is added during the treatment process [ULT]. This oscillation is produced by an actuating system in the machine spindle. This oscillation along the Z-direction combined with the rotating tool allows a very fine treatment of the material, as illustrated in figure 10.

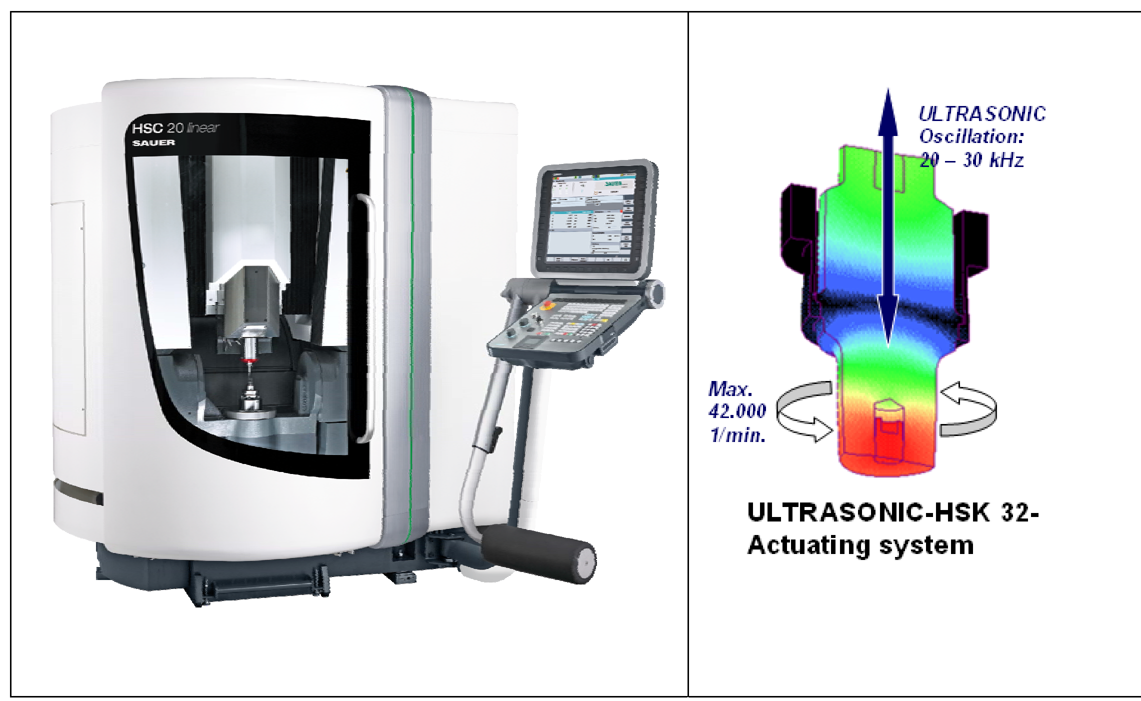

Figure 10: The combined treatment principle.

This method, combined with a qualified control panel, allows to obtain excellent surface qualities, for instance the parameter arithmetical mean deviation of the roughness profile Ra<0.2 µm, which is described in § 2.3.3.2. In addition to this, the forces applied to the sample material during the process are reduced, which means a reduction of the micro cracks.

2.2 Defect layers as a result of mechanical crystal processing

Any mechanical surface treatment produces a defect layer below the crystal surface. The defects cause variations in the real crystal structure which come in addition to the inherent deformations from the crystal growing process. Thereby, different defect types are generated. The depth with respect to the surface is specific for the characterisation of the defects. In general, this depth is called defect depth or deformation depth [see [HER]].

2.2.1 Defect model

In the literature [HER] a defect model for mechanical treatment is established, which distinguishes four layers:

1) Polycrystalline zone: The strongly fissured surface region, with many cracks varying in length and direction. Polycrystalline structures with non-aligned, twisting, crystallites and crystal particles are clamped between the cracks. This layer has generally a thickness of a few microns.

2) Crack zone: In this area, micro cracks dominate. Elastic stress appears with these cracks, which means, there exists also twisted and deviating crystal areas.

3) Changing zone: Is the zone of the maximal crack depth. There exist some particular micro cracks and elastic stress far into the material.

4) Elastic stress zone: In this area there are no structure defects generated by the mechanical processing, but solely mechanical stress of the crystal structure.

Fig.11 shows schematically the four zones of the model.

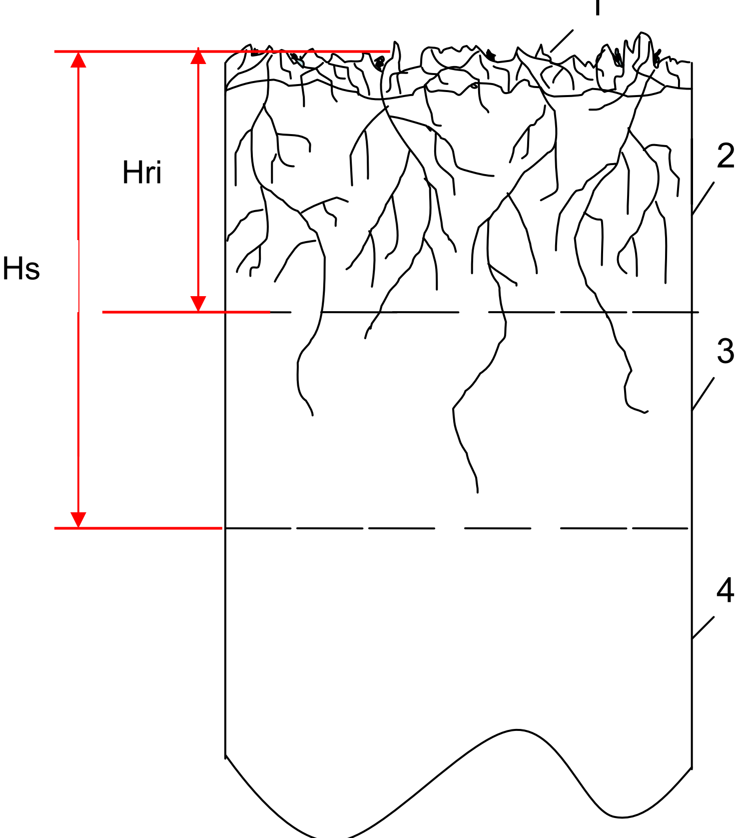

Figure 11: Defect model: the Polycrystalline zone (1), the crack zone (2), the changing zone (3) and the elastic stress zone (4). Layers one and two generate the crack zone Hri, which is approximately the grain diameter of the treatment material. The crack zone Hri and changing zone generates the defect depth H_S, which depends on the maximum roughness depth Rt (see § 2.3.3.1) as well as on the intensity of the treatment. Normally the depth of these three layers is about 30 to 100 µm.

The mechanically produced structure defects are most probable in the first three layers. Depending on the intensity of the treatment, these three layers (Hs) have depths from 30 to 100 µm. In particular, different types of dislocations are dominant in the crack zone. In general, the different layers overlap and interact with each other.

The defect depth (Hs) is dependent on the crystal- and processing parameters and is determined empirically by:

$$Hs \approx d1 \times Rt \times Hri \qquad \textbf{(2.1)}$$

where d1 is the grain diameter of the treatment material, Rt the maximum roughness depth and Hri the crack zone. The crack zone Hri is approximately:

$$Hri \approx d1 \qquad \textbf{(2.2)}$$

The maximum roughness depth Rt, described in § 2.3.3.1, depends on the treatment material, for example Corundum or Silicon carbide. Thus, a measurement of this parameter is performed in the surface characterisation chapter 3.

2.2.2 Characterisation of semiconductor surfaces

Thus, the mechanical treatment is the origin of the defects and their consequences. Some of these defects can be detected with optical methods during the machining process. Other defects are indicative in the subsequent manufacturing process, mainly after the etching or can be detected with different depth measurement systems after the process. In addition to the mechanical treatment, surface defects may be induced by the cleaning and etching processes. All the relevant observables are discussed in the following:

• Micro cracks:

Surface cracks with crack lines. The schematic of this defect is shown in figure 11 in the defect model in section 2.2.1.

• Scratches:

Linear striations on the surface of the crystal (see figure 12). They are created by irregular treatment of the material, by different feed speed of the treatment machine and by different treatment rate of the tool.

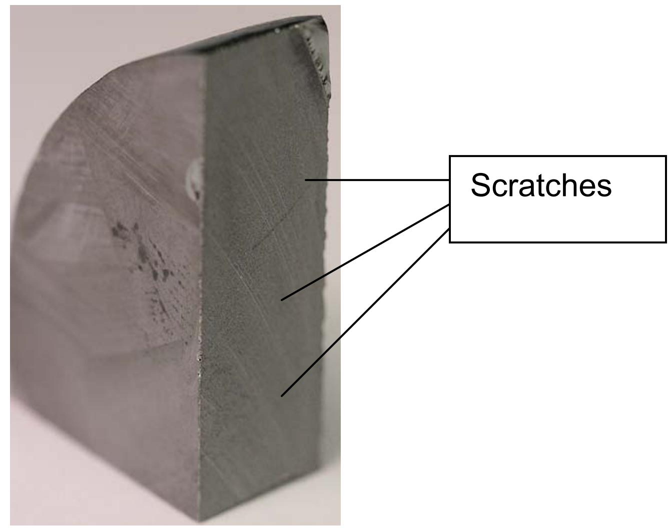

Figure 12: Example of mechanically produced scratches.

• Haze:

A haze is a surface distortion which is produced by an irregular treatment. A haze can be produced by grinding, lapping or polishing.

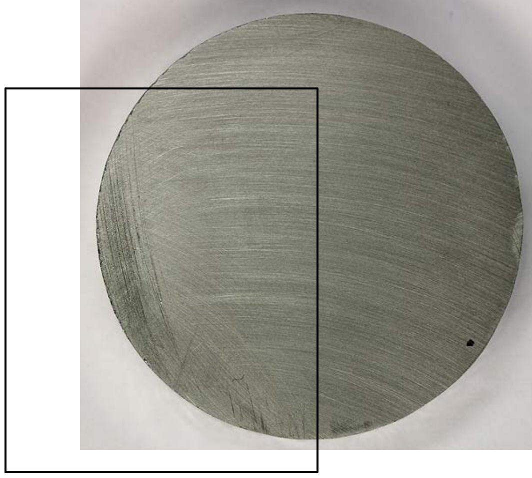

Figure 13: Example of mechanically generated haze.

• Edge chips

Flat plate-shaped chips with different geometric shapes and different sizes (see figure 14). These defects appear always along the corners of the surface and are produced in different ways: Responsible for these defects are the feed speed of the machine, the transmission and speed of the tool, the material character of the crystal, and the sharpness and the configuration of the tool.

Figure 14: Example of edge chips.

• Cleaning contamination:

Cleaning is essential to remove undesirable substances from the mechanical treated surface [HAL]. In this case, there are two important considerations:
1. The cleanliness of the crystal surface.
2. The cleanliness of the machine, the fixing device and the environment. Also chemical processing steps may induce contaminations. There are different types of contaminations, which are mainly created by workers, the ambient air, the chemicals (gases, solutions) and by the equipment.

Those are:
- Microscopic contaminations: for example, particle in the ambient air. Microscopic contaminations are particles, which are deposited on the surface of the semiconductor. Sources of this contamination are the ambient air,

clothing of workers, abrasions of flexible parts in process equipment and inadequately filtered liquids, like etching and cleaning solutions or etching residues after this process. Microscopic contaminations create shadowing effects. In addition, they can obstruct ions in the implantation process or affect the etching of the surface.

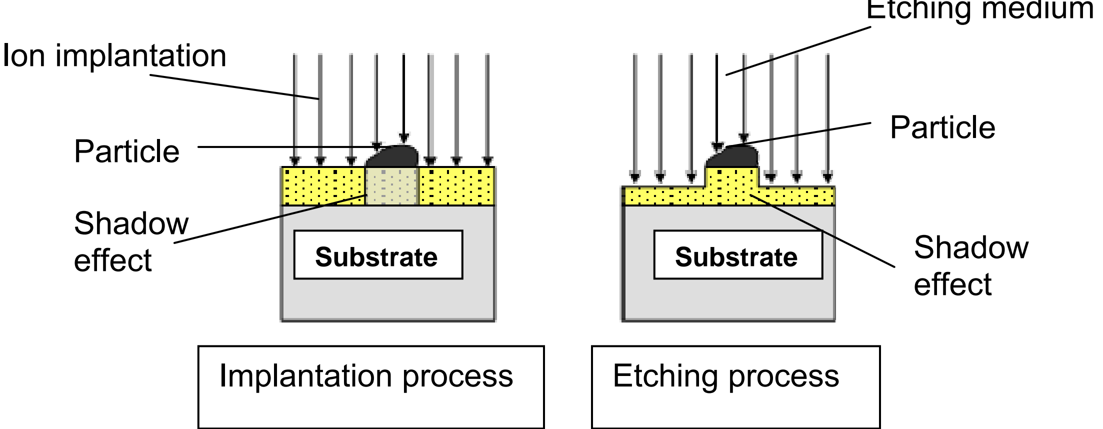

Figure 15: Microscopic contamination during the implementation and etching process.

Particles can be trapped by layers and create irregularities in thickness and adjacent layers may burst at these places (see figure 16).

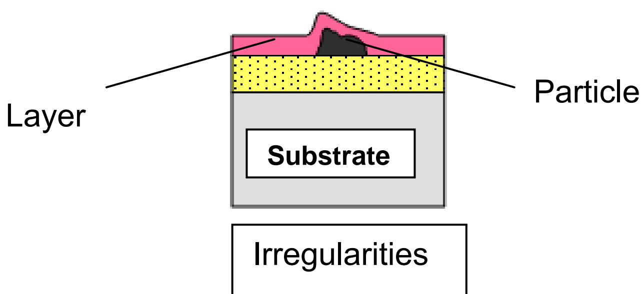

Figure 16: Irregularities in thickness.

- Molecular impurities: for example, carbon hydride from oils.

Molecular contaminations may result from solvent residues on the surface or through deposits of oil, which are generated by the cooling fluid of the mechanical treatment. These contaminations can be located on the surface or diffuse into the surface layer affecting the electrical characteristics of the

final detector.

The main sources of contaminations are:

- Ionic, e.g. hand perspiration
- Atomic, e.g. heavy metals from solutions
- Alkaline and metallic contaminations

The main source of contamination is the human factor, through salt transported by skin and through the air. Another source is inadequately deionised water delivering ions of sodium or potassium to the crystal surface. Heavy metals are immanent in etching solutions, and may yield to a contamination too.

• Orange peel effect:

The orange peel effects named after their particular appearance are surface defects recognised after the chemical processing. The sources of this defect are micro cracks, scratches and small edge chips. In the etching process the etching speed depends on the surface structure and thus can enhance the defects.

Figure 17: Orange peel effect.

• Dimples:

Flat depressions in relation to the normal surface. Likewise, these defects appear visible after the etching. In principle, they arise like the orange peel

effect, by diffusion of etching material in the rough mechanical defects of the surface. The difference is simply in the depression and in the expansion of the defect as well as the number of dimples.

Figure 18: Dimples of a Ge-crystal.

• Waves

For the sake of completeness, the largest deviations from the ideal surface are called a wave. It describes the deviation of the highest to the lowest point of an ideal reference area [HAM].

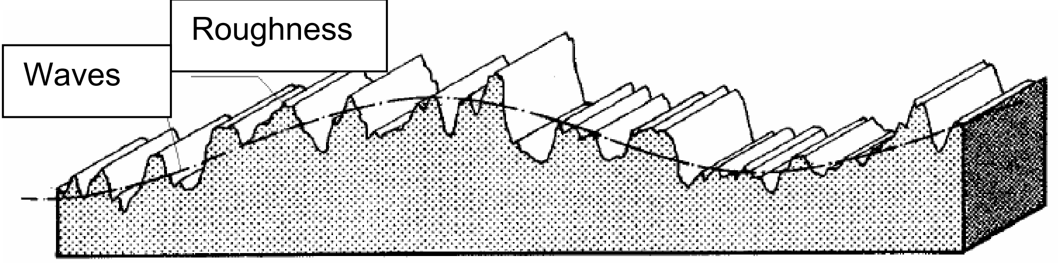

Figure 19: Waves of the surface.

2.3 Basics of surface measurement

A surface represents the limit between two media, for example, the limit between a solid material and the air [DUB]. The "real surface" is the detected surface of a work peace. The "geometrical surface" is the ideal surface, which is defined by drawings and/or other technical documents [DIN1982]. A completely smooth surface is extremely difficult to produce but unnecessary for the proper function of a Ge semiconductor. Naturally, discrepancies exist between the "geometric surface" and the "real surface". These deviations are specified as form deviations and can be divided in six orders. Form deviations of different orders usually appear concurrently [HAM]: Form deviation (1st order), waviness (2nd order), roughness (3rd and 4th order), structural conditions (5th order) and lattice structure (6th order). Figure 20 shows the essential form deviations for this work.

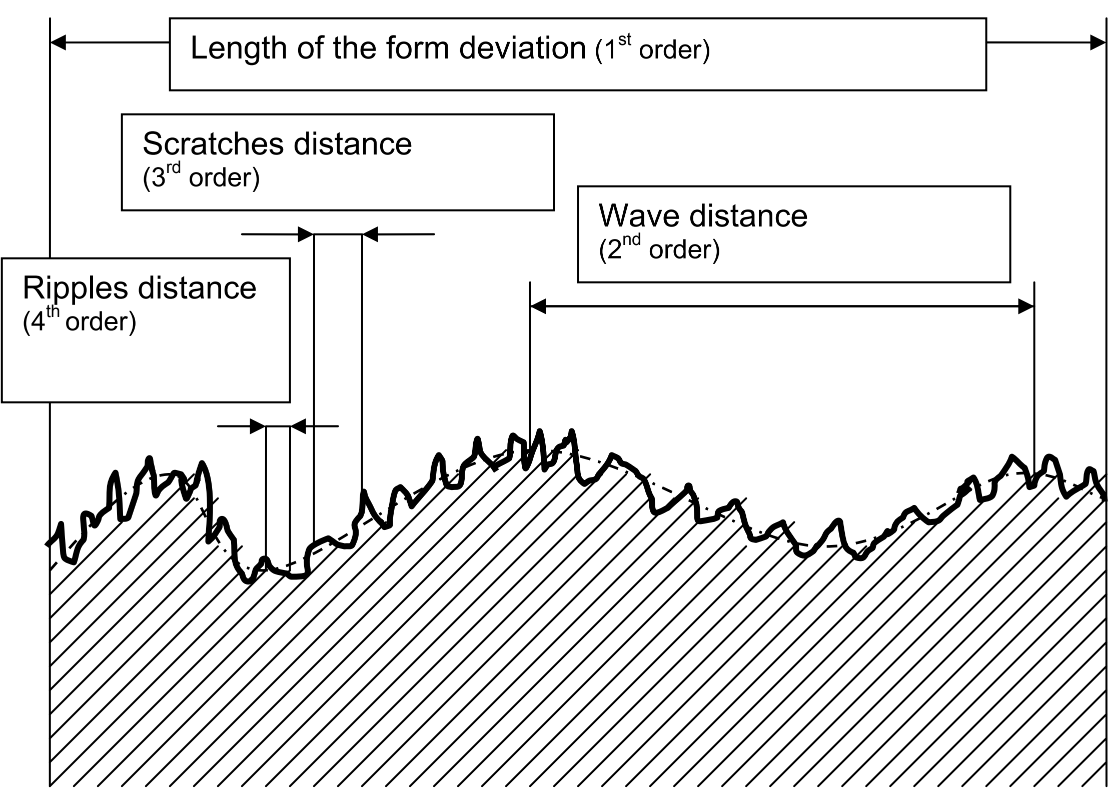

Figure 20: Form deviation: 1st to 4th order.

2.3.1 Orders of the form deviations

The reasons of form- and waviness variations are identifiable in the system: work piece – tool - machining. Oscillations due to tool wear, for example, are a source of waviness [BOD]. The reasons of roughness variations are located in the manufacturing processes. Roughness variations have special effects on the micro-systems. For example, the surface roughness affects electrical characteristics of micro-systems, as capacity and the electrical conductivity [PAT]. The deviations of the ideal shape shown in Fig. 20 can be attributed for instance to:

- Deficiencies in the mechanical guidance
- Clamping of the work piece to the fixing device
- Vibrations and shocks
- Deformations as a result of shape-, mass-, and centrifugal forces
- Cutting geometry and cut formation

In practice the produced shape of the work piece deviates more or less from the ideal geometric shape. These variations of the work piece are described by the order of the form deviations as indicated in table 4 following DIN 4760.

Table 4: The DIN 4760 determines the form deviations of surfaces. It is divided in six different orders, 1st till 4th orders define the surface characteristic.

Surface irregularity	Example	Reason
1st order: Form deviation	Unevenness Non-circularity	- Machine tool axis error - Deflection of workpiece or tool - Error in chuck
2nd order: Waviness	Waves	- Vibrations - Tool/eccentric clamping - Form defects of the cutter
3rd order: Roughness	Grooves Scratches	- The form of the cutter edge - Feed rate - Infeed of the tool
4th order: Roughness	Ripples	- Chip forming process - Shear procedures
5th order: Structural conditions	Grain boundaries	- Grain boundaries cracking - Crystallisation procedure
6th order: Lattice structure	Lattice structure of the work piece	- Hole - Between atoms - Dislocations

The form deviation represents the first group and defines the largest deviating areas. The following group (waviness) characterises such an area. For the present work, the significant parameters are in the 3rd and 5th group.

2.3.2 Roughness

Commonly one has a feeling for the classification of a surface e.g. in evenly plane, smooth, rough, wavy, bright or matted. Our tools are the eyes or the fingers, which detect and evaluate the surface. By roughness what is understood is the fine structure of the surface at the microscopic or sub microscopic level. In this range, the eyes can not assess the roughness. In physical meaning, roughness is defined as statistical and stochastic distribution of profile peaks and profile valleys. A defined sector of the total area is described by several roughness parameters: The surface parameters (see next section). Micro structural influences, for example, pores or dimples in the detected surface, may affect the measurement of the roughness parameters. Measurement errors may appear by:

- Dimples
- Particles, like dust, polish or grind particles
- Striations and grooves

In particular, roughness measurements of germanium are dependent on the typical material surface morphology.

2.3.3 Surface parameters

Surface parameters are defined and standardised to characterise the shape deviations. Every measurement refers to a section along a line (see figure 21). The surface parameters are determined from the un-filtered actual profile, from the filtered roughness profile or from the filtered waviness section.

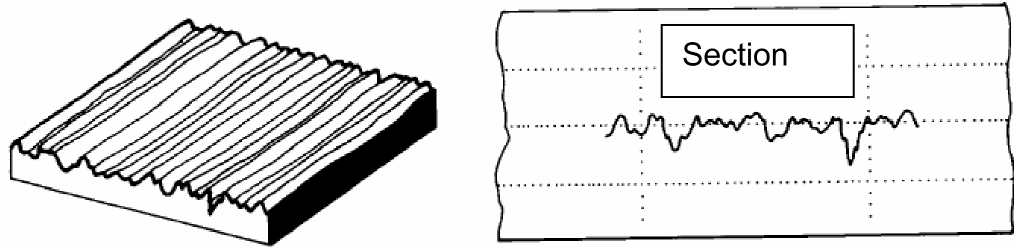

Figure 21: Metrologically detected surface.

In the following subsection the parameters, which are used in this work are listed according to [DIN1990].

2.3.3.1 Maximum roughness depth *Rt*

The roughness profile is generated ignoring long-wave profile variations. The roughness depth *Rt* is defined as the distance between two parallel reference lines, including the highest point (reference profile) and the lowest point (basic profile) within a given profile section lm

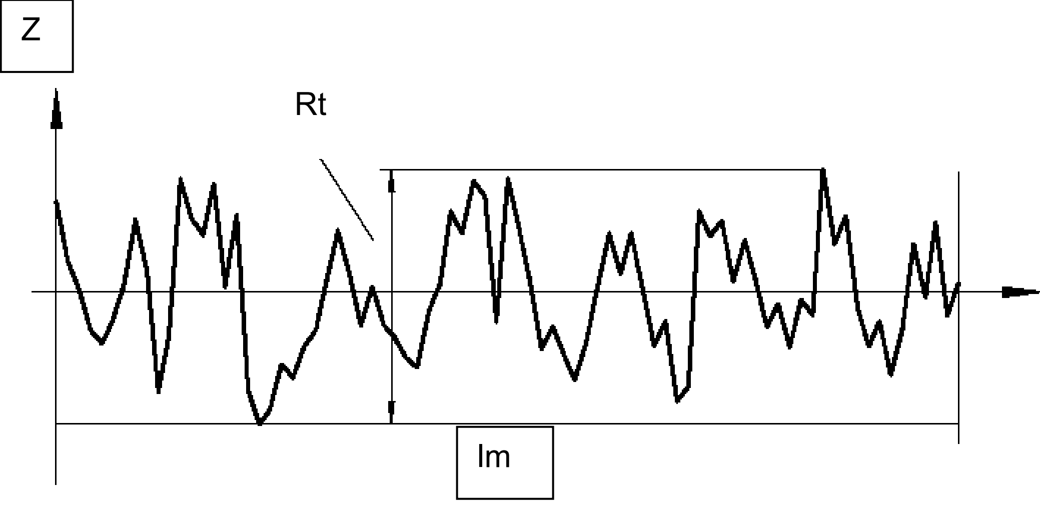

Figure 22: Roughness depth *Rt.*

2.3.3.2 Arithmetical mean deviation of the roughness profile *Ra*

The arithmetical mean deviation of the roughness profile *Ra* is the mean value of the absolute values of the profile variations inside of the measured section lm. (see 2.1; profile value of the roughness profile=Z(X))

$$R_a = \frac{1}{l}\int_o^l \left|z(x)\right| dx \qquad \textbf{(2.1)}$$

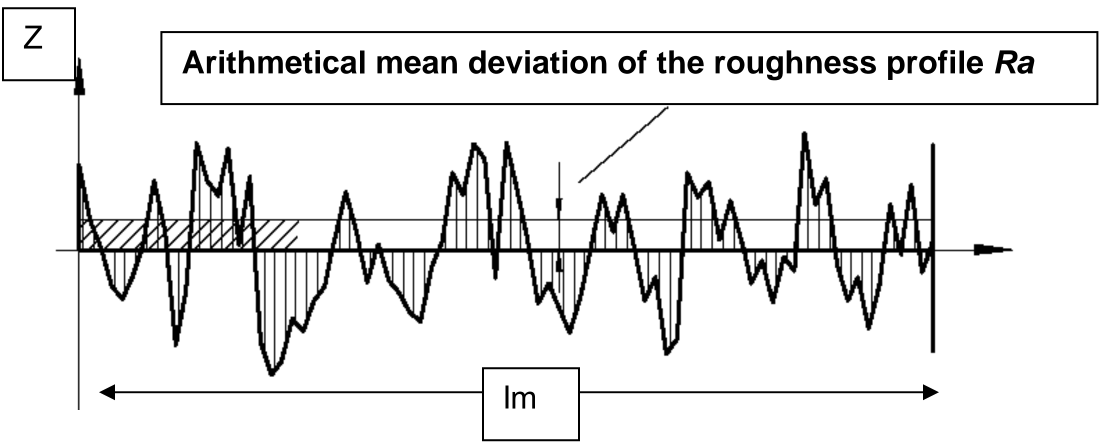

Figure 23: Arithmetical mean deviation of the roughness profile *Ra.*

2.3.3.3 Root mean square surface roughness value *Rq*

The root mean square surface roughness *Rq* is the squared mean value of the profile variations of the mean line. *Rq* is similarly defined as *Ra*, but more sensitive to peaks and waves. *Rq* is calculated with the following formula 2.2:

$$R_q = \sqrt{\frac{1}{l}\int_o^l Z^2(X)dx} \qquad \textbf{(2.2)}$$

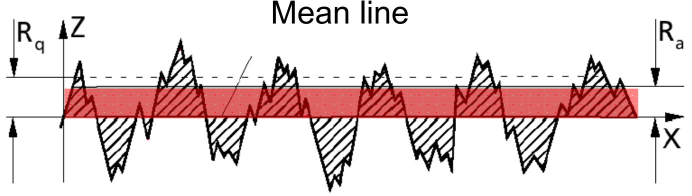

Figure 24: Root mean square surface roughness value *Rq* [DIN 1998e].

Note: This description is taken of the DIN EN ISO 4287:98

2.3.3.4 Average surface roughness *Rz*

The average surface roughness is the mean value of five single depths of roughness Rz_i in a surface profile of five evenly divided sectors and describe the largest distance between the highest and lowest point of the surface profile. This parameter is calculated with 2.3:

$$R_z = \frac{1}{5}\sum_{i=1}^{5} Z_i \qquad \textbf{(2.3)}$$

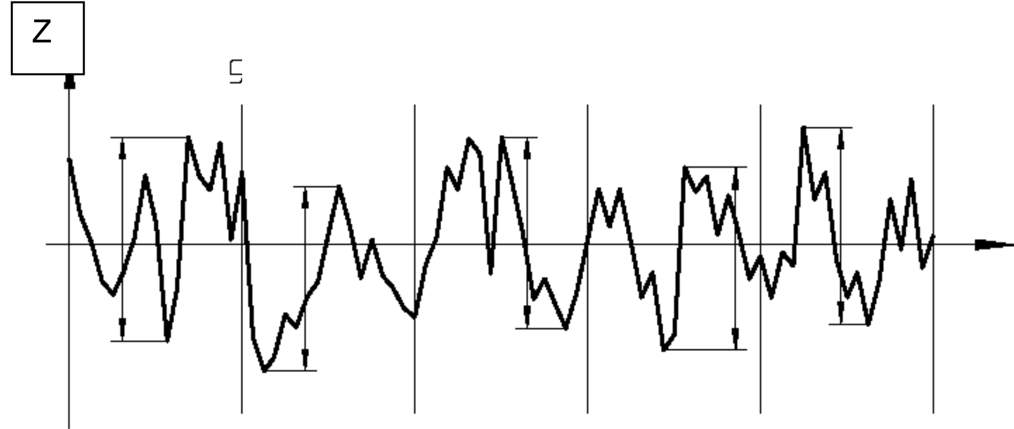

Figure 25: Average surface roughness *Rz.*

2.3.3.5 Maximum Peak to Valley of Waviness *Wt*

The parameter Wt equals approximately the roughness parameter *Rt*. This parameter presents the maximum wave depth of the directed and filtered profile and is the mean shape, which is created with this profile filter. The wave depth *Wt* is the distance between two parallel reference lines, which include the waviness profile within the measured section lm.

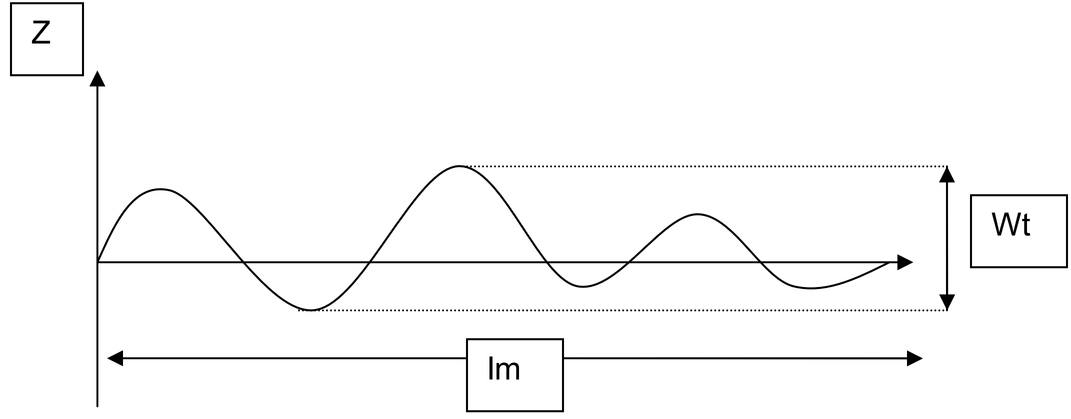

Figure 26: Waviness profile *Wt.*

2.4 The applied measuring methods

For the characterisation of the germanium detector surface structure, mostly microscopic methods were utilised. The mapping of the surface yields an accurate picture of the morphology, the degree of roughness and the defect structure. The classical methods of microscopy, namely the optical microscopy and the scanning electron microscopy (SEM), are limited in their spatial resolution. For the mechanical characterisation, the profilometer and the atomic force microscope are the significant methods. Additionally, the general characterisation of germanium detector surfaces was complemented by an element analysis called electron probe micro analyzer (EPMA). The

above mentioned methods used for detector surface characterisation are explained in more detail in the following sections.

2.4.1 Profilometer

A profilometer is an instrument for 2D or 3D measurement and characterisation of surfaces and microstructures. A profilometer operates either with visual methods or a tactile, where a small needle maps the surface [PRO]. The employed profilometer (Model: Dektak 8 [MKR]) works by one-dimensional scanning of the surface with a needle tip radius of 12.5 µm. The tip is placed on the surface with a certain adjustable force, which is an important factor for the result of the mapping. The core of the Dektak 8 is a rocker, which controls the movement of the needle on one side, while the other side is connected to two coils. This principle is shown in figure 27.

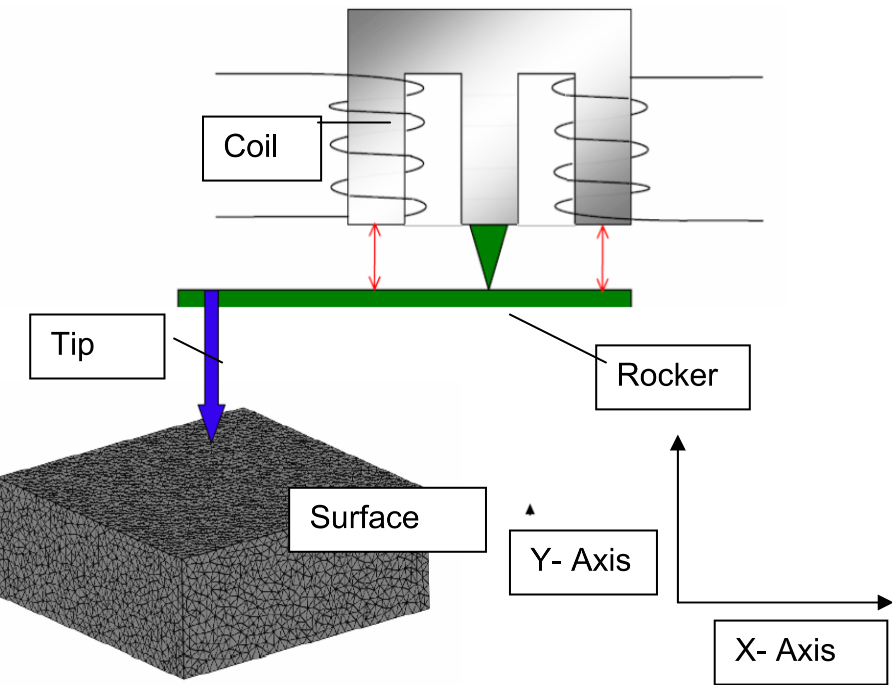

Figure 27: Functional principle of a profilometer.

The tip moving along the x-direction of the surface creates shifts along the y-direction, which then are detected. This process changes the distance between the coils and the rocker. Thus, there is a change in inductance, which then is detected and converted to a surface profile by a connected computer with help of software. The measured profiles are analysed with standardised procedures, for example with ISO 25178 or other methods of geometrical product specification (GPS) in order to deduce characterisation parameters. The technical relevance of profilometers derives from the important influence of the surface characteristics on material characteristics. They enable a graphical presentation of the abrasive parameters and the inference of abrasive mechanisms and abrasive types. Profilometry allows for a two- and three-dimensional as well as a quantitative description of a surface. With this method a determination of the following surface parameters is possible:

- Arithmetical mean deviation of the roughness profile *Ra*
- Maximum roughness depth *Rt*
- Average surface roughness *Rz*
- Root mean square surface roughness value *Rq*
- Waviness depth *Wt*
- Analysis of surface texture

2.4.2 Atomic Force Microscope (AFM)

With an atomic force microscope the morphology and the topography of the surface can be established with a resolution in the nanometre range [SNM] and [CAS]. This method characterises the surface in the range of 1-5 Å [Ångström, 1Å=10^{-10} m] and is independent of the sample material's conductivity. For surface mapping, the atomic force microscope employs forces between the surface and a sensor. The sensor, the so-called cantilever, is a flat spring of about 100-400 µm in length made of silicon or silicon nitride and its tip is pyramidal in shape. The needle scans the surface

line by line using a piezo element. In very uneven places the needle is offset in z-direction either by lifting it or by deforming the spring. A laser beam is reflected off the back side of the flat spring into a segmented photodiode. The differences in the photocurrents of the individual segments reproduce the position of the laser beam, and thus, the angle of the flat spring. The function principle is shown in figure 28.

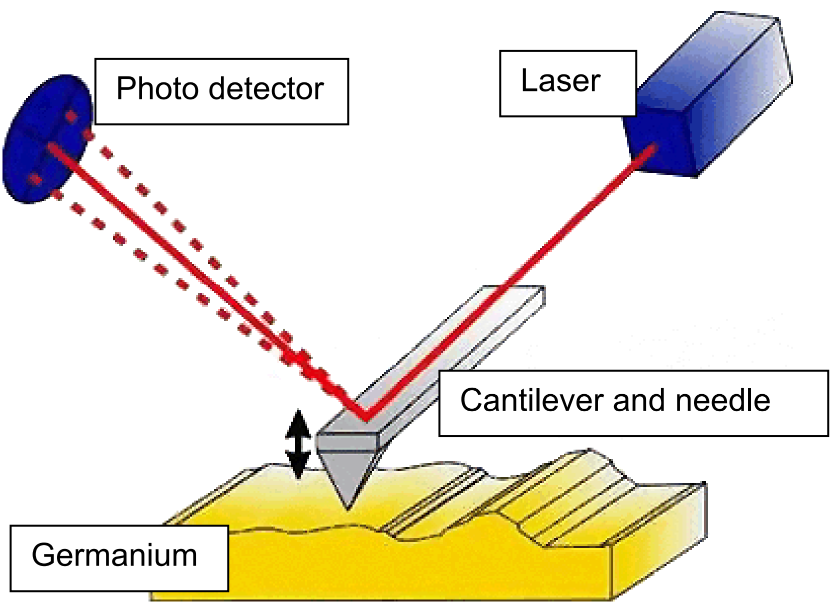

Figure 28: Functional principle of an Atomic Force Microscope (AFM).

The optical detection of the needle action yields an additional factor 1000 in magnification. The resolution of the atomic force microscope thus reaches the sub- Ångström range. There are basically two different operating modes in atomic force microscopy: the contact and the non-contact mode. In the case of the contact mode the needle is in mechanical contact with the sample surface. While in the non-contact mode case, the needle hovers above the surface without penetrating the electron shells of the sample atoms. In this work the parameters measured by the AFM technique is labelled Ra, Rt, Rz and Rq.

2.4.3 The Field Emission Scanning Electron Microscope (FESEM)

The scanning electron microscope (SEM) can measure the morphology and the topography of germanium surfaces with a large depth of field and high resolution. The penetration depth of this analysis method is approximately 1-5 Ångstrøm [[KJK] and [HTA]]. The SEM picture is a map of the sample, which is generated by the interactions between an electron beam and the sample surface. For this purpose, the sample surface is scanned with a focussed electron beam. Interactions between the sample's surface and the primary electrons give rise to two different physical events: secondary- (SE) and backscattering electrons (BSE), which are measured and which yield an accurate map of the sample.

The original field emission microscope is a simple version of the electron microscope (REM), which is based on very high electric field intensities at a mono crystalline, fine, needle-shaped sample. The field electron microscope and the field emission microscope are high resolution microscopes with spatial resolutions in the atomic range. In principle, this instrument is composed of a highly evacuated bulb, which acts as an anode. This operating principle is shown in figure 29. In the bulb a very fine needle, for example a tungsten crystal, represents the cathode. A potential difference of a few kV between cathode and anode creates an approximately spherically symmetric electrical field. Through the tunnel effect, which is favoured by the high electric field intensity, electrons are freed from the cathode. These free electrons are then used for the mapping with the (tungsten) needle. In this process local defects like uneven structures become clearly visible because of the strong field dependence.

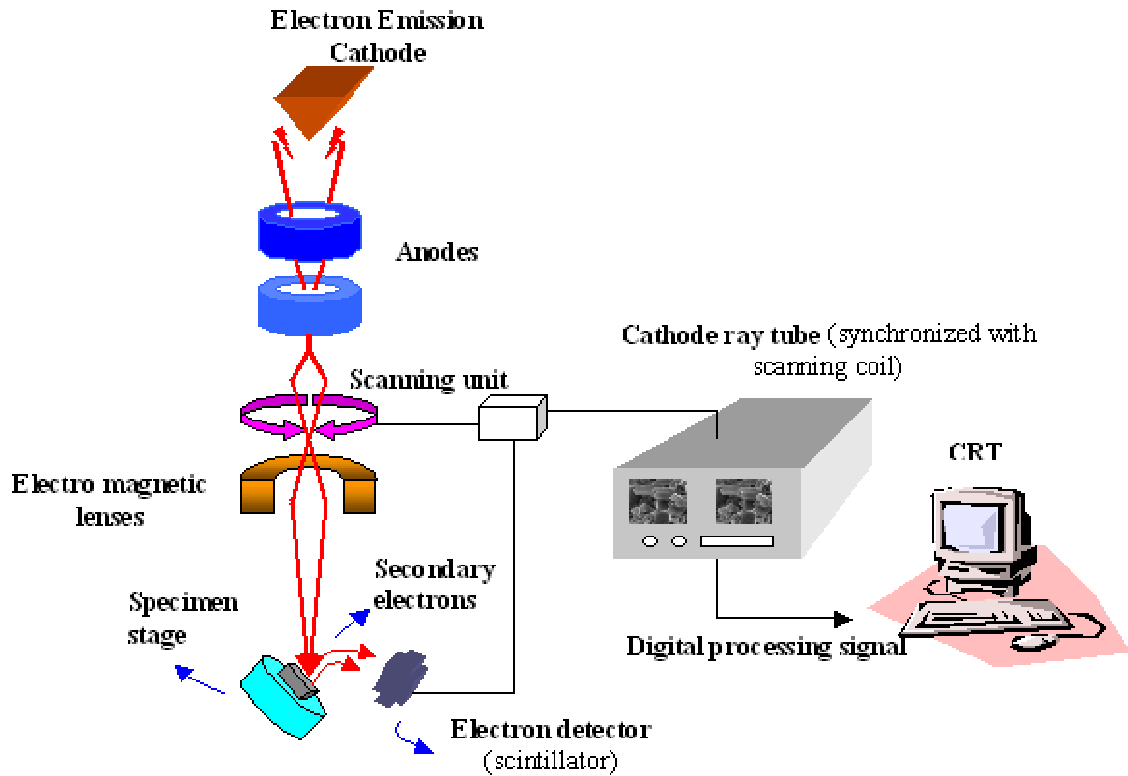

Figure 29: The operating principle of the Field Emission Scanning Electron Microscope (FESEM).

The secondary electrons (SE) have energies of a few eV. They are coming from the scattering events of the primary electron beam and are the mostly used source of information. These SE originate from the first few nm of the surface. Another imaging technique is detecting back scattered electrons (BSE). These electrons come from reflected primary electrons and have energies of several keV. Heavy elements generate intense backscattering, which in the mapping correspond to bright areas, while areas with light elements appeared darker. Thus, the BSE image is referred to as material contrast image, which enables us to draw conclusions on the chemical nature of the object material and the distribution of different elements in it.

2.4.4 Electron Probe Micro Analyzer (EPMA)

The electron probe micro analyzer allows for non-destructive identification of the chemical configuration of a solid surface at a highly localised point on the surface. A modern EPMA is able to determine all elements between boron (Z=5) and uranium (Z=92). In an EPMA, a concentrated beam of monochromatic, high energy electrons (5-30 keV) is focused on a sample surface. Part of the electrons penetrate into the sample and cause the emission of X-rays. These X-rays have element-specific energies and thus allow for element identification. The operating principle is shown in figure 30.

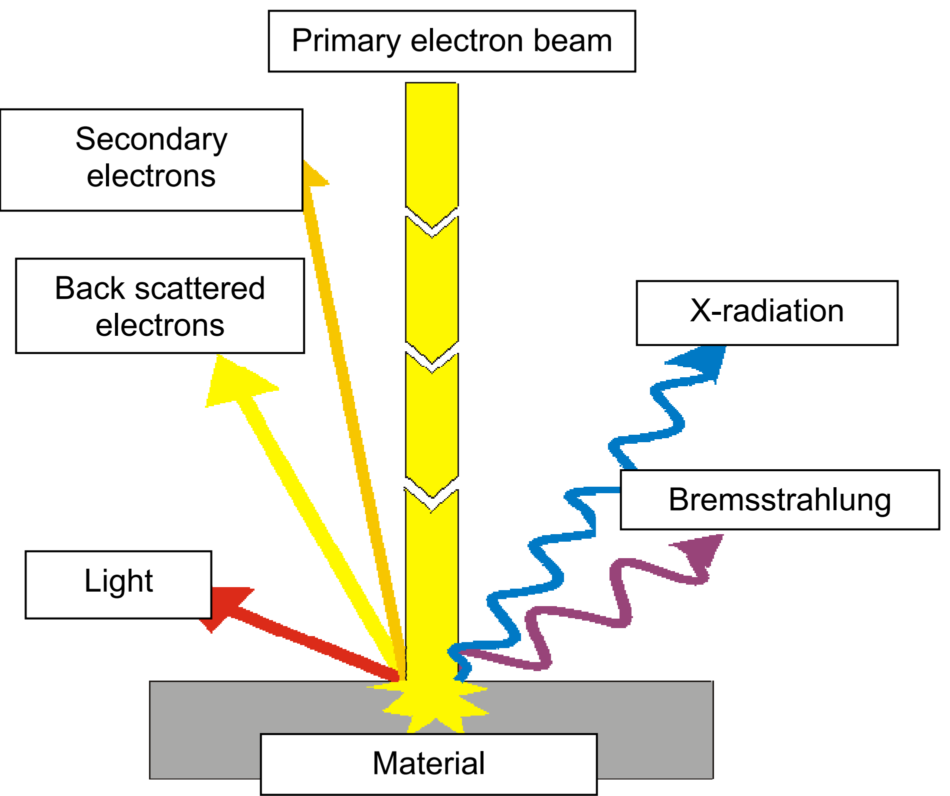

Figure 30: The operating principle of an Electron Probe Micro Analyzer (EPMA).

Chapter 3

3. Characterisation of Ge-detectors and crystals

In order to investigate germanium detector surfaces in detail, Ge-crystals were treated and some of them developed into fully functional probe detectors in collaboration with the company SEMIKON detector GmbH [SEM]. On one hand, the processing of the Ge-crystals was realised using conventional manufacturing methods, like grinding and lapping. On the other hand, a new processing method, ultrasonic grinding, was carried out employing one Ge-crystal.

3.1 Design and development methods of the Ge- detectors and crystals

The fully developed detectors and surface treated crystals were designed to fit into supports for subsequent installation into the available microscopes. The original crystal was an n-type crystal with major carrier impurity concentration of $0.4 \sim 0.5 \times 10^{10}\,cm^3$ [SEM]. All crystals were shaped into small cubes with the dimensions: length ~ 8 mm, width ~ 7 mm and height ~ 10 mm. For the surface studies, the Ge-crystals have been fixed to their respective contacts horizontally with a screw, vespel-isolators and indium contacts in special aluminium housings. The basic structure of the germanium detectors is shown in figure 31.

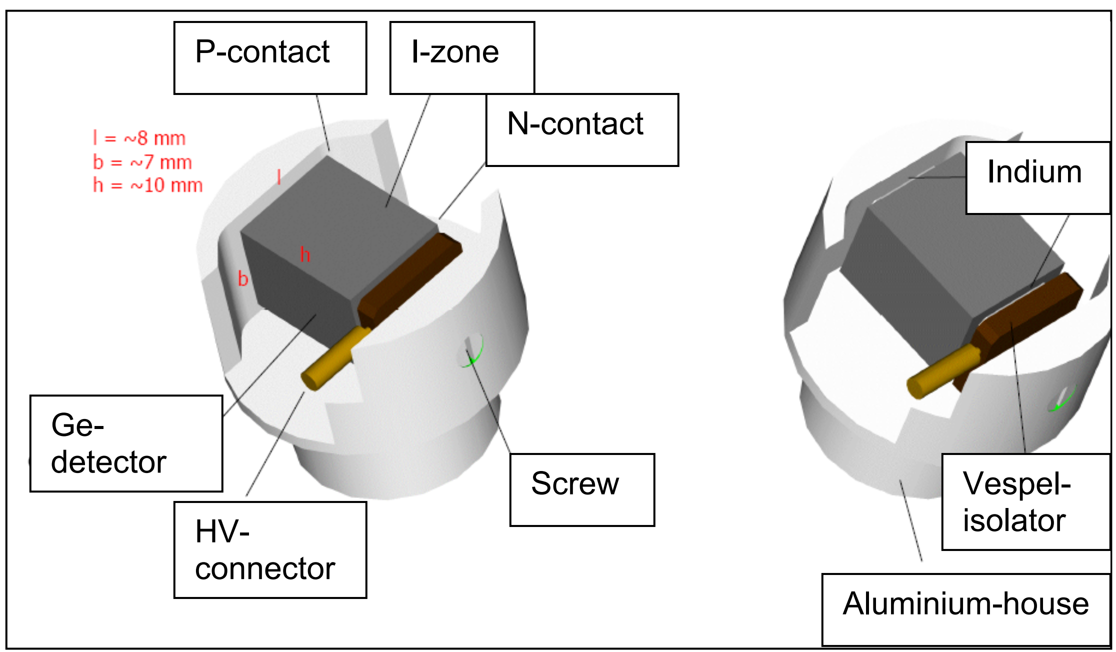

Figure 31: Basic structure of germanium probe detectors.

Seven germanium crystals have been formed using conventional surface treatment methods. Five of these crystals have been further developed into detector diodes. Another essential component of the detector development was the different chemical processes, because the question came up, how the number of etching cycles on the crystal impacts on the properties of the surface, and hence the functionality. Thus, the intrinsic surfaces of the crystals B1 to B7 were differently etched after lapping. In order to analyse the surface parameters after each stage of the treatment, and to be able to make a conclusion about the surface quality, crystals B10 and B11 were fixed in the aluminium housings after the grinding and lapping processes were complete. These two crystals were used solely for a mechanical characterisation. The crystal B12 was developed with a new manufacturing method for germanium and also characterised. An overview of the conventionally and ultrasonic grinded Ge-detectors and crystals is shown in table 5 and figure 32.

Table 5: Overview of the processed Ge-detectors and crystals.

Component	Ground Contact	Top area	
B1	n+-side	lapped, 4x etched	Detectors
B2	p+-side	lapped, 2x etched	Detectors
B5	p+-side	"old" etched area	Detectors
B6	p+-side	lapped, 3x etched	Detectors
B7	p+-side	"old" etched area	Detectors
B10	p+-side	only lapped	Crystals
B11	p+-side	only grinded	Crystals
B12	-	Ultrasonic-Grinding	Crystals

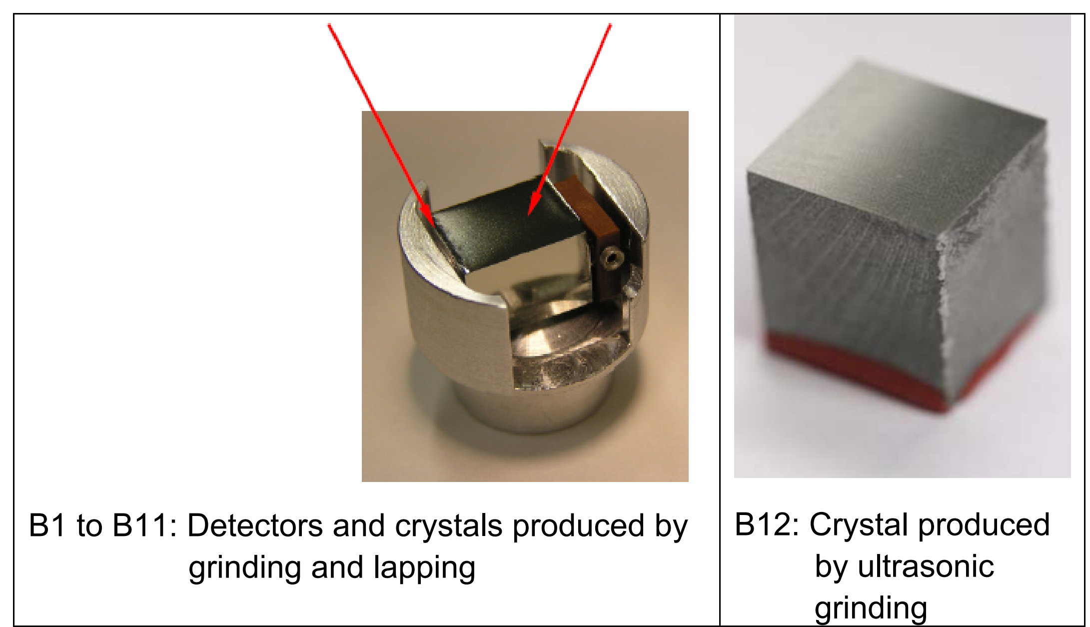

B1 to B11: Detectors and crystals produced by grinding and lapping

B12: Crystal produced by ultrasonic grinding

Figure 32: Overview of developed Ge-detectors and crystals.

3.1.1 Current-voltage tests of the produced Ge- detectors

The functional characteristics of five detectors (B1 to B7) were tested prior to their surface characterization. The five crystals have been installed onto a common cooling plate of a conventional type cryostat especially developed for the characterisation test as shown on figure 33, and cooled by liquid nitrogen. After certain vacuum conditioning the assembly was cooled and the operational temperature was found to be -175°C. Each crystal had direct coupling of the insulated contact to the high voltage feedthrough and common ground with the cryostat and the other crystals. This assembly enables measurement of the V-A characteristics, however requires also the whole cryostat to be electrically shielded by a Faraday cave. Of course, the preamplifiers had to be used in AC coupling. The disposition of the crystals (counted clockwise and starting from the leftmost crystal) is as following B1, B2, B5, B6 and B7.

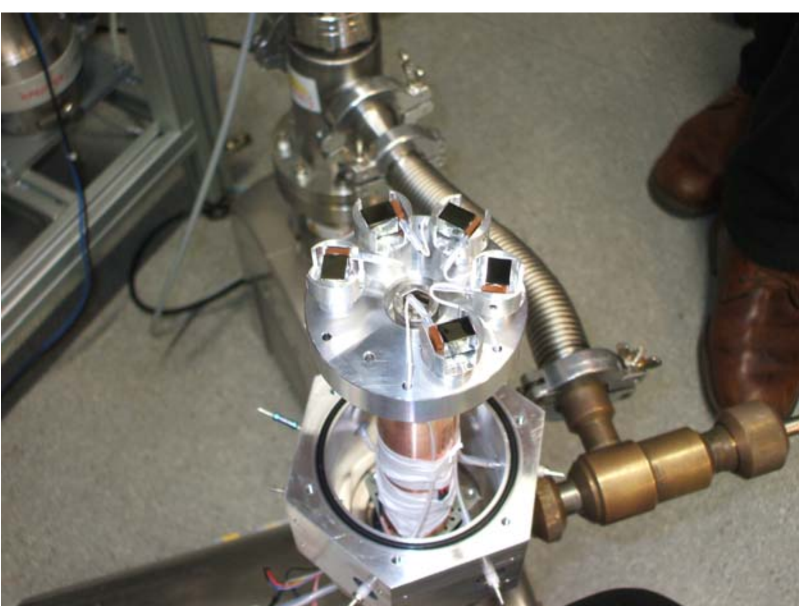

Figure 33: Ge-detectors installed in a cryostat.

A current voltage test was realised to measure the leakage current of the detectors in the cryostat. For this test, the complete cryostat with the integrated detectors was measured in a Faraday cave with a picoampermeter Type Keithley, model 6485. The results are shown in figure 34.

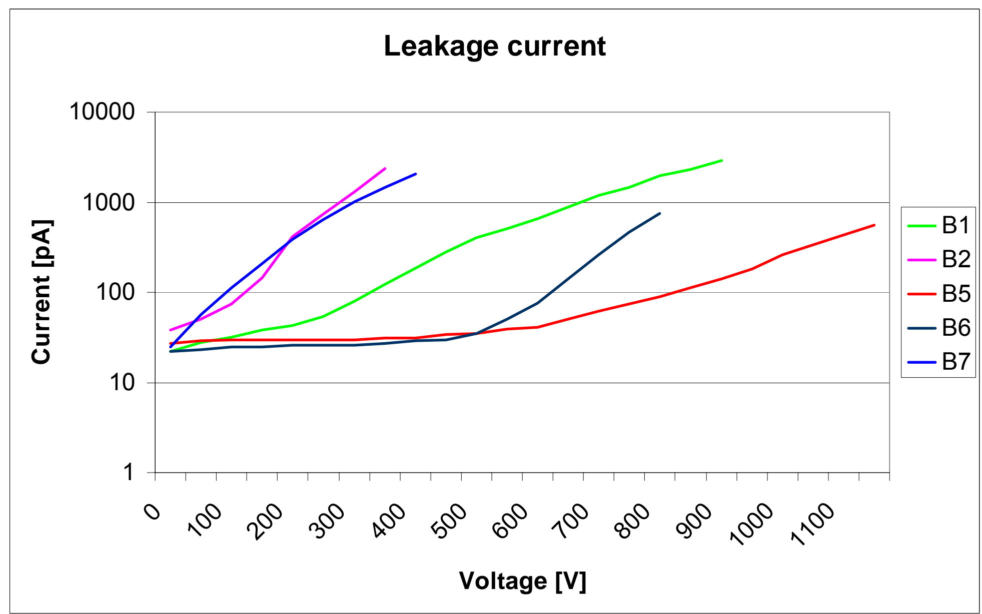

Figure 34: Current-voltage test.

There are obvious differences between the current-voltage curves of the detectors. The crystals B5 and B6 exhibit typical diode characteristics. After an almost constant low current up to ~600 V the current through detector B5 (red curve) begins to increase. Detector B6 (black curve) also shows a low current value until ~500 V followed by an exponential-like rise. Taking into account the expected depletion voltage of 285 V, these two diodes would be the most suitable one's for use as detectors. In contrast the V-A characteristics of detectors B2 (pink) and B7 (blue) are linear. The behaviour is thus resistor-like and could be explained by damaged contacts or open surface. Detector B1 (green) shows also a diode characteristic, however the plateau section is relatively short and unlikely can be operated at full depletion voltage or higher.

3.1.2 Spectroscopic test of Ge-detectors

Due to the mechanical configuration, the subsequent spectroscopic tests of the detectors could not be performed according to IEEE standard. However, they should only confirm the results obtained from the current-voltage characteristics, which are described in section 3.1.1.

The spectroscopic equipment used was:

- Preamplifier: PSC 821M
- Amplifier Ortec 672
- MCA-Silena
- ADC Model: 7423UHS

Sources of ^{57}Co, ^{241}Am and ^{137}Cs were used for the test and the γ ray irradiation of the detectors was effected by the aluminium housing of the cryostat with a wall thickness of 1mm. A example of the spectrum of detector B1 is shown in Fig. 35 and table 6 lists the resolution and parameters.

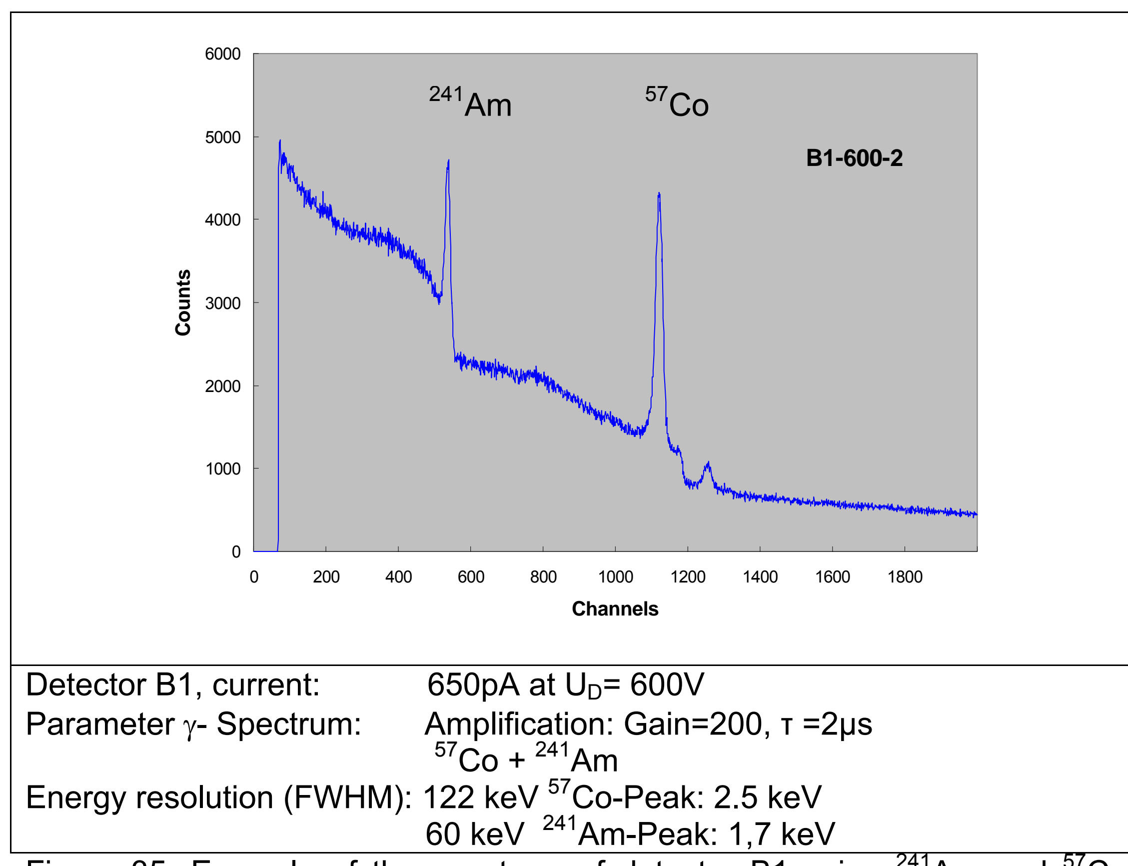

Detector B1, current: 650pA at U_D= 600V
Parameter γ- Spectrum: Amplification: Gain=200, τ =2µs
^{57}Co + ^{241}Am
Energy resolution (FWHM): 122 keV ^{57}Co-Peak: 2.5 keV
60 keV ^{241}Am-Peak: 1,7 keV

Figure 35: Example of the spectrum of detector B1 using ^{241}Am and ^{57}Co source

Table 6: Overview of the measured resolution and used parameters of the detectors B1, B2, B5, B6 and B7.

Detector B1, current: -1175pA at U_D= 700V Parameter γ- Spectrum: - Amplification: Gain=200, τ =3μs - ^{57}Co + ^{241}Am Energy resolution (FWHM): - 122 keV ^{57}Co-Peak: Double Peak - 60 keV ^{241}Am-Peak: 1,6keV	Detector B2, current: - 705pA at U_D= 230V Parameter γ- Spectrum: - Amplification: Gain=200, τ =3μs - ^{241}Am Energy resolution (FWHM): - 60 keV ^{241}Am-Peak: 1,8keV
Detector B5, current: - 31pA at U_D= 400V Parameter γ- Spectrum: - Amplification: Gain=200, τ=3μs - ^{57}Co + ^{241}Am Energy resolution (FWHM): - 122 keV ^{57}Co-Peak: 2.5 keV	Detector B5, current: - 62pA at U_D= 700V Parameter γ- Spectrum: - Amplification: Gain=200, τ=3μs - ^{57}Co + ^{241}Am Energy resolution (FWHM): - 122 keV ^{57}Co-Peak: 2.6 keV
Detector B5, current: - 140pA at U_D= 900V Parameter γ- Spectrum: - Amplification: Gain=200, τ=3μs - ^{57}Co Energy resolution (FWHM): - 122 keV ^{57}Co-Peak: 1.57 keV	Detector B6, current: - 26pA at U_D= 300V Parameter γ- Spectrum: - Amplification: Gain=200, τ =3μs - ^{57}Co + ^{241}Am Energy resolution (FWHM): - 122 keV ^{57}Co-Peak: 2.2 keV - 60 keV ^{241}Am-Peak: 2,2 keV
Detector B6, current: - 27pA at U_D= 350V Parameter γ- Spectrum: - Amplification: Gain=200, τ =3μs - ^{57}Co + ^{241}Am Energy resolution (FWHM): - 122 keV ^{57}Co-Peak: 2.1 keV - 60 keV ^{241}Am-Peak: 2,2keV	Detector B7, current: - 1020pA at U_D= 300V Parameter γ- Spectrum: - Amplification: Gain=200, τ=3 μs - ^{57}Co Energy resolution(FWHM): - 122 keV ^{57}Co-Peak: 3.7 keV

One can note that the detector B1 shows rather regular energy resolution despite the high detector current. The detector B5, which should exhibit excellent spectroscopy properties, indeed does it rather oddly. It collects the charge carriers poorly, even at operational voltages much higher than the depletion voltage. Even at higher operational voltages the spectrum is much distorted, 122 keV line is multiplied which indicates complications in the

charge collection process. In contrast, detectors B2 and B7, despite the Ohmic behaviour of the V-A characteristic show good energy resolution. Detector B6, as one can anticipate, shows proper energy resolution. The results indicate that the V-A characteristic could not be solely used as figure of merit for the detector performance. Since the V-A characteristic depends on the quality of the contacts and quality of the open surface, their interplay with the charge collection may explain the inconsistency of some of the results. For example, open surface with a defect will result in high leakage current, which indeed does not substantially affect the charge collection. Since the preamplifier is AC coupled, this current would not be integrated and only current noise through the coupling capacitor would affect the energy resolution.

3.2 Characterisation of the surface morphology and topography

The aim of this characterisation is to find the correlation between the surface characteristics and the detector properties. No systematic analysis was possible since only 5 detectors were produced with at least 3 different "classes". Furthermore the surfaces were only partly analysed, which is insufficient in comparison of what is recommended for standards. Despite this known limitation it should be possible to learn more about detector surfaces, for example, if certain detected surface defects can be excluded as cause for bad resolutions.

For the characterisation of the surface roughness the crystals B10, B11 and B12 were analysed and evaluated with the help of a profilometer and an AFM. To detect contaminations in the detector production processes, the surfaces of the germanium detectors B1 to B7 were studied with the aid of an FESEM and an EPMA.

3.2.1 Profilometer

The surface roughness characterisation of the germanium crystals was measured with a Veeco DEKTAK 8 profilometer. The contact force was 3 mg. An area of 1 mm^2 was scanned in each measurement. The surface parameters were evaluated, and an example of a 2D and a 3D plot are presented in figures 36 and 37 for the crystal B10, respectively.

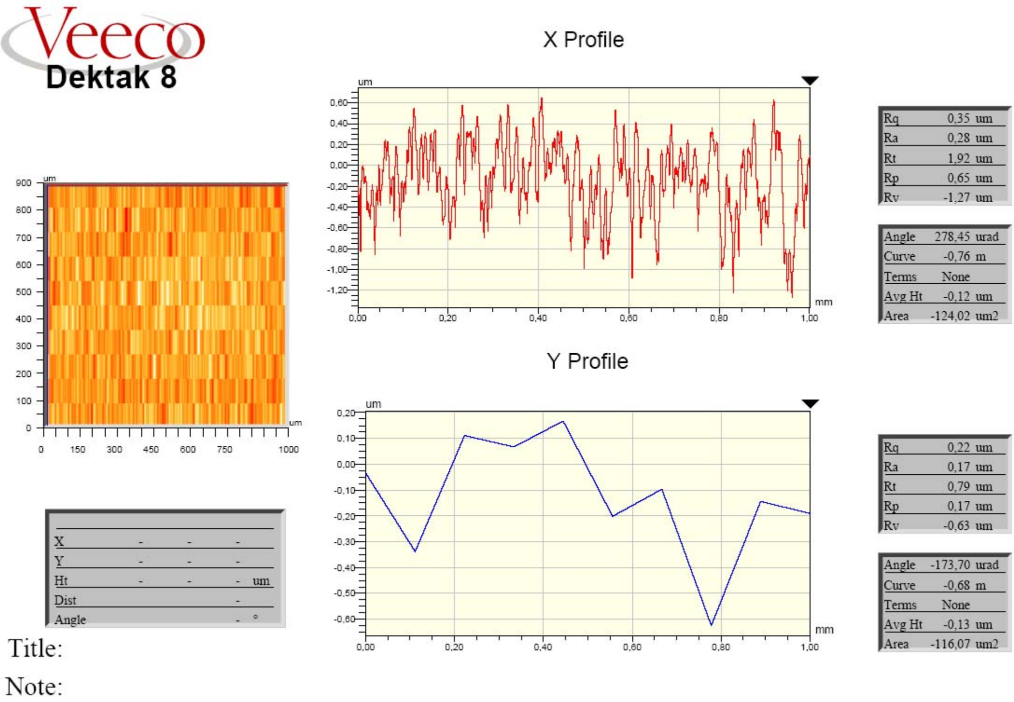

Figure 36: 2D parameter identification with a Profilometer.

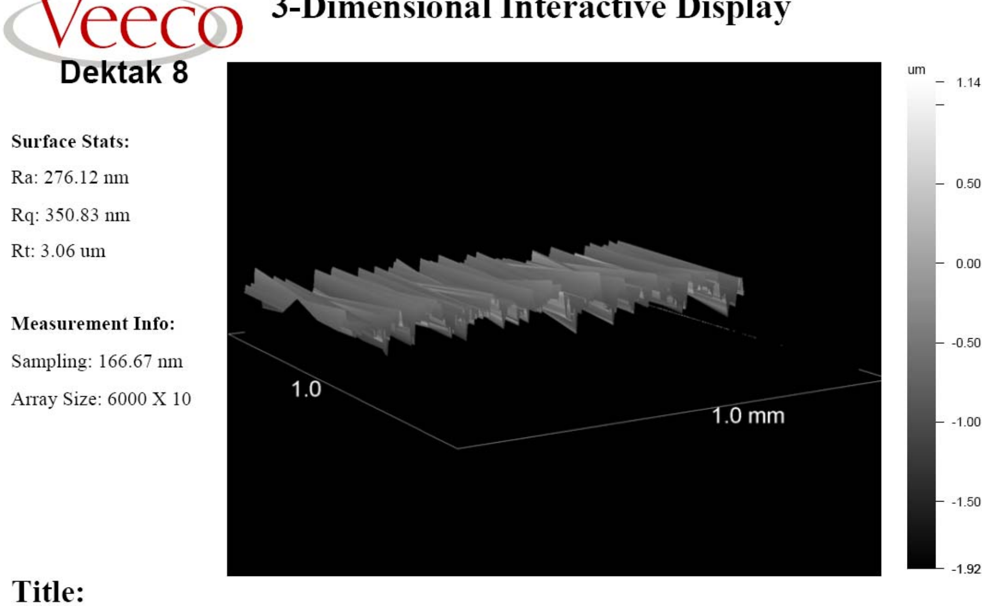

Figure 37: 3D surface using the Profilometer.

Because of the limited time available to use the profilometer, the measurements have been done only for three positions for crystals B10 and B11 and four positions for crystal B12. The selected positions were randomly chosen close to the centre on one of the open surfaces. The following roughness parameters of the germanium crystals B10, B11 and B12 determined with profilometry are shown in tables 7 to 9. A summary of the measured data is presented in table 10.

Table 7: Roughness parameters of Ge-Crystal B10.

	Pos.1	Pos.2	Pos.3
Ra [nm]	317,42	276,12	263,95
Rq [nm]	399,32	350,83	326,51
Rz [µm]	7,56	2,66	3,01
Rt [µm]	4,18	3,06	2,06

Table 8: Roughness parameters of Ge-Crystal B11.

	Pos.1	Pos.2	Pos.3
Ra [nm]	713,35	615,84	651,05
Rq [nm]	886,30	775,07	799,74
Rz [µm]	5,70	11,59	12,17
Rt [µm]	6,75	12,22	6,86

Table 9: Roughness parameters of Ge-Crystal B12.

	Pos.1	Pos.2	Pos.3	Pos.4
Ra [nm]	190,31	183,84	205,54	186,53
Rq [nm]	320,16	251,75	294,25	278,32
Rz [µm]	10,84	11,25	5,35	5,73
Rt [µm]	11,29	3,92	5,75	3,37

Table 10: Summary of the roughness parameters.

	B10	B11	B12
Ra [nm]	285,83	660,08	191,55
Rq [nm]	358,88	820,37	286,12
Rz [µm]	4,41	9,82	8,29
Rt [µm]	3,1	8,61	6,08

As expected, the values obtained for crystals B10 and B11 reveal, upon closer inspection of table 4, significant differences between the grinded and lapped surfaces. The surface parameters of the lapped Ge-crystal are finer and have values of Ra~2,3, Rq~2,3, Rz~2,2 and Rt~2,8. The reason for this level of fineness is the treatment process, because the lapping technique is used for the final cutting, which optimizes the crystal surface after the grinding process, resulting in a very fine and smooth surface. Marked differences are seen with the surface parameters of crystal B12, treated by ultrasonic grinding, compared to the parameters of B11. Crystal B12 has a finer surface with values of Ra~ 3,4, Rq~2,9, Rz~1,2 and Rt~1,4. The parameters Ra and Rq of the Ge-crystal B12 are better by 70% compared to the B10 values. However, the parameters Rz and Rt are worse by a factor of ~1,9.

The rougher surface of crystal B12 is explained by the available tools and non-optimised machine parameters at the time it was processed. In the course of the project, optimisation of the tools and the machine parameters was achieved (see Chapter 5). However, the comparison of the surface parameters of B11 and B12 shows that germanium can be treated by ultrasonic grinding. Furthermore, by refinement of this manufacturing method and further testing, a final cutting yielding the best possible surface smoothness may be attained.

Based of this profilometry characterisation, a classification of roughness can take place after each specific stage of mechanical crystal development.

3.2.2 Atomic Force Microscope (AFM)

The atomic force microscopy was performed with a BIO22M and a measuring head SMENA-B of the company NT-MDT [KOV]. The task of this study was two fold, to study the topography of the surface and then to compare it to the classical 2D profilometry. The scanned surface was in each case 15x15 μm^2 per measurement, which is a factor 4444 smaller than the one of the profilometer. For crystals B10, B11 and B12 different numbers of measurements are performed at arbitrarily chosen surface positions. The mapped representations and measured values are presented in appendix A, for the current discussion a sample of each crystal is shown in figures 38 to 40. The roughness values of these measurements are summarized for discussion purpose in table 11.

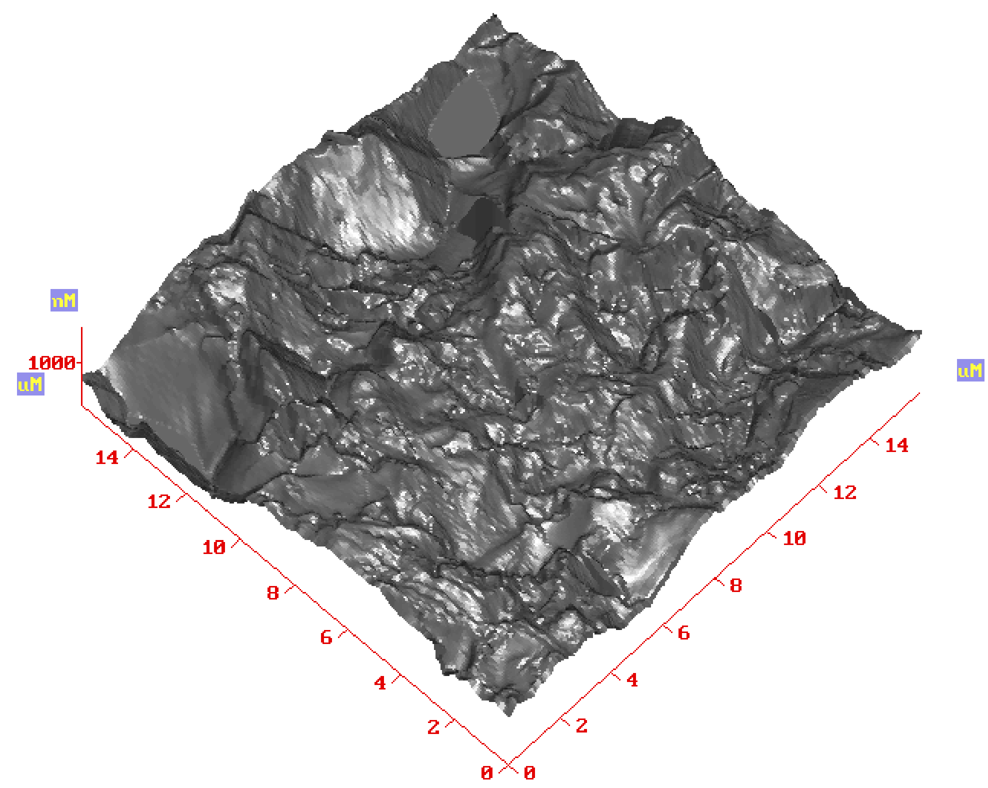

Figure 38: Lapped crystal B10.

The inspection of the scanned surface of the crystal B10 presented in figure 38, shows a very deeply fissured surface. The use of lapping as manufacturing process is reflected in the unevenness, torsions and shift in direction of the surface. All AFM-micrographs from lapping shown in the appendix present these characteristics. The size of the grains and their free motion during the lapping process produce such surface characteristic: unevenness and small size irregularities. This conclusion is confirmed in table 11. Chemical etching of a surface with so small surface irregularities will produce a very even surface, this being the reason of the use of lapping in conventional germanium surface treatment.

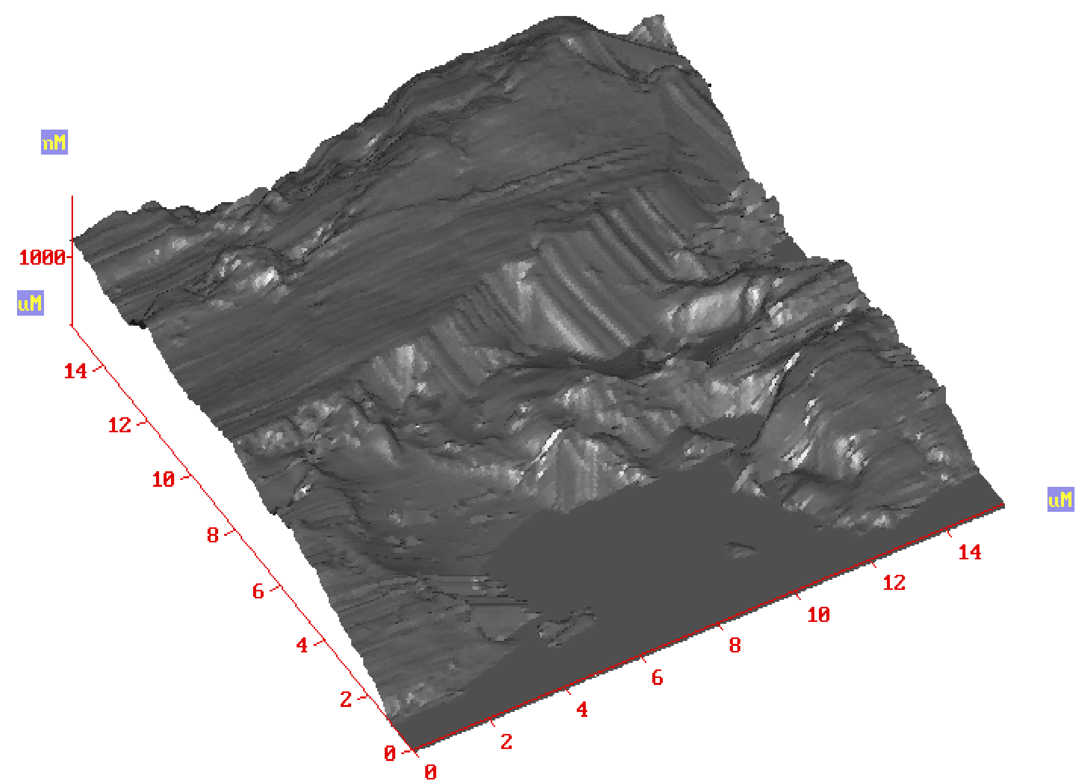

Figure 39: Grinded crystal B11.

On a closer inspection of the mapping of crystal B11, an inhomogeneous surface can be observed. A significant feature in the AFM of figure 39 is a flat area in the forefront. This flat area does not represent a particular roughness, but it reflects a measurement error. The needle of the AFM could not record the depth of this area and stopped at the maximum value of the needle oscillation, then recording a constant depth. This type of fake flat areas was present in 60% of the measurements performed on the crystal B11. Due to these findings the conclusion can be drawn that this type of treatment process (grinding) will remove parts or entire blocks of material of several 100 µm linear size.

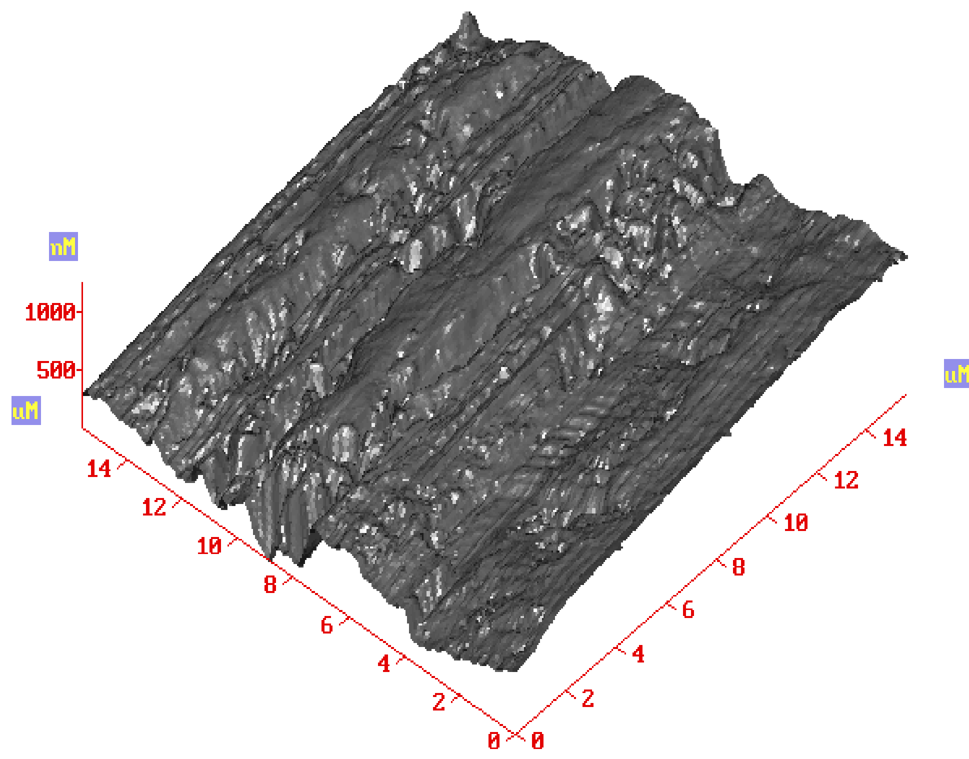

Figure 40: Ultrasonic-treated crystal B12.

The detected surface of crystal B12 shows several form variations distinct from the classical treatment processes, i.e. a lot of grooves, scratches and ripples. The homogeneous linear transmission and phased ordered structures of the surface formations are due to the machining treatment and are present in all mapped measurement of this crystal. However, the quality of the treatment process can be seen in the AFM-micrographs.

To recall, the small surface structures present on the lapped B10 crystal will assure, following the etching process, a good surface quality minimising all shape deviations. On the crystal B11 and likewise on the crystal B12 a pronounced alignment of the surface structure is clearly identifiable, which infers the use of an automatic process or a treatment in a preferred direction. In these analyses of the surfaces, shape deviations of 1st to 4th order (as defined in table 4) are detected on all crystal types. Measurement errors

giving fake flat areas exist on all three crystals, but significantly more on the crystal B11. Indeed this type of error appears only once in the micrographs of crystals B10 and B12. The AFM results confirm the trend obtained with the profilometer, as summarized in table 10. The measured values show that the ultrasonic treated crystal B12 exhibits the finest surface structure. Based on this analysis, the needed surface quality in the different treatment levels in the detector development process (cf. chapter 1) can be defined and used for further germanium treatment.

Table 11: Summary of measured values with the AFM. (See chapter 2 for the definition of Ra, Rt and Rq.).

	Ra [nm]	Rt [nm]	Rq [nm]
Lapped B10	258	1571	320
Grinded B11	394	1785	453
Ultrasonic grinded B12	155	1063	188

3.2.3 The Electron Probe Micro Analyzer (EPMA)

To investigate qualitatively the nature of detector surface contaminations, studies of their chemical element distribution have been realised with an electron probe micro analyzer JXA-8900RL [BSD] of the company JEOL at the University of Mainz. To get a full characterisation of the defects (contaminations) these results were joined afterwards with the result obtained with the FESEM. This EPMA analysis has been applied to the detectors B2 and B7 because their surfaces showed in the analysis of the FESEM data all significant types of contamination defects. With this approach the EPMA analysis allows to check the chemical composition of defect types identified by FESEM. The assumption is then made that all defects presenting the same physical structure in the FESEM analysis will have the same chemical

composition as the ones of the detectors B2 and B7. This is used in the following discussion of defect classification in table 12.

With the EPMA technique the germanium surface can be moved below the electron beam, allowing focusing it on contamination spots. The beam spot had a diameter of 2 µm permitting to analyse very small contamination points. The anode voltage was 20 kV with a beam current of 20 mA. In the following figures 41 to 44, significant points are presented on the top picture with help of SEM-mapping and on the down picture the energy dispersive X-ray analysis spectrum is shown. The analysed points of the surface are highlighted with a red circle on in the right side of the figure.

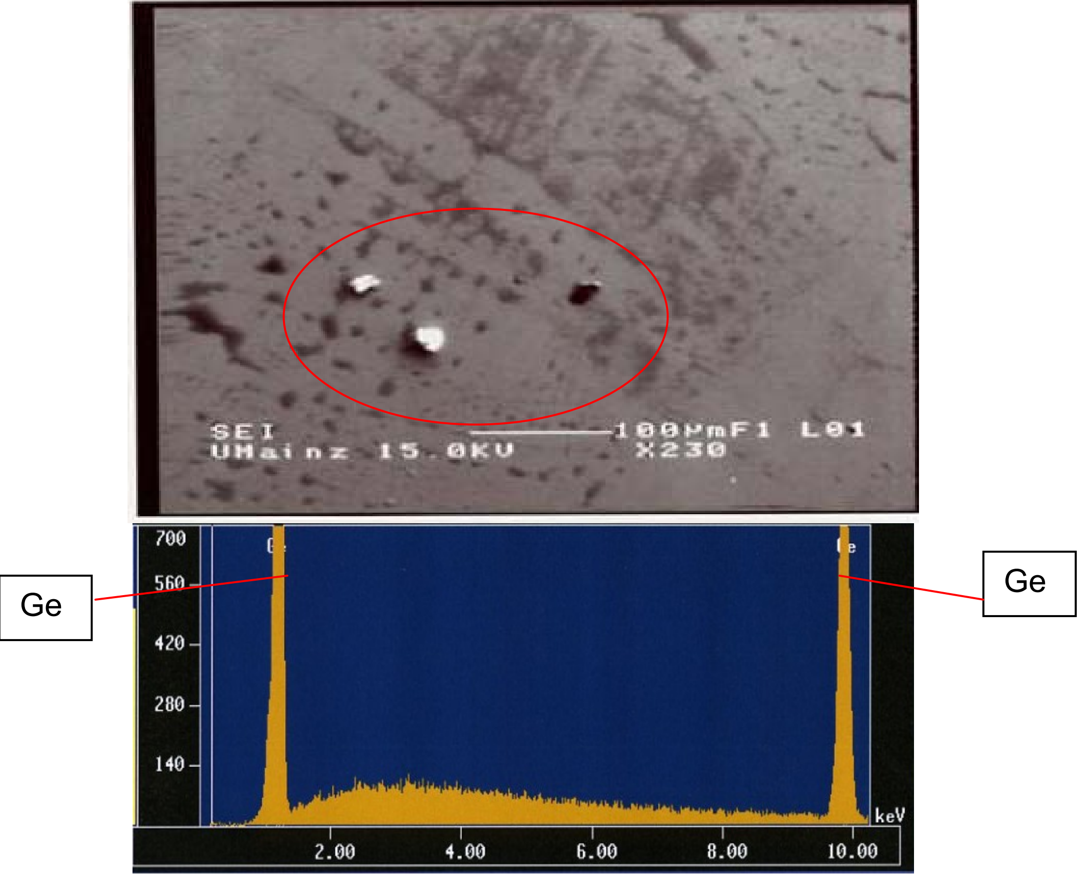

Figure 41: Ge-particles. The encircled zone of the SEM-mapping shows germanium particles, which are determined with the energy spectrum of the EPMA.

In figure 41 is shown that the energy spectrum obtained from the EPMA corresponds to Germanium and no other spectral components are visible, meaning that the encircled particles are germanium grains. It is concluded that these grains were produced with the mechanical treatment, which following the list presented in chapter two, categorise them as microscopic contamination. Three hypotheses can be made to explain the presence of those particles/microscopic contaminations:

- Not all germanium particle contaminations have been removed by the cleaning and etching process of the detector surface.
- The grains were too big in volume before the etching process to be completely removed.
- The grains could have been incrusted in the surface after the etching process, which would indicate a polluted environment, and/or from the handling of the crystal.

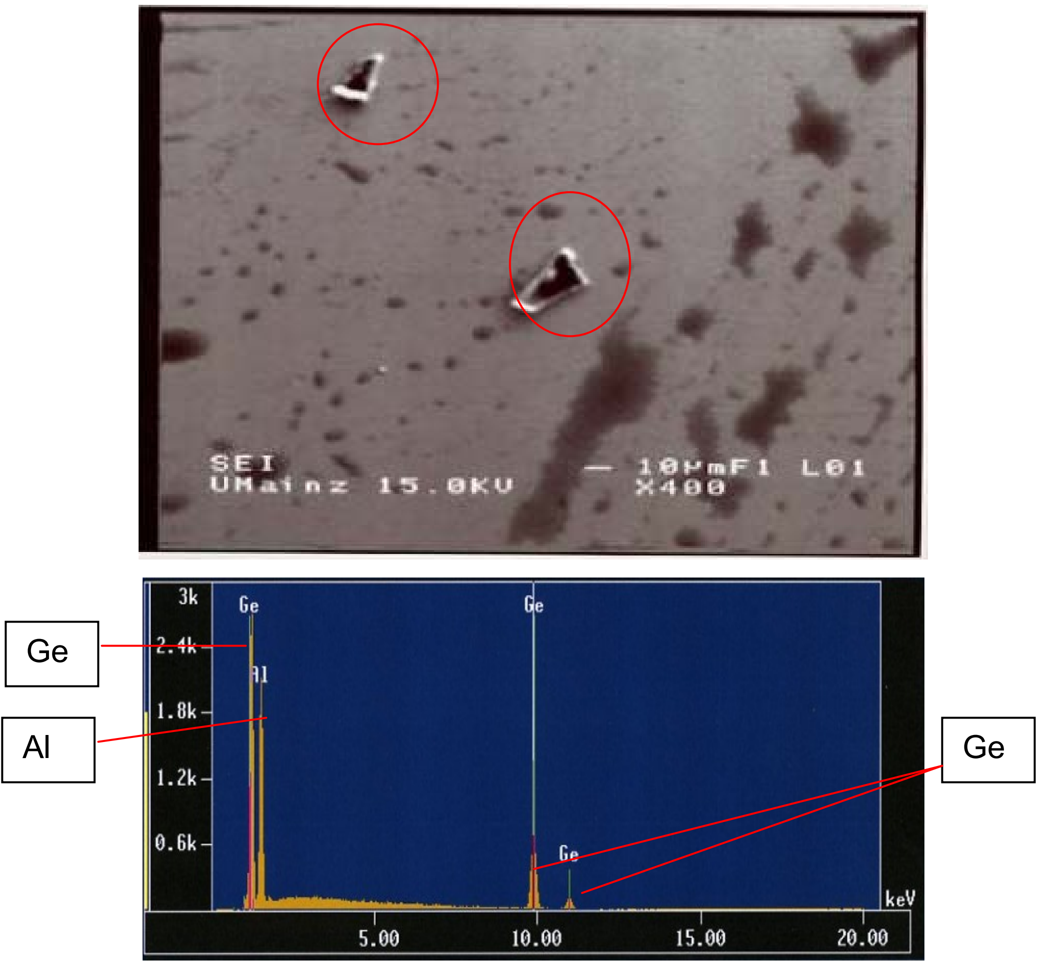

Figure 42: Aluminium particles. The encircled zone of the SEM-mapping shows aluminium particles, which are determined with the energy spectrum of the EPMA. The element germanium is explained by the sample material.

The X-ray spectrum of figure 42 shows clearly the germanium lines again, but also a line originating from the element aluminium, which lists those particles as microscopic contamination too. The element germanium is explained by the sample material. The element aluminium most likely was also brought in during the mechanical processing, and was not completely removed during the cleaning and etching process. Indeed aluminium in the form of aluminium oxide was used as lapping material in the manufacturing process of the detectors, explaining the presence of this element on the surface.

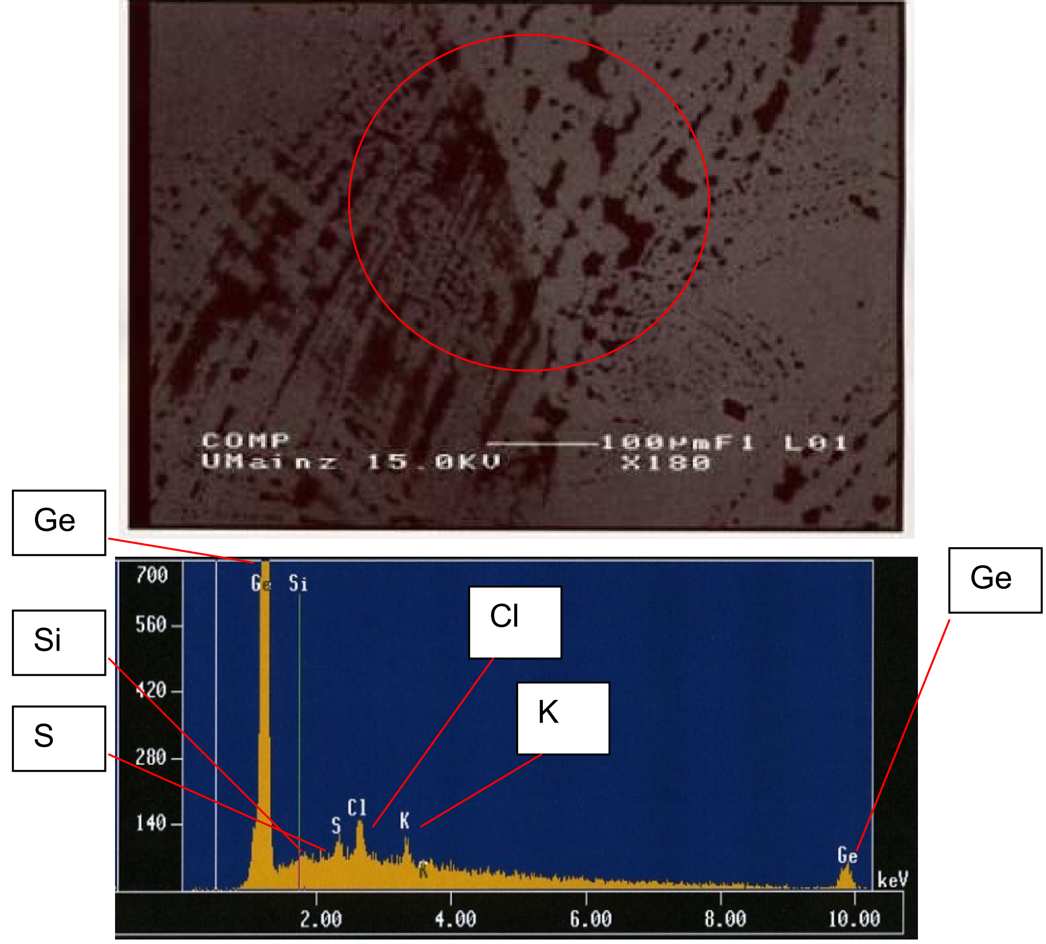

Figure 43: Organic contamination (weak). The encircled area of the SEM-mapping shows an organic contamination. The energy spectrum of the EPMA shows the elements Ge, Si, S, Cl, and K.

The spectrum of figure 43 shows lines for the elements germanium (Ge), silicon (Si), sulphur (S), chlorine (Cl) and potassium (K). The germanium is explained as the base material of the sample. The element silicon could be a measurement error from the detector of the EPMA measurement system [BSD]. The elements chlorine and potassium can be due to insufficiently filtered rinsing water or by an organic adhesive of synthetic base, both would also explain the presence of sulphur. Any of the options would explain the structure of the REM-image on the right side, because those residues are deposited on the surface after the cleaning and etching. For both options, this defect is listed as microscopic contamination. In the resulting classification in

table 12 in the following section, this form of contamination is labelled "organic weak".

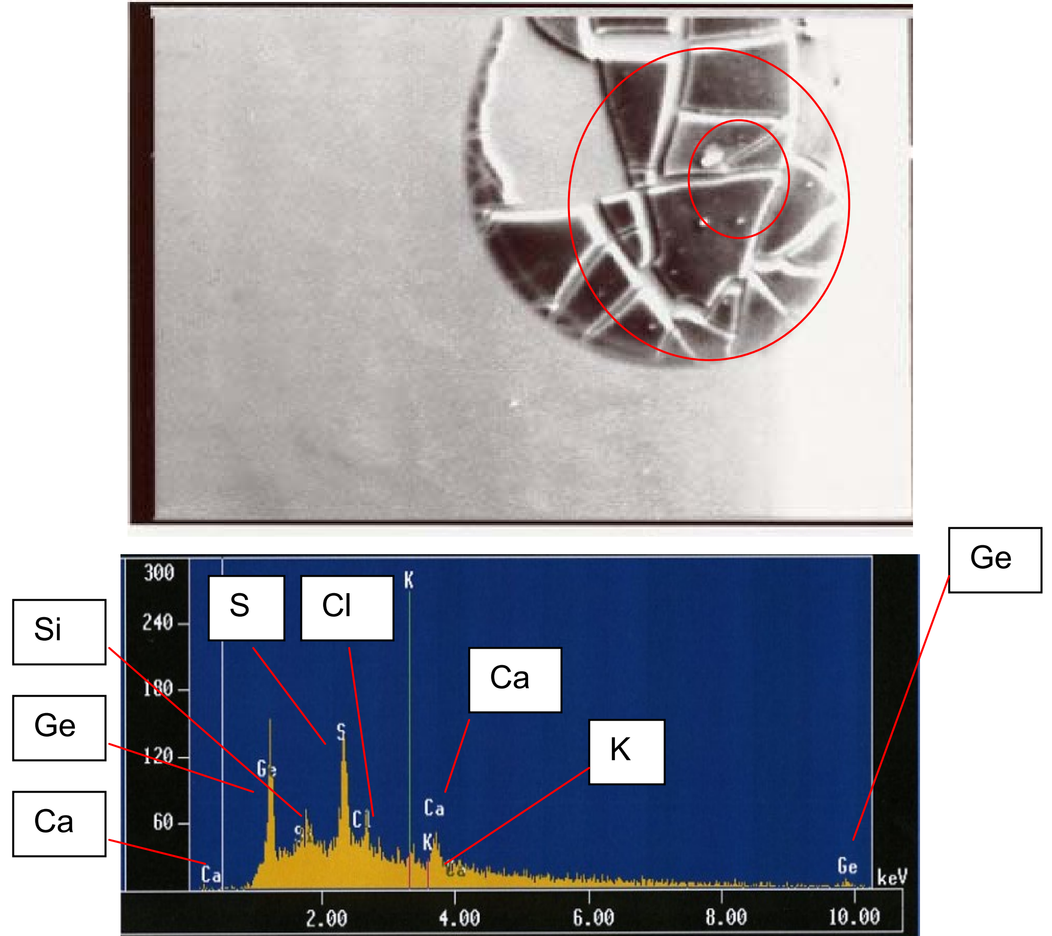

Figure 44: Organic contamination (strong). The encircled area of the SEM-mapping shows an organic contamination (strong), which is analysed with the energy spectrum of the EPMA- the elements are: Ge, Si, Ca, S, Cl and K.

Figure 44 shows a spectrum with lines of the elements germanium, silicon, sulphur, chlorine, potassium and calcium. The presence of the element Ge, is explained again as the sample material. The silicon line is explained like for figure 43 by the Si detector of the EPMA system. The presence of the elements chlorine, potassium and sulphur is explained as in the comment of

figure 43, i.e. by insufficiently filtered water or by an organic adhesive of synthetic base. The REM-image resembles the form of a dried drop. The element Ca could then result from the lapping material. Indeed this element is an alloy addition of aluminium oxide, which was used for the lapping in the manufacturing process. Another option to explain the appearance of Ca is that it could have been brought on the surface as dust. However, this element is mixed with the organic substance and is detected in the little spots of the smaller red circle of the REM image. In both cases, these materials are applied during the development process and are also listed as microscopic contamination. This type of contamination is labelled in the following section as "organic strong".

3.2.4 Field Emission Scanning Electron Microscope (FESEM)

The usage of a Field Emission Scanning Electron Microscope is a popular method in surface analysis and was performed with a JSM-7401F [OVP] of the company JEOL with an operating voltage of 2 kV. Herewith the accessible open faces of all the germanium detectors B1 to B7 were scanned to characterise surface defects and contaminations. To achieve a thorough investigation of the surface defects the "worst" detectors (B2 and B7) were rotated in their aluminium housing in order to scan all their four sides. The numbering of the sides of these detectors is specified in table 12 (from one to four). The measured images are shown in appendix B.

The analysis showed that the distribution of the defects was not homogenous on the detectors surfaces. However, defects were detected on all surfaces of all detectors that were analysed with the FESEM. Using the combination of the FESEM technique to localize the defects and, as explained in the previous section, the EPMA analysis to characterize their chemical

composition allowed to characterize as completely as possible structure defects and contaminations.

Table 12: Summary of the findings.

	B1	B2_1	B2_2	B2_3	B2_4	B5	B6	B7_1	B7_2	B7_3	B7_4
Scratches	x			x				x		x	
Haze		x	x		x			x	x	x	x
Edge chips	x	x		x	x	x	x	x	x	x	x
Edge flaking								x	x		
Orange peel effect	x	x	x	x		x	x	x	x	x	x
Dimples	x	x	x	x	x		x		x	x	
Waves	x		x	x	x	x					
Striation											
Grooves	x		x			x					
Contamination: organic strong		x		x	x					x	
Contamination: Dust	x	x	x	x	x	x	x	x	x	x	x
Contamination: Germanium particle	x	x	x	x	x	x	x	x	x	x	x
Contamination: Organic weak	x	x	x	x	x	x	x	x	x	x	x
Contamination: Aluminium	x	x	x	x	x	x	x		x	x	x
Burst place										x	

In particular, the inspection of the data shows the presence of mechanically produced defects as described in Chapter 2: Scratches, Haze, Edge chips, etc… For example scratches are present on the detectors surfaces B1, B2_3, B7_1 and B7_3. But the defect of B1, being shallower, is described as a capillary compared with the other detected scratches. Remarkable are the scratches of detectors B2 and B7. Indeed it was possible to deduce that they were produced during the mechanical processing, because their structure showed that they were washed out during the etching process. The haze defect was also seen on the surfaces of detectors B2 and B7. This defect appeared at every image with an organic light contamination. Edge chips were detected on all surfaces and particularly on the one's of detector B7. When this defect is particularly strong it is listed as edge flanking in table 12. The orange peel effect was present on all surfaces with the exception of the surface B2_4. This effect is mainly located in the border areas and appears

with light organic contaminations. In general, all cavity defects are good sites for the presence of such contaminations. Indeed the chemical contamination is also present in dimples. This last defect (dimple) is present on all surfaces, with exception of B5, B7_1 and B7_4. A wavy surface (waves defect) is difficult to detect with our analysis methods, it is however easier to notice it at the flanks of the surfaces. This structure was found on detectors B1, B2 and B5. More surprising, no striation was found on any detector surface, demonstrating the quality of the surface treatment. Grooves have been detected on the surfaces of the detectors B1, B2_2 and B6, however those defects were very rare. A closer inspection of table 11 shows, that the contaminations defects (dust, germanium particles, aluminium particles and “organic weak”) are present on all scanned detector surfaces. The “strong organic” contaminations is only found on the detectors B2 and B7, more frequently on B2_1 and B2_4 sides.

A special defect was detected on the detector surface B7_3 and was described as burst place, which is shown in figure 49. This burst place is ovoid and the dimensions are 1040 µm in length and 607.6 µm in width.

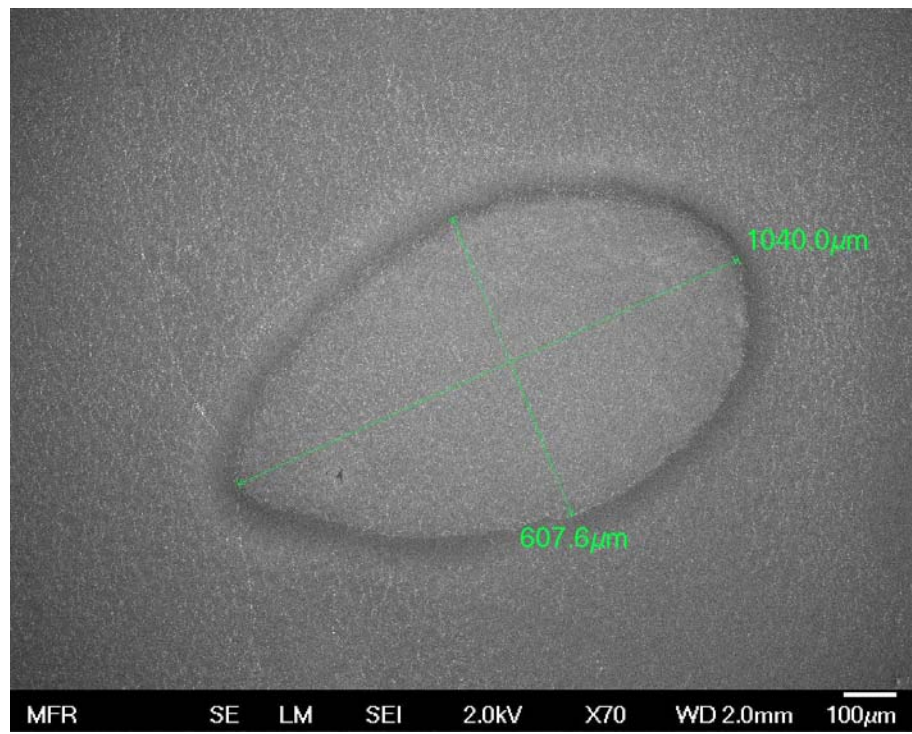

Figure 45: The defect burst place detected with FESEM.

This burst place is a bubble trapping a particle that was opened during or after the etching process. This gives rise to a non homogenous spot surrounded by an etched surface. A detailed explanation of this type of defect is given in chapter 2.

3.3 Evaluation of the surface characterisation

First of all this characterisation of detector surfaces demonstrates the significance of the mechanical treatment in the development process. It shows which defects can be avoided and which ones will appear depending on the mechanical treatment option chosen, and which ones will appear in the following detector processing steps. The clear influence of certain defects on the functionality of the detectors can be concluded. Indeed detector B2 and B7, which have the most substantial defects, are exhibiting the worst performance in the current-voltage test and in the γ-spectroscopy function test. A correlation is seen between the performance of the different detectors and the presence, type and number of defects. Indeed it is possible to use the current-voltage test and the functional γ-spectroscopy test to evaluate the detector performance. In this case the detector B2 and B7 could be rated as "bad" while B5 and B6 as "good" and B1 as "fair".

The presence of mechanically produced defects is highly dependent on the treatment process and on the handling of the crystal. Scratches for example can be reduced or eliminated with a cautious handling in the development process and during the installation in a cryostat. Another important information obtained comes from the contamination defects. Those defects can be reduced or avoided to some degree when the necessary facility and equipment is available. The presence of the burst place defect is another important information obtained, which is explained in detail in chapter 2. Indeed these kind of mechanical defects generate possible deposits of

contaminations on the semiconductor surfaces which are very difficult to clean in following processes.

A further important information concerns the number of etching cycles a detector is submitted to. Indeed it seems multiple etching should be favoured because the multiple-etched surface of detectors B1 and B6 were much cleaner than the less etched ones of detectors B2 and B7. The classification of B2 as a dirty surface comes from the presence of the labelled “strong organic” contamination. As mentioned above the detectors with the cleanest surface had the best results in the current-voltage test and in the functional γ-spectroscopy test which advocate a good cleaning and etching.

Chapter 4

4. Mechanical Ultrasonic-treatment

As mentioned in previous chapters, in parallel to the characterisation of detector surfaces a new manufacturing process for crystalline germanium has been tested: the ultrasonic-grinding. Based on the very positive results of the surface parameters for this application (see chapter 3), a high purity germanium crystal was treated and processed into a detector diode. This work was performed in collaboration with the company SEMIKON Detector GmbH.

4.1 Ultrasonic-grinding experiment

To test this method for monocristalline germanium, and thus for the detector development, different tests, in collaboration with the company Sauer GmbH [ULT], were realised. These tests were aiming at answering the following questions:

1) Can ultra-sonic grinding be applied to monocrystalline germanium?
2) Which surface quality is achievable?

For this purpose, two germanium crystals were used to analyse the surface quality with our previously introduced analysis methods. The analysis and the results of the crystal characterisation obtained with the small crystal shown in figure 46 are explained in chapter 3.

Another aim was to test the applicability of this method to produce different non-standard geometries. These geometries were chosen to investigate if mechanically generated defects were present after the process. An optical investigation after the treatment did not provide indications for any edge chips on the germanium crystal (see figure 46). The only structure defects detected were on the right side of the crystal. This is explained by particular process

parameters of the machine. After optimizing those parameters the treated left side showed no structure defects.

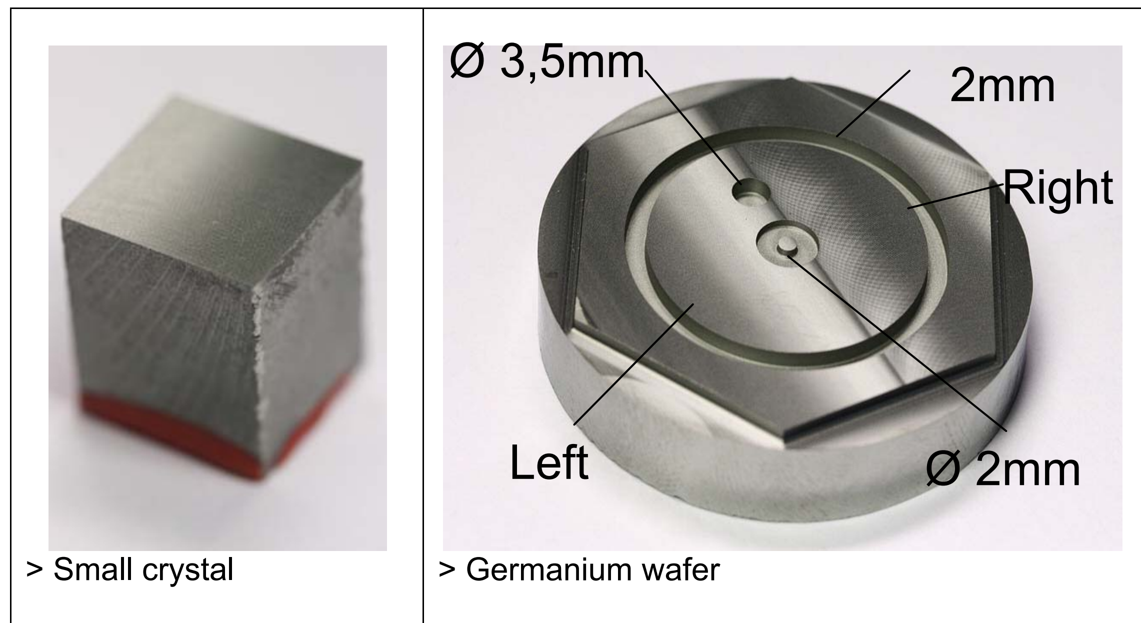

> Small crystal

> Germanium wafer

Figure 46: Samples used for the ultrasonic grinding experiments.

Based on the results of those preliminary tests, an available Ge(Li)- crystal was subjected to a more advanced treatment. This test aimed to establish refined criteria for the treatment of high purity germanium crystals.

The Ge(Li)-crystal used was meant to be a mechanical test case having the geometry of a quasi-planar detector structure. The shape and dimension of this detector structure were defined following the field line simulation of [JKO]. The geometry taken from this simulation is 32.5x32.5x15.0 mm^3 with rounded edges with a radius R = 5 mm along one plane.

The test treatment of the Ge(Li) to obtain this shape aimed to:

1) Find out the best parameters of the tool and the machine.
2) Programme the machine to the required geometry.
3) Guarantee the process reliability and reproducibility.
4) Integrate the mechanical procedure in the detector development process.

Optimizing the parameter of the grinding process with respect to the tool, the machine and the germanium was the main point of this experiment. These parameters determine the surface quality. However, these parameters could be optimised in the further treatment of germanium, which would produce a finer surface.

Furthermore, during the treatment great care was taken in assuring the process stability and reproducibility. The reproducibility mainly depends on the above defined parameters and on the programming of the machine. In this context, the machining process and the way of fixing the crystal determines the process stability. An experimental protocol describing the procedure of this treatment and giving information about the used parameters is provided in appendix C. The result of this process is shown in figure 47 and reflects the final geometric shape of a finished detector after the detector development process.

For a real detector the Li-contact would be on the rounded lower side and the p+-contact on the top, as shown in figure 47. The groove serves to separate the contacts and to assure a low leakage current. In a detector development process this groove would be created after implantation.

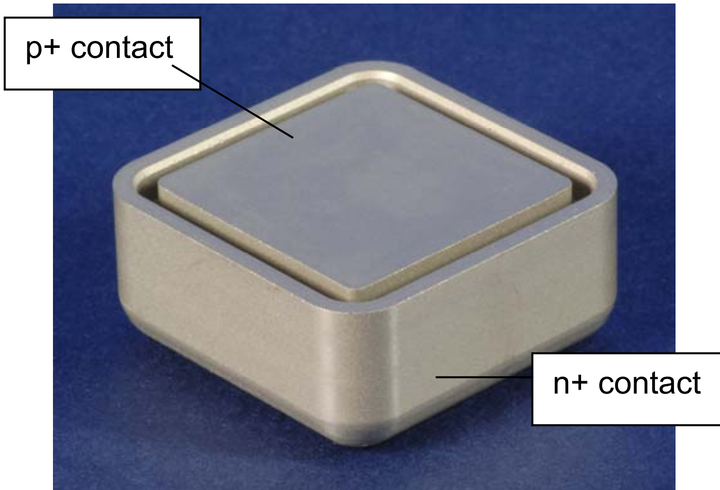

Figure 47: Quasi-planar geometry realized by ultrasonic grinding with a Ge(Li) test crystal.

Following this mechanical treatment the crystal was subjected to the regular detector development processes, i.e. the crystal was cleaned and etched. This treatment would uncover structure defects and mechanical defects not visible after the mechanical treatment. Indeed only after the etching it is possible to make a statement about the surface quality and thus get a conclusion about the treatment strategy. In figure 48 a picture of the crystal is shown were it is possible to see the effects of the etching process. In the left picture, which represents the front side of the crystal, etching generated structure defects are visible. These structure defects were detected as funnel formed dimples and are shown in appendix D in detail. The right picture is significant: no structure defects are detected on the side of the crystal.

Figure 48: Quasi-planar crystal after etching.

The circumferential treatment[2] which was applied to the side faces, seemed preferable to avoid structure defects as seen on the front side, which was subjected to a frontal treatment[1]. Therefore this treatment procedure was chosen further on.

In a final step a high-purity germanium crystal was treated with the optimized parameters and introduced to the detector development process to obtain the same quasi-planar geometry. The physical parameters of this high-purity

---

[2] *The difference between circumferential and frontal treatment is the chosen tool configuration with respect to the work piece depending on the treatment direction. In circumferential treatment, the tool is controlled sidewise to the work piece. In frontal treatment the tool is controlled at the top of the work piece.*

germanium crystal are given in appendix E. The geometry of the high purity germanium crystal after the ultrasonic treatment is shown on the left side of figure 49. The right side of figure 49 presents the germanium detector status in the first test stage. In this first stage the proposed groove was not yet created with ultrasonic-grinding. However, contacts are separated by a plasma etching process and this preliminary detector was then characterized by a spectroscopic test.

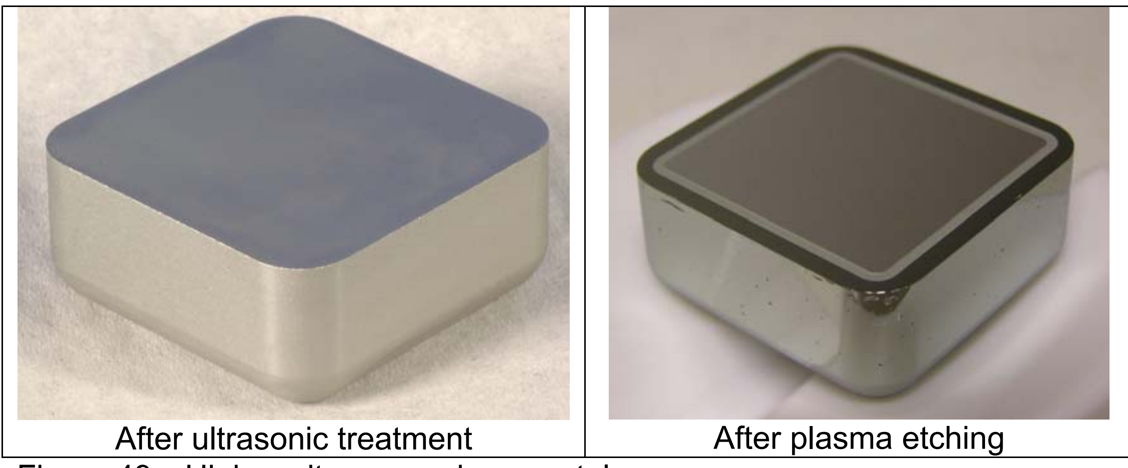

After ultrasonic treatment | After plasma etching

Figure 49: High-purity germanium crystal.

4.2 Spectroscopic test of the germanium detector

For the first spectroscopic test in this development stage, the detector was mounted in a multi-purpose test cryostat of the company SEMIKON. The Al end cap wall thickness is 1 mm. The crystal mounting consist of a 10 mm brass structure partly shielding the detector crystal from low energy γ rays. The high voltage was applied on the p+-side and the Li-side was grounded. To determine the current-voltage characteristic, the detector was calibrated with a Silena power supply. Figure 50 shows the current-voltage graph of the detector.

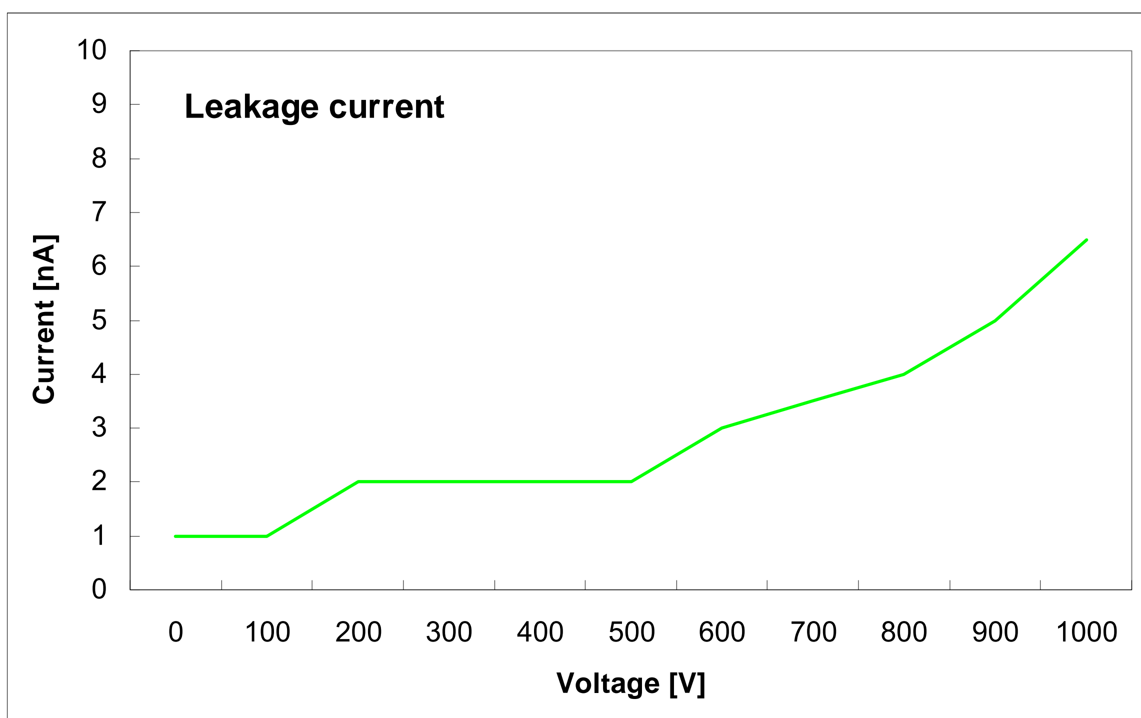

Figure 50: Current-voltage characteristic of the quasi-planar detector produced by ultrasonic machining.

The current-voltage line shows that the depletion voltage of this detector is at about 500 V. The plateau of the detector is located between 200V and 500V and the following rise of the characteristic line is nearly linear. Based on the configuration of crystal in the cryostat, a spectroscopic test was performed,

not following the IEEE-standards. The aim of this spectroscopic measurement was just to check the performance of the detector at a fixed voltage.
The spectroscopic measurement conditions were:

- Preamplifier: CI2002 [SEM], 2.14GΩ
- Shaper gain 200, shaping time 1µs
- ADC Range 2k
- Measurement time 600 Seconds
- Voltage. 500V

The γ-source used was ^{241}Am. In parallel a pulser was used as input to the pre-amplifier to test the electronic resolution.

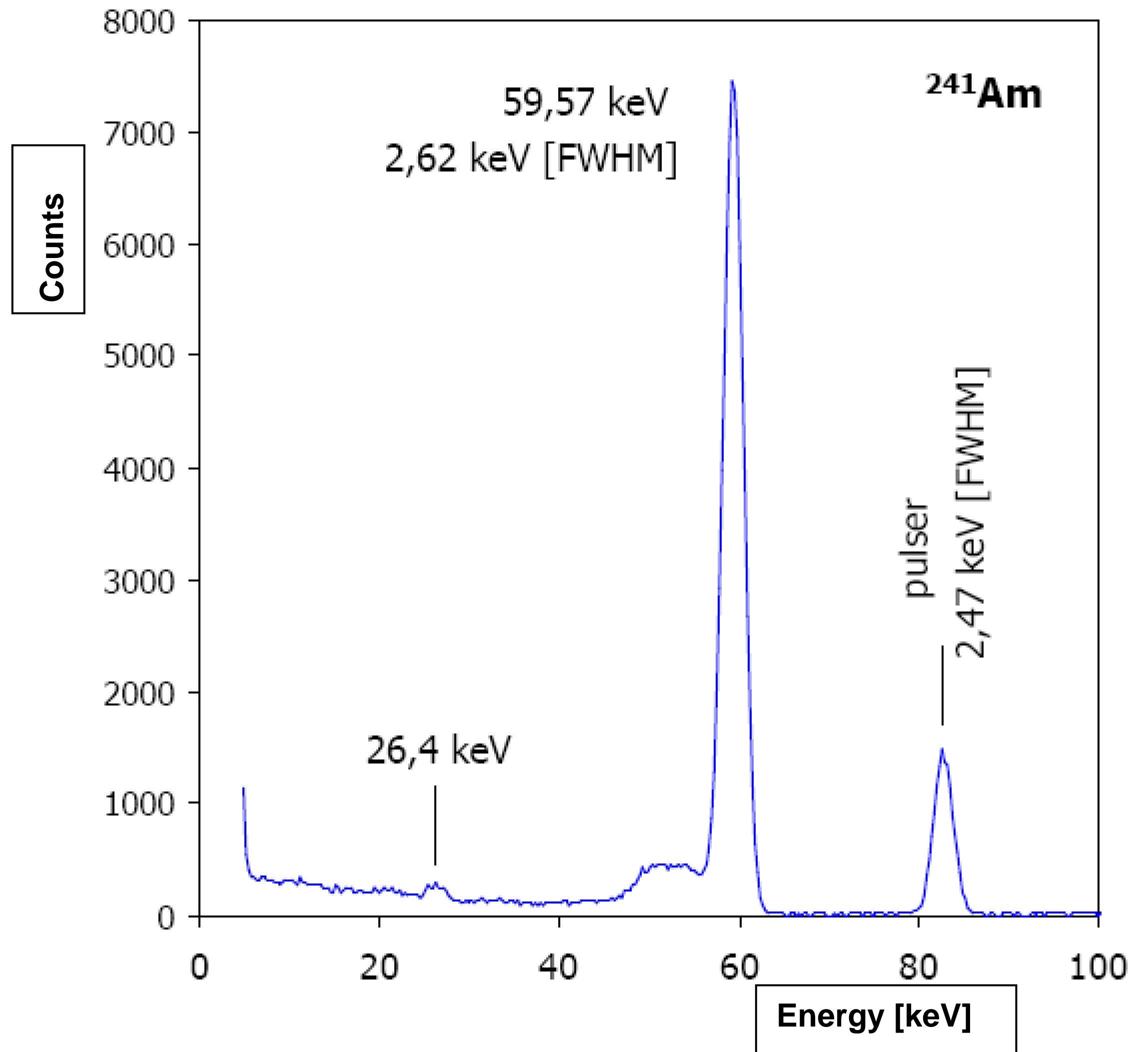

Figure 51: Result of the spectroscopy test of the detector.

The first test of the detector shows good spectroscopic results with the Americium source and a pulser using a bias voltage of 400 V. At this voltage a detector current of 2 nA was measured. Further spectroscopic tests with higher voltage and other sources are planned to get a better characterisation of this detector.
This test was sufficient to demonstrate that ultrasonic-grinding as a mechanical treatment can be used in the detector development process. The advantage of this mechanical process is significant; it allows producing germanium detectors with complex geometric shapes, which is not possible with standard manufacturing techniques.

4.3 Segmentation

4.3.1 Mechanically generated segmentation

The creation of mechanical segmentation lines on a germanium crystal was an additional application of the ultrasonic-grinding technique. After the segmentation stage, in the detector development process, the grooves and the surface need to be submitted to a short etching, which could lead to an expansion of any segmentation groove. To avoid unwanted wide dead space between segments, grooves with small width have to be produced. The groove width is predefined by the applied tool. A grinder of the company HAEFELI was used for our test. This diamond grinder has a diameter of 0.2 mm and a diamond coating of 0.6 mm in length. According to this, segment grooves of 0.2 mm in the width and 0.6 mm in depth are possible. The depth of the grooves should be around 0.04-0.05 mm. Different segments with different depths were produced on a Ge crystal surface as shown in figure 55. The left hand side shows the segmentation scheme, while the right hand side shows the grooves produces by ultrasonic grinding. The intended segmentation was the outlining groove, with a depth of 0.05 mm.

The inner grooves served only as depth reference for the etching process. The protocol of this manufacturing test is documented in appendix C.

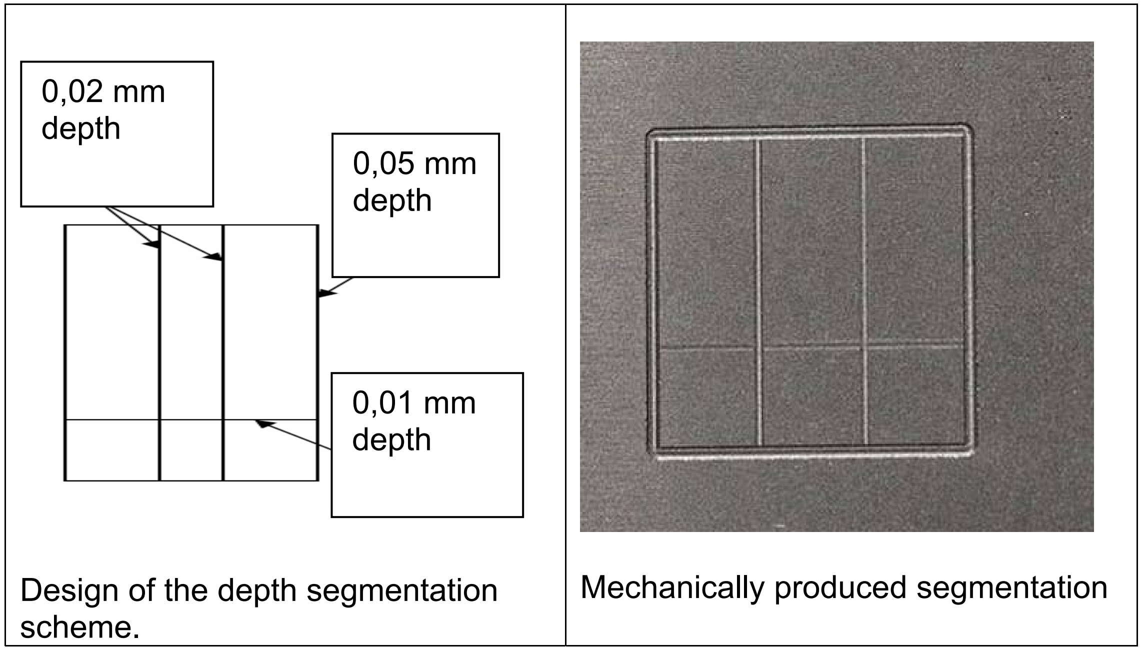

Figure 52: Segmentation produced with ultrasonic grinding.

4.3.2 Verification of the segmentation by profilometry

After mechanically generating this segmentation by ultra-sonic grinding the depth and width of the grooves were verified. This study was performed through profilometry, with the aim to evaluate the width and depth of the grooves. Two sets of measurements were carried out, one after the mechanical treatment and one after etching. The following measured results of the DEKTAK 8 VECCO profilometer were preformed with a contact force of 3 mg. An area of 64 mm^2 was scanned in each measurement.
The figures 53 and 54 show the results of the 2D analysis by profilometry, before (figure 53) and after (figure 54) the etching process.

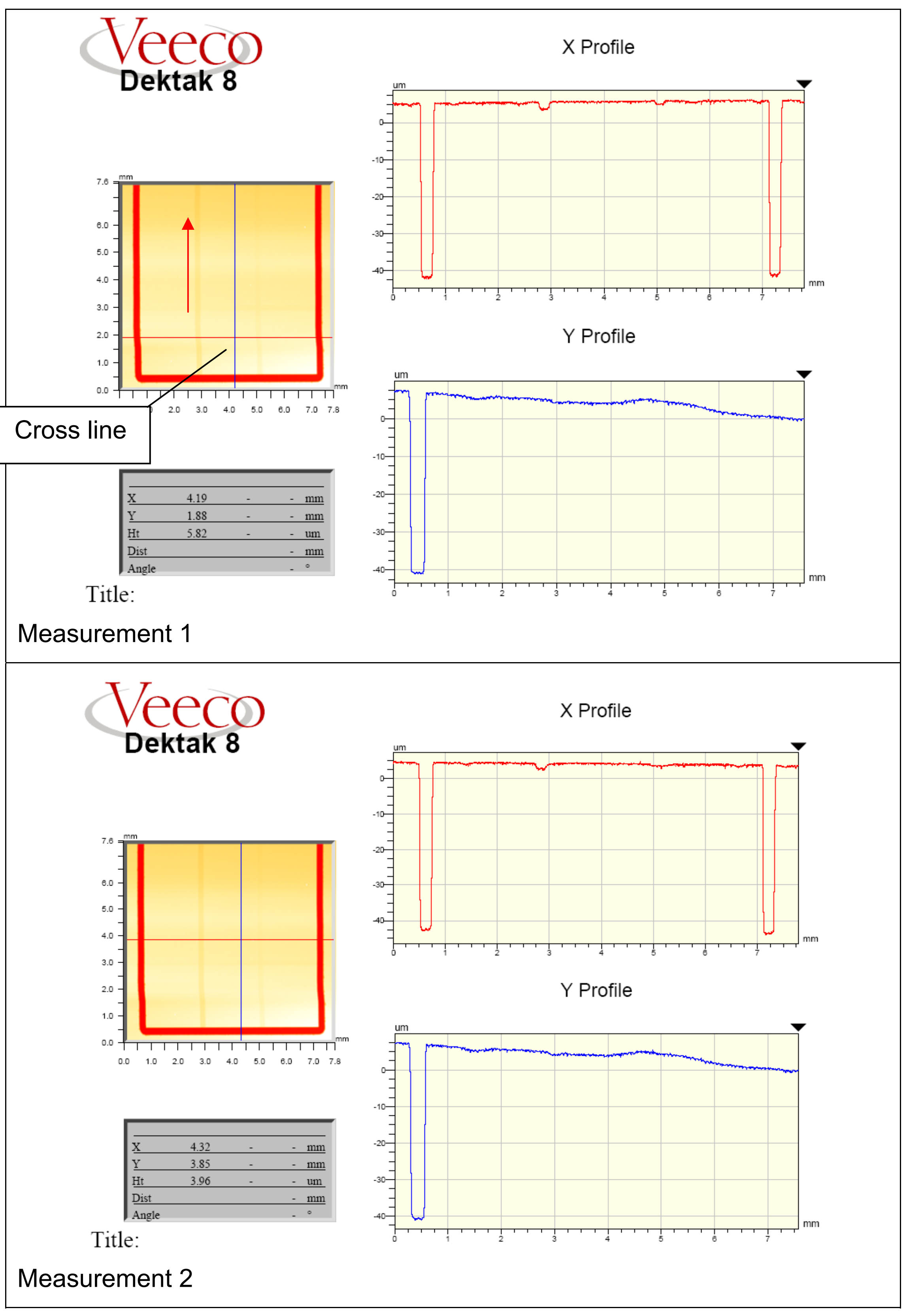
Veeco
Dektak 8
X Profile
Y Profile
Cross line
X 4.19 - - mm
Y 1.88 - - mm
Ht 5.82 - - um
Dist - mm
Angle - °
Title:
Measurement 1
Veeco
Dektak 8
X Profile
Y Profile
X 4.32 - - mm
Y 3.85 - - mm
Ht 3.96 - - um
Dist - mm
Angle - °
Title:
Measurement 2

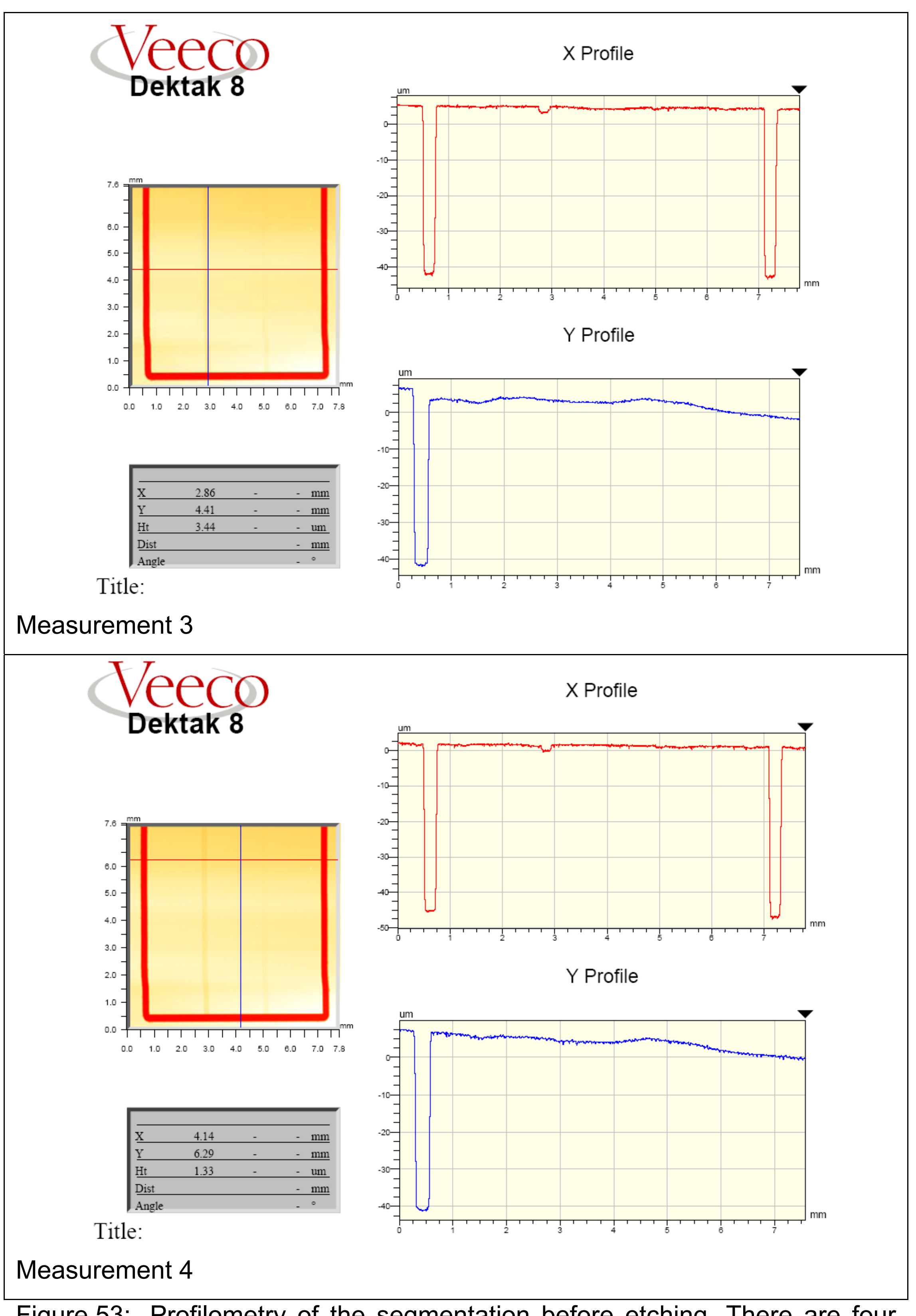

Figure 53: Profilometry of the segmentation before etching. There are four measurement points of the segmentation, defined by a cross line

(see measurement 1) on the mapped sample (left). The treatment direction is also given in measurement 1 with a red arrow. The X and Y profile on the right side shows the form, width and depth of the segmentation along the axis.

Four profilometry measurement were performed, each of them consisting of a scan of the sample in a cross line along the X and Y axis, so for each measurement the X profile and Y profile are shown together with the cross lines along the sample (left picture). The bold red contour on the sample represents the outside groove, the smaller inside grooves are not visible.

The X profiles of the measurement were obtained by moving the cross line along the treatment direction which is shown in the viewgraph of measurement 1 with a red arrow. The X profile of measurement 4, being further away in the treatment direction and the first measurement of the figure 56, the cross line, was applied in the beginning of the segmentation. The X and Y profile show a depth of 0.05mm in the outer section, while the grooves of the inner profile show only small grooves in a µm range. The depth of the outer grooves was constant (0.05 mm) in all four measurements. Following the measurements along the treatment direction one can see in the X profile that the inner grooves of the segmentation are shallower at each step. The reason for this is the tool wear during the treatment procedure. First the outer grooves were produced. During the following treatment, the used tool was used to produce the inner grooves. So the fixed depth could not be achieved and the differences in depth along the treatment direction represent the tool wear. The width of the grooves was measured to be constant: 0.2 mm, which was predefined by the tool size.

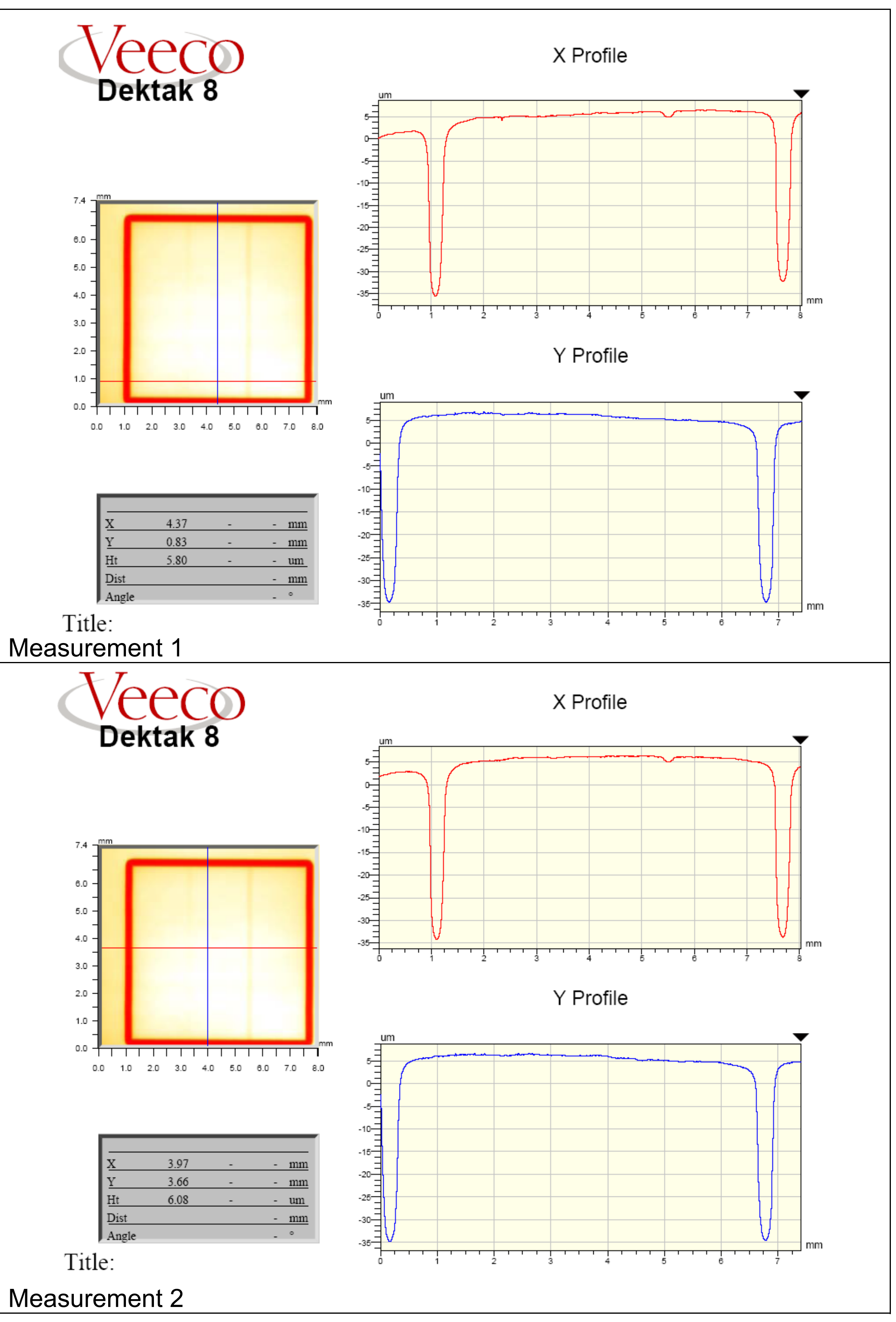
Veeco
Dektak 8
X Profile
Y Profile
X 4.37 - - mm
Y 0.83 - - mm
Ht 5.80 - - um
Dist - mm
Angle - °
Title:
Measurement 1
Veeco
Dektak 8
X Profile
Y Profile
X 3.97 - - mm
Y 3.66 - - mm
Ht 6.08 - - um
Dist - mm
Angle - °
Title:
Measurement 2

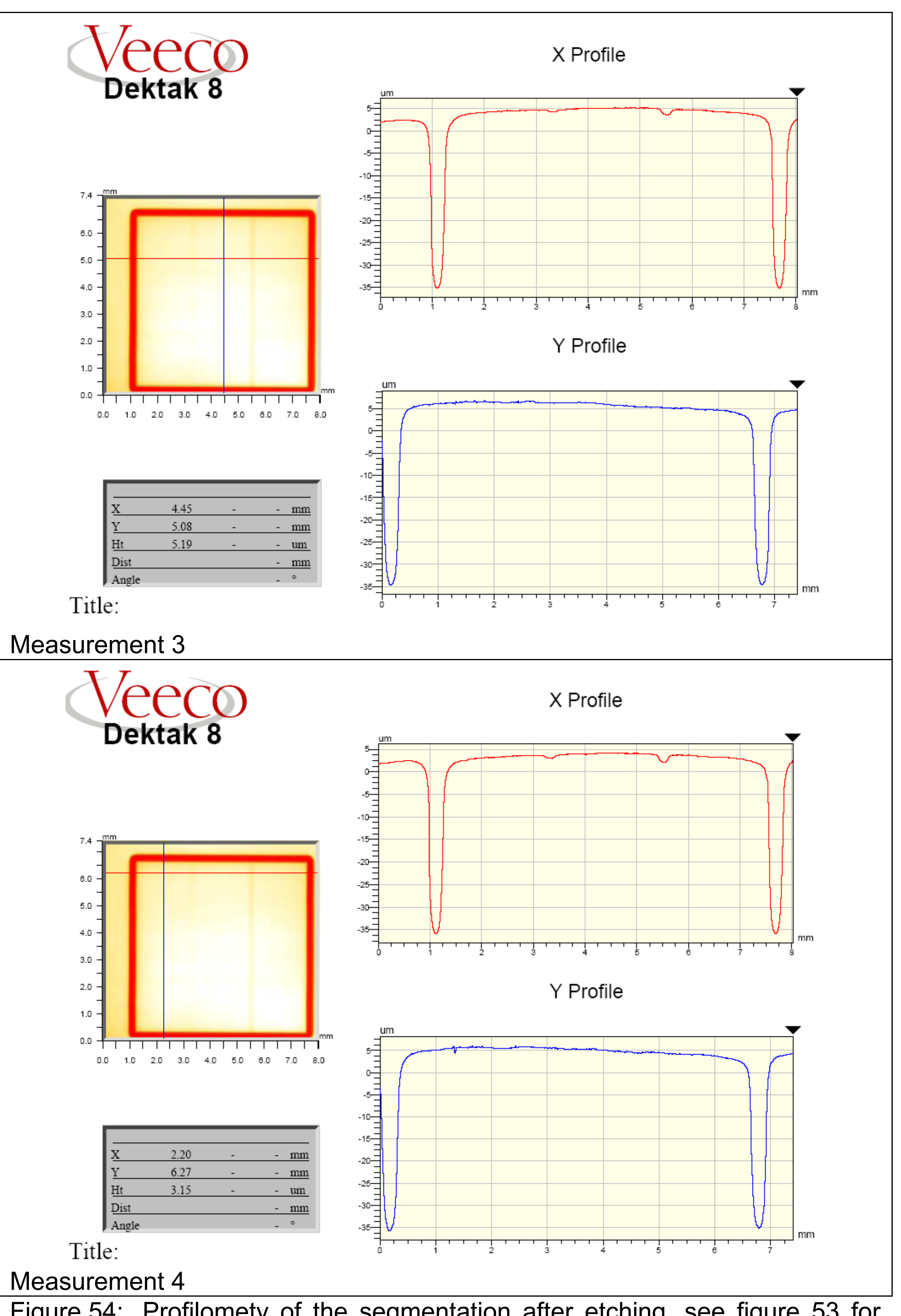

Figure 54: Profilomety of the segmentation after etching, see figure 53 for detailed explanation.

The study of the segmentation after the etching process confirmed, in all the measurements, the loss of material and an expansion of the segmentation grooves through this process. In particular, the upper areas of the grooves have a funnel-shaped width. These funnels have a width increase of approximately 0.2 mm in the upper region, which defines in the following the gap width of the segments. Furthermore, a depth of approximately 0.04 mm for the outer grooves was measured after the etching process. This is explained by the etching process causing a somewhat stronger material loss on the surface. The etching liquid enters into the grooves of the segmentation but there the fluid exchange is smaller so a larger loss of material is expected on the surface. The inner grooves mostly disappeared after the etching, as it was expected.
This is illustrated in figure 55 where, on a picture taken of the crystal after etching, the inner grooves, are almost invisible.

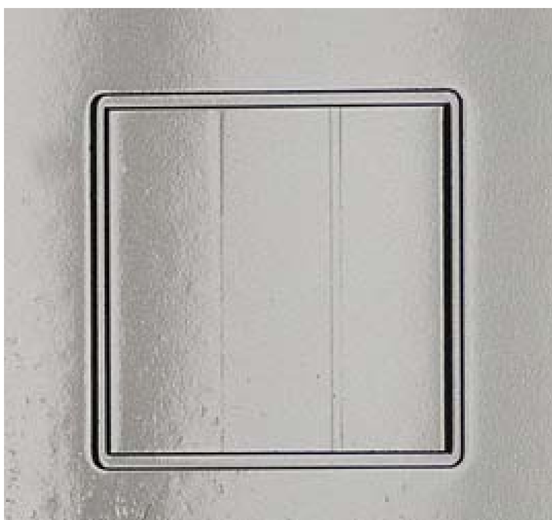

Figure 55: Picture of the segmented crystal after the etching process.

4.4 Evaluation of the ultrasonic grinding

The manufacturing process of ultrasonic grinding has proven to be suitable for this application. Using this method a germanium crystal was manufactured and successfully processed further to a detector. The procedure established

for this development process has proven to be useful. With every treatment step, new technological expertise could be obtained on the ultrasonic grinding when applied to the germanium material, thus improving the final surface quality. Mechanically generated defects like edge chips, etc. were not detected which in conjunction with the programming of the machine assures the process reliability. However, by future optimisations of the mechanical parameters like speed and feed of the machine and the grinding material, an even higher degree of the surface quality may be achieved. This is planned in future treatments.

The produced segmentation and the following verification can be described as successful mechanical test. The understanding of etching and of the following removal of material completes this result. This mechanically generated segmentation will be used in future treatment investigations of the detector development process in order to confirm the actual results and further improve the segmentation line geometry.

Mechanical segmentation yields new possibilities for germanium processing as well as segmentation production in future developments of germanium detectors. Indeed it will permit to produce semiconductor crystals with complex geometrical shapes. This enlarges the scope of exotic detector array structures. Moreover, segmentations could be also produced for any geometry, which was hardly possible in the past.

Chapter 5

5. Capsule Unit

5.1 The encapsulated detectors

As mentioned before, single Ge-crystals have been encapsulated and several of those detectors have been mounted in one unit in a cryostat, in order to build efficient spectrometers. This kind of crystal encapsulation offers advantages compared to standard set-ups.

The basic aim of the following chapter is to describe the development of a new capsule technology, in particular concerning the high-vacuum tightness and the temperature influence during the sealing procedure. The difficulty is the complexity of the detector and the germanium crystal respectively, which reacts very sensitive to external influences. Consequently there is a risk that the germanium is no longer suitable for a detector because of an incorrectly employed manufacturing process. Another difficulty is the wall thickness and the material of the capsule as well as the complicated geometrical shape of the detectors. To be able to understand all the essentials of this partially complicated production, both physical and economic aspects must be taken into account.

5.2 Encapsulation technology used for EUROBALL detectors

In the following, the manufacturing process of the capsule unit for EUROBALL is presented to have a comparison for later sections. The information shown in this section is from the patent DE 4324709 A1 [DPM]. The technology described in this patent could have been optimised over time, but it appears that there have been no attempts to do so. In figure 56 the detector manufacturing principle is presented. The detector encapsulation

process can be understood with the help of the following description and attached legend.

The capsule cup (1), with a wall thickness of 0.7 mm mode from an aluminium alloy, encloses the detector sector (3), which is subdivided in sector (3a) and sector (3b). In sector (3a) a germanium crystal is used as detector (4). This detector (4) is actuated by a disk spring (5). The disk spring (5) compresses the detector (4) to the axis (7) with help of the centring device (6). In the sector (3b) the disk spring (5) is actuated on a ceramic plate (8), and a pressure ring (9) with a support surface (10) is fixed as a centring against the capsule lid (2). The length of the cylinder of the pressure ring (9) in sector (3b) defines a distance between the capsule lid (2) and the pressure ring (11). This distance is used as thermal protection for the detector during the electron beam welding process which closes the capsule cup (1) with the capsule lid (2). Electrical feedthroughs (13+14) are installed in the capsule lid (2). About a current feedthrough (13), a getter element (14) baked out electrically up to 900°C and thus the getter element (14) is activated. The task of the getter element (14) is to guarantee the continuance of the high vacuum over years by sorption of N_2, CO and other oxygenated gases. The getter element (14) is inside a getter box (17) which is open at the front side. The getter box (17) is fixed at the capsule lid (2) and the bottom (18) shows in the direction of the detector (4). The getter box (17) is used as thermal protection for the detector (4). Besides the getter box, the ceramic disk (8) is used as thermal protection.

The capsule cup (1) is electron beam welded with the capsule lid (2) on the weld position (22). The produced welding gases of the electron beam welding process are conducted in special rings (23) to a pipe connector (16). Before electron-beam welding the capsule lid (2) containing the installed getter element (14) is locked in the capsule cap (1) and actuated by a disk spring (5). The capsule lid (2) with the installed getter element (14) is actuated by the disk spring (5) in the capsule cup (1) before the electron beam welding.

Therefore, a cone-shape outer (24) is produced in the capsule lid (2). This cone-shape outer (24) is also used as a flue gas stopper during the electron welding process. For the evacuation of the detector sector (3) and the getter sector (15) a pipe (16) is installed in the capsule lid (2). The high vacuum is generated by this pipe connector (16). The pipe connection (16) is closed by using the pinch-off-technique after high vacuum in the sectors is produced.

Legend: 1
(1a+1b): Capsule cup
2: Capsule lid
3 (3a+3b): Detector sector
4: Detector
5: Disk spring
6: Centring device
7: Axis
8: Ceramic plate
9: Pressure ring
10: Support surface
11: Pressure ring
12: Electrical feedthrough
13: Electrical feedthrough
14: Getter
15: Getter sector
16: Pipe connector
17: Getter box
18: Ground
19: Open
20: Open
21: Step
22: Weld-position
23: Ring
24: cone-shape outer (flue gas stopper)

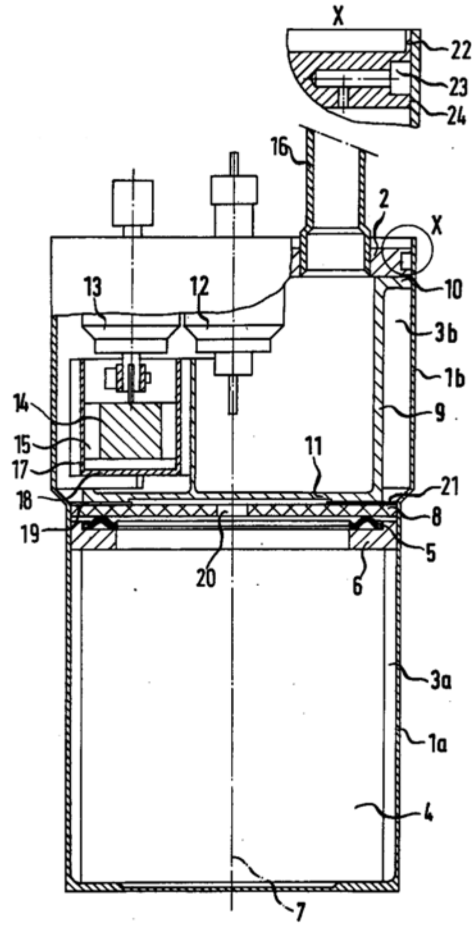

Figure 56: The EUROBALL capsule principle.

5.3 The new Encapsulation

For the planned AGATA (Advanced Gamma Tracking Array) experiment, semiconductor detectors made of germanium will be used to detect γ-radiation emitted by nuclei excited in nuclear reactions. For this purpose

three Ge detectors are integrated in a cryostat. A total of 60 of these triple detectors are necessary to complete the full spherically shaped (4 π) 180-detector array. In the centre of this spherical shell the described nuclear reactions take place. To reach the maximum coverage with as little gaps between the detectors as possible, they have a hexagonal shape, which is conical in the front and evolves into a cylinder in the back. The basic structure of a single AGATA detector is shown in figure 57.

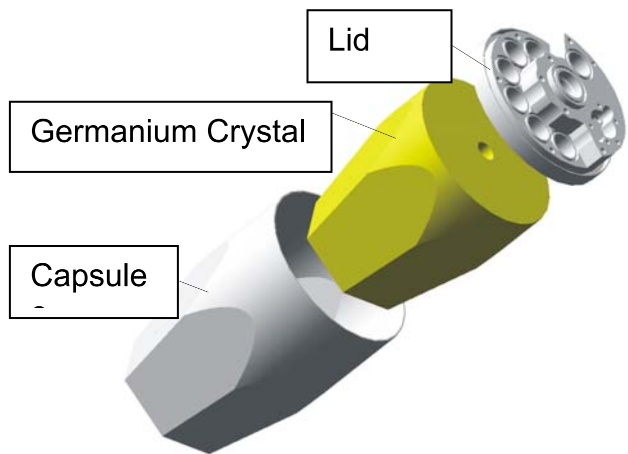

Figure 57: Basic structure of AGATA germanium detectors.

To act as reference for our further developments presented below the AGATA specification was used. This capsule unit has to fulfil the following conditions:

1. Protection of the intrinsic surface of the Ge-Crystal while maintaining a vacuum of ≤ 10^{-8}mbar for an expected life span of 10 years in a temperature range from -190°C (operating temperature of a Ge-detector) to +125°C (bake-out temperature of a neutron damaged HPGe- detector).

2. Vacuum tight capsule unit, which allows for easy handling of composite detector systems and increases the system's reliability.

3. Thin-walled capsule closely fitting the Ge crystal to reduce absorption and avoid dead volume.

4. AC extraction of the detector signals to allow the outside wall to be on ground potential, thus simplifying a compact arrangement of several detectors.

The mechanical specifications for the capsule unit based on above mentioned requirements are listed in table 13:

Table13: Specification of the capsule unit.

High accuracy grade, accuracy in shape and accuracy of position	
Material	AlMg 4.5Mn
Wall thickness	0.7 mm
Ultra-high vacuum sealing	10^{-8} mbar
Working temperature range	-196°C to 150°C
Bake out temperature	up to 150°C

To construct a capsule with these specifications, the following essential points have to be considered:

-- The welding of the capsule with a lid.

-- The creation of the vacuum.

-- The getter for maintaining the vacuum.

In the following sections, these three major points of the development framework will be treated separately.

5.3.1 Welding of the capsule with the lid

To achieve a high-vacuum tight capsule for a germanium detector, a particular manufacturing technique was developed. The main difficulties in

this process have to be ascribed to the complexity of the detector and the germanium material itself, which is extremely sensitive to external factors. A risk is that the germanium no longer can be used as a detector if an incorrect manufacturing process is applied. Another difficulty is the wall thickness and the aluminium alloy of the capsule as well as the complicated geometry of the AGATA detectors. The process of welding the capsule with the lid by a laser is shown in the following section, which encompasses the first stage of the complete development of the encapsulation. In order to better understand the complicated manufacturing technique, both physical and economic aspects have to be taken into account.

5.3.1.1 Welding experiments

As mentioned in chapter 5.3.1, welding was chosen as joining process between the capsule and the lid in order to meet all requirements for the closing of the capsule unit. One constraint is to keep the temperature of the germanium crystal inside the capsule low during the welding operation. The laser welding technique was chosen because a suitable parameter setting of a CO_2 laser can prevent the heating of the semiconductor, and because this solution is cheap. Currently the encapsulated germanium detectors, which are needed for AGATA, are manufactured with a licensed electron beam welding process utilised in detector production by third parties. Electron-beam welding can only be applied in vacuum and is usually employed only in mass production, which is too cost-intensive for our purpose. However, laser equipment is easily available and demonstrates an economically better alternative in prototype- and single component-building.

5.3.1.1.1 Test capsules

Two different capsule models were designed. Both are identical in the essential parts of the geometry - in the weld area, and height and width dimensions of the detectors. Model type 1 was used for adjusting the laser

parameters, while model type 2 depicts the real experiment with the optimal parameters obtained from the tests with the model type 1. An integrated KF-flange in the lid allows the evacuation of the capsule.

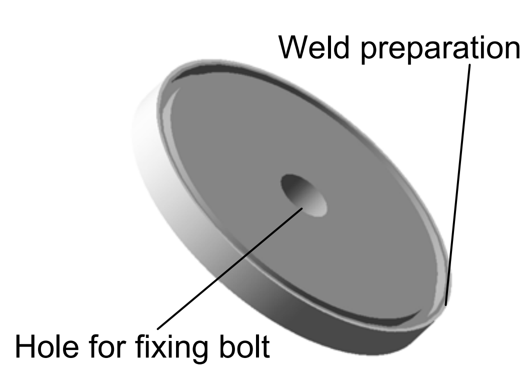

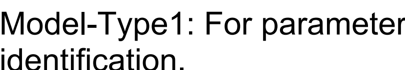
Model-Type1: For parameter identification.

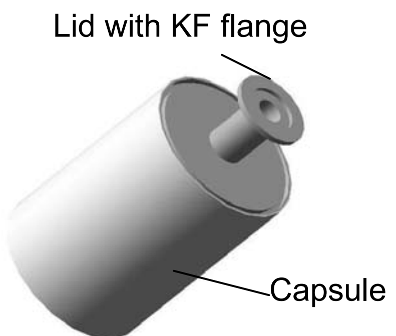

Model-Type 2: Implementation of the experiment and temperature analysis during the welding process.

Figure 58: Capsule types.

After welding, a high vacuum should be producible inside the capsule of type 2, which is possible only if the weld quality fulfils our requirements. As capsule material the aluminium alloy AlMg 4.5Mn is used. The insulation thickness is 0.7 mm and the diameter of the total capsule is 84 mm. To be able to diagnose the influence of the welding on the temperature inside the capsule, an aluminium dummy-crystal was positioned inside the capsule. The distance between dummy and lid is in accordance with the real geometry of an AGATA detector.

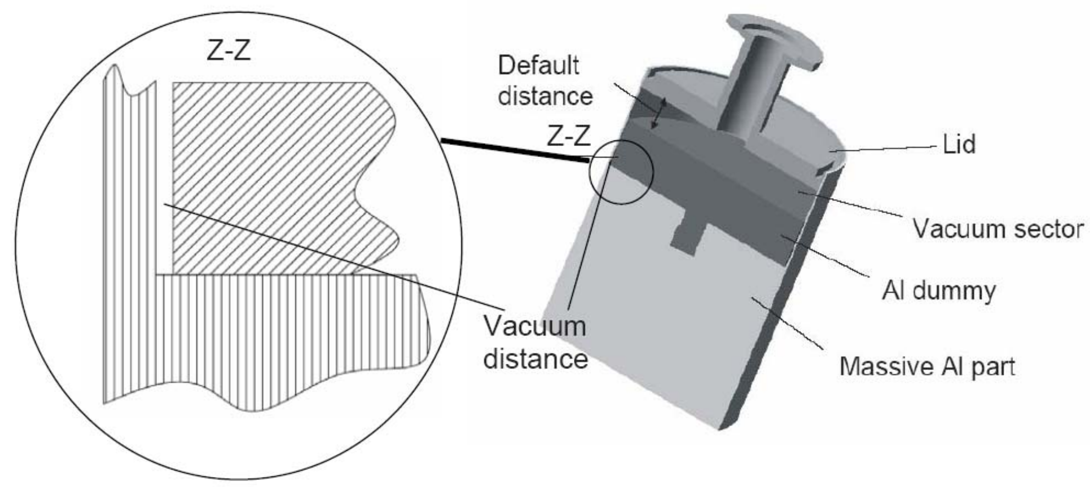

Figure 59: Sectional view of Model-type 2.

The idea of the particular manufacturing process is shown in figure 60 and is a combination between laser welding and the construction of the closing part of the capsule unit which is described in the following. The lid is fixed in height with the help of a step, which existed in the capsule cup. This step gives a constant height between the lid and the crystal also after multiple opening and closing of the capsule unit. In the lid is yielded a weld preparation, which has a low wall thickness at the cup side. The number of possible opening and closings is dependent on the weld position and the weld preparation depth, which is designed with 4 mm depth for the moment. The wall thickness of the lid and the cup generates the weld material, which is shown red in the figure, and is melt with the help of the laser beam intensity. Between the walls of the lid and cup exists a clearance. The melt flows through the clearance and thus, the lid and the cup are connected. The inert gas for this weld process comes from an inert gas injector and produces a cross jet. The inert gas is used to protect the melt from outside influences. The produced cross jet blows rest particles, which are generated during the welding, in the weld preparation at the same time. Hence, no particles come inside of the capsule unit during the closing.

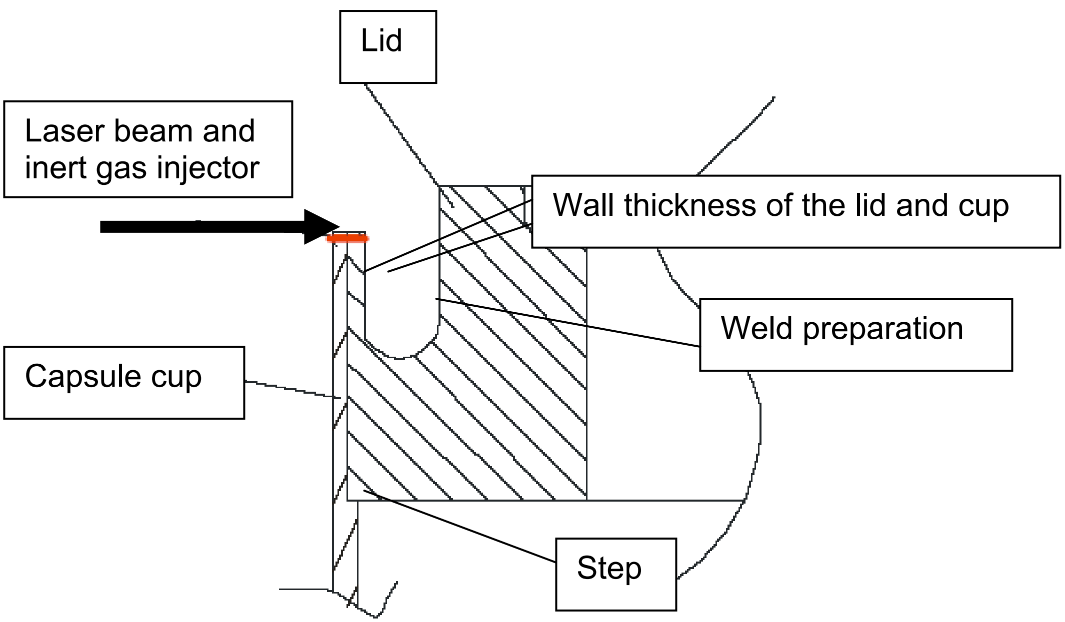

Figure 60: Principle of the manufacturing process.

5.3.1.1.2 Measuring setup

To perform temperature measurements of all models, eight PT100 sensors per capsule were fitted in different positions inside. The different positions of the PT100 sensors are decelerated with numbers. It is important to ensure that all significant regions in the assembly are taken into account. As already mentioned in Chapter 5.3.1 the review of the influence of the welding on the temperature of the germanium crystal is the main concern. For this reason, the measurement set-ups were equipped with the sensors directly on the surface of the dummy crystals. In addition, sensors were mounted at the locations of electronic feedthroughs on the lid, as well as in the cavity of the capsule with the help of special mounting rings. A schematic representation of one sample measurement setup is shown in figure 61.

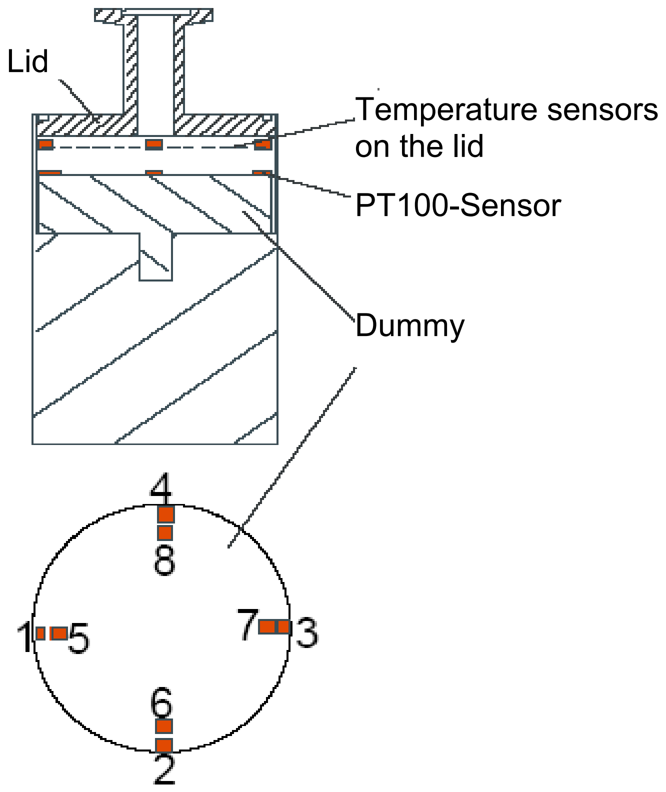

Figure 61: Schematic representation of a measurement set-up with PT100 sensors.

5.3.1.2 Laser beam welding of the models

The laser welding process has been carried out with a CO_2 laser owned by the company Rofin Sinar [MSC]. The laser of the type DC025 has a maximum laser power of 2.5 kW at a wavelength of 10600 nm. This laser was chosen for the study because in the later mass production of capsules the operating costs of a CO_2 laser system are significantly lower as compared to other laser systems operating at different wavelengths. For the positioning and the welding process, fixtures were attached to a pivot on an x-y table. The laser head and the inert gas injector were mounted on the Z-axis. This system is shown in figure 62.

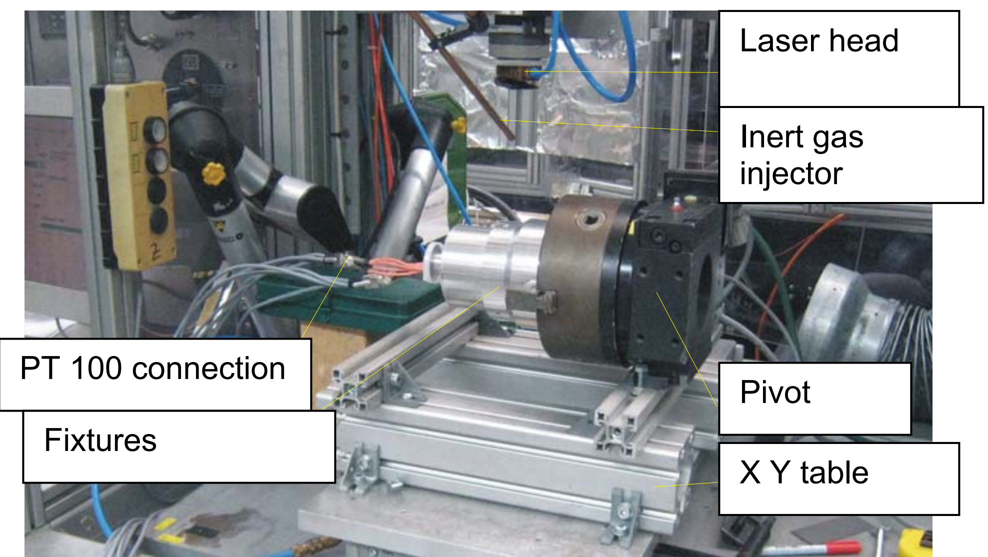

Figure 62: Experimental setup.

For the first welds both laser power and feed speed were varied. The displacement of the welding process was, analogous to the sample diameter, about 84 mm. To screen the process from the ambient air, helium was applied as an inert gas by a gas injector. At the beginning, a computer program was developed for the welding process and consecutively the focus position was defined. To protect the focusing optics against spatter and flue gas, a cross-air flow (cross-Jet) with compressed air was used. The different gases are activated by the computer program in the beginning of the welding process.

5.3.1.3 Results

In the first series of the tests a total of 7 samples of Model-type 1 were produced with a standard clearance of H7. Table 14 documents the experimental parameters for the individual samples and the test results. For this first test series, important parameters were the rotational speed, the laser power and the focus distance to the sample. The first sample was welded with a power of 2 kW and an initial rotational speed of 4 meters per minute (m/min).

Table 14: Type1: Documentation of the experimental parameters.

Type 1 Nr.	Power [kW]	Speed [m/min]	Weld angle [°]	Result
1a	2	4	120	several defects
1b	2	5	120	several defects
1c	2	6	120	good connection
2a	2	6	120	incorrect clearance >0,1 mm
2b	2	6	250	incorrect clearance >0,1 mm
3	2	6	360	incorrect clearance >0,1 mm
4	2	6	360	incorrect clearance >0,1 mm
5	2	6	370	incorrect clearance >0,1 mm
6	2	6	370	good connection
8	2	6	370	good connection

The samples 1 and 2 were divided into several azimuthal sections to increase the number of usable samples. With model 1 three welds have been produced, all using different rotational speeds. The feed rate was varied in three steps from 4 to 6 m/min. The welding results were very satisfactory at a feed rate of 6 m/min. Based on experience the power was adjusted to 2 kW. By default the process was laterally fed with 35 litres of helium per minute as inert gas.

From the second sample on there were some irregularities caused by the gap between the lid and the capsule. The gap is permitted to have a maximum width of one tenth part of the wall thickness of the welded component for the laser beam process without filler. Due to the large clearance (>0,1 mm) there was a sag from the welding seam and therefore there was no good connection. This was seen up to sample No. 5. Furthermore there was an irregularity at the end of the weld as figure 63 shows. With the help of a power ramp[3] the observed craters could be largely avoided.

---

[3] The laser power was progressively reduced at the end of the welding process.

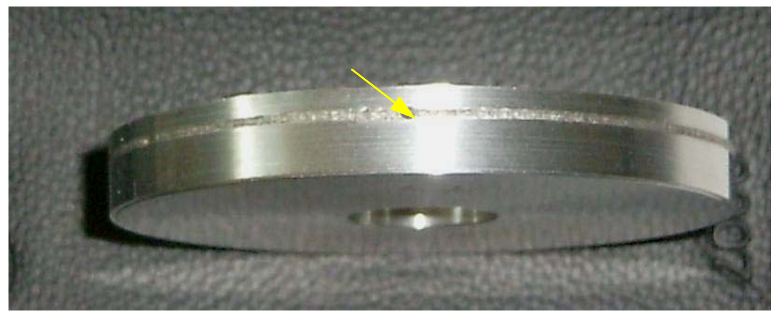

Figure 63: Welding micro crater.

To obtain a closed weld along the circumference and to simplify the adjustment of the welding process and the control of the rotation, the rotation angle was fixed to 400° which means an overlap of 40°. The welding process itself continued only to a welding angle of 370° and therefore an overlap of seam of about 10° developed. In this overlapping area the beam power of the laser was ramped down to zero at the end of the process in order to avoid welding scratches at the weld end. The best results were reached by a focus depth of 160 mm, a beam power of 2 kW and a speed of 6 m/min. With this speed and the diameter of 84 mm of the capsule a welding process duration of about 2.7 s is reached. Fillers were not used in order to keep the beam power as small as possible and therefore to produce less heat.

Using a helium leak detector ULTRAREST UL 500 of the company INFINICON and a vacuum pump the vacuum tightness could be demonstrated for capsule type 2. The lowest measurable leak rate of the device with a time constant of < 1s is in the order of $2x10^{-10}$ mbar•l/s [INU], which is defined as vacuum tight and fulfils the specification of the capsule unit.

The mode of operation of a helium leak detector is described in the following [INU]: The samples are flange connected to the detector. To detect the leak rate with the leak detector the sample is evacuated employing the turbo pump unit of the tester. The test gas helium is charged from the outside of the

sample, infiltrates through possible leaks in the sample, and is then measured in the detector. The principle is shown in figure 64.

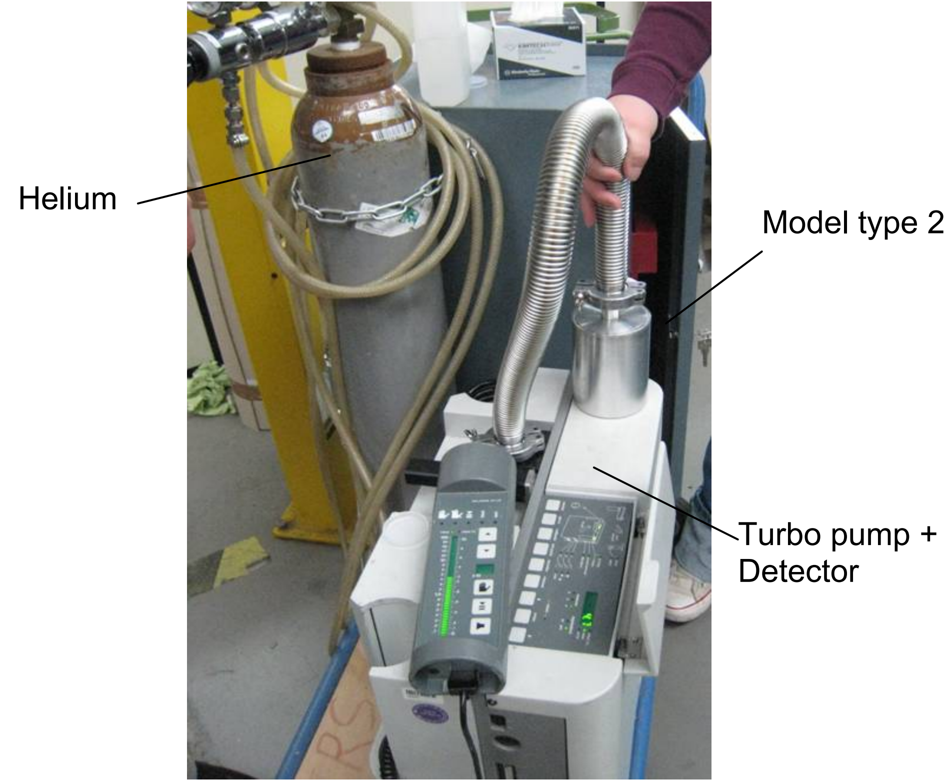

Figure 64: Principle of a leak test with a helium leak detector.

Sample 1 was the first to be used for the test series of type 2. The first weld with it was not vacuum-tight. This was detected with a helium leak detector. It was noted that a continuous pore existed at one point of the weld. To cure this failure the weld was again melted (see Fig. 65) and the tightness was checked again. The following helium leak test of sample 1 was vacuum-tight. The welding parameters and the results are summarised in table 15.

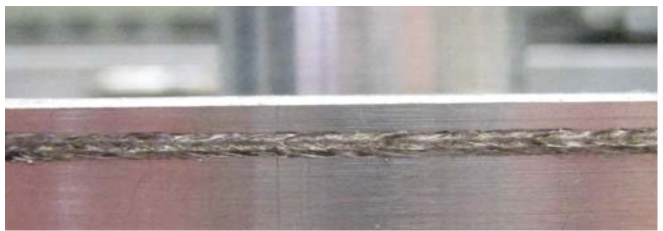

Figure 65: Capsule model 1 with a double weld.

Table 15: Type 2: Documentation of the experimental parameters.

Typ 2 Nr.	Power [kW]	Speed [m/min]	Welding position	Terms	Result
1	2	6	2,5 mm	good clearance	vacuum-tight
2	2	6	1,6 mm	Incorrect clearance >0,1 mm	not tight
3	2	6	2,5 mm	Incorrect clearance >0,1 mm	not tight
5	2	6	0,8 mm	Incorrect clearance >0,1 mm	not-tight
6	2	6	4,0 mm	Incorrect clearance >0,1 mm	not tight
8	2	6	1,5 mm	very good clearance	vacuum-tight
7	2	6	1,5 mm	very good clearance	vacuum-tight
10	2	6	2,0 mm	good clearance	vacuum-tight
9	2	6	1,0 mm	Incorrect clearance >0,1 mm	not tight
4	2	6	1,0 mm	good clearance	vacuum-tight

Table 15 shows the used parameters of the laser, the welding position of the capsule, the quality of the gap and the vacuum results of the helium leak test. All vacuum-tight capsules achieved a vacuum of $2x10^{-10}$ mbar•l/s, whereas other capsules were not tight.

The second sample welded was capsule model 5, because an optical test showed the "biggest" clearance. Before circumferential welding four welding points at a distance of 90° were created to protect against a possible shearing introduced by the heat. Analogous to model 1 a vacuum leak was obtained, which could be demonstrated by the leak detector. Like it was done with model 1 the first weld was melted again. Nevertheless, because of the large clearance vacuum-tightness couldn't be reached. The same problem has been detected for the capsules 2, 3, 6 and 9.

The capsule model 8 shows a very narrow clearance compared to the previous samples. Consequently the welding produced a regular, homogeneous seam and resulted in a vacuum of $2x10^{-10}$ mbar•l/s. The welding of capsule model 7 showed an identical result. The capsules 9 and 10 showed irregularities in the seam. As a result they could not reach vacuum-tightness. Again the large clearance of the components is assumed to be the reason.

The last part welded was capsule sample 4. After the first weld the material was melted repeatedly in the identical track. Checking the weld using the leak detector this sample also showed vacuum-tightness.

As a result of the welding experiments 5 out of 10 capsules could be welded vacuum-tight with these laser parameters. All of those capsules had a good clearance of ≤0.1 mm and showed a regular, homogeneous seam. This means, that the welding section of the capsule must show a clearance of H7/h7 and according to this a circularity of this section. The welding position of the weld is not important for this process.

5.3.1.4 Influence of heat during the welding operation

To measure the influx of heat during the welding process, PT100 sensors, which were described in section 5.3.1.1.2, were connected to converter units coupled to PCs. To get a visual impression of the heat distribution and to be able to compare the results, a further temperature measurement was carried out with a thermal imaging camera (see chapter 5.3.1.4.2).

5.3.1.4.1 PT100 measurements

Using the PT100 sensors it was possible to measure the temperature variation during the welding process on the crystal dummy as well as on the capsule and on the lid. On the surface of the crystal-dummies, temperatures above 150 °C would correspond to a critical value for germanium. Thus, for every capsule unit a PT100 temperature measurement setup in the capsule has been performed but in the following, only the major measurement setup is shown schematically in figure 66. The graph of the associated temperature evolution is shown in figure 67. The maximum temperature measured on the surface of the crystal dummies was 32 °C, which was a very satisfying result. Therefore, one criterion of the qualification of the laser beam welding for

sealing the capsule was fulfilled. Further sensors which were fixed inside of the capsule wall showed maximum values of 50 °C. Both measurement points had the same distance to the weld, therefore the reason for this temperature difference was assumed to be the gap between crystal and capsule. Also the sensors of the lid showed lower temperatures than it was suspected. The highest recorded temperature of the complete experiment was 78.9 °C, measured at position 4 of the measurement setup 2 on the bottom side of the lid. The temperature distribution of this welding is shown in figure 67.

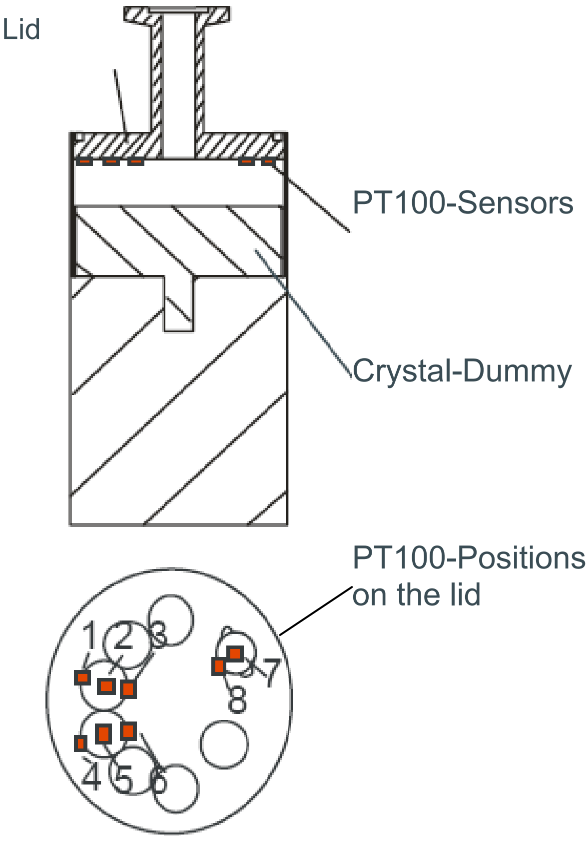

Figure 66: Schematic diagram of the measurement setup 2 with the placement of the PT100 sensors.

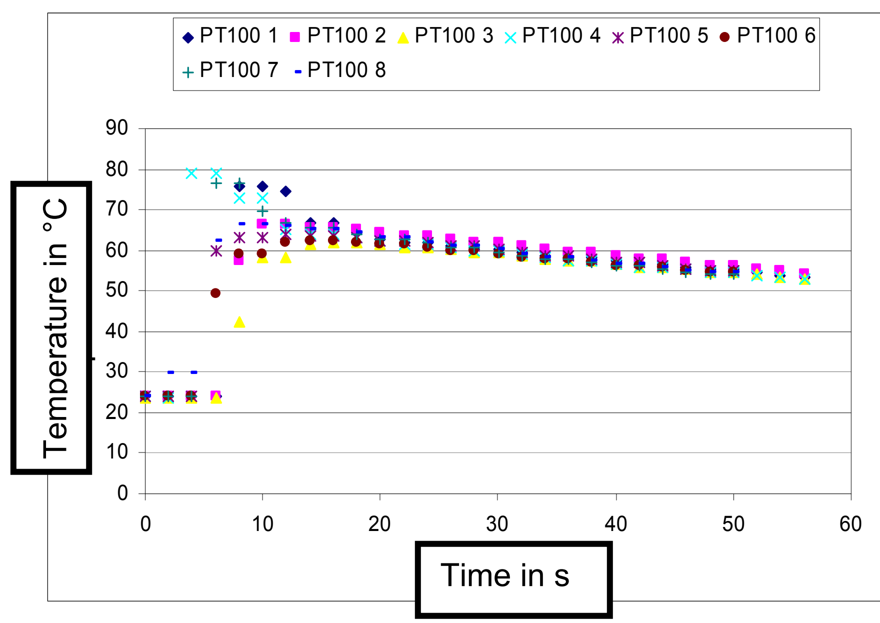

Figure 67: Graph of the PT100 sensors 1-8 of the measurement setup 2.

The temperature variation of the PT100 sensors in figure 67 shows the room temperature of 23°C at the first 8 seconds. The welding process has been carried out between 8 and 11 seconds, which explains the temperature rise of the sensors up to 78.9°C. The rise of all sensors nearly at the same time is explained by the fast welding process, which is 3 seconds. After the welding time, the temperature variation shows the cooling time of the sample.

5.3.1.4.2 Thermal imaging camera

A thermal imaging camera was used during the experiment in order to get a comparison between the temperature effects inside the capsule and the heat affected zone outside of the weld. This camera had four selectable temperature ranges which overlapped with the temperatures observed in the welding process. In the first range, which lies between 24.4 °C and 42.9 °C, the geometry of the capsule could be clearly seen. Figure 68 shows a picture taken just before starting the welding process to enable a comparison with the pictures after the welding process. The ambient temperature was approximately 22 °C during the entire experiment.

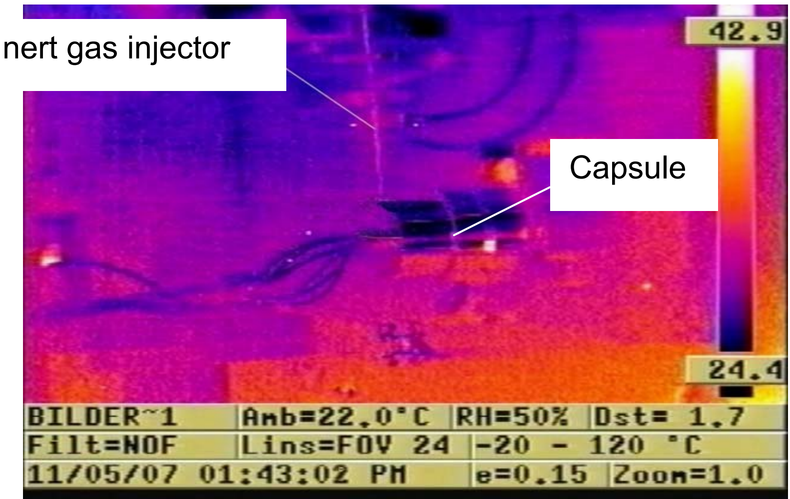

Figure 68: Absorption image of the thermal camera in the temperature range of 24.4 °C to 42.9 °C before the welding process.

Immediately after the welding process, the heat affected zone was limited to the weld. Figure 69 shows a picture of the capsule unit, 7 s after the end of the welding process. The hot weld seam is clearly observable. The lid and in particular its flange are heated to temperatures above 40 °C, while the capsule walls are only moderately warmed up.

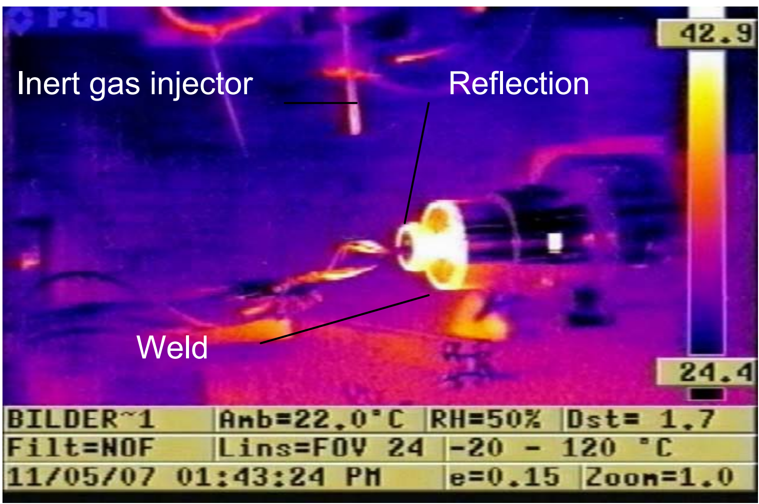

Figure 69: Absorption image of the thermal camera in the temperature range of 24.4 °C to 42.9 °C seven seconds after the welding process.

In the following two measurement settings, images are only shown for the welding process. In the temperature range from 56.6°C to 509°C it is visible that, immediately behind the beam focus, the weld, in which the material is melted, has a purple colour corresponding to a temperature of 150 °C to 300 °C. In the focus itself the beam intensity produces a temperature beyond the shown range, sufficient for melting of the aluminium oxide layer.

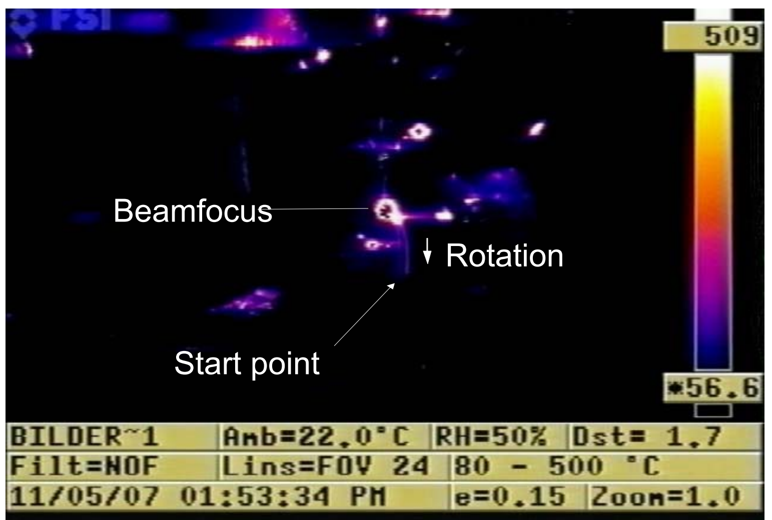

Figure 70: Absorption image of the thermal camera in the temperature range of 56.6°C to 509°C during the welding process.

Even in the last and highest temperature range the limiting temperature of 711°C, recognized in the laser beam focus is above the melting temperature of aluminium (660°C) but still below the melting temperature of the oxide layer (2050°C).

Figure 71: Absorption image of the thermal camera in the temperature range of 217°C to 711°C during the welding process.

5.3.1.5 Thermal stress

All vacuum-tight capsules underwent two different thermal stress tests. The capsules of type 2 were dipped into liquid nitrogen until they cooled down completely 20 times periodically. Between the dip-cycles a warming up to room temperature took place. Later the capsules were also heated 20 times periodically in a blast furnace. An example of the heating cycles is shown in figure 72.

Temperature in °C

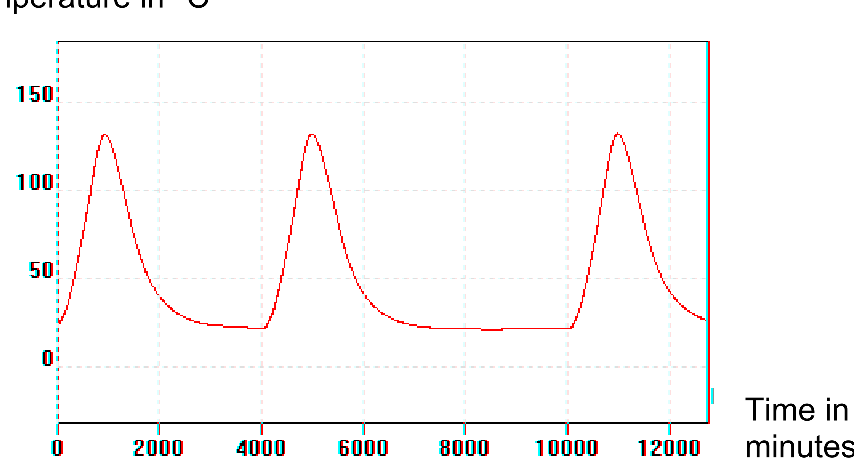

Figure 72: Temperature diagram of the periodical heat test.

After these thermal stress tests vacuum tests were carried out successfully! This means that the same vacuum results as before the thermal stress were obtained. The shape distortion and tolerance checks, which proved that there is no thermally critical region situated around the weld seam, were successful.

5.3.1.6 Evaluation of the capsule welding

It was shown that a vacuum-tight weld can be realized by using a laser beam welding process with a CO_2 laser. Excessive heating does not appear in any important zones, so the damage of semiconductor because of too high temperatures can be excluded. Cases of vacuum leaks in the welding seams are accounted for by too large clearances between lid and capsule. The reproducibility of the positive results can be warranted however, through constructive changes in the capsule or lid. This means that the clearance must be in accord with a tolerance class of H7/h7.

Because of the genuine combination of inert gas injection, clearance and weld preparation, flue gases or other processing particles cannot arrive at the vacuum part. This was detected by inspections of cross-sectional weld seam cuts of the weld type 1 under the microscope.

Based on these positive characteristics, capsules produced by this method do not require any shielding against high temperature nor constructive measures against treatment particles and flue gases. Therefore, additional material in the capsule can be neglected, making high vacuum more effective, and reducing the cost of production.

Furthermore, the thermal stress tests have confirmed the positive result of the experiments. Whether the resistance of the weld is constant for a longer period of time, e.g. for 10 years, however requires long term testing.

During the investigations different mechanical welding arrangements could be evaluated. The most suitable one turned out to be the butt seam. By

introducing a step in the capsule, the lid distance to the crystal could be kept constant. Depending on the weld preparation a re-closing could thus be guaranteed, which means in the later application servicing of encapsulated detectors, keeping the same caps and lids would be possible. This feature provides another economic advantage.

5.3.2 Creation of the vacuum

To realize the second essential point in the construction of a detector capsule, evacuating the capsule unit and permanently maintaining high vacuum, an ultrasonic manufacturing process was considered. Ultrasonic welding processes are commonly used in the refrigeration and air conditioning industry. In addition ultrasonic welding is employed in various other branches of industry for diverse applications, for example in the thermostatic technology to seal the welding of capillary tubes or for sealing copper pipes in the production of solar collectors in the field of solar engineering. Fig. 73 shows examples of ultrasonically welded pipes.

Leak proof welded aluminium and copper pipes. Since no melt is generated, both the microstructure and the material-specific properties remain unchanged.	Ultrasonically welded copper and aluminium capillary pipes.

Figure 73: Leak proof welded aluminium and copper pipes [SSS].

The evacuation device considered consists of an aluminium pipe that is connected to the lid of the capsule unit by a traditional welding method. At the

other end of the pipe evacuation of the air can take place by using a standard vacuum pump. After arriving at the desired vacuum, ultrasonic welding is used for crimping the aluminium pipe at a certain position in order to reach high vacuum tightness. This process was evaluated for our purpose and is discussed in this chapter.

5.3.2.1 Operating principle of the process

During the ultrasonic welding process, bonding takes place in a solid state, which means that joined parts are not melted. This is accomplished by overlapping the weld metals and rubbing them against each other by using low-pressure and high-frequency mechanical oscillation. Within a fraction of a second, a permanent, solid and metallurgically clean connection with outstanding physical properties is created. As a rule, all non-ferrous metals are suitable for this joining technique, however, copper, aluminium and their respective alloys are particularly well-suited. In contrast to conventional welding methods, ultrasonic welding also allows the welding of materials with different melting temperatures, as aluminium and copper for example. The ultrasonic welding process offers the user a number of economical, technological and not least important ecological advantages which form the foundation for the worldwide success of this method:

- high-quality metallic bond
- excellent physical properties
- low thermal load to welding materials
- economical due to low operating costs
- comprehensive process control
- short welding times
- No generation of particle residues
- No production of flue gases
- No filler material

5.3.2.2 Experiment

To test the suitability of the process for this application 15 aluminium pipes from AlMg4,5Mn were used, with an inside diameter of 8 mm, a wall thickness of 0.5 mm and a length of 8 cm. With the help of ultrasonic welding one end of the aluminium pipe was closed and the pipe filled with helium gas. After the filling the other side of the pipe was also closed. The result of the subsequent tests with a leak detector presented 100% tightness of the sample. Like with the capsule tests before, all vacuum-tight pipes were subjected to two different thermal stress tests 14 days after production. On the one hand, the pipes were dipped in liquid nitrogen until they completely cooled down 20 times periodically. Between the dip cycles a warming up to room temperature took place. On the other hand the pipes were heated also 20 times periodically in a blast furnace. The up and down of the temperature as well as the chronological sequence was identical to the capsule test before. An example of the heating cycles is shown in figure 74.

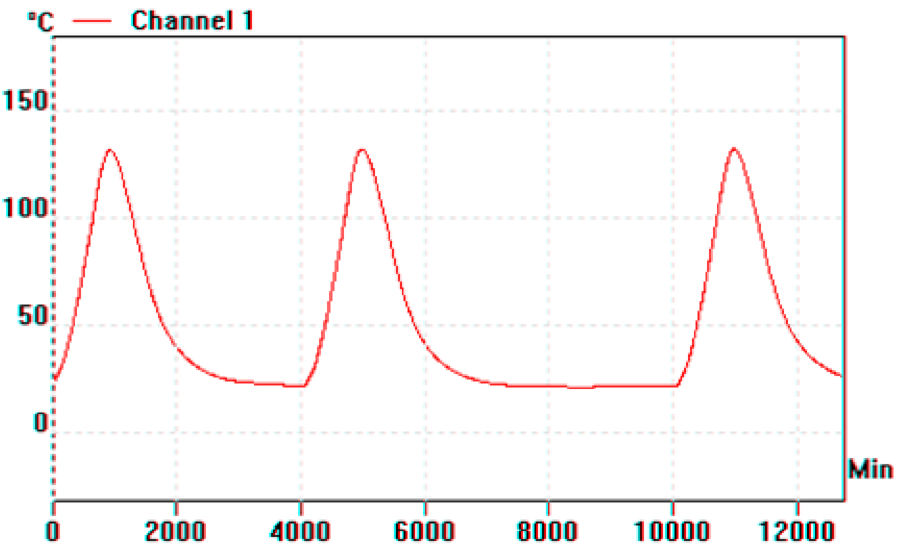

Figure 74: Temperature diagram of the periodical heat test.

Between these temperatures stress tests the pipes were checked with the leak detector. In doing so no helium was detected. After the ending of all thermal stress tests all pipes were opened and inspected with the leak detector at the same time. Helium could be detected in all of the 15 aluminium pipes, which proves the tightness of the pipes, the welding seams and consequently the soundness of the process for the application could be shown.

5.3.2.3 Evaluation of the vacuum process

The reliability of the ultrasonic welding process was confirmed successfully by the experimental investigations. A further advantage of the process is that there is no production of flue gases or particle residues while closing the pipe. Therefore, a contamination of the vacuum or the surface of the semiconductor with particles or flue gases can be excluded. The thermal strain of the material is constant, because the ultrasonic welding uses no filler material. This was confirmed by the thermal stress tests. Another advantage of the process is the possibility to use the aluminium alloy AlMg4,5Mn, because the complete capsule unit can be manufactured using the same material. Furthermore, this aluminium alloy welds well with conventional welding processes, which simplifies economically and technically the positioning of such a pipe into the lid of the capsule. The only disadvantage of the ultrasonic process might be the length and the width of the weld-area, because this area may interfere with the cooling system of the detector. The length of the weld-area is shown in figure 75. In the experiments, lengths between 8 mm and 5 mm were tested, but a further reduction is planned to be tested in future.

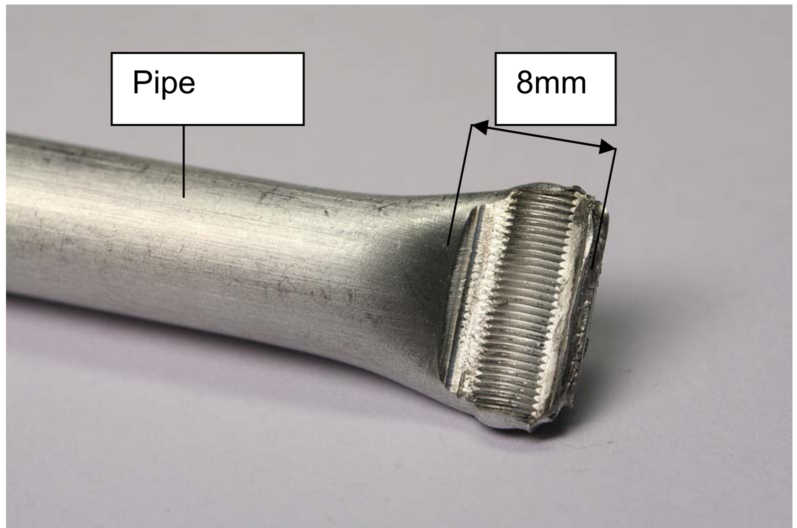

Figure 75: The lengths of the weld-area.

5.4 The Getter element for maintaining the vacuum

Another significant characteristic of the encapsulation technology is the use of an internal getter element to keep high vacuum over a long period. The task of a getter in this closed high vacuum system is the bonding of the rest gas particles. For this purpose, gas particles are connected by a chemical bond with the atoms of the getter surface or the gas particles be retained by sorption. The integration of such getter element in a detector system has proven to be successful with the previously encapsulated semiconductor detectors in the past. However, this technical configuration has several deficiencies for qualified future projects in the detector development, for example, the activation temperature of the getter element and the associated getter box. Therefore, to fix such a getter element in the capsule, a constructive, economic and physically meaningful solution has been searched for. In this case, the problems were the lid material aluminium, the activation of the getter with electrical heating, the capacity of the getter element and the specific place in the capsule unit. A suitable getter element was selected in

collaboration with the company SAES Getters [STP], and integrated into the lid of the capsule unit.

5.4.1 The Getter configuration

After specifying all inner materials and surfaces of the capsule unit the company SAES Getters suggested a getter element based on zirconium oxide with the trade name ST172/HIS/7-6/150C. The advantage of this getter element is the activation and regeneration temperature. Thermally activated getters of this type are activated at a relatively low temperature of 450 °C with approximately 10 minutes of periodic application time and with a sufficient preparation of the components of the detector capsule, which means, degreasing, cleaning, baking and polishing of the component surfaces. Thus, this getter type could be integrated directly into a getter section in the lid of the capsule unit, without high-capacity thermal safety measures against the lid or the detector. The activation of the getter is realised by electrical heating with an electrical feedthrough, which is integrated in the lid.

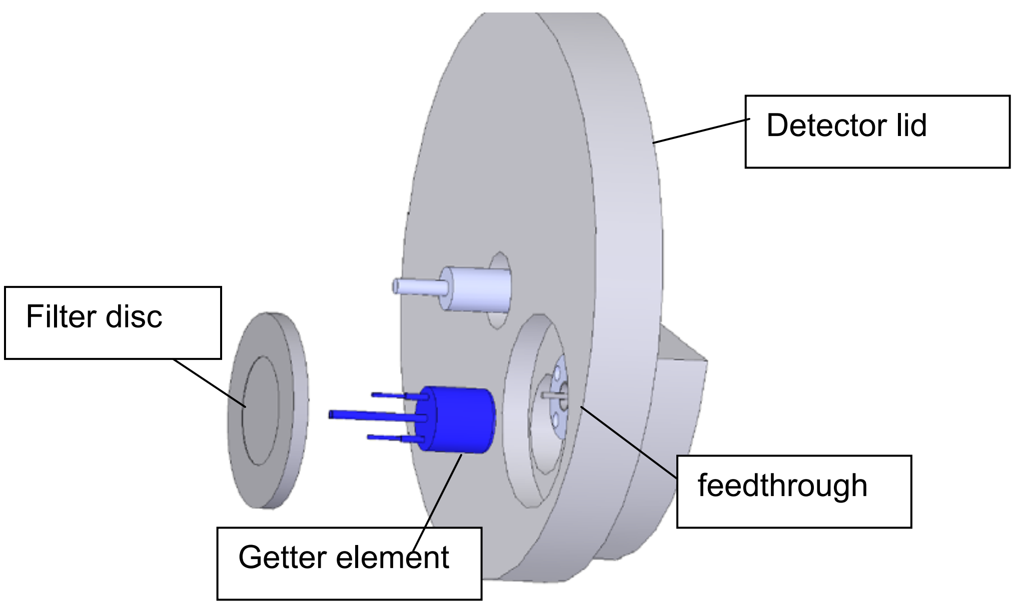

Figure 76: Configuration of the getter element in the detector lid.

The used activation values of the getter element are shown in figure 77. For an activation temperature of 450 °C, a current is needed of approximately 2 A and a corresponding voltage of approximately 5V.

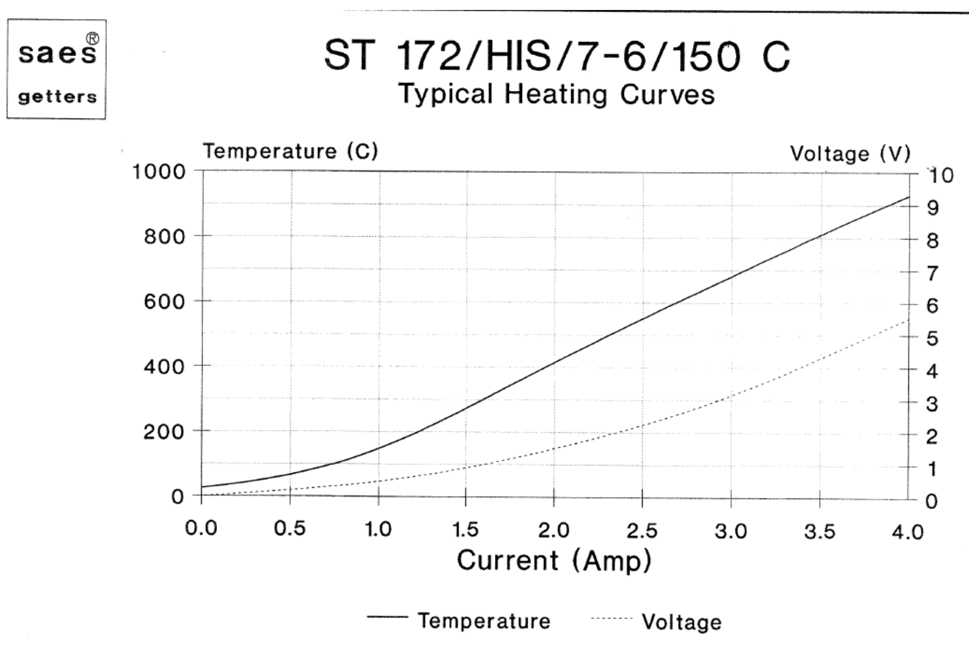

Figure 77: Typical heating curves from a ST172/HIS/7-6/150C.

A disadvantage of this getter type is the possible flaking of getter material during the heating period of the thermal activation and/or the handling with the capsule unit over time. A contact of getter particles with the detector surface may cause damage of the detector and must be avoided. Therefore a filter disk has been realised as protection of the semiconductor and to separate the getter sector from the detector sector. This principle is also shown in figure 78.

5.4.2 Filter disk

On one hand, the task of the filter disk is to block getter particles on the other hand, to have an optimal getter function, a gas exchange must be guaranteed between the detector and the getter section. To fulfil these requirements the

filter disc (see figure 78) consists of a wire cloth, which is stacked in several fine and micro mesh layers. The cloth is made of stainless steel wires and the frame is made of aluminium.

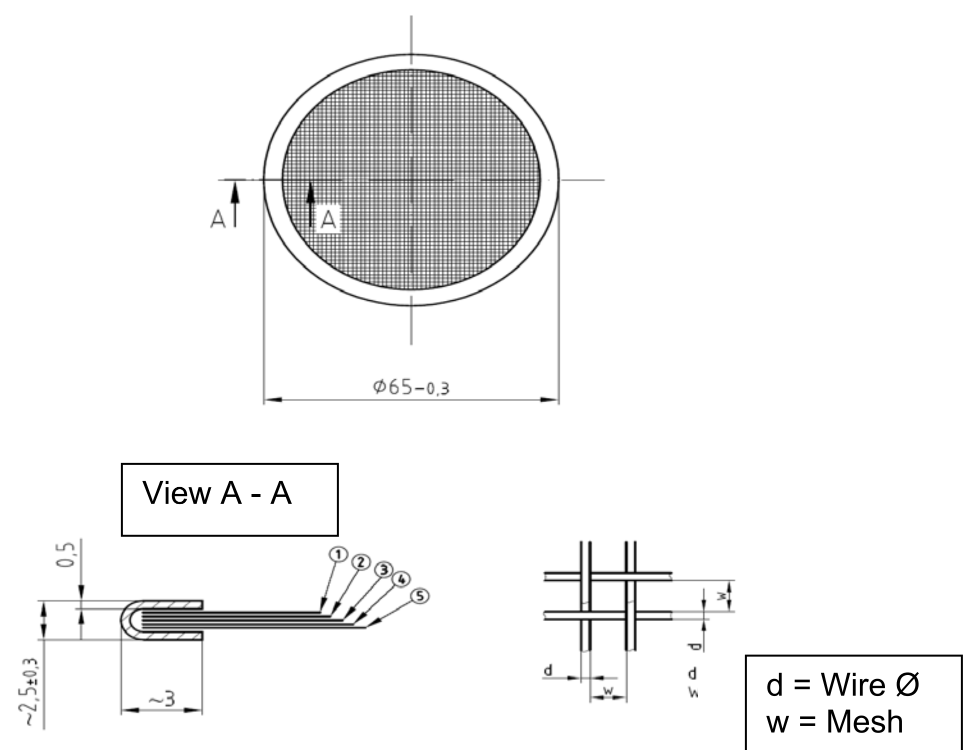

Figure 78: Basic structure of the filter disk.

5.4.3 Evaluation of the getter configuration

A new getter element is suggested which has a lower activation temperature compared with conventional getters and well below the melting temperature of aluminium. Sufficient volume for this application is provided by the getter element ST172/HIS/7-6/150C of the company SAES Getters. Another critical point, flaking of getter particles spoiling the semiconductor crystal, has been solved with a filter disc, which allows a gas exchange between the sectors. This combination of the individual components like filter disc, getter element, lid material and lid volume, a constructive, physically meaningful and economic option was developed, which has been patented by GSI.

Chapter 6

6 Conclusion and future work

6.1 Conclusion

The performed characterisation of Ge-detector surfaces demonstrates the significance of the mechanical treatment in the presented development process. It shows which defects can be avoided, and which ones will appear depending on the mechanical treatment option chosen, and which ones will appear only in the following detector processing steps. The clear influence of certain defects on the functionality of the detectors can be concluded. The presence of mechanically produced defects is highly dependent on the treatment process and on the handling of the crystal. Other important information obtained relates to contamination defects. Those defects can be reduced or avoided to some degree when the necessary facility and equipment is available. A further important information concerns the number of etching cycles a detector is submitted to. Indeed multiple etching steps lead to better quality surfaces. As mentioned above the cleanest surfaces showed the best results in the current-voltage test and the functional γ- spectroscopy test which advocate a good cleaning and etching.

The manufacturing process of ultrasonic grinding has proven to be suitable for this application. Using this treatment method a germanium crystal was manufactured and successfully processed further to a detector. The procedure established for this development process has proven to be useful. With every treatment step, new technological expertise could be obtained on the ultrasonic grinding when applied to the germanium material, thus improving the final surface quality. Mechanically generated defects were not detected on the Ge-crystal. However, by future optimisation of the mechanical parameters like speed and feed of the machine and the grinding material, an

even higher degree of the surface quality may be achieved. This is planned in future treatments.

The produced segmentation and the following verification can be described as successful mechanical test. The understanding of etching and of the following removal of materials completes this result. This mechanically generated segmentation will be used in future treatment investigations of the detector development process in order to confirm the actual results and further improve the segmentation line geometry. Mechanical segmentation yields new possibilities for germanium processing as well as segmentation production in future developments of germanium detectors. Indeed it will permit the production of semiconductor crystals with complex geometrical shapes. This enlarges the scope of exotic detector array structures. Moreover, segmentations could be produced for any geometry, which was hardly possible in the past.

Concerning the new capsule cup/lid welding approach it was shown that a vacuum-tight weld can be realized by using a laser beam welding process with a CO_2 laser. Excessive heating does not appear in any important zones, so the damage of semiconductor due to too high temperatures can be excluded. The genuine combination of inert gas injection, clearance and weld preparation, prevents flue gases or other processing particles to arrive at the vacuum part. Based on these positive characteristics, capsules produced by this method do not require any shielding against high temperature nor constructive measures against particles and flue gases. Furthermore, thermal stress tests have confirmed the positive result of the experiments. Whether the resistance of the weld is constant for a longer period of time, e.g. for 10 years, however requires long term testing. During the investigations different mechanical welding positions could be evaluated. The most suitable one turned out to be the butt seam. By introducing a step in the capsule cup, the lid distance to the crystal could be kept constant. Depending on the weld preparation a re-closing could thus be guaranteed, which means in the later

application servicing of encapsulated detectors, keeping the same caps and lids would be possible.

To realize the creation of the vacuum in the capsule unit, a pipe closing by ultrasonic welding process was considered and confirmed successfully by experimental investigations.

Another significant characteristic of the encapsulation technology is the use of an internal getter element to keep high vacuum over a longer period. For this purpose, a new getter element is suggested having a lower activation temperature compared with conventional getters, and well below the melting temperature of aluminium. Another critical point, the flanking of getter particles spoiling the semiconductor crystal, has been solved with a filter disc, which allows a gas exchange between the getter and semiconductor sectors. This combination of the individual components like filter disc, getter element, lid material and lid volume, a constructive, physically meaningful and economic option was developed.

6.2 Future work

Based on the presented work the following steps are suggested:

- The ultrasonic grinding parameters, like speed and feed of the machine and the grinding material should be optimised in future germanium treatment tests. With these optimisations still better surface qualities could be achieved. Furthermore, to confirm the mechanically generated segmentation, a segmented detector should be developed and tested again.

- After acquiring and improving the mechanical processing steps of the HPGe detector technology in this work, future work should concentrate on investigating the wet chemistry processes. Subsequently, the passivation

and the implanting processes should be developed and tested with the aim to fully command all processing steps as a prerequisite to advance the Ge detector technology.

- Finally, the newly developed encapsulation technology should be confirmed in a system with a HPGe detector.

Chapter 7

7. Summary

Germanium-detectors are the most sensitive high-resolution γ detectors available and are used in nuclear structure physics to obtain information about the structure of atomic nuclei. In this work novel techniques for the production of high purity Germanium detectors are presented, motivated by the need for a new mechanical treatment procedure in order to obtain better surface quality. In addition a new more cost efficient encapsulation to protect the sensitive detector surface has been developed.

Seven germanium crystals with different surface qualities depending on the mechanical treatment have been used for the characterization of their surfaces. While five of the crystals were fully processed to obtain working detectors, two non-detector crystals were used only for the mechanical characterization. One has been grinded only while the other one was lapped in addition.

In a first step surfaces have been investigated with an Atomic Force Microscope and a Profiler, followed by measurements with an Electron Probe Micro Analyzer and a Field Emission Scanning Microscope.

Ge-treatment and shaping tests with a new ultrasonic grinding machine have been carried out. The investigations have shown very fine surface structures with tight tolerances of 2 μm. The achieved roughness is a factor of 3.9 times smaller than using standard grinding techniques and a factor of 1.8 smaller as compared to standard lapping processes. This kind of sophisticated mechanical treatment allows also complicated shapes to be achieved. On the basis of these characterization and treatment results a novel type of planar HPGe-Detector has been developed and tested.

Additionally it was possible to develop a new hermetic capsule unit with better physical properties, using a more cost-effective novel manufacturing method. For this purpose, a laser welding process has been developed to weld

aluminum capsules and lids with a low wall thickness. As for these processes the temperature is a critical factor it has been constantly monitored at different locations in the capsule units. The maximal temperature of 79 °C measured in the capsule is considered save for the detector.

To evacuate the capsule units an aluminum pipe has been integrated in the lid and was closed by means of ultrasonic welding after achieving the desired pressure. To keep the vacuum over a long period of time an internal getter material has been inserted as well as to additionally remove the rest gas particles by adhesion.

Based on the developed mechanical treatment presented in this work it is now possible to produce Germanium detectors with difficult geometrical shapes, and excellent surface quality in a safer and more cost-efficient way. It was shown that a vacuum-tight weld can be realized by using a laser beam welding process with a CO_2 laser and it allows for new encapsulation options of semiconductors. Even recycling of the capsule and lid material is possible, further increasing the cost efficiency of this method.

8. Appendix

Appendix A: AFM results of crystals

Appendix B: FESEM measured images of the crystals

Appendix C: Treatment protocol

Appendix D: Structure defects

Appendix E: Germanium crystal data

APPENDIX A

AFM results of the crystals

Detector: B10

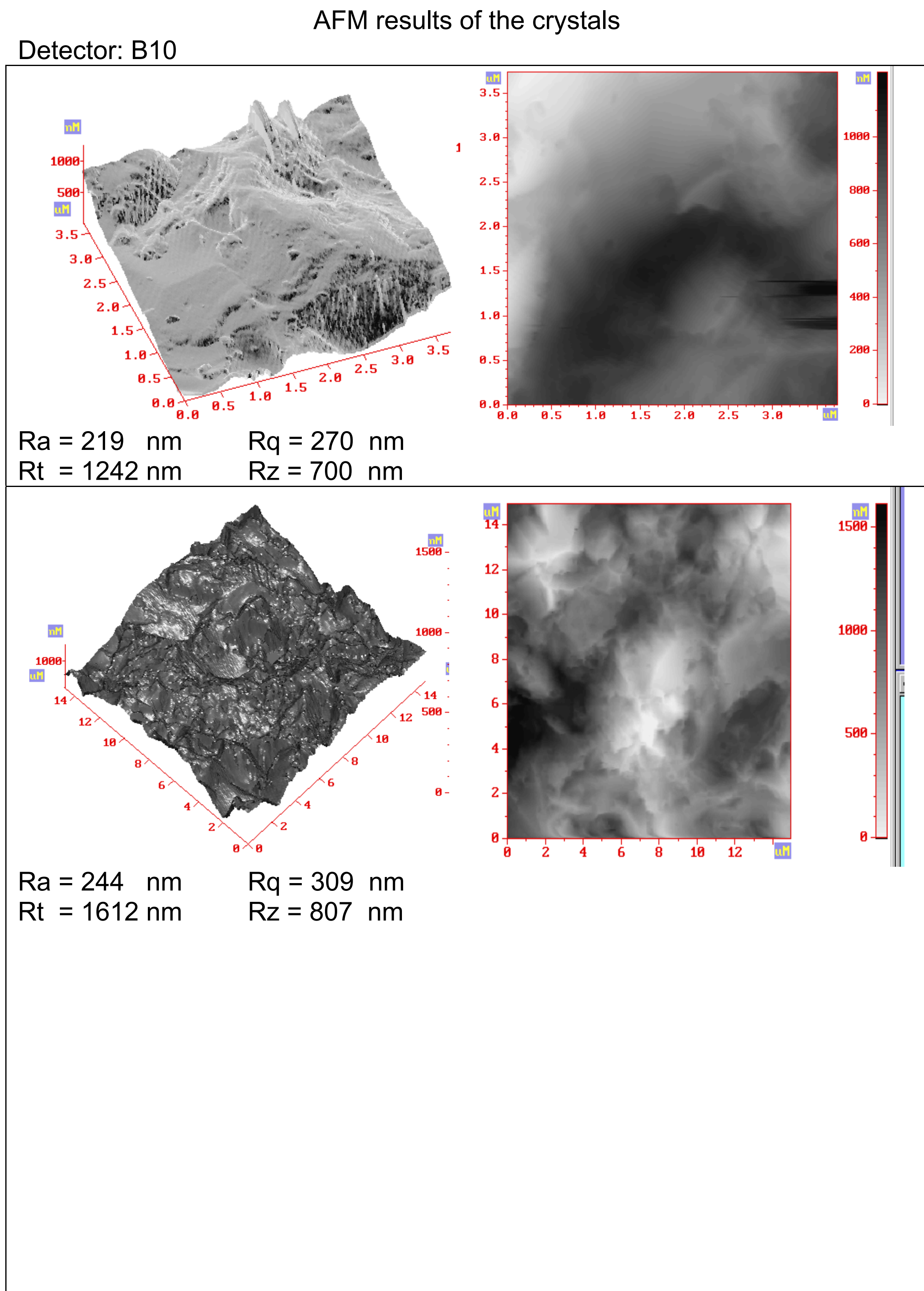

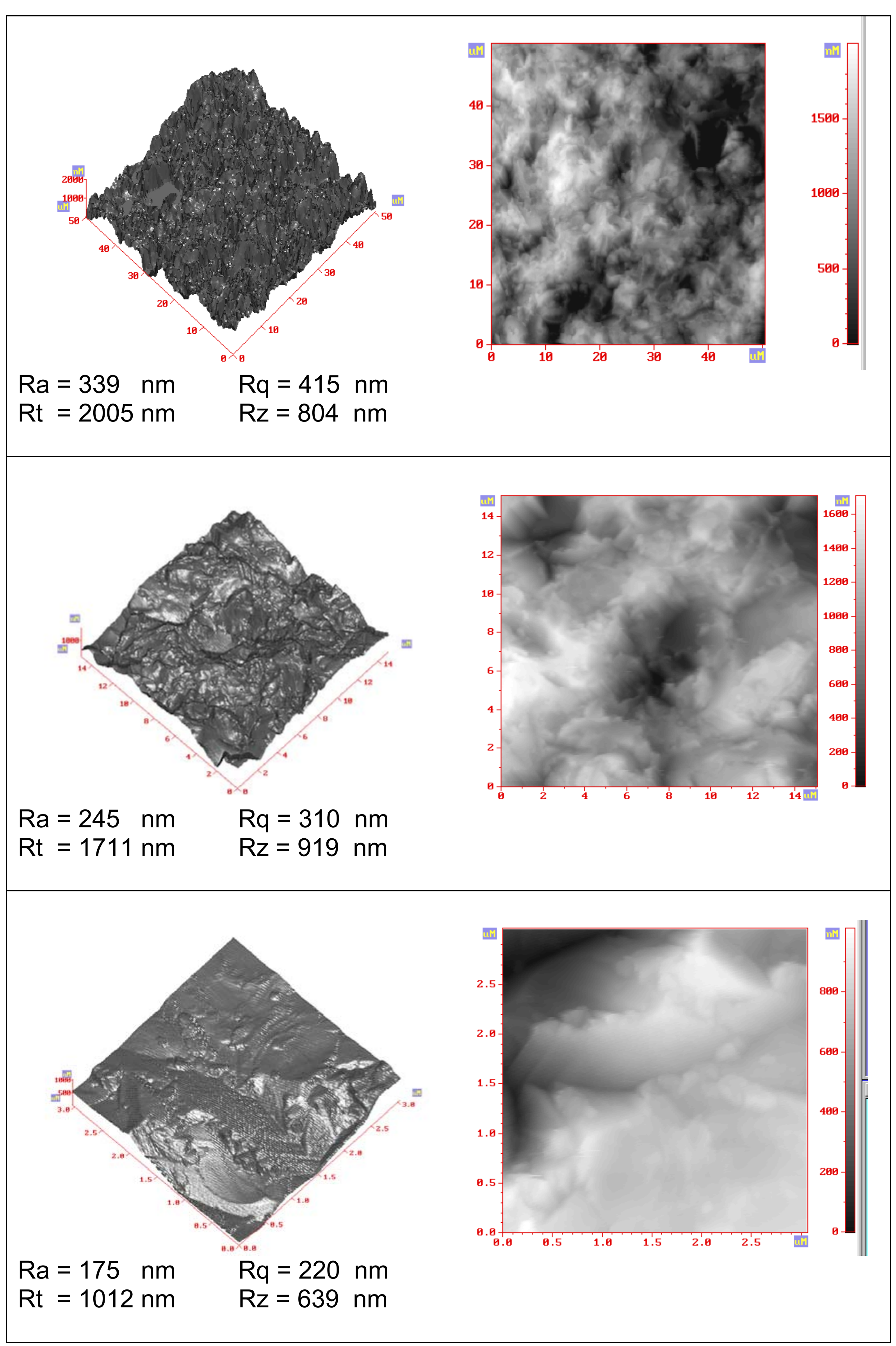
Ra = 339 nm
Rq = 415 nm
Rt = 2005 nm
Rz = 804 nm
Ra = 245 nm
Rq = 310 nm
Rt = 1711 nm
Rz = 919 nm
Ra = 175 nm
Rq = 220 nm
Rt = 1012 nm
Rz = 639 nm

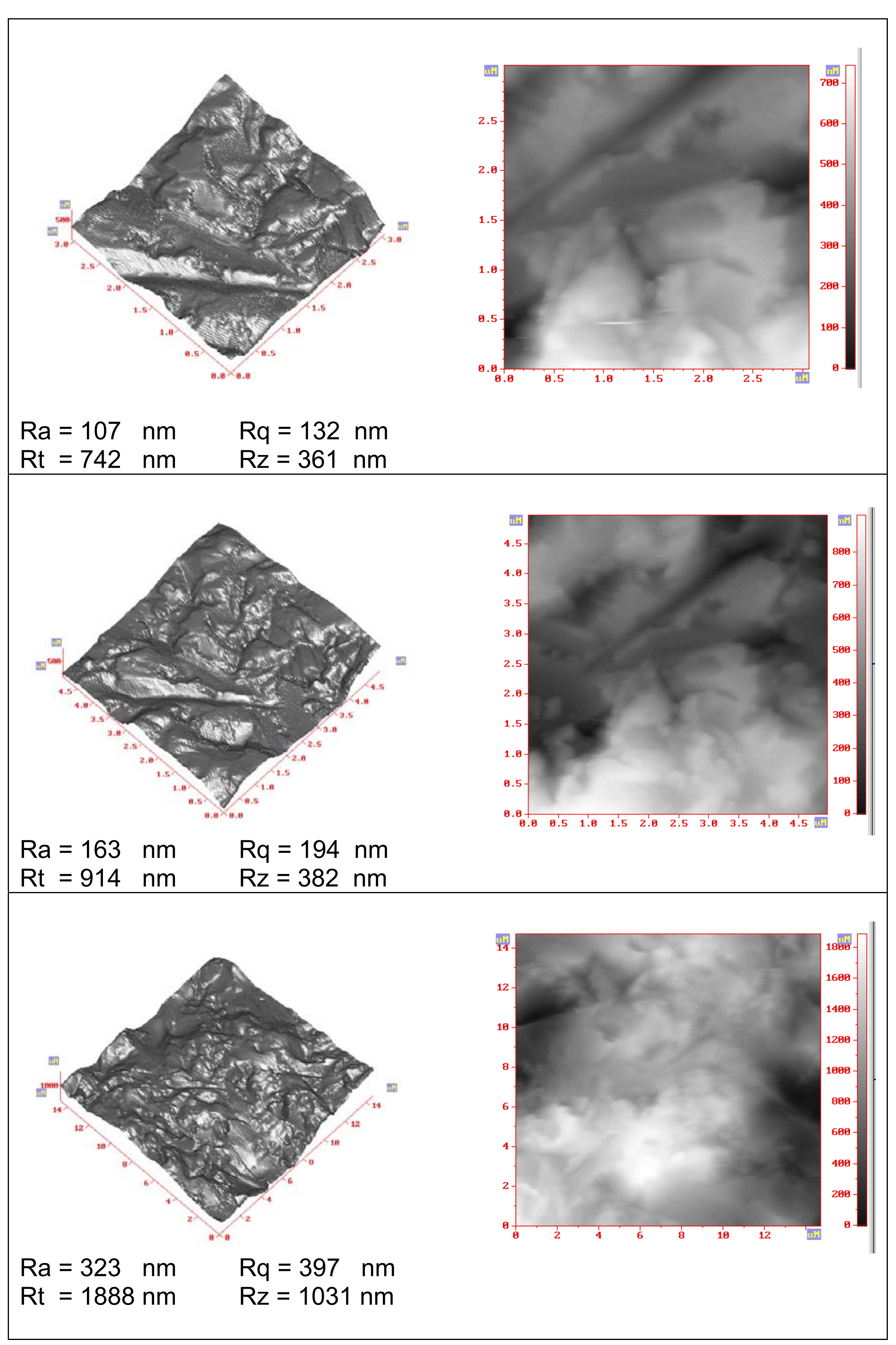
Ra = 107 nm
Rq = 132 nm
Rt = 742 nm
Rz = 361 nm
Ra = 163 nm
Rq = 194 nm
Rt = 914 nm
Rz = 382 nm
Ra = 323 nm
Rq = 397 nm
Rt = 1888 nm
Rz = 1031 nm

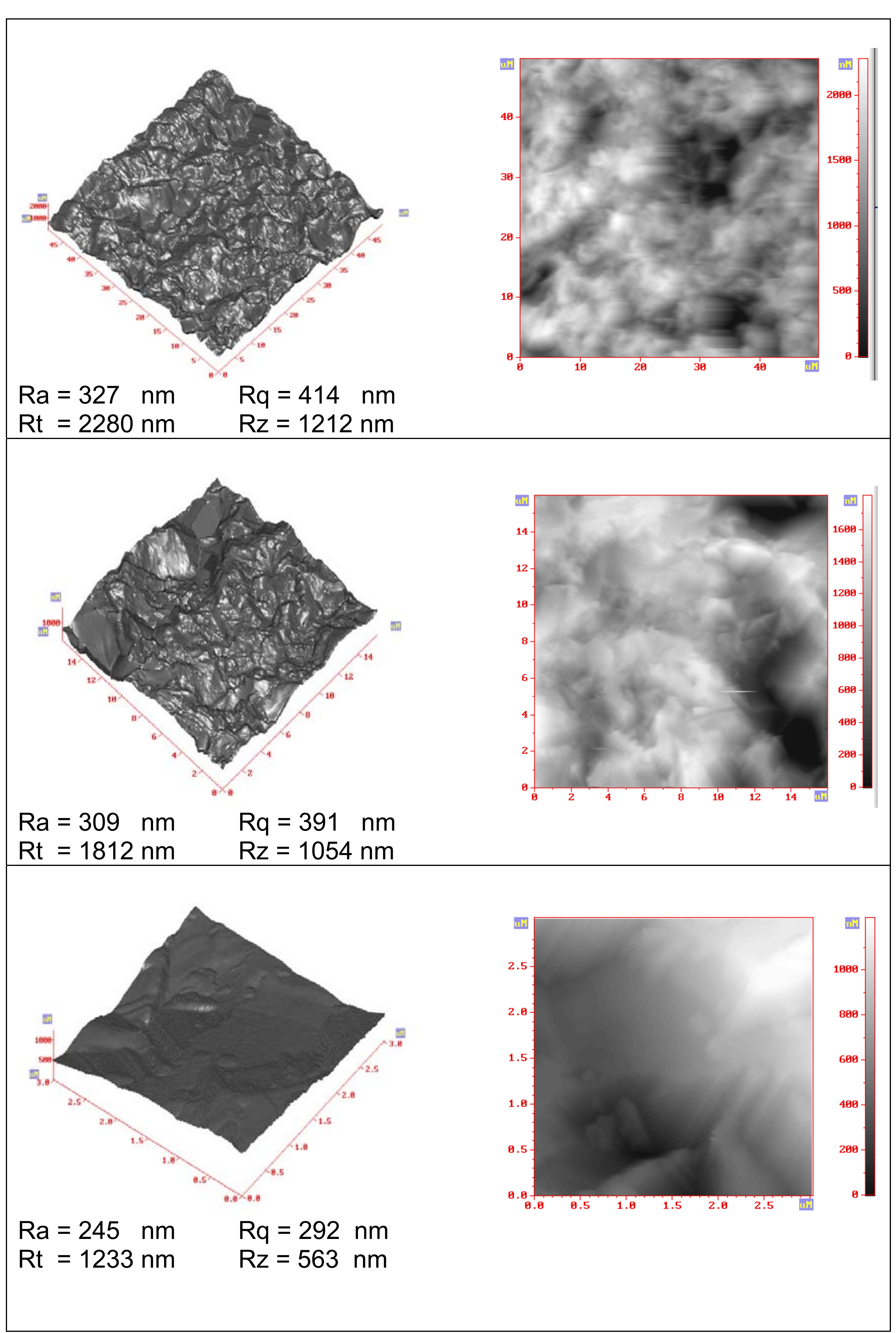
Ra = 327 nm
Rq = 414 nm
Rt = 2280 nm
Rz = 1212 nm
Ra = 309 nm
Rq = 391 nm
Rt = 1812 nm
Rz = 1054 nm
Ra = 245 nm
Rq = 292 nm
Rt = 1233 nm
Rz = 563 nm

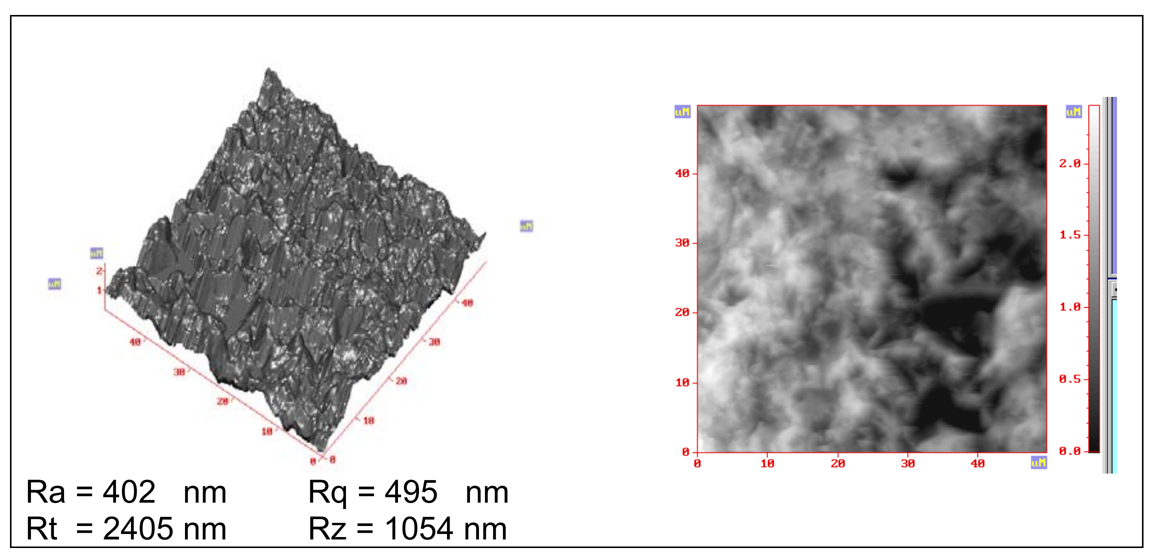

Ra = 402 nm Rq = 495 nm
Rt = 2405 nm Rz = 1054 nm

Detector B11

Ra = 225 nm Rq = 644 nm
Rt = 2405 nm Rz = 1468 nm

Ra = 490 nm Rq = 559 nm
Rt = 2019 nm Rz = 897 nm

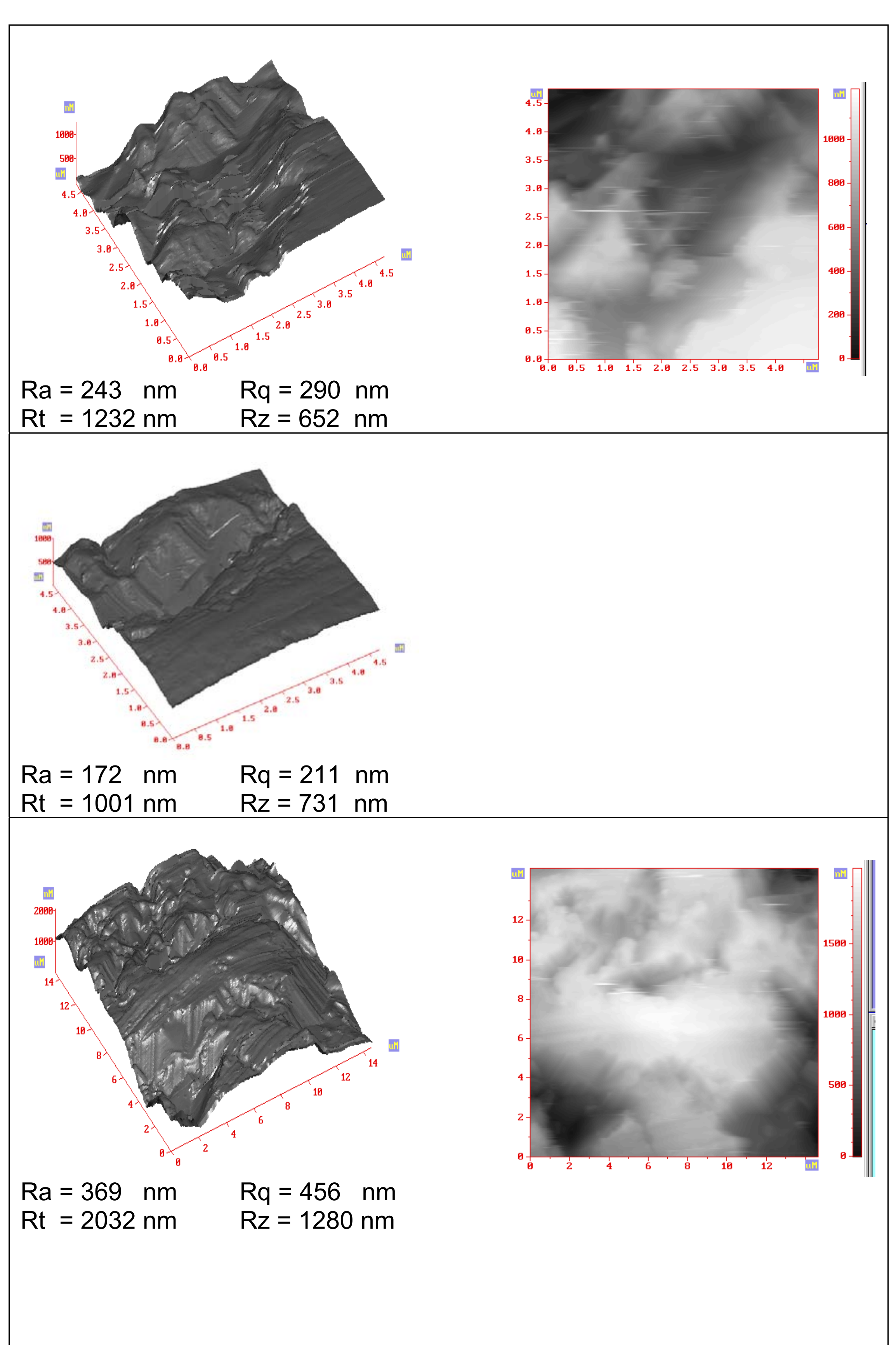
Ra = 243 nm
Rq = 290 nm
Rt = 1232 nm
Rz = 652 nm
Ra = 172 nm
Rq = 211 nm
Rt = 1001 nm
Rz = 731 nm
Ra = 369 nm
Rq = 456 nm
Rt = 2032 nm
Rz = 1280 nm

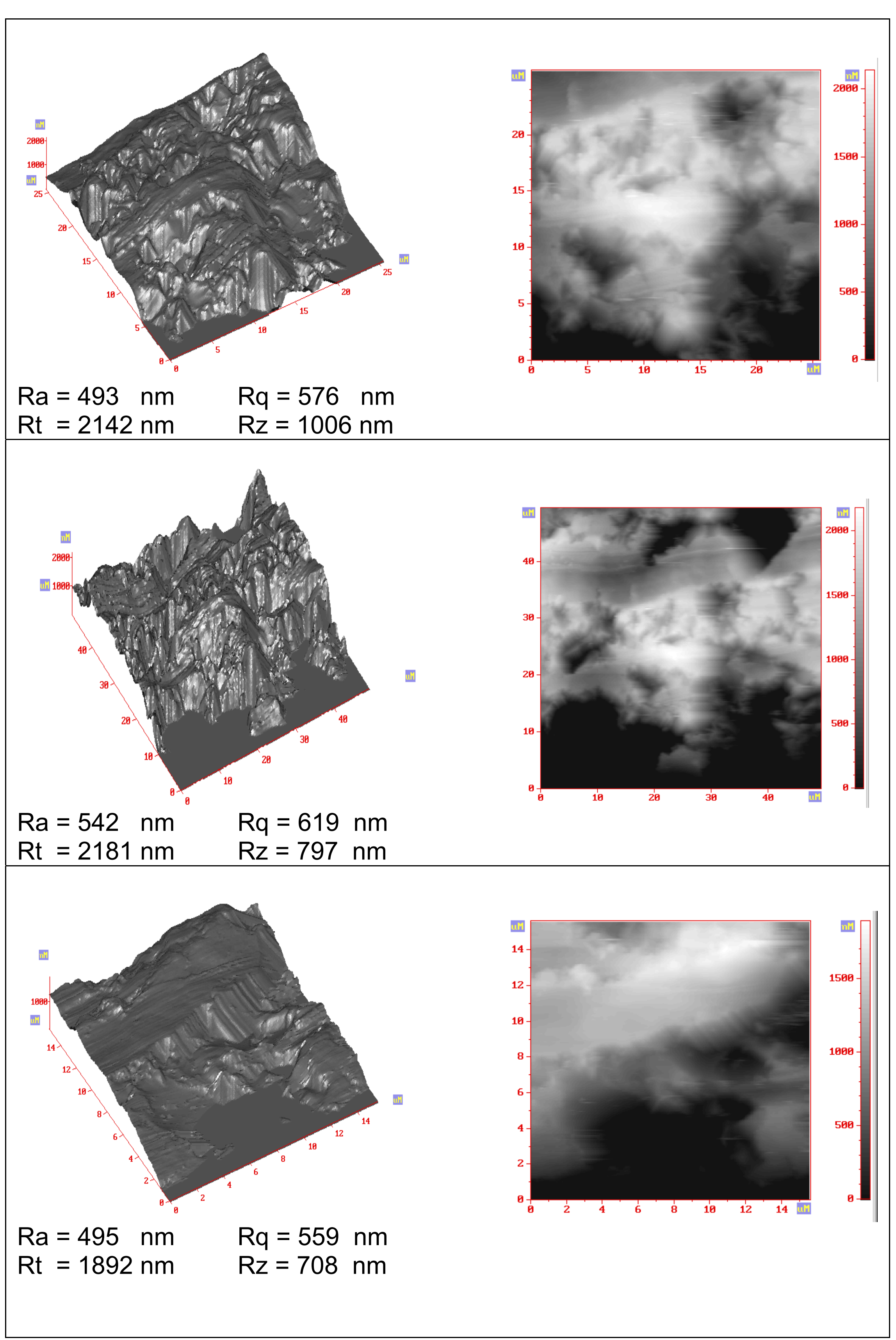

Ra = 493 nm
Rq = 576 nm
Rt = 2142 nm
Rz = 1006 nm
Ra = 542 nm
Rq = 619 nm
Rt = 2181 nm
Rz = 797 nm
Ra = 495 nm
Rq = 559 nm
Rt = 1892 nm
Rz = 708 nm

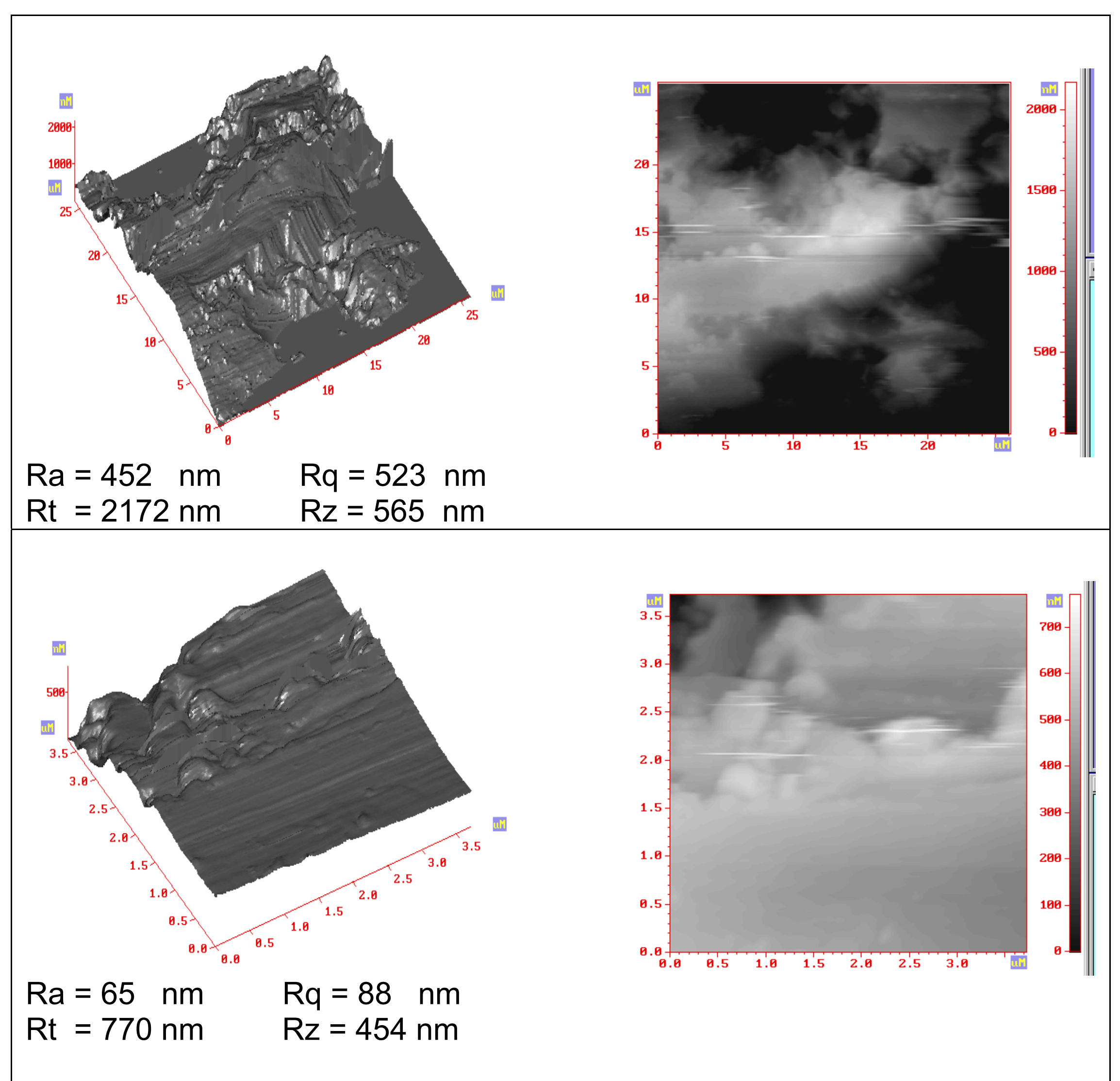
Ra = 452 nm
Rq = 523 nm
Rt = 2172 nm
Rz = 565 nm
Ra = 65 nm
Rq = 88 nm
Rt = 770 nm
Rz = 454 nm

Detector B12

Ra = 178 nm   Rq = 216 nm
Rt = 1247 nm   Rz = 750 nm

Ra = 80 nm   Rq = 96 nm
Rt = 495 nm   Rz = 307 nm

Ra = 391 nm   Rq = 468 nm
Rt = 1970 nm   Rz = 865 nm

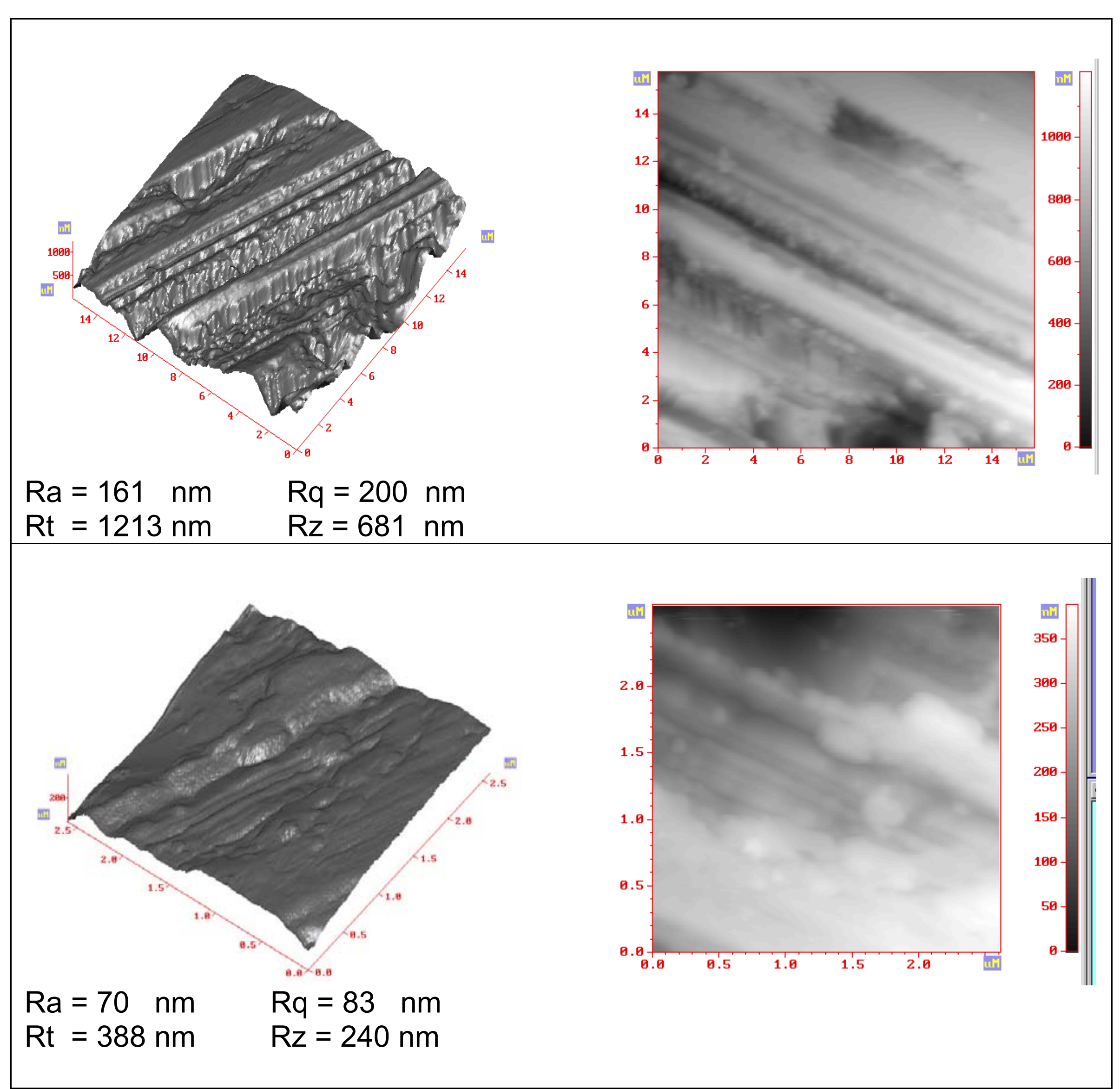
Ra = 161 nm
Rq = 200 nm
Rt = 1213 nm
Rz = 681 nm
Ra = 70 nm
Rq = 83 nm
Rt = 388 nm
Rz = 240 nm

APPENDIX B

FESEM measured images of the crystals

Detector: B1

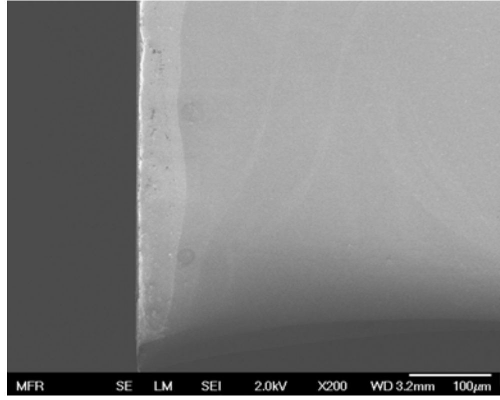

Figure: B1_1

Figure: B1_2

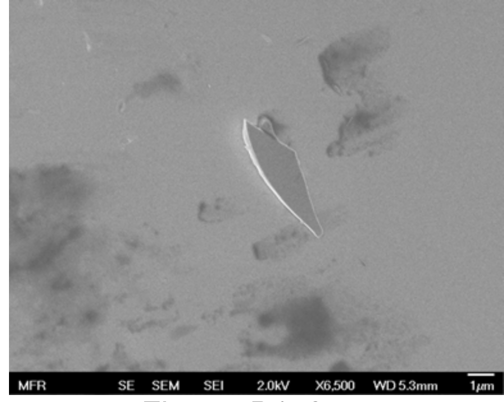

Figure: B1_3

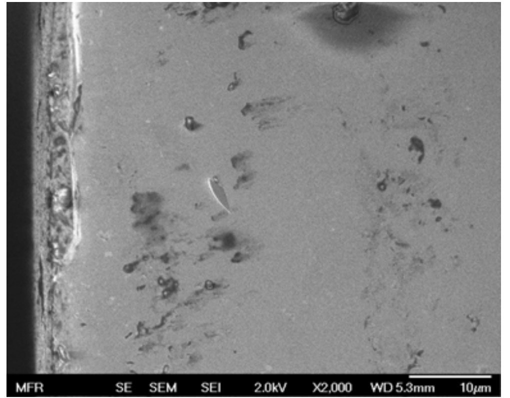

Figure: B1_4

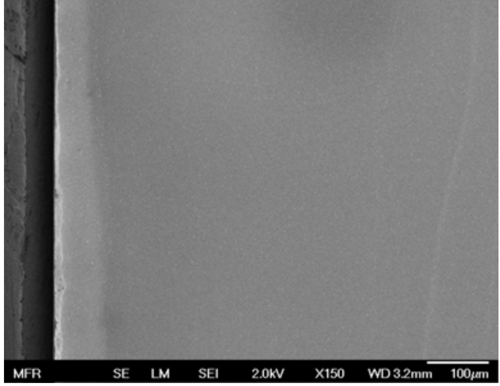

Figure: B1_5

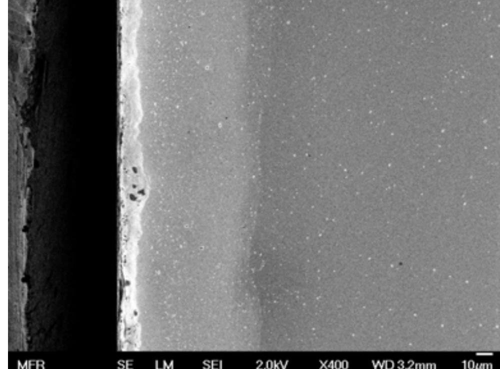

Figure: B1_6

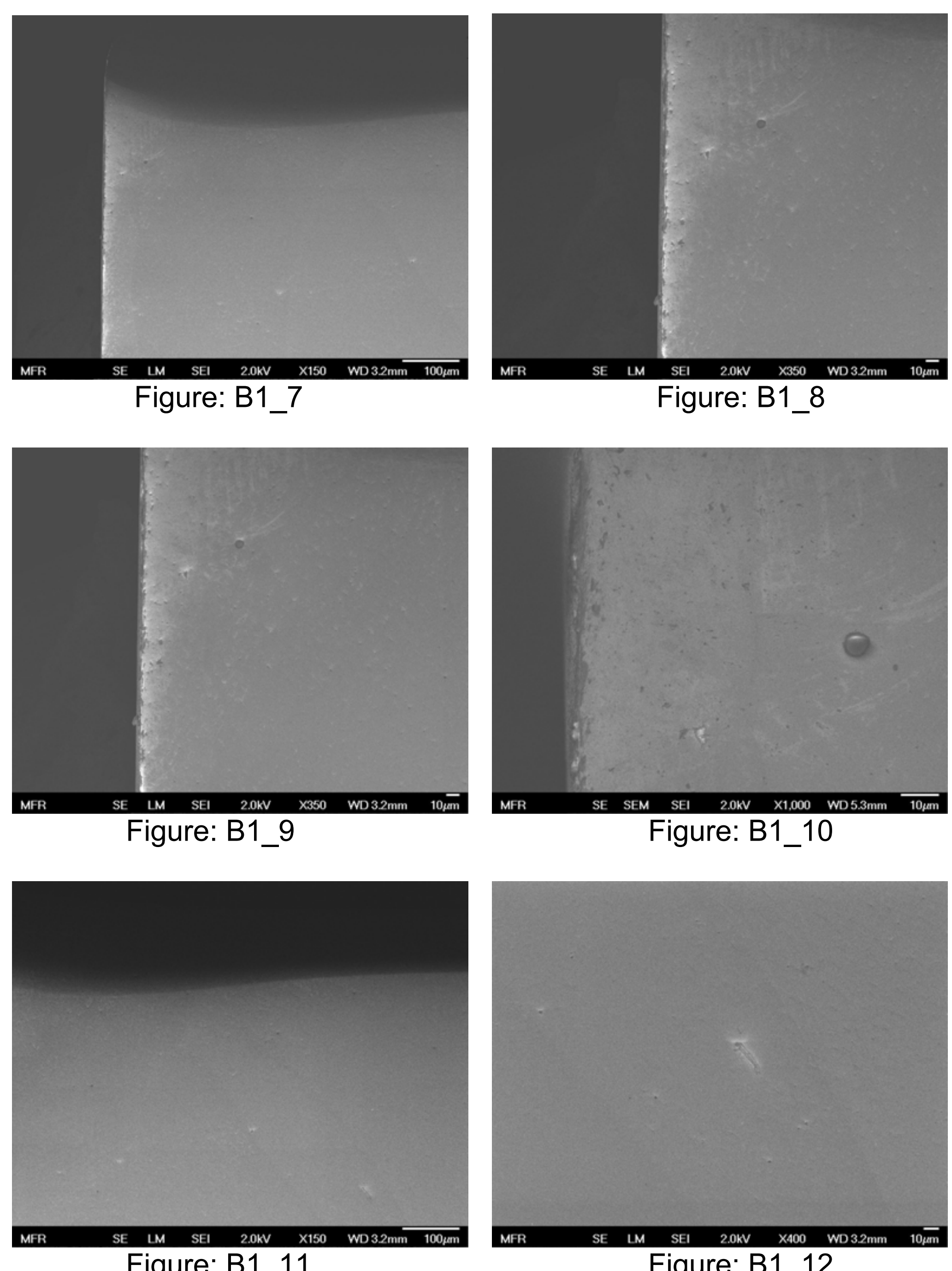

Figure: B1_7

Figure: B1_8

Figure: B1_9

Figure: B1_10

Figure: B1_11

Figure: B1_12

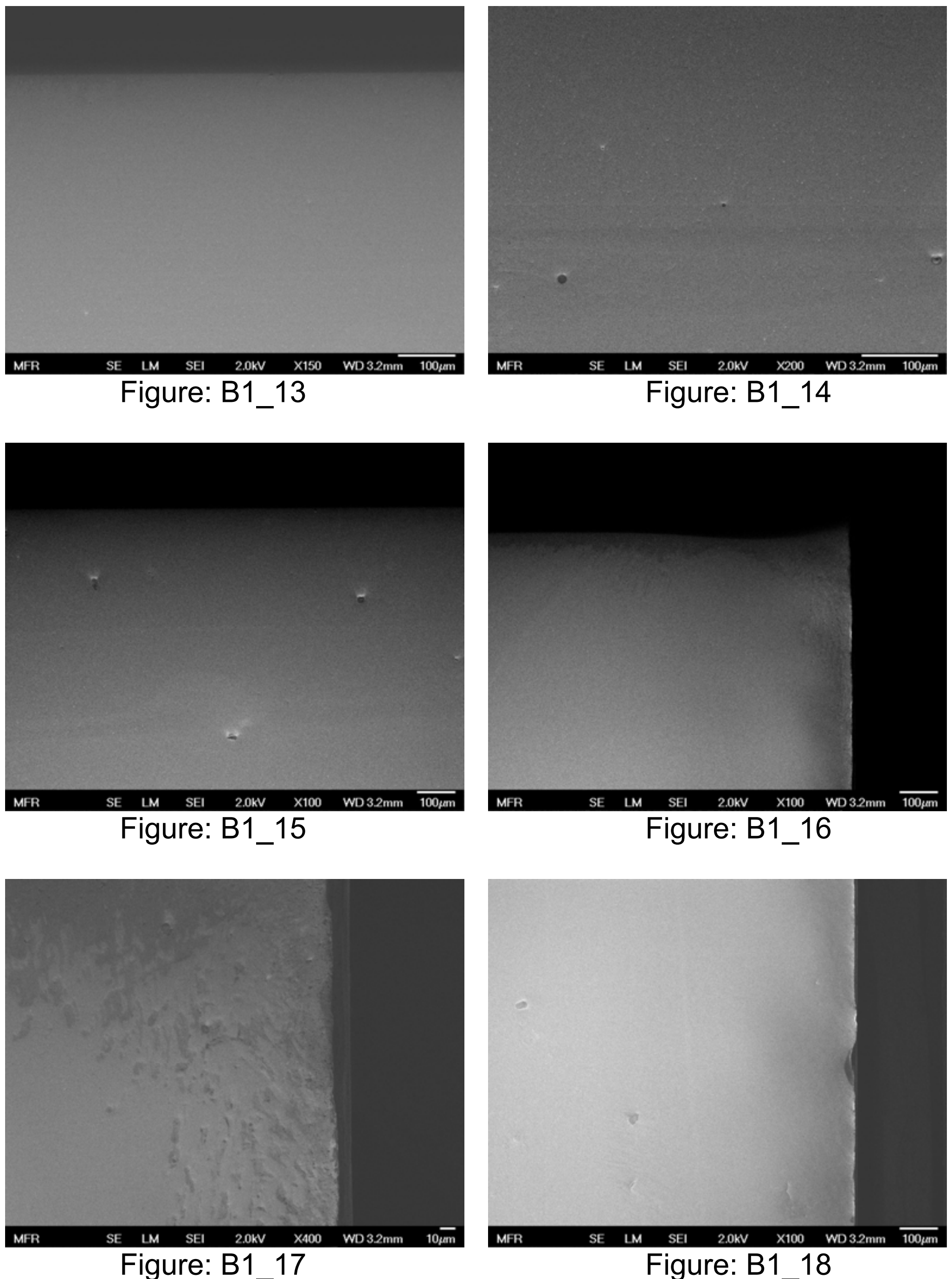

Figure: B1_13

Figure: B1_14

Figure: B1_15

Figure: B1_16

Figure: B1_17

Figure: B1_18

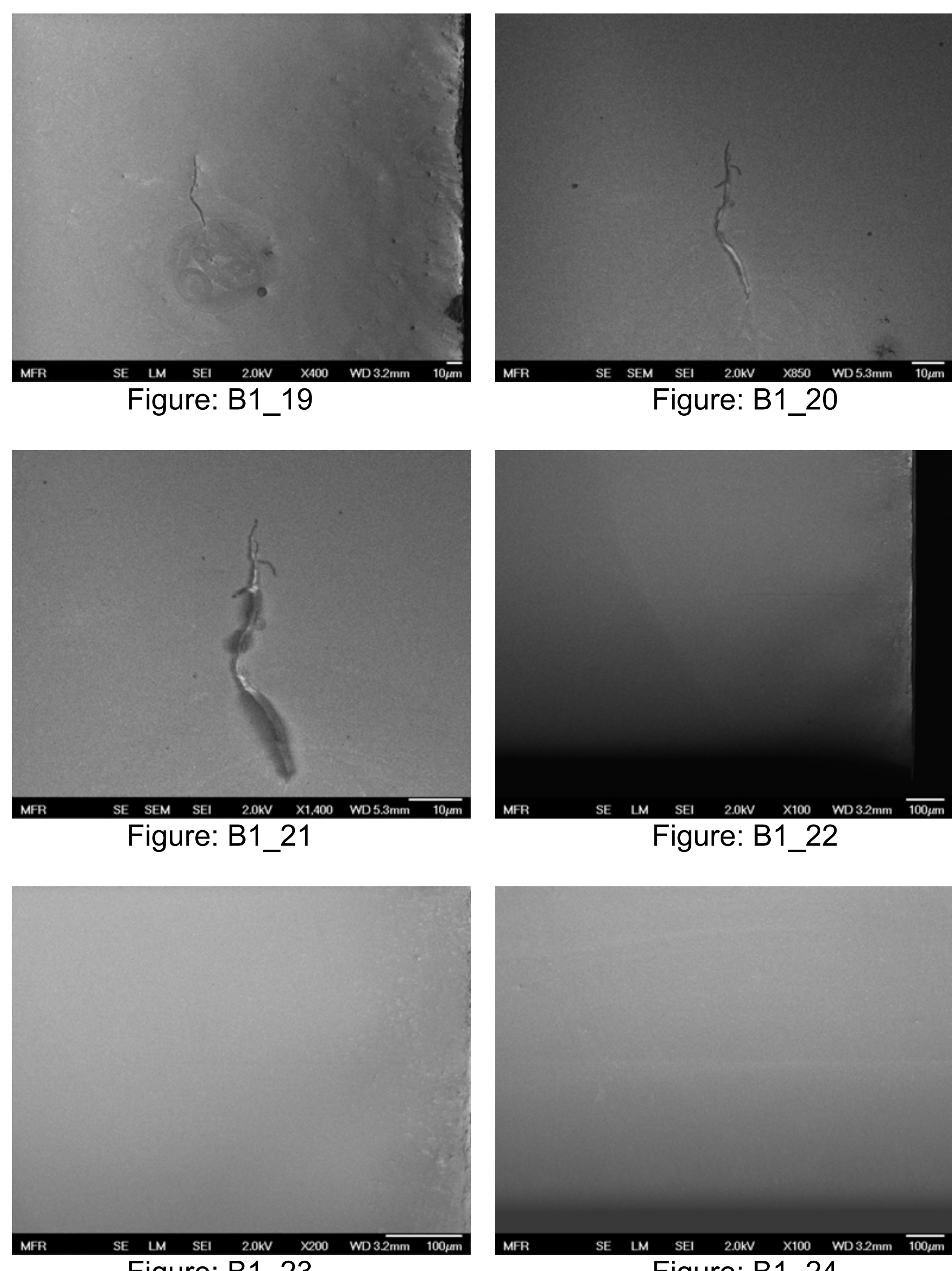

Figure: B1_19

Figure: B1_20

Figure: B1_21

Figure: B1_22

Figure: B1_23

Figure: B1_24

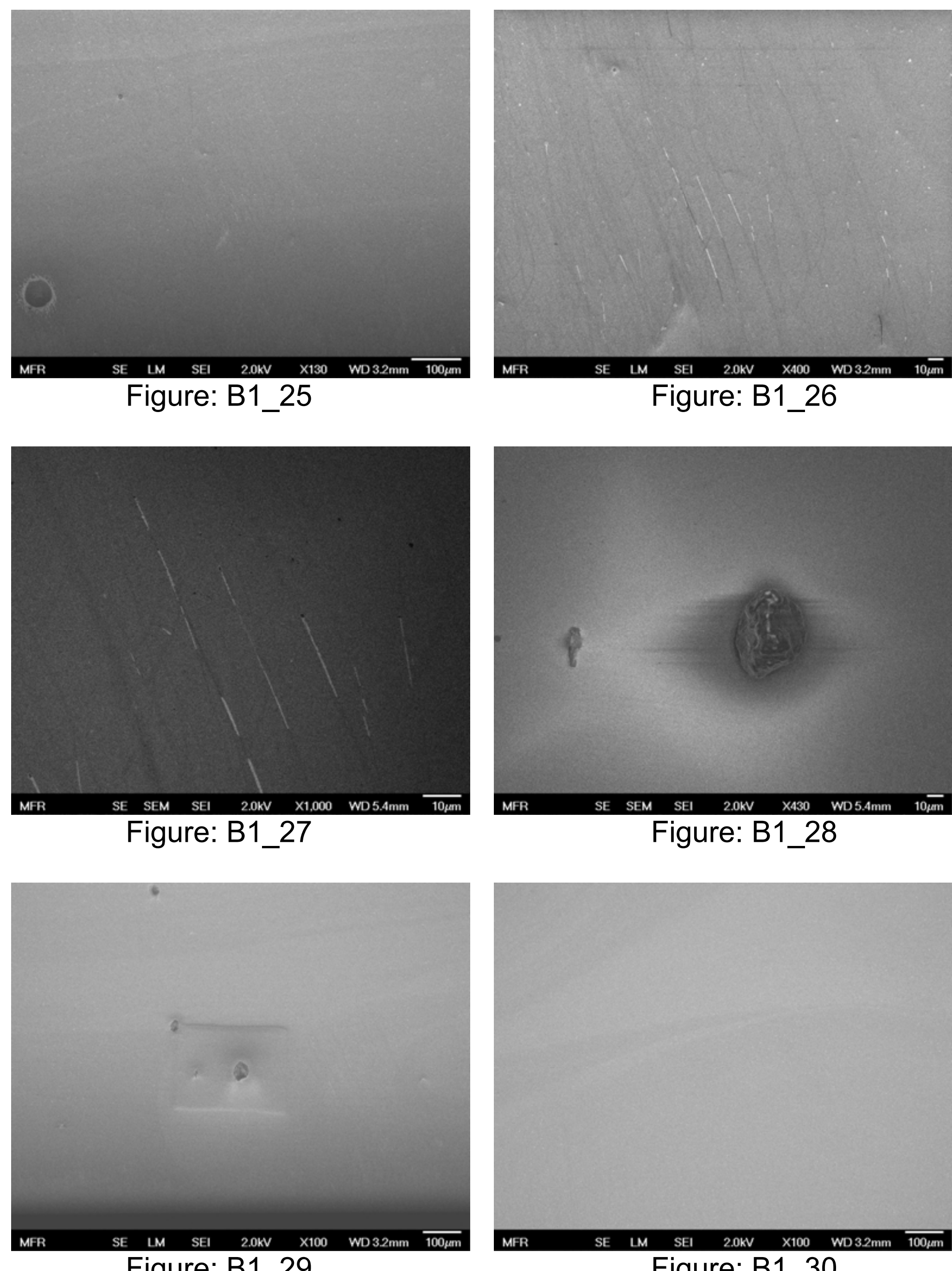

Figure: B1_25

Figure: B1_26

Figure: B1_27

Figure: B1_28

Figure: B1_29

Figure: B1_30

Detector: B2, Side 1

Figure: B2_1

Figure: B2_2

Figure: B2_3

Figure: B2_4

Figure: B2_5

Figure: B2_6

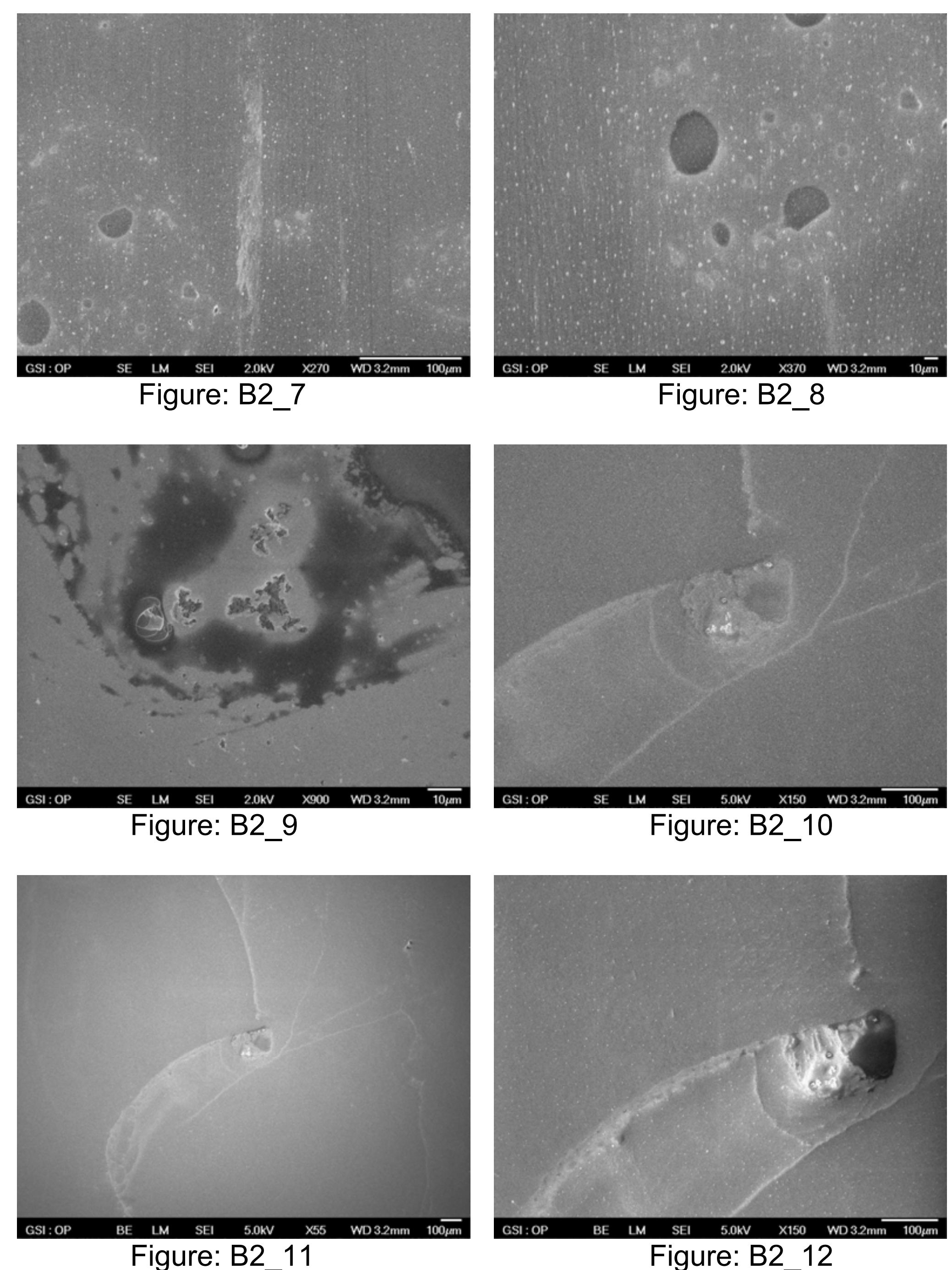

Figure: B2_7

Figure: B2_8

Figure: B2_9

Figure: B2_10

Figure: B2_11

Figure: B2_12

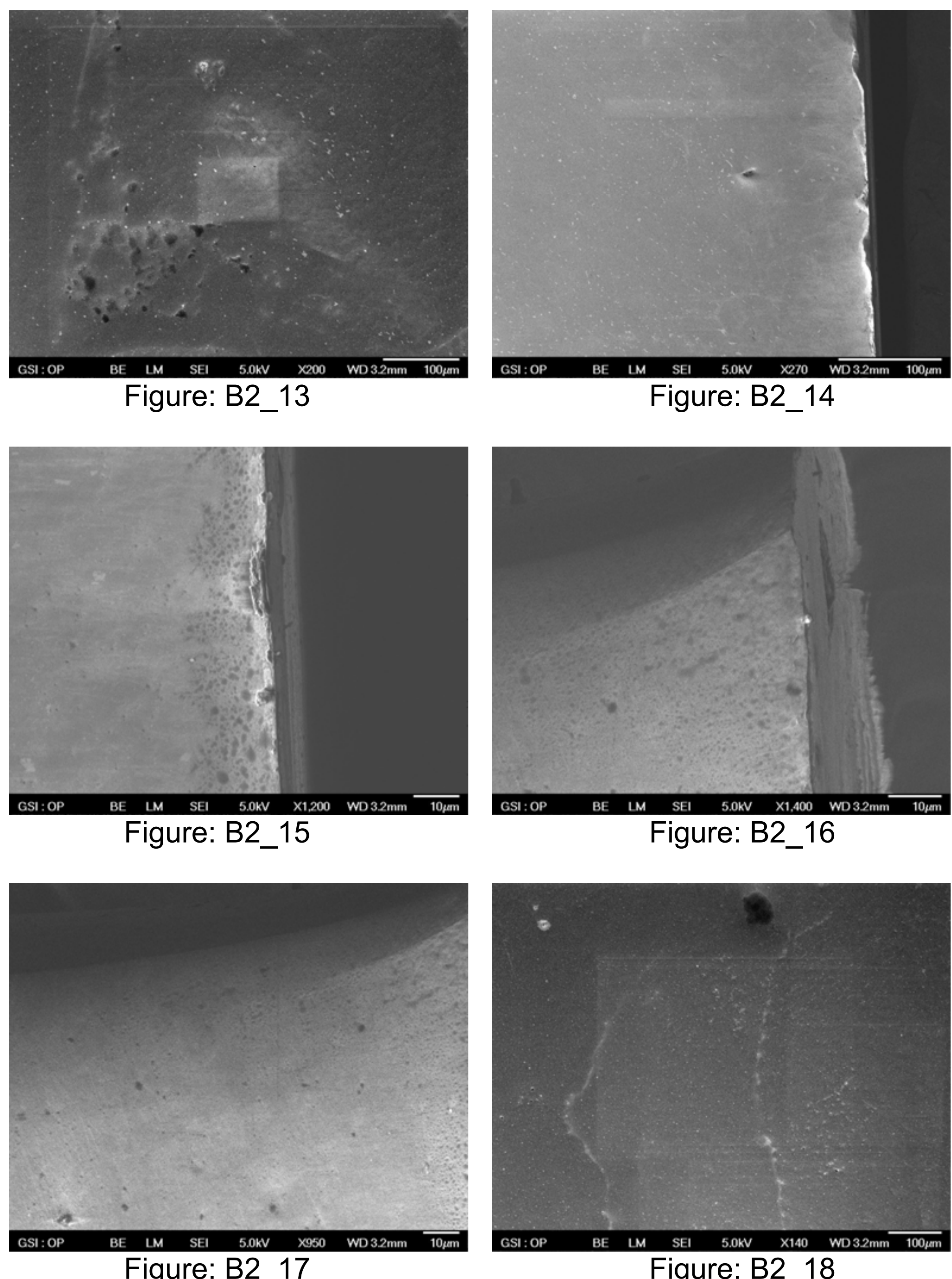

Figure: B2_13

Figure: B2_14

Figure: B2_15

Figure: B2_16

Figure: B2_17

Figure: B2_18

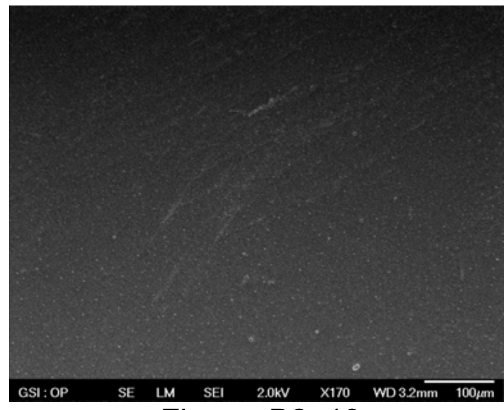

Figure: B2_19

Appendix : B2, Side 2

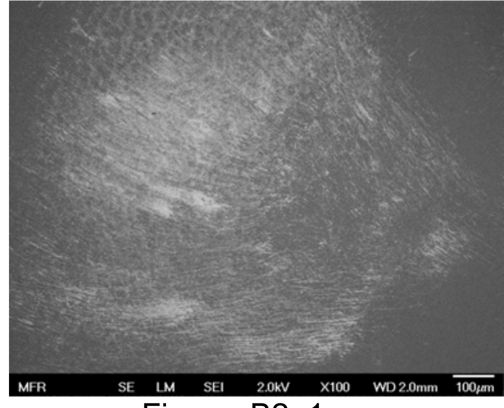

Figure: B2_1

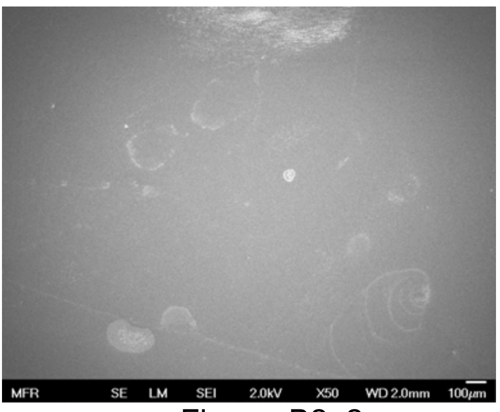

Figure: B2_2

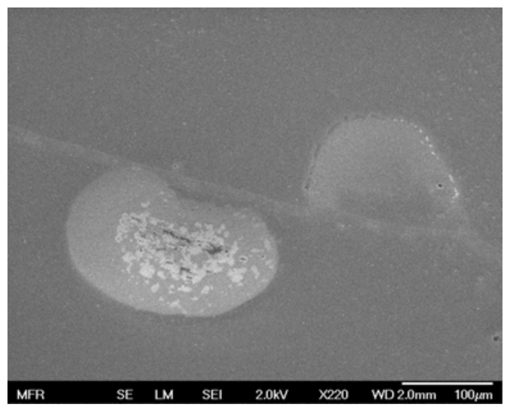

Figure: B2_3

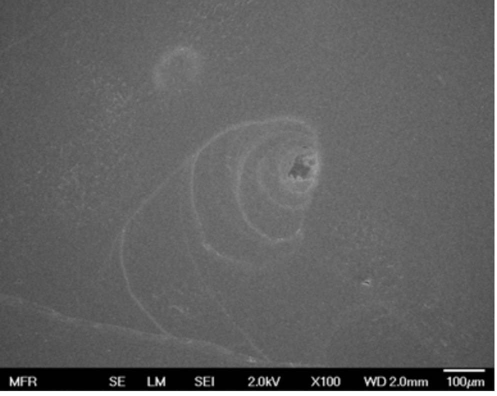

Figure: B2_4

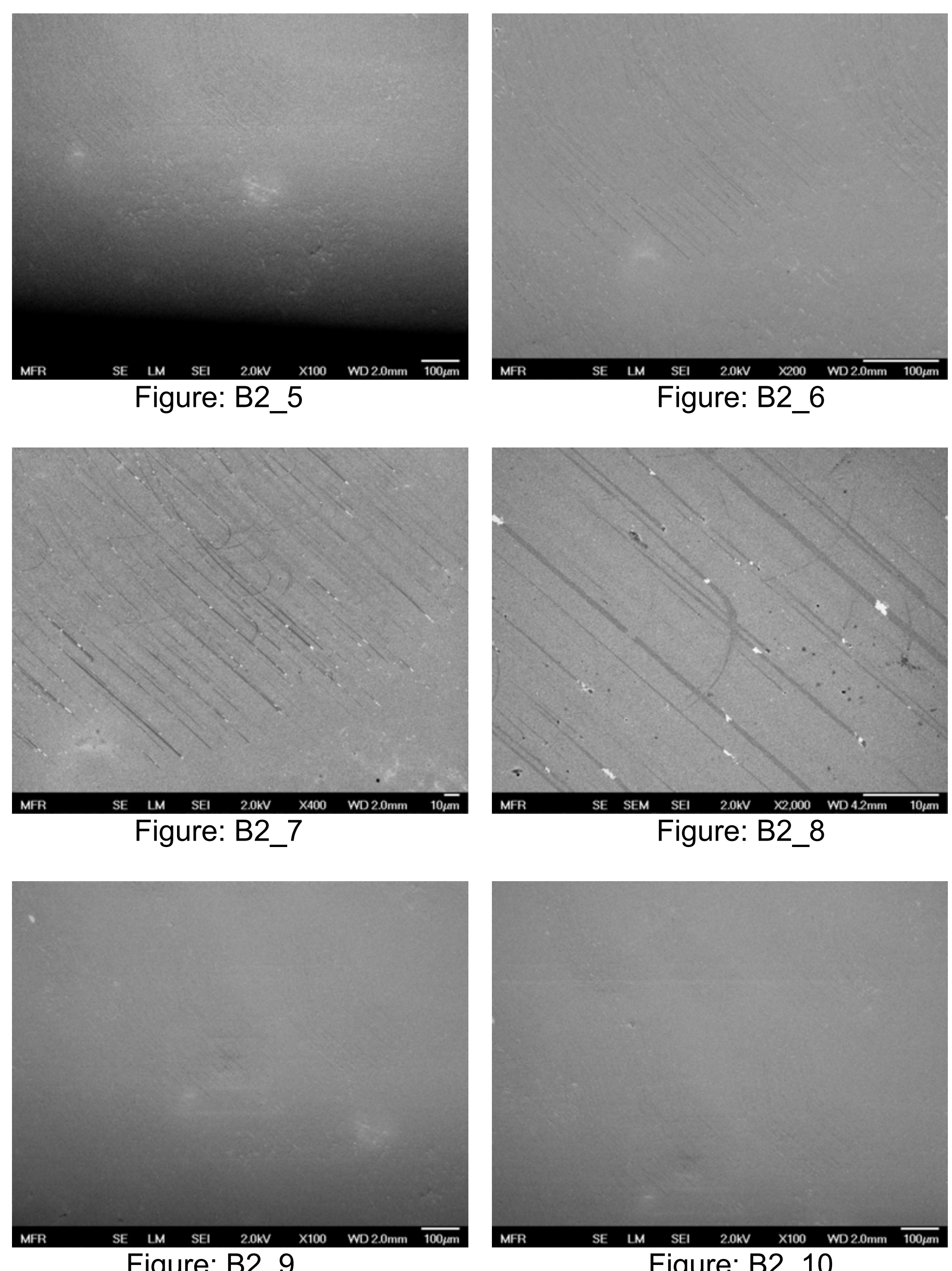

Figure: B2_5

Figure: B2_6

Figure: B2_7

Figure: B2_8

Figure: B2_9

Figure: B2_10

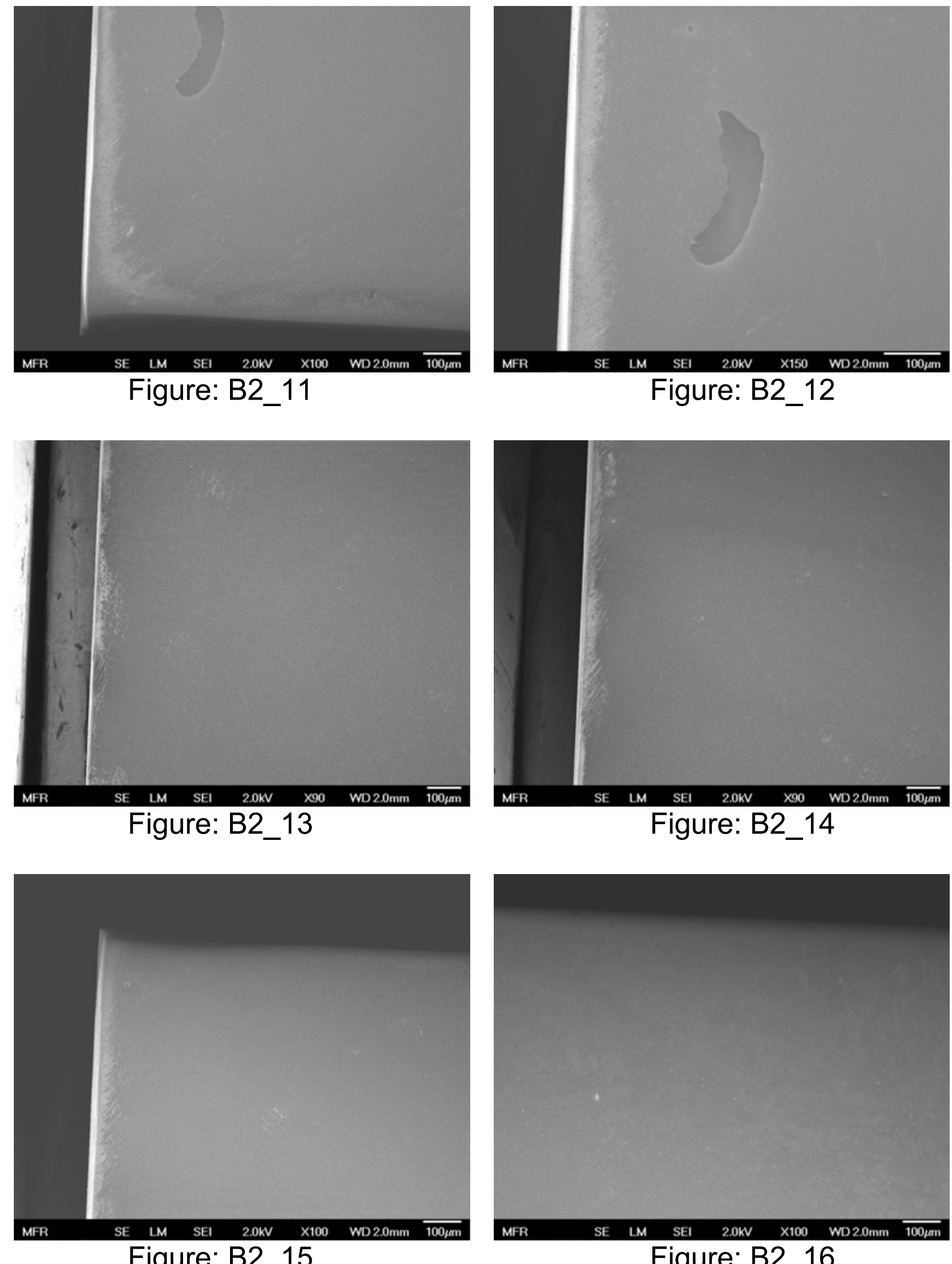

Figure: B2_11

Figure: B2_12

Figure: B2_13

Figure: B2_14

Figure: B2_15

Figure: B2_16

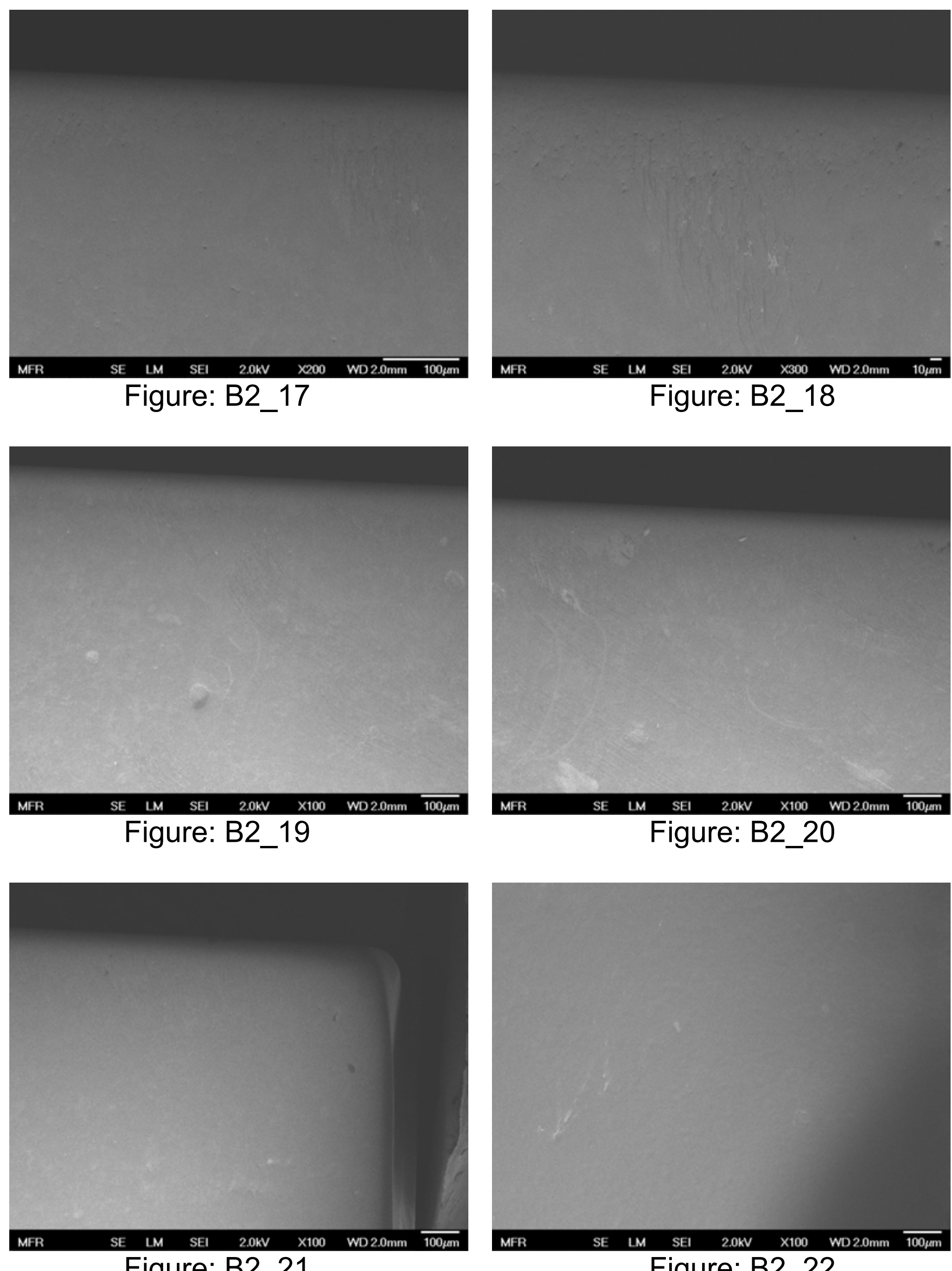

Figure: B2_17

Figure: B2_18

Figure: B2_19

Figure: B2_20

Figure: B2_21

Figure: B2_22

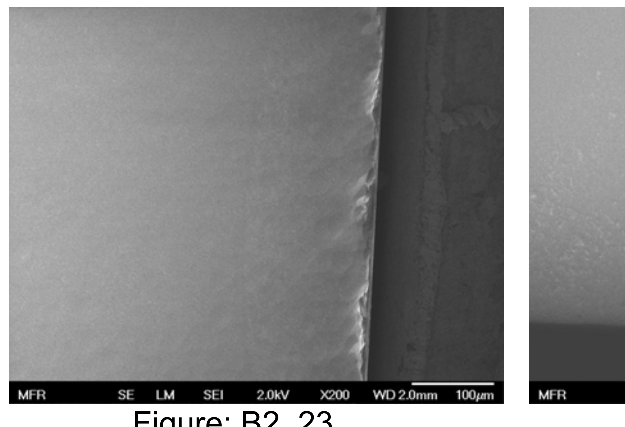

Figure: B2_23

Figure: B2_24

Detector: B2 Side 3

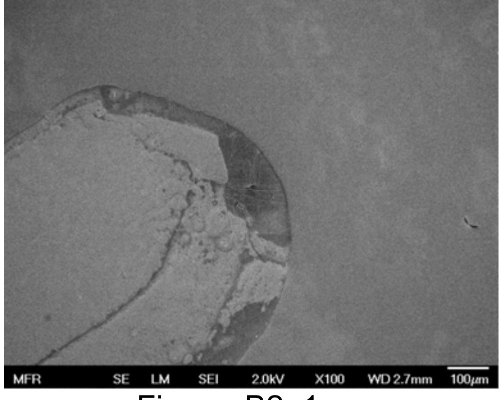

Figure: B2_1

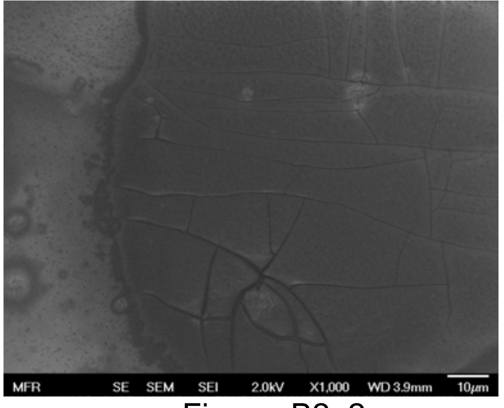

Figure: B2_2

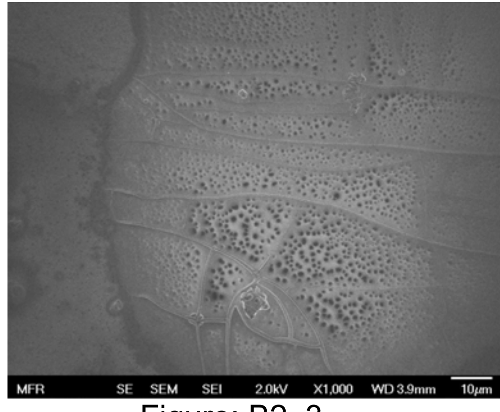

Figure: B2_3

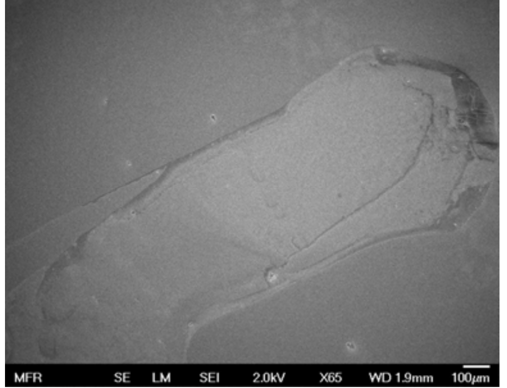

Figure: B2_4

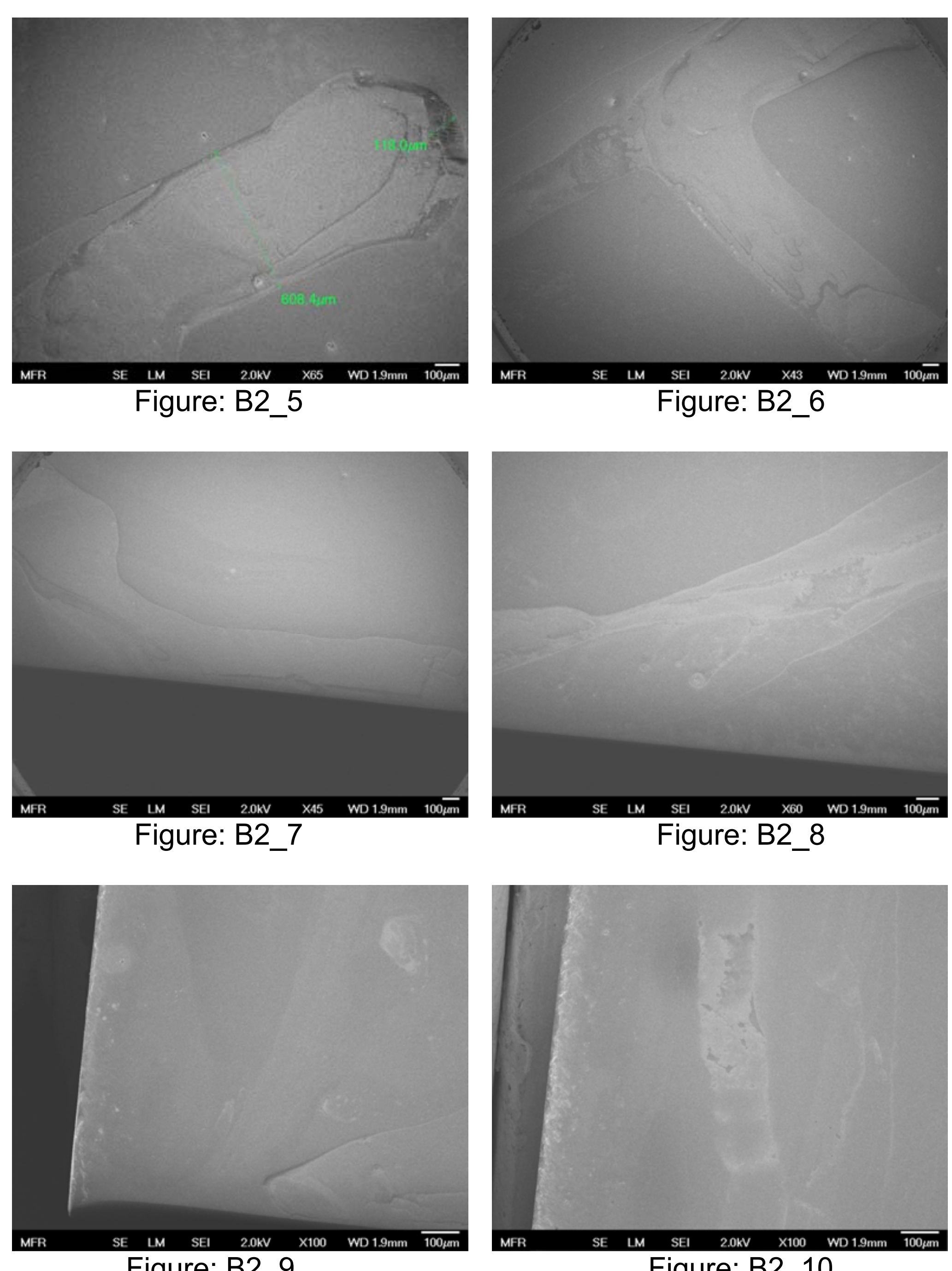

Figure: B2_5

Figure: B2_6

Figure: B2_7

Figure: B2_8

Figure: B2_9

Figure: B2_10

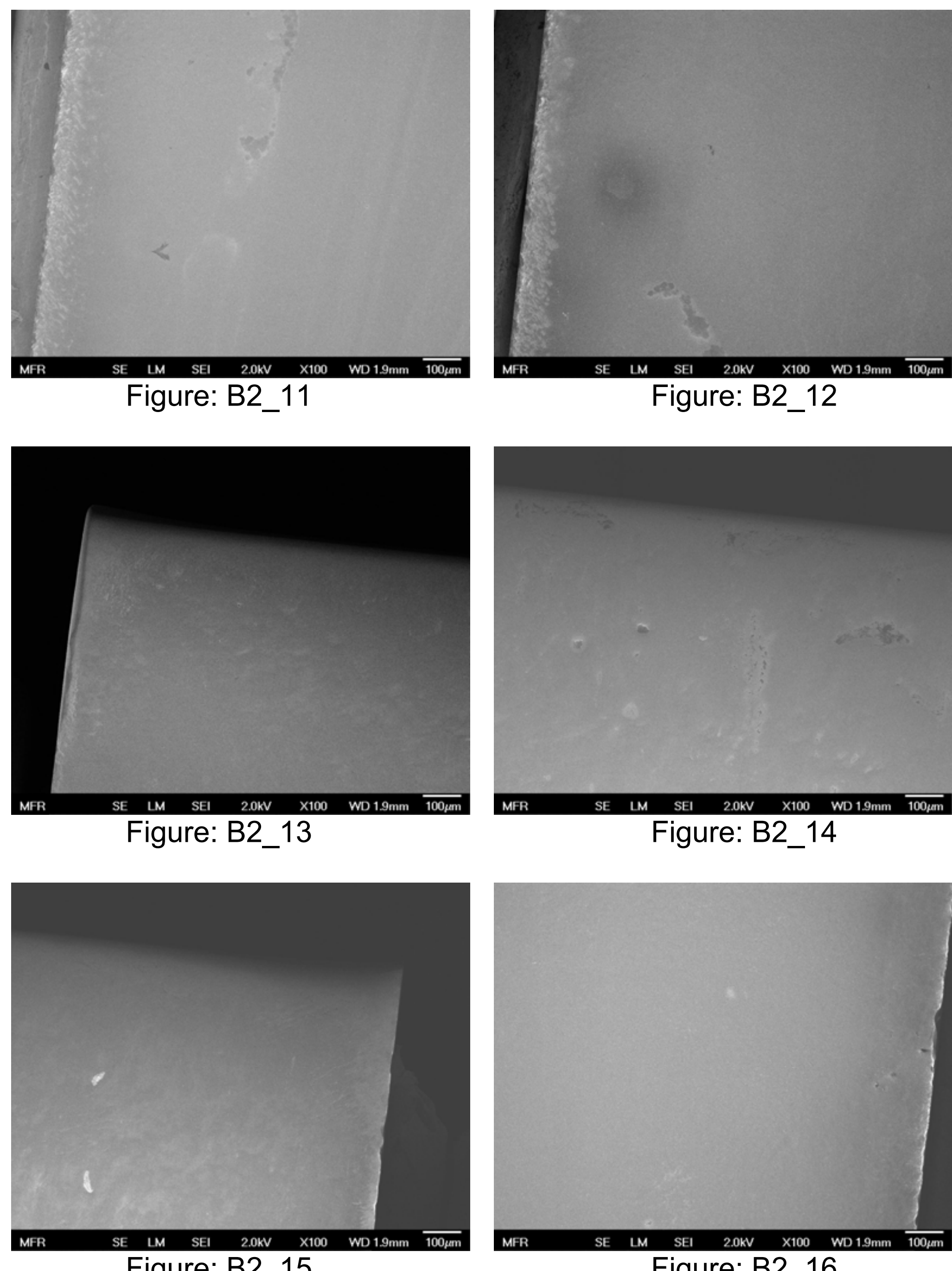

Figure: B2_11

Figure: B2_12

Figure: B2_13

Figure: B2_14

Figure: B2_15

Figure: B2_16

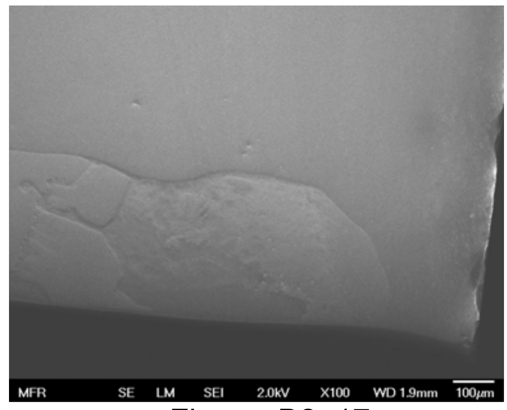

Figure: B2_17

Detector: B2,Side4

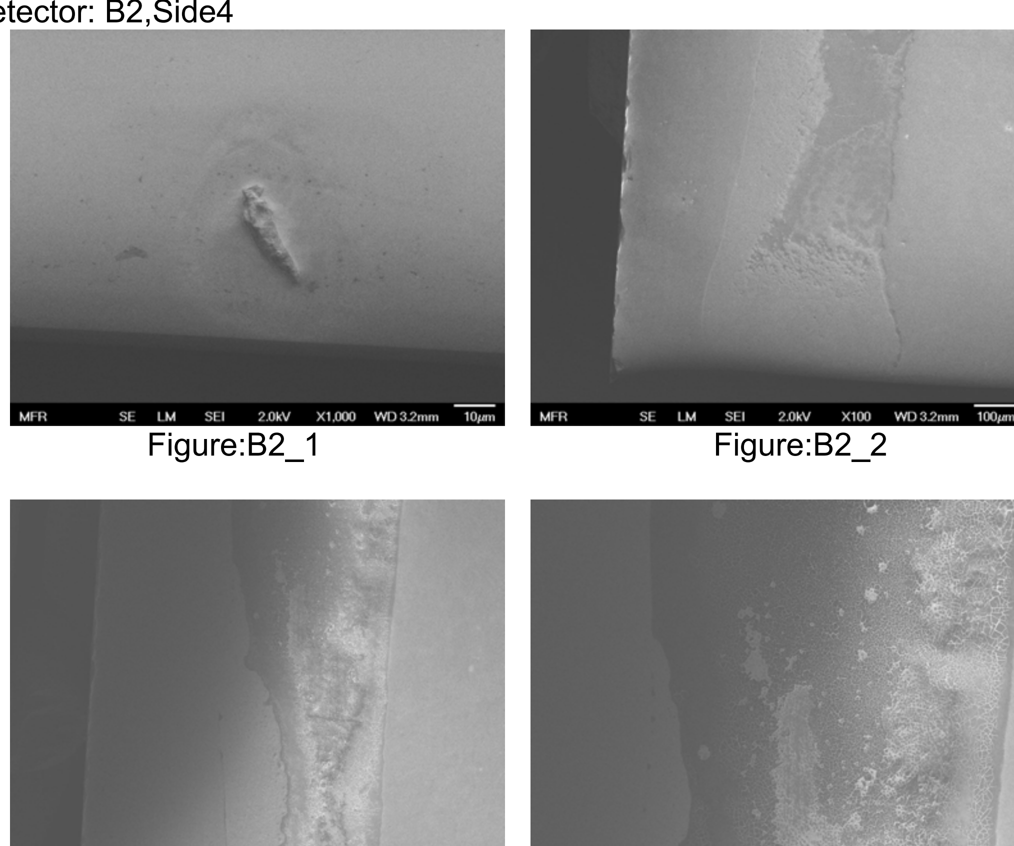

Figure:B2_1

Figure:B2_2

Figure:B2_3

Figure:B2_4

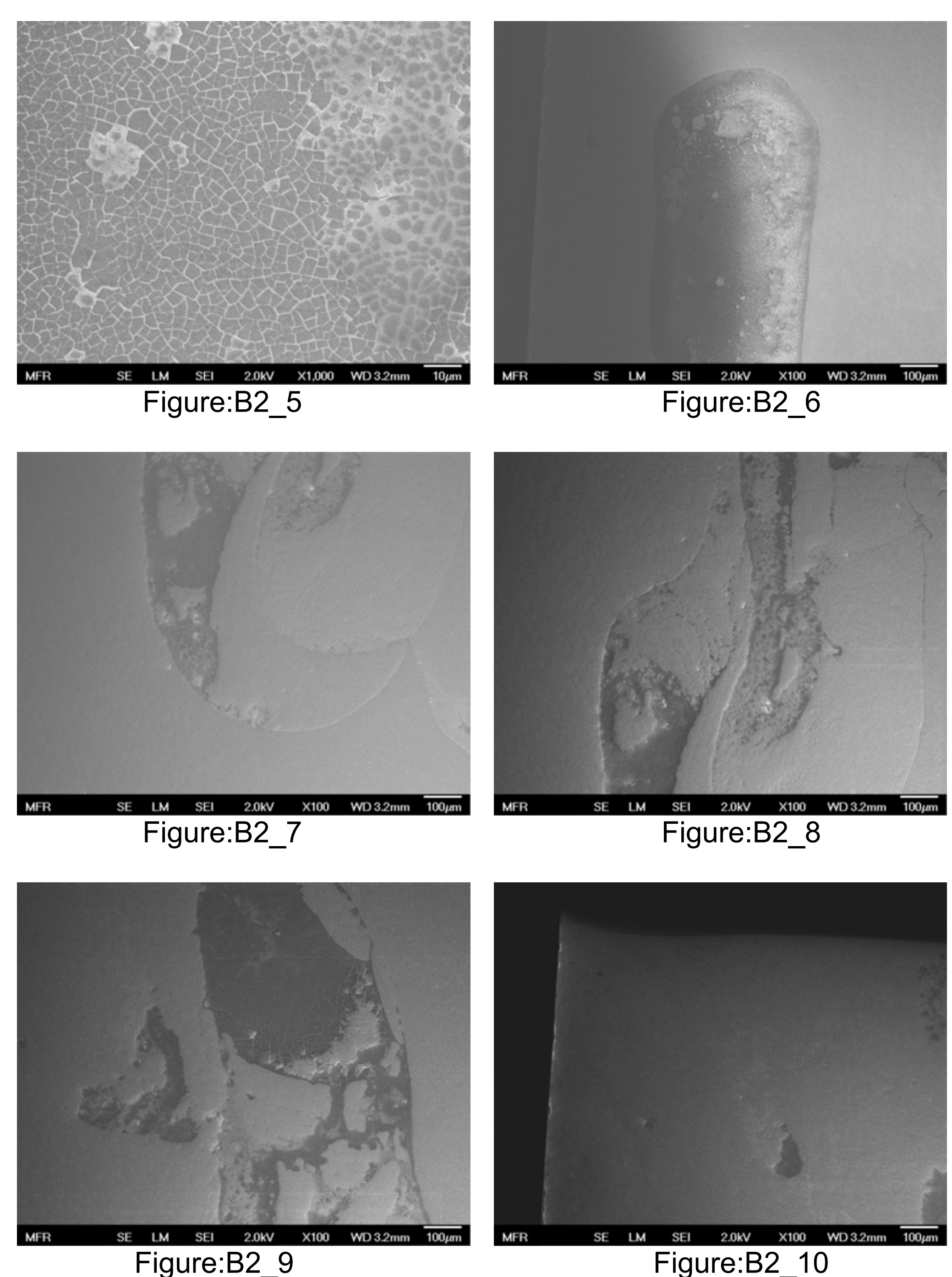

Figure:B2_5

Figure:B2_6

Figure:B2_7

Figure:B2_8

Figure:B2_9

Figure:B2_10

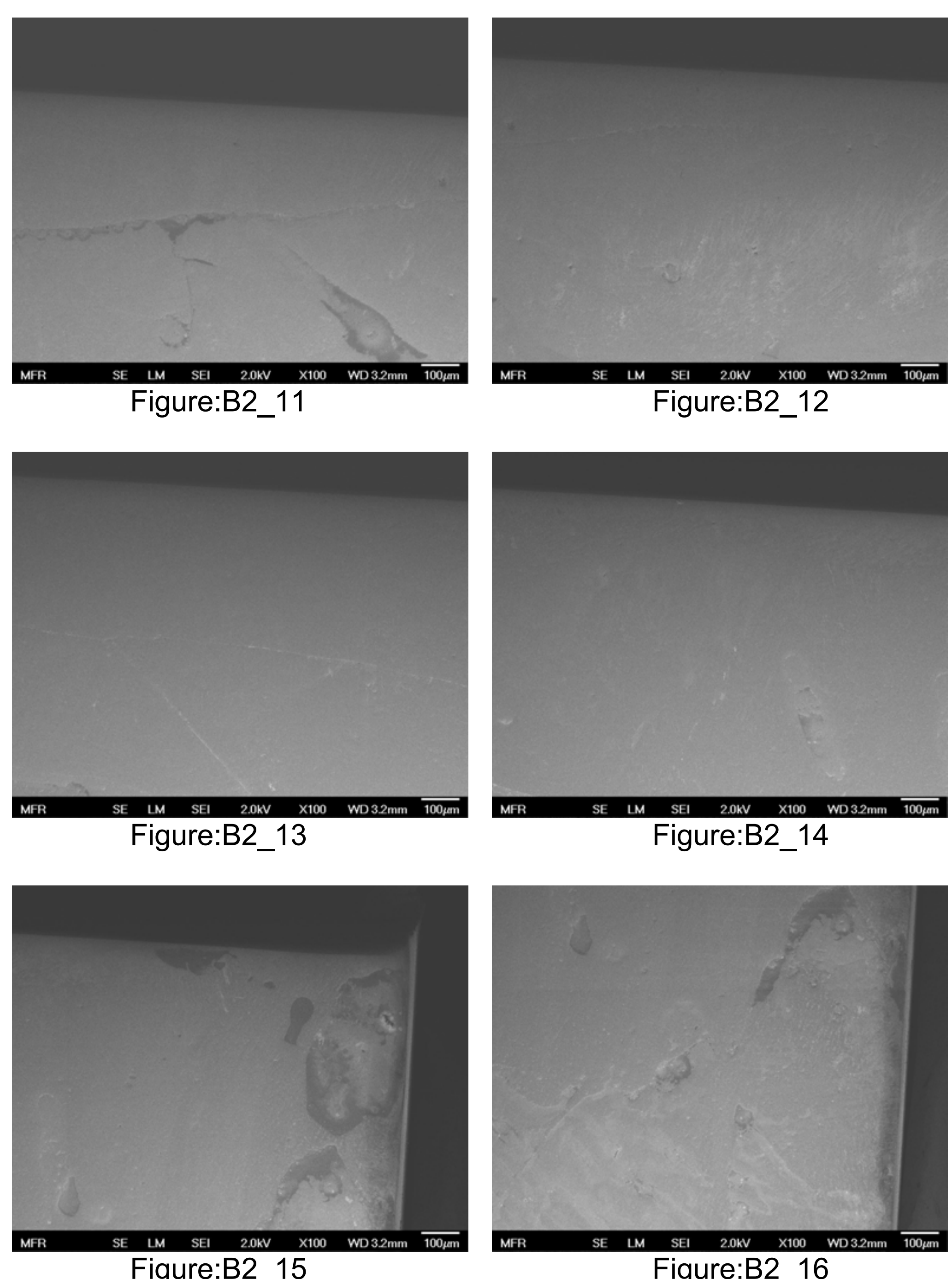

Figure:B2_11

Figure:B2_12

Figure:B2_13

Figure:B2_14

Figure:B2_15

Figure:B2_16

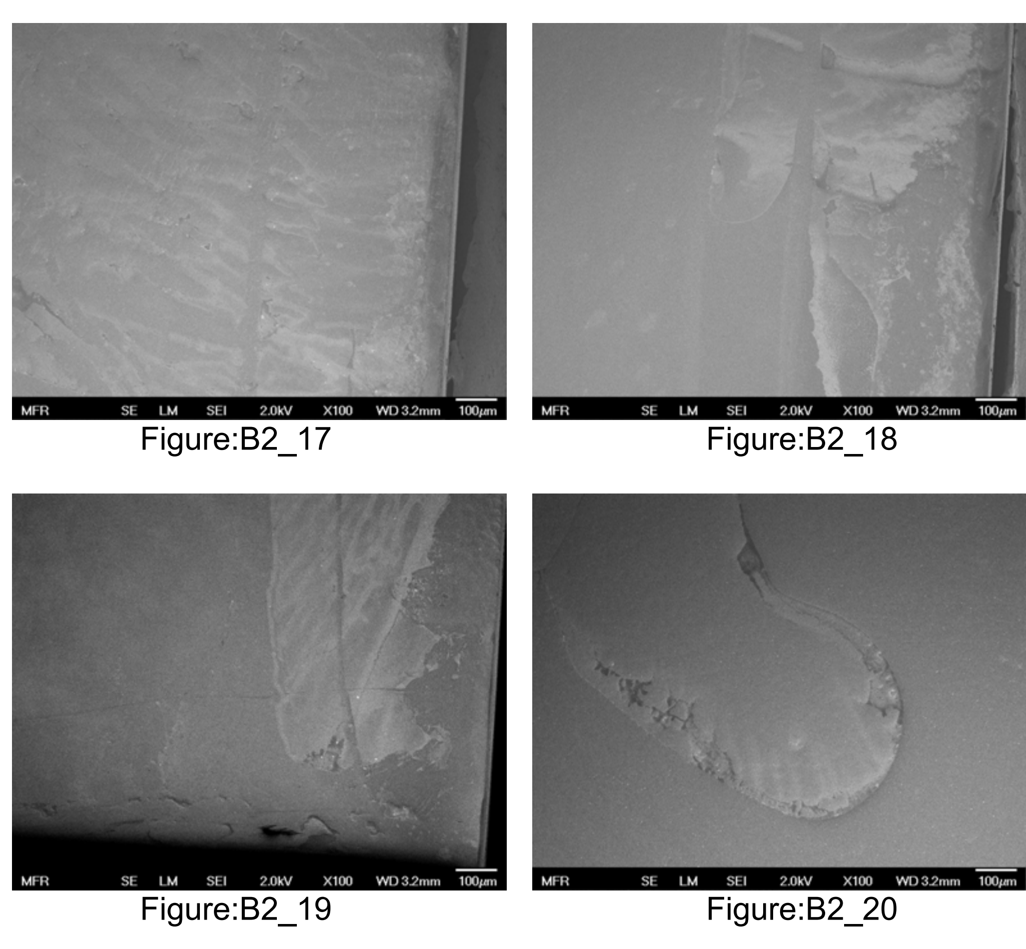

Figure:B2_17 Figure:B2_18

Figure:B2_19 Figure:B2_20

Detector: B5

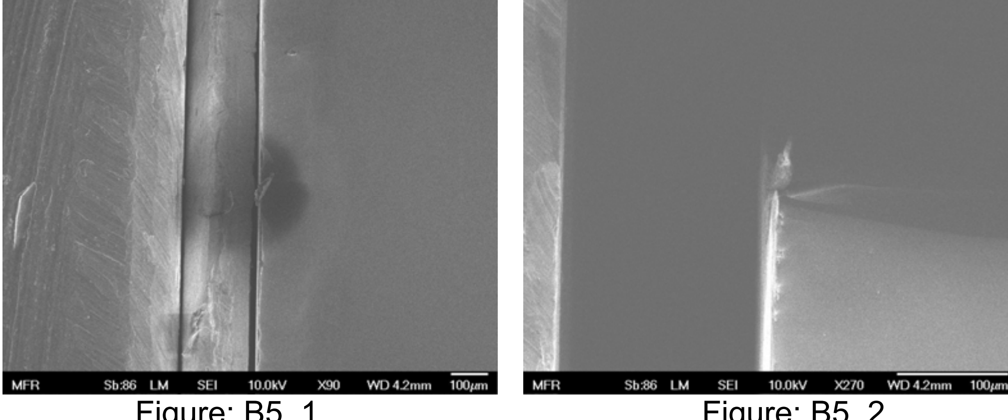

Figure: B5_1 Figure: B5_2

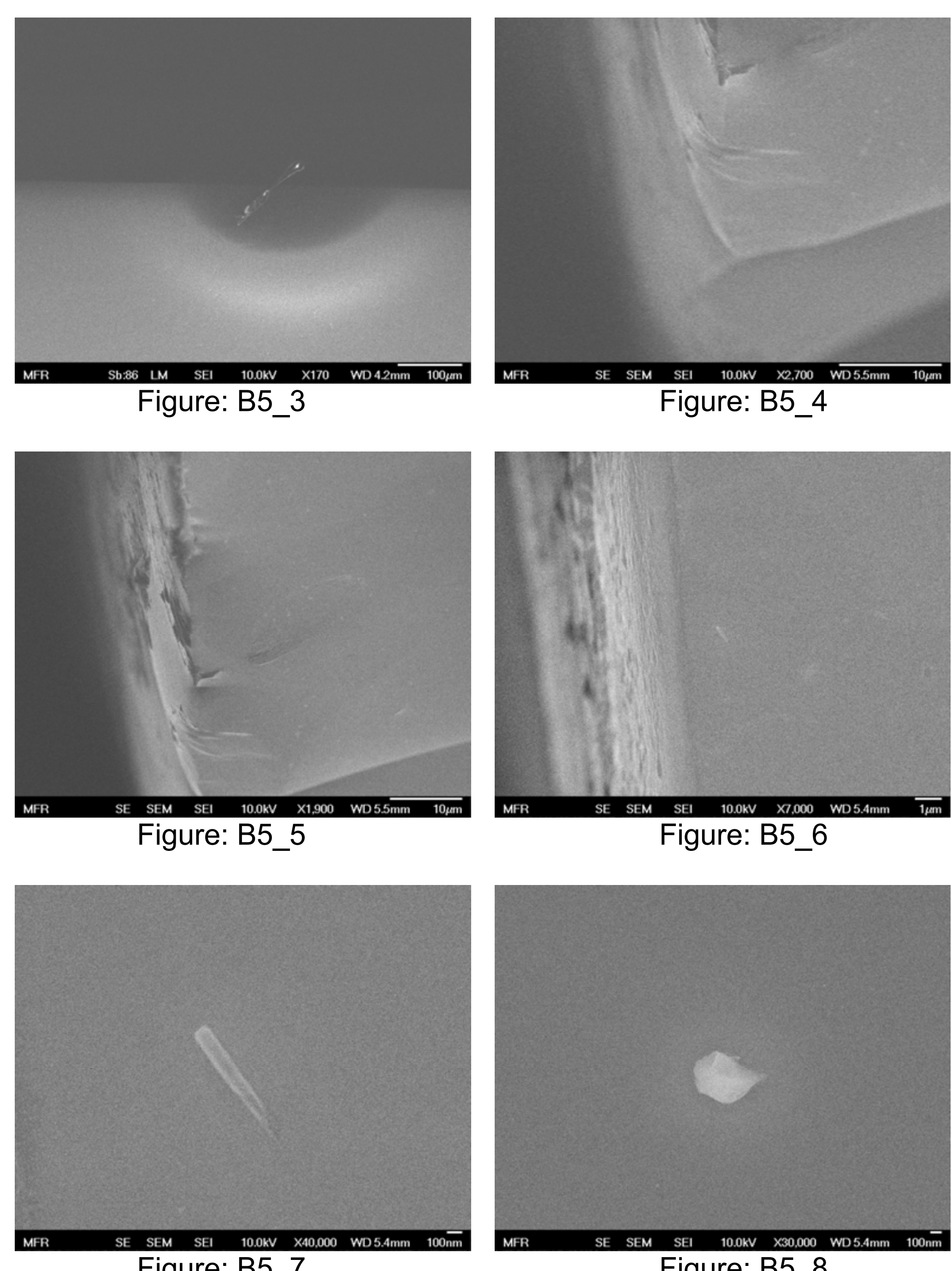

Figure: B5_3

Figure: B5_4

Figure: B5_5

Figure: B5_6

Figure: B5_7

Figure: B5_8

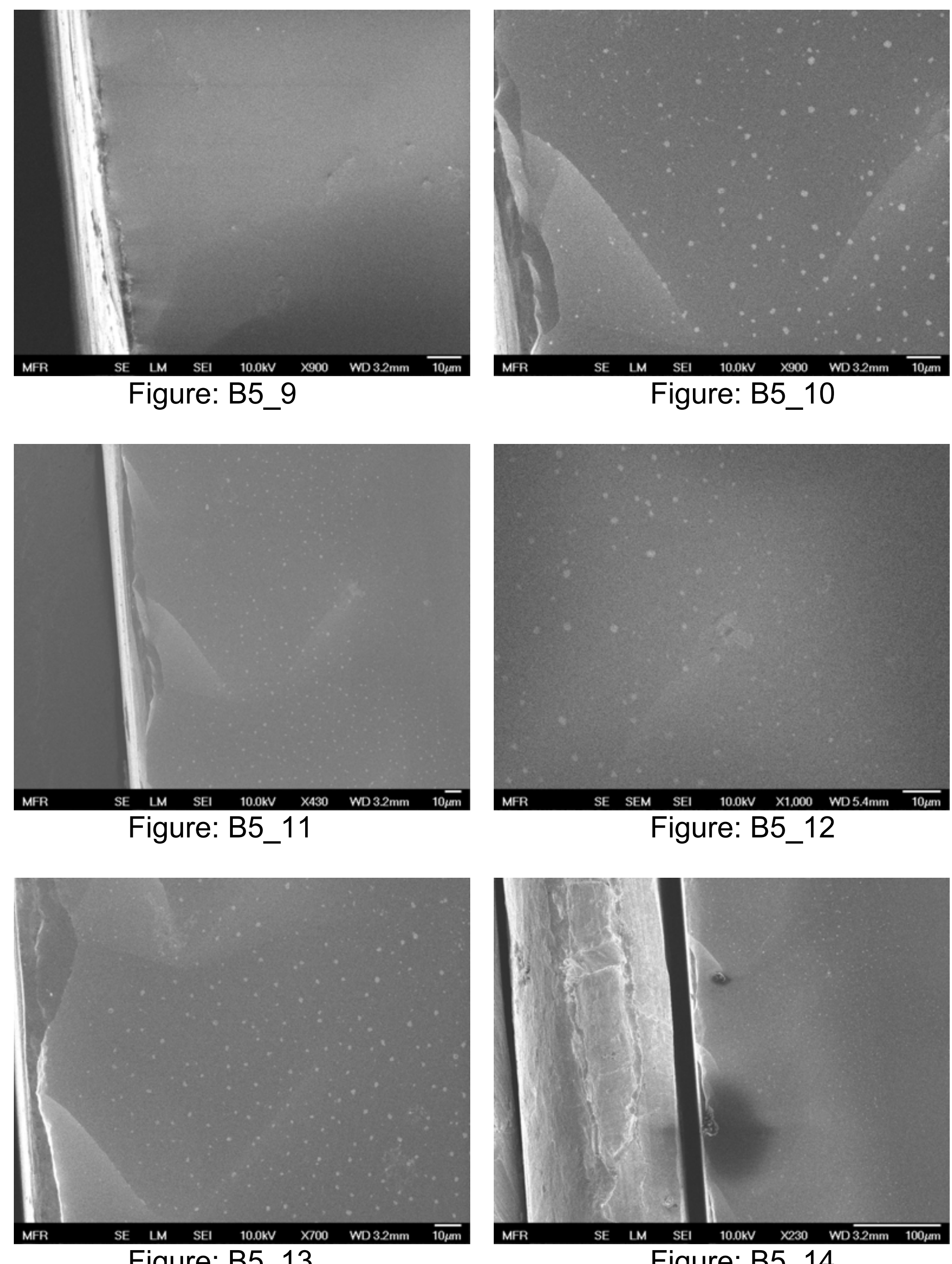

Figure: B5_9

Figure: B5_10

Figure: B5_11

Figure: B5_12

Figure: B5_13

Figure: B5_14

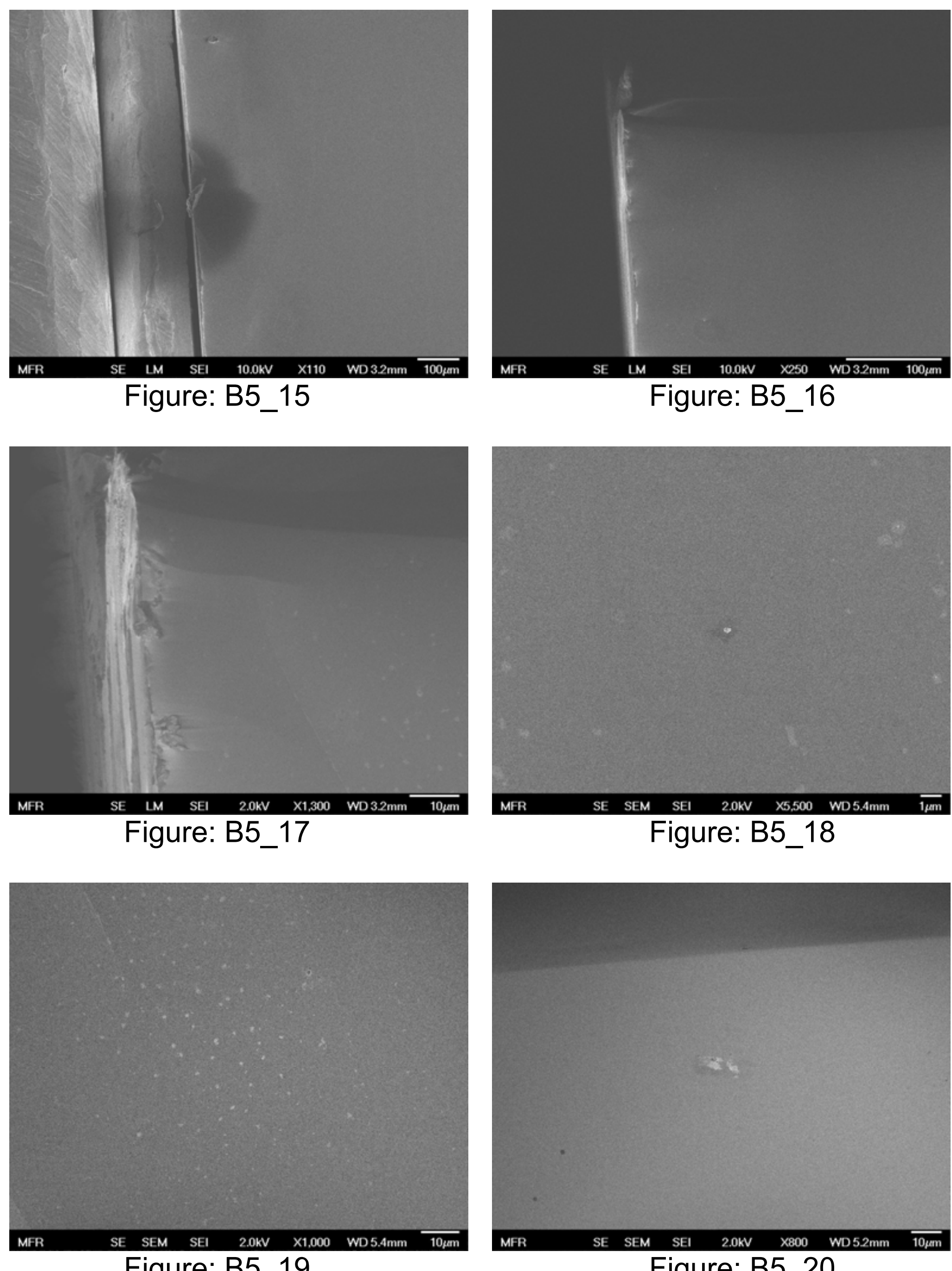

Figure: B5_15

Figure: B5_16

Figure: B5_17

Figure: B5_18

Figure: B5_19

Figure: B5_20

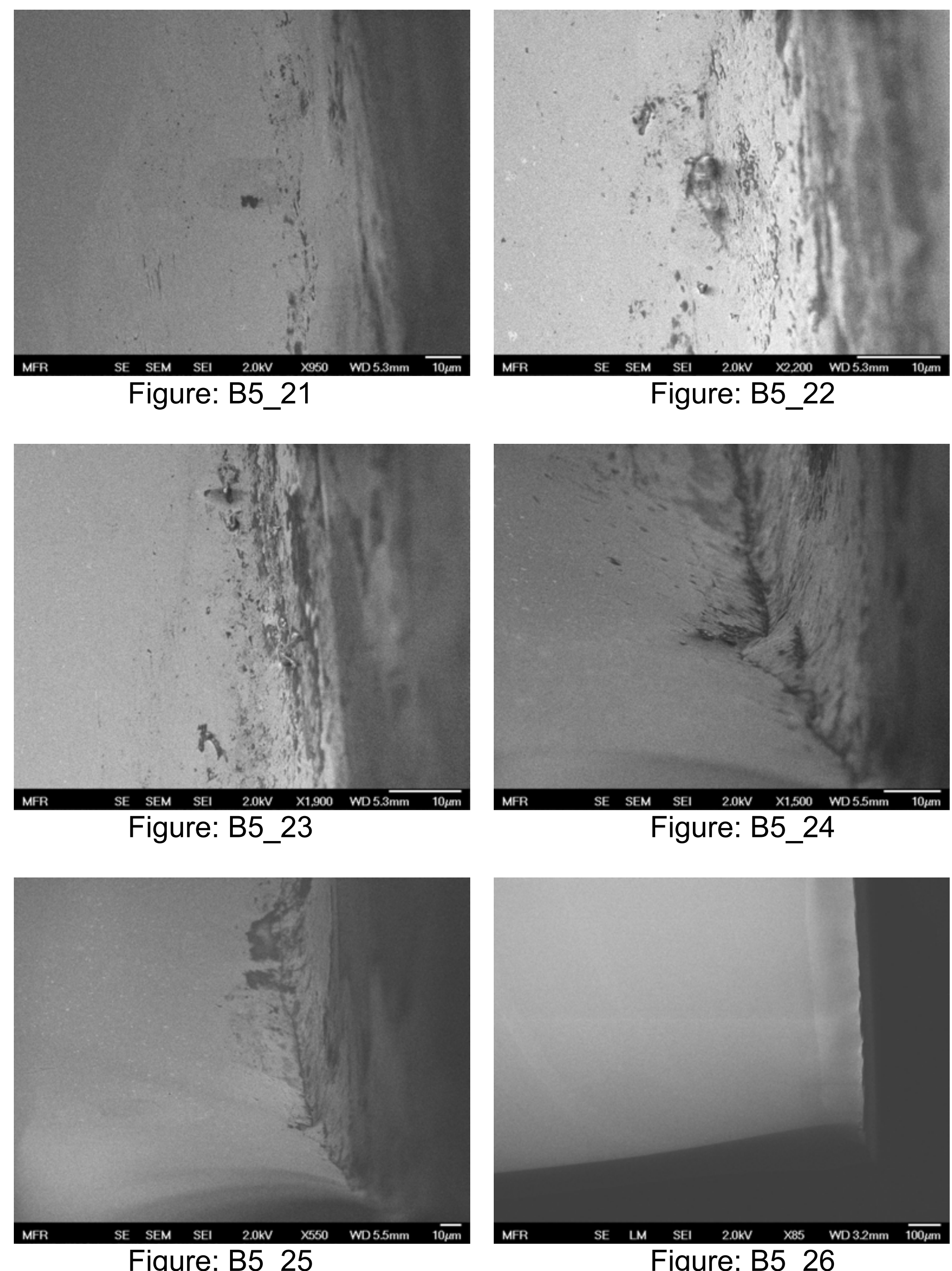

Figure: B5_21

Figure: B5_22

Figure: B5_23

Figure: B5_24

Figure: B5_25

Figure: B5_26

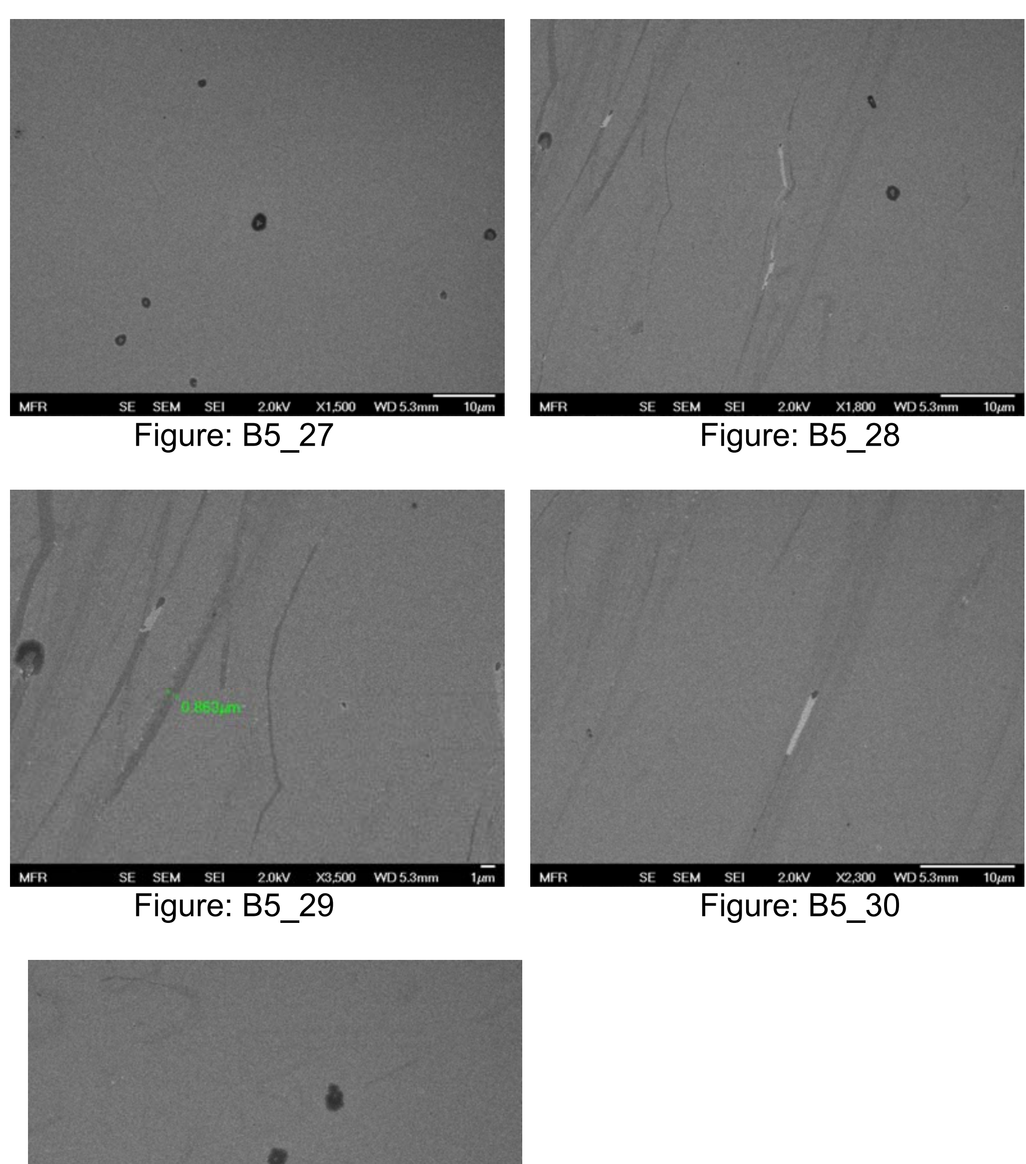

Figure: B5_27

Figure: B5_28

Figure: B5_29

Figure: B5_30

Figure: B5_31

Detector: B6

Figure:B6_1

Figure:B6_2

Figure:B6_3

Figure:B6_4

Figure:B6_5

Figure:B6_6

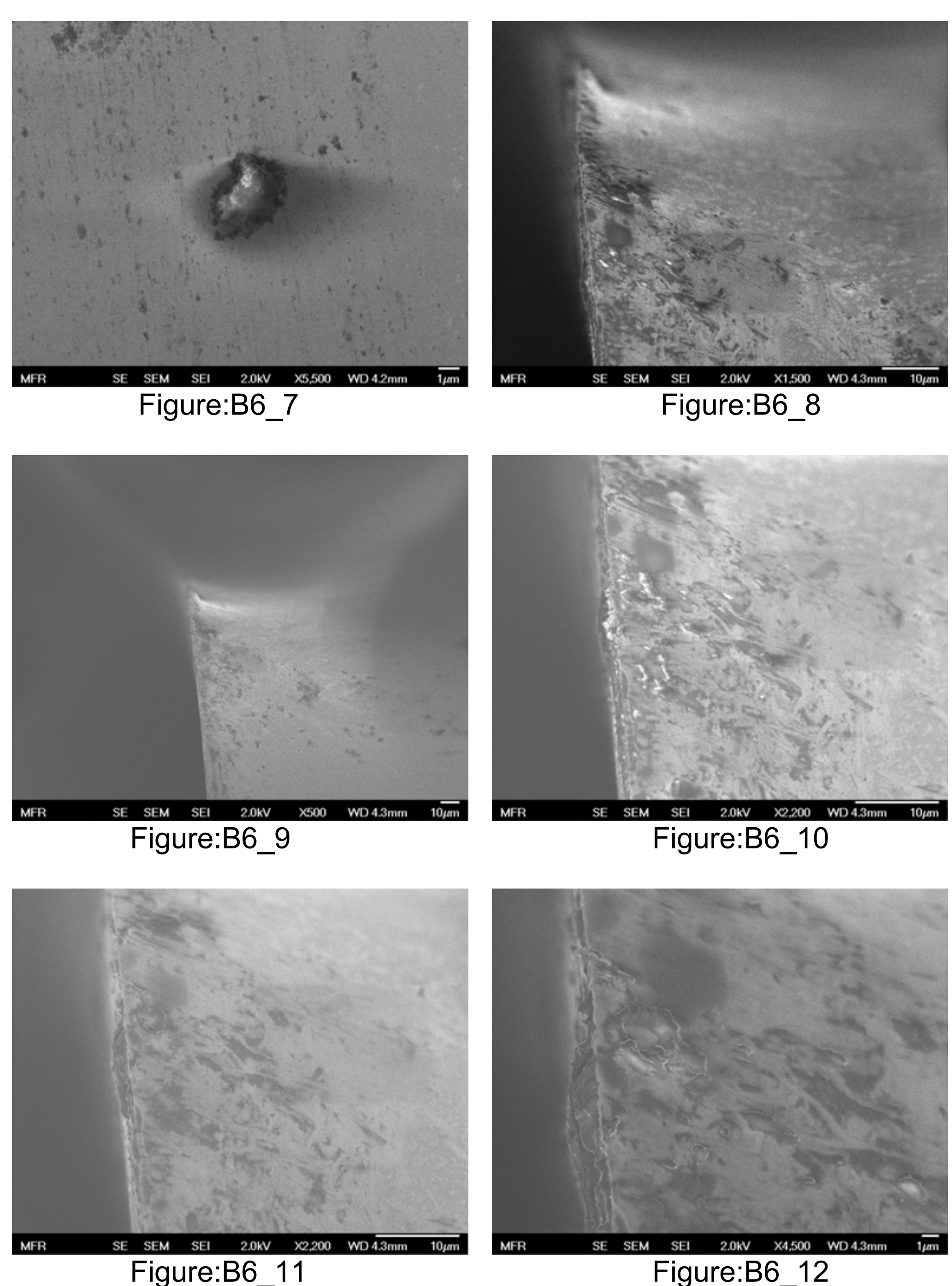

Figure:B6_7

Figure:B6_8

Figure:B6_9

Figure:B6_10

Figure:B6_11

Figure:B6_12

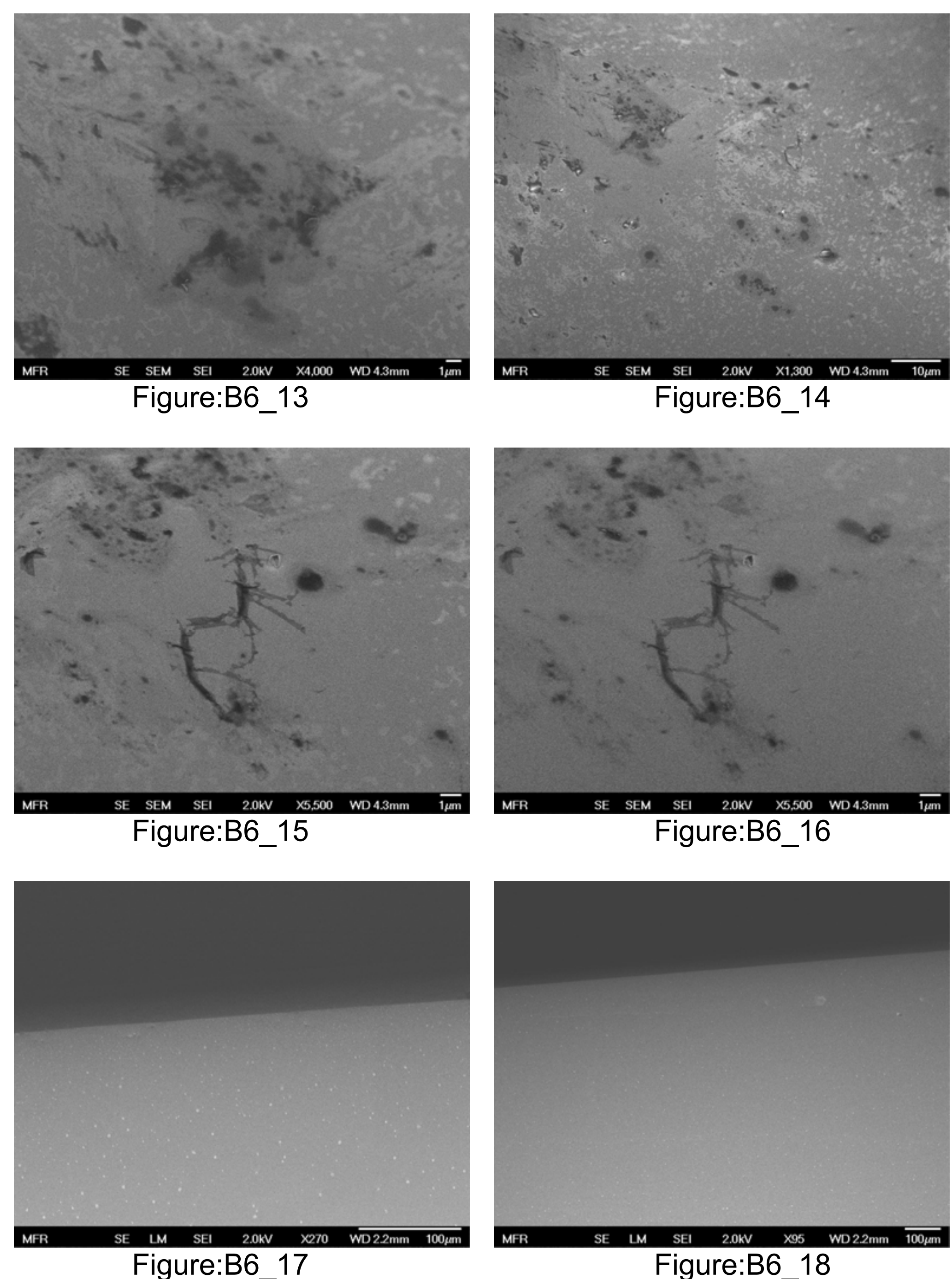

Figure:B6_13

Figure:B6_14

Figure:B6_15

Figure:B6_16

Figure:B6_17

Figure:B6_18

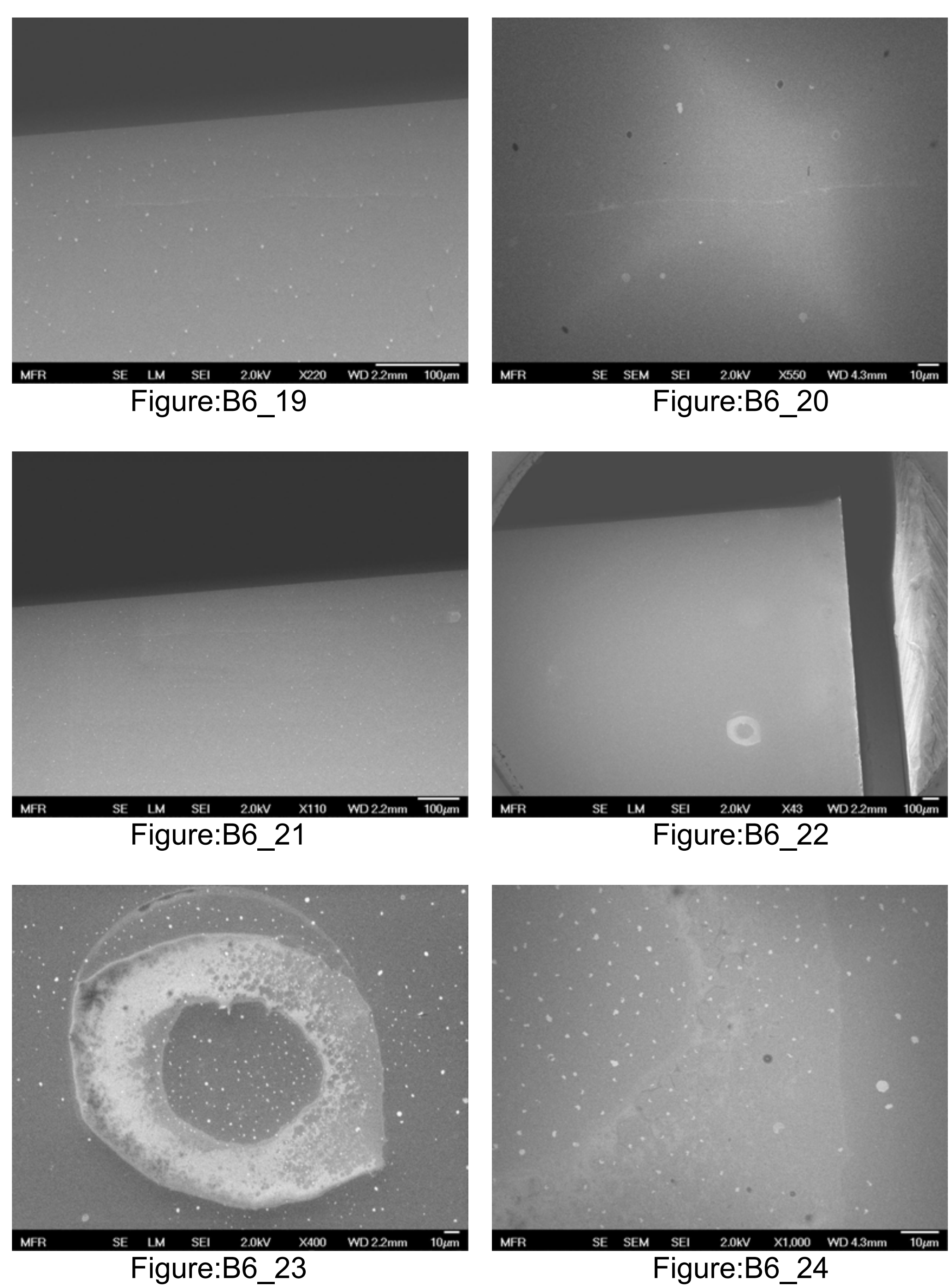

Figure:B6_19

Figure:B6_20

Figure:B6_21

Figure:B6_22

Figure:B6_23

Figure:B6_24

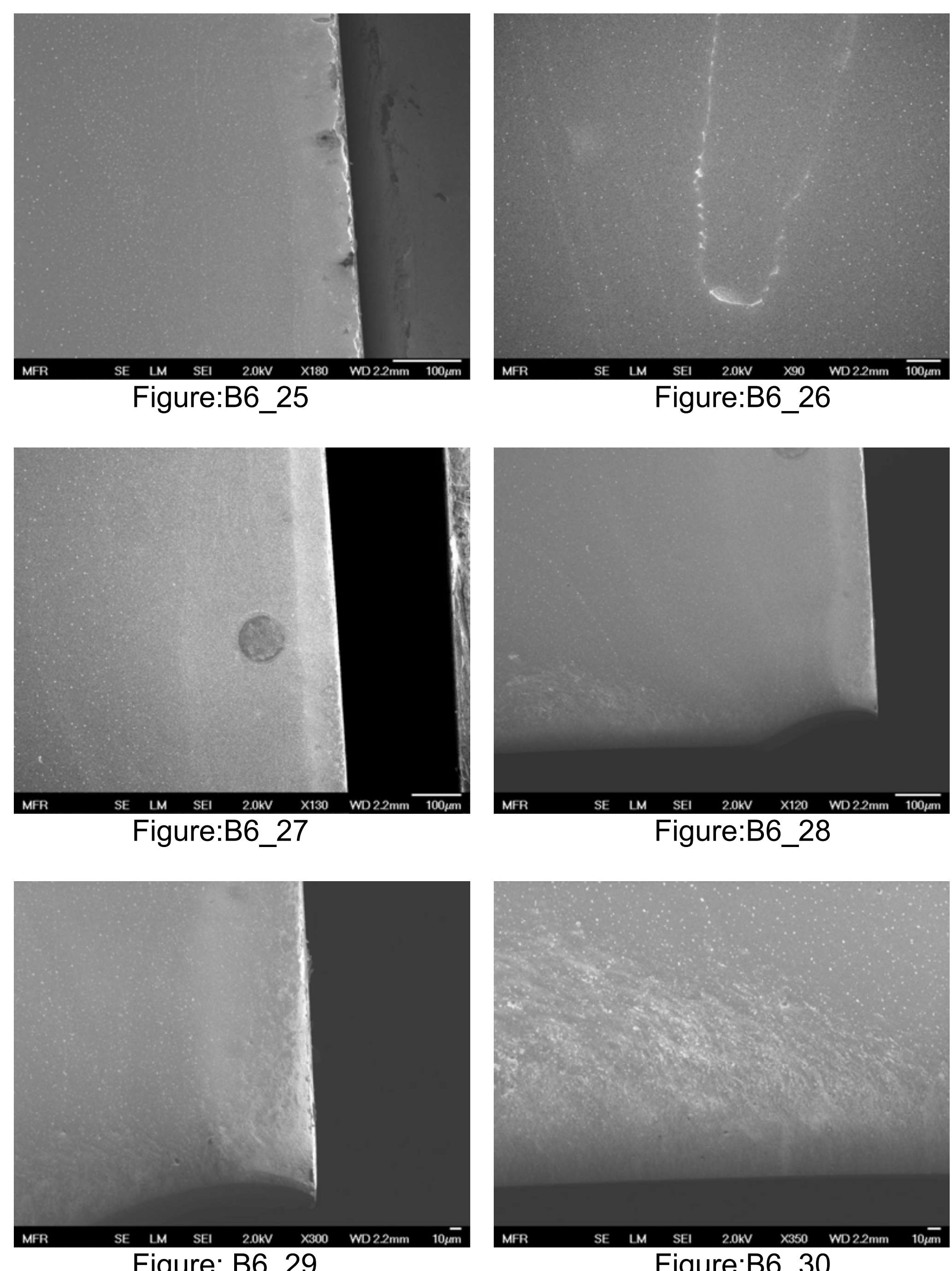

Figure:B6_25

Figure:B6_26

Figure:B6_27

Figure:B6_28

Figure: B6_29

Figure:B6_30

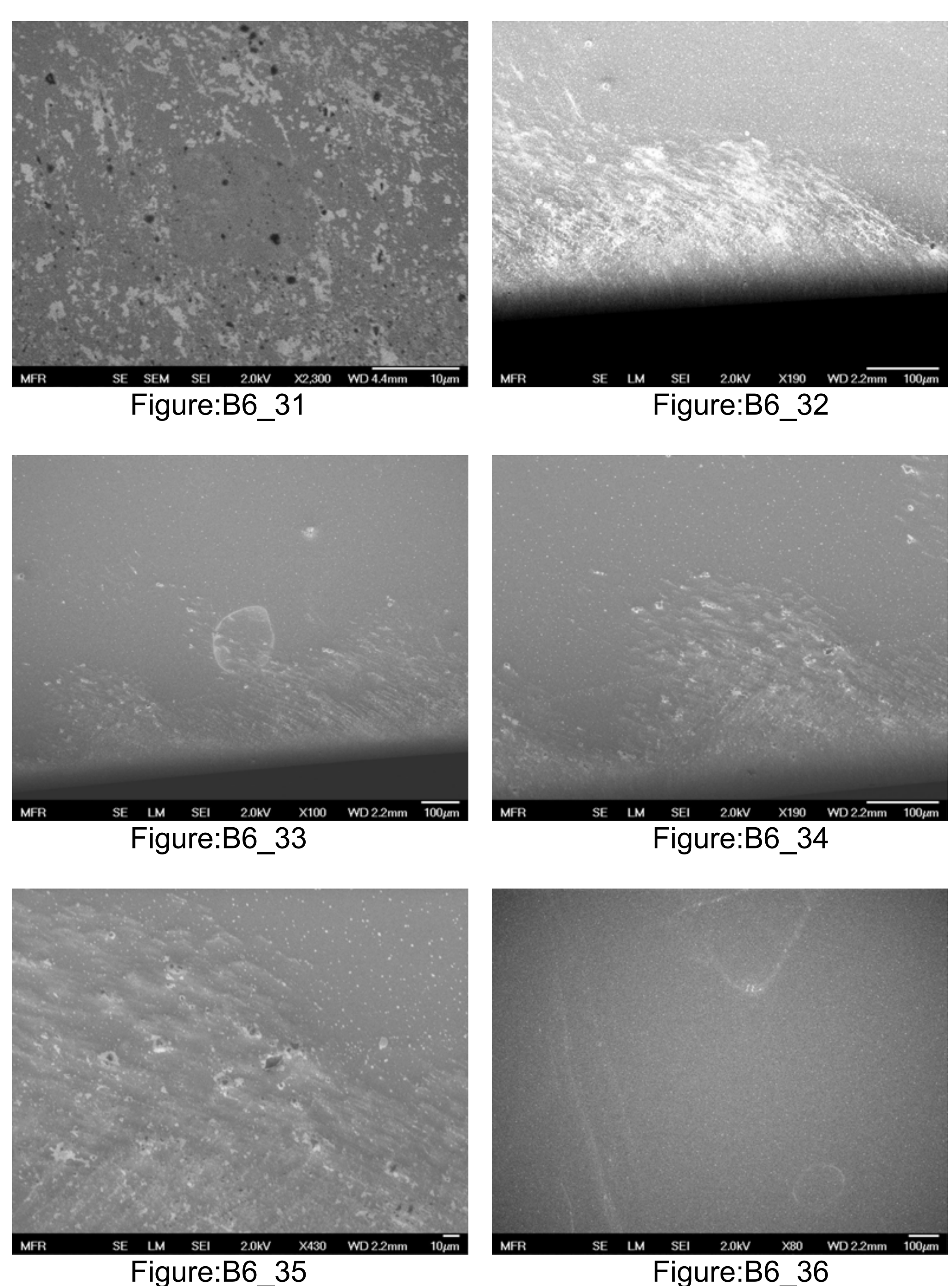

Figure:B6_31

Figure:B6_32

Figure:B6_33

Figure:B6_34

Figure:B6_35

Figure:B6_36

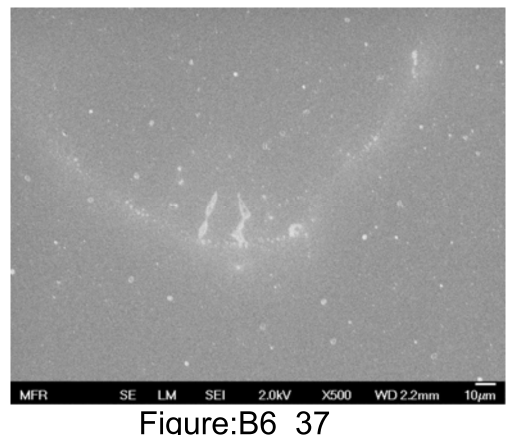

Figure:B6_37

Figure:B6_38

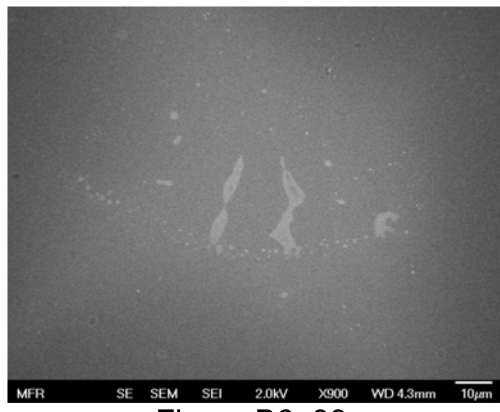

Figure:B6_39

Detector: B7, Side 1

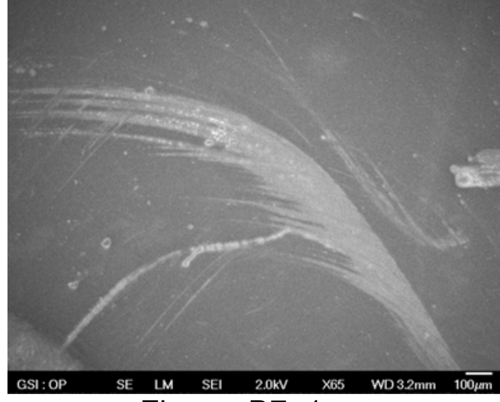

Figure: B7_1

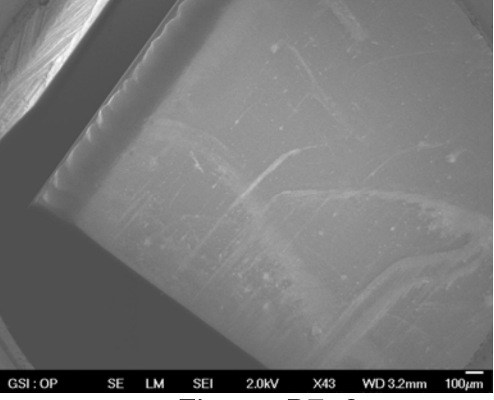

Figure: B7_2

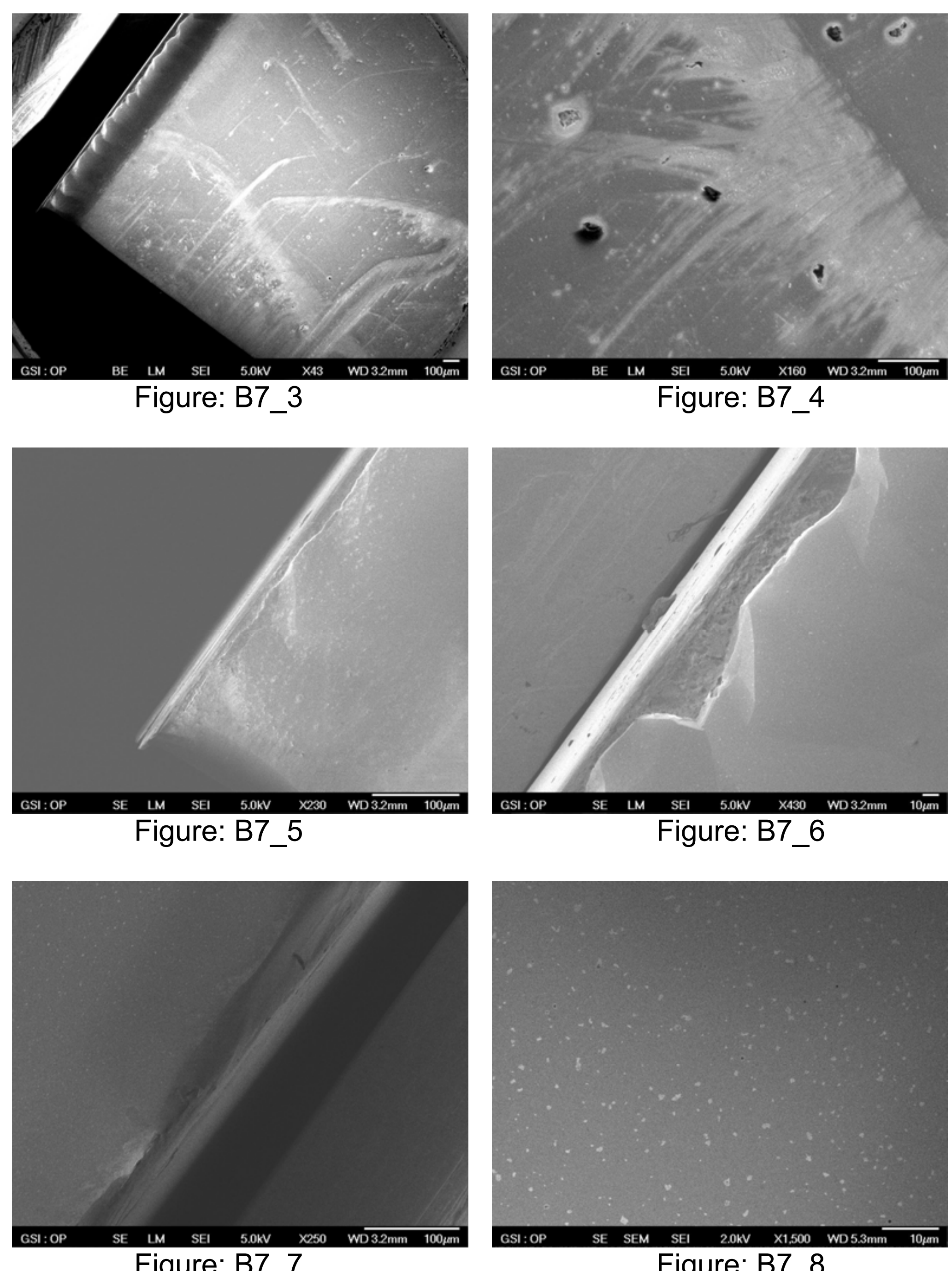

Figure: B7_3

Figure: B7_4

Figure: B7_5

Figure: B7_6

Figure: B7_7

Figure: B7_8

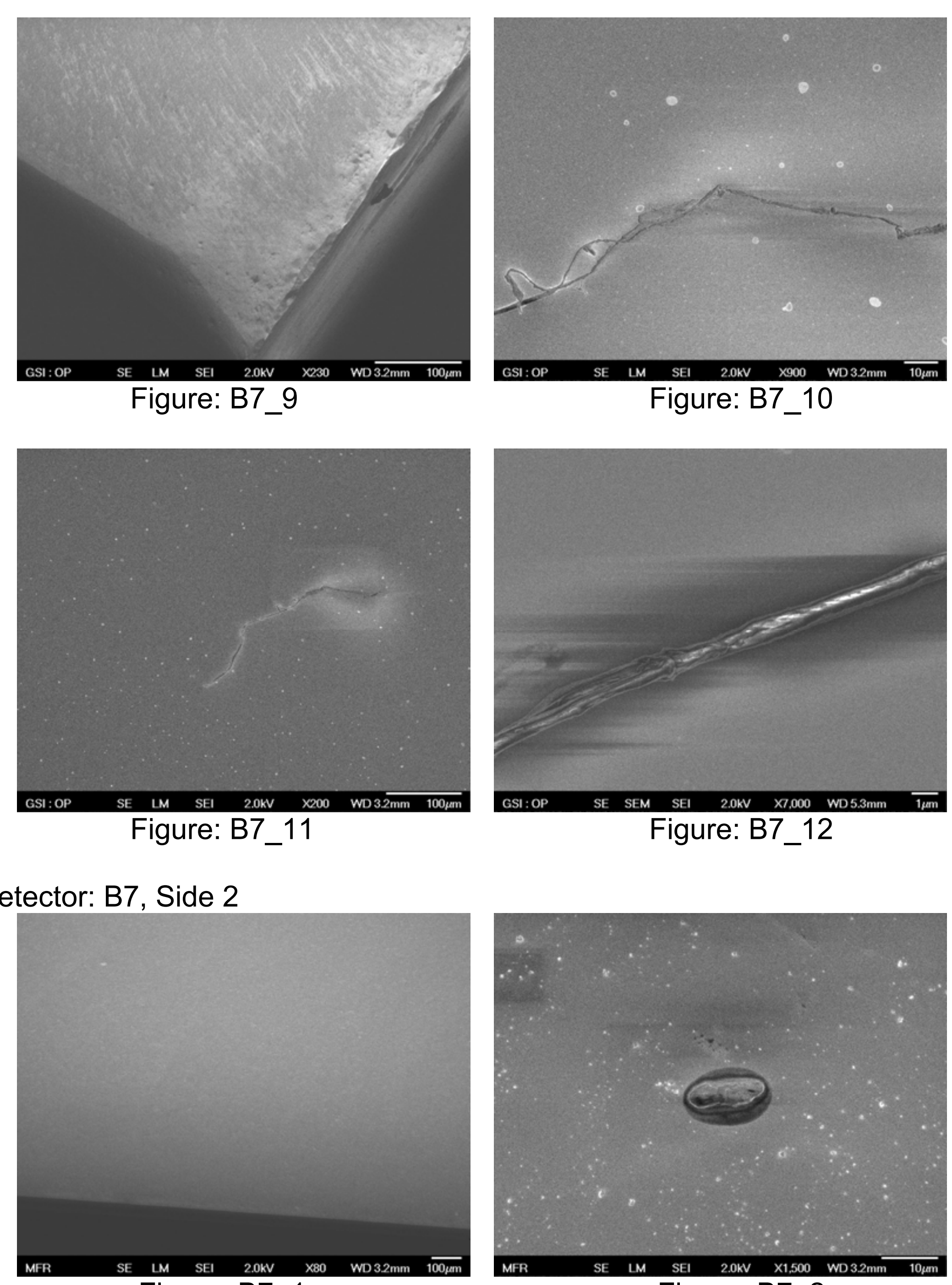

Figure: B7_9

Figure: B7_10

Figure: B7_11

Figure: B7_12

Detector: B7, Side 2

Figure: B7_1

Figure: B7_2

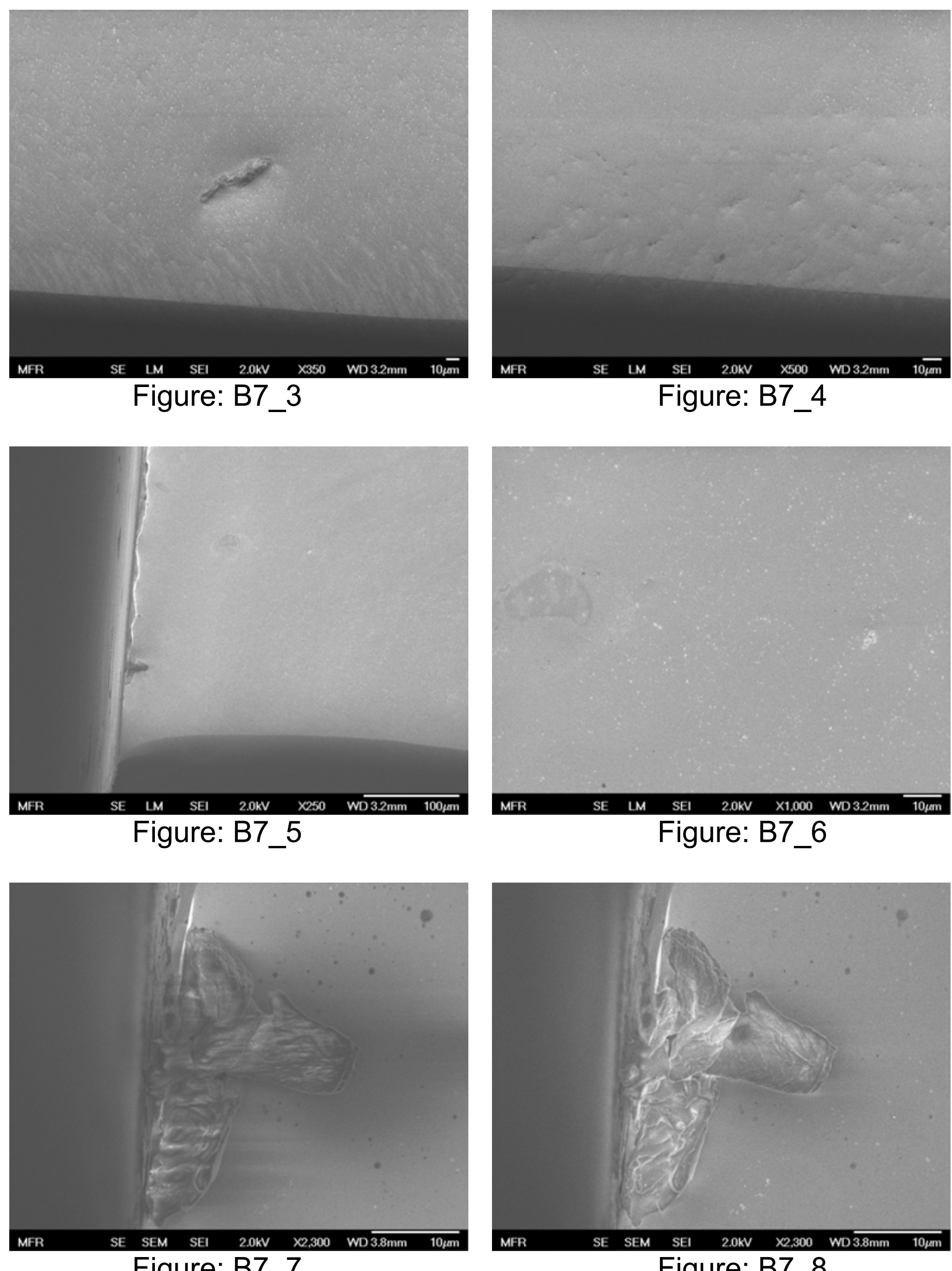

Figure: B7_3

Figure: B7_4

Figure: B7_5

Figure: B7_6

Figure: B7_7

Figure: B7_8

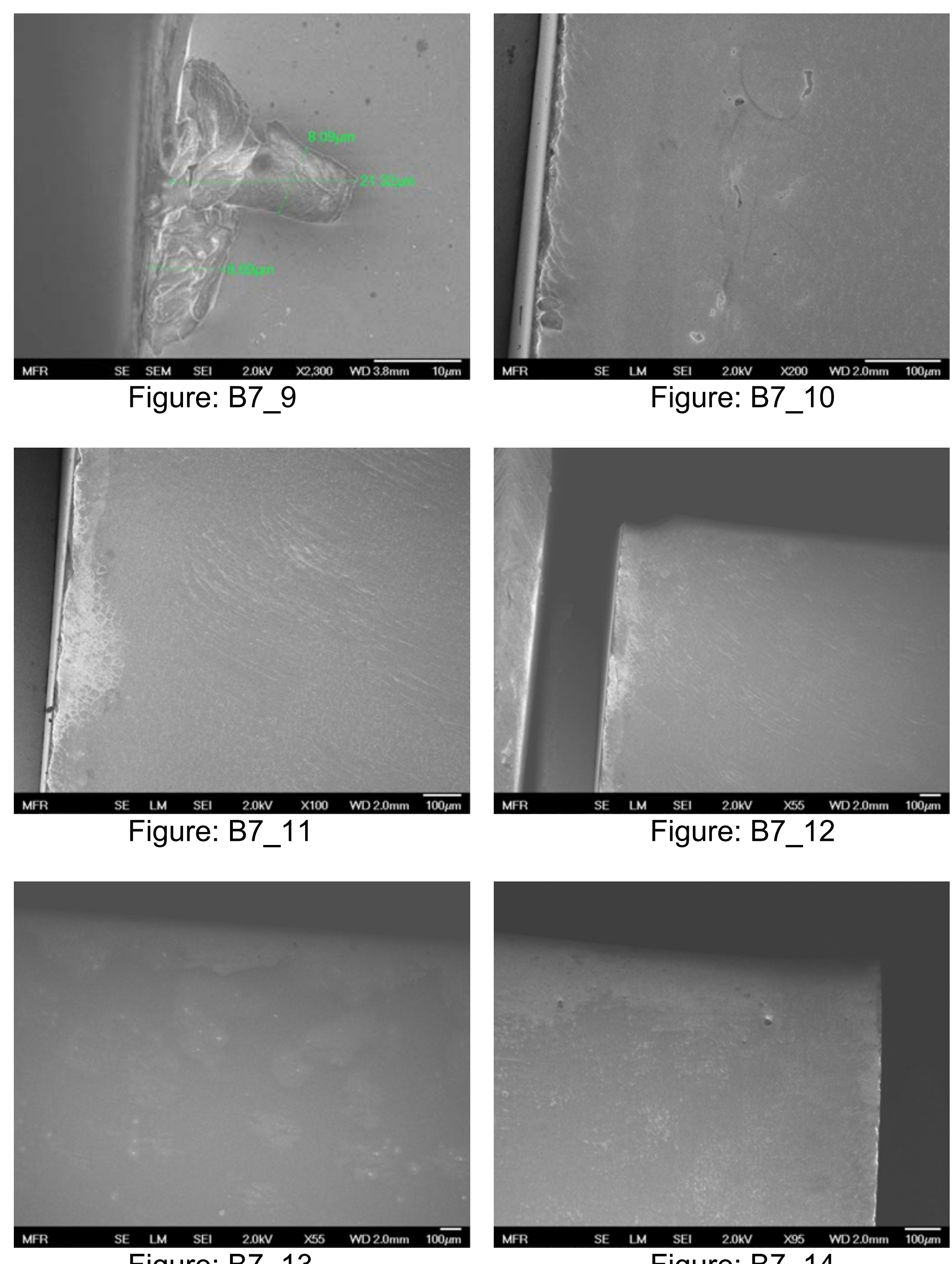

Figure: B7_9

Figure: B7_10

Figure: B7_11

Figure: B7_12

Figure: B7_13

Figure: B7_14

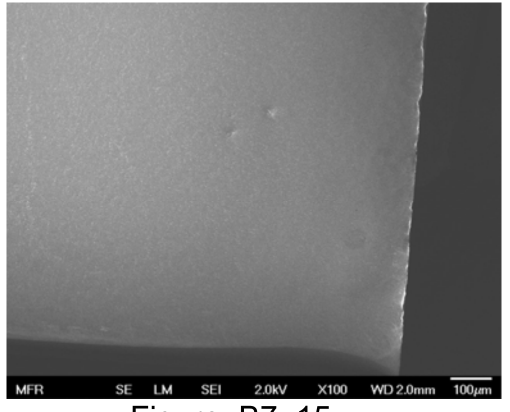

Figure: B7_15

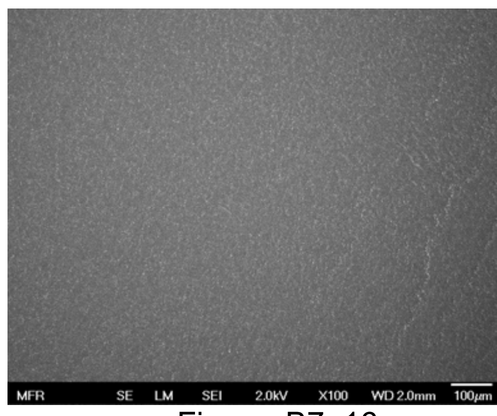

Figure: B7_16

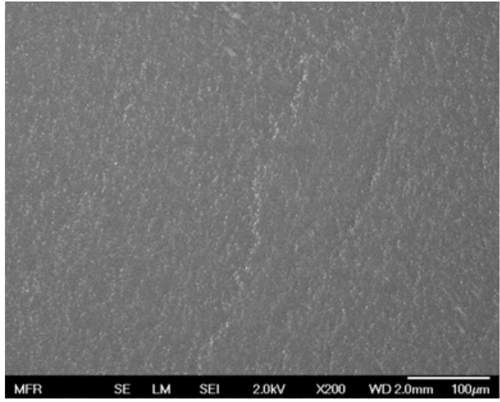

Figure: B7_17

Detector: B7, Side 3

Figure: B7_1

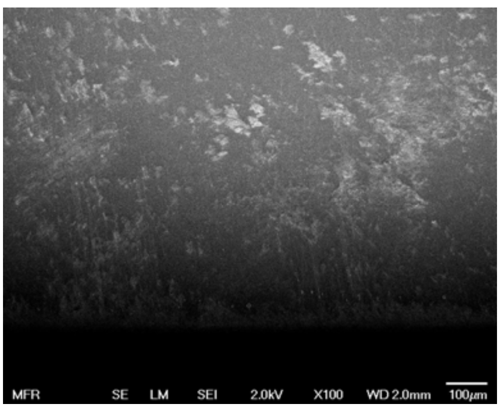

Figure: B7_2

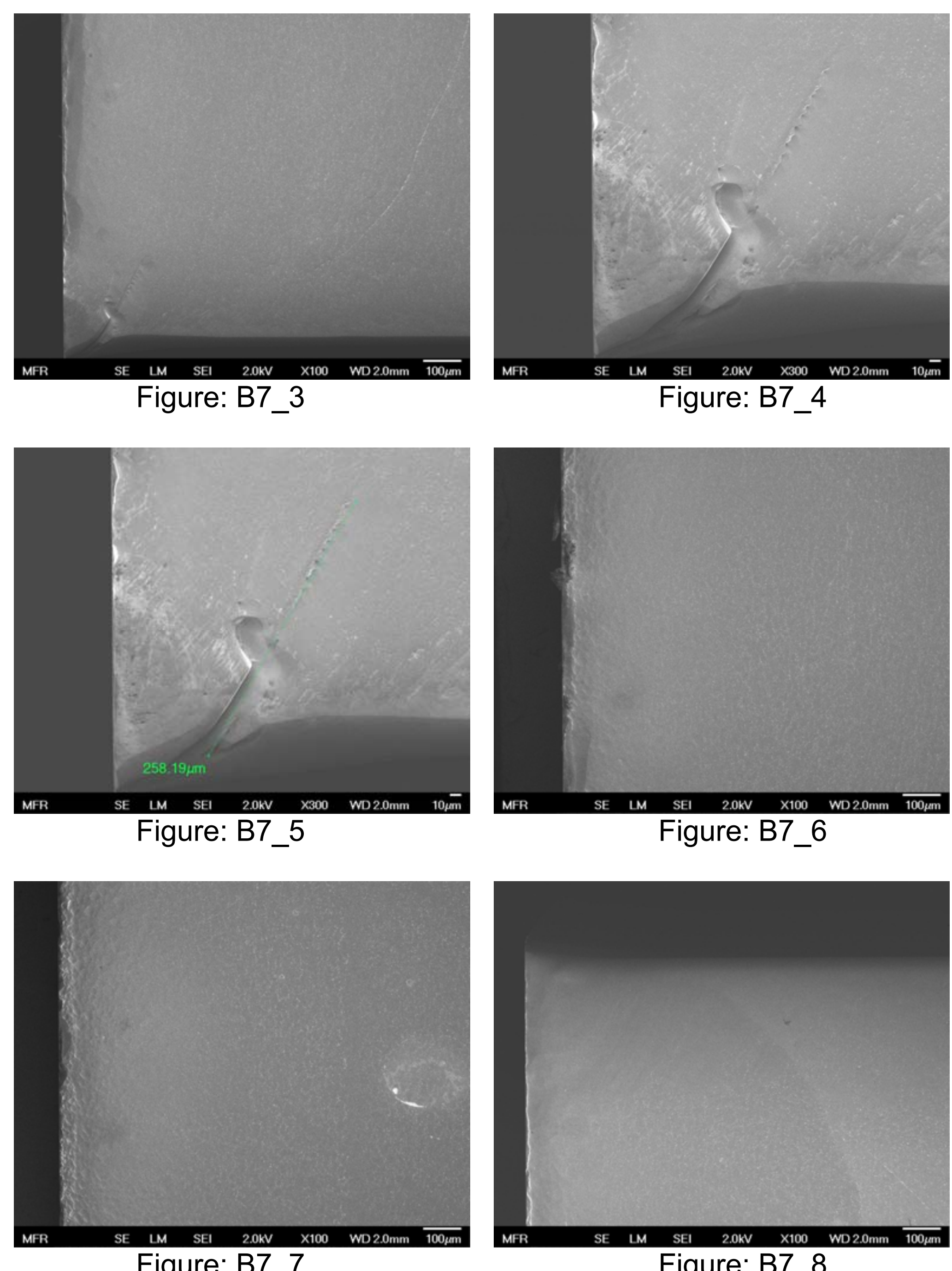

Figure: B7_3

Figure: B7_4

Figure: B7_5

Figure: B7_6

Figure: B7_7

Figure: B7_8

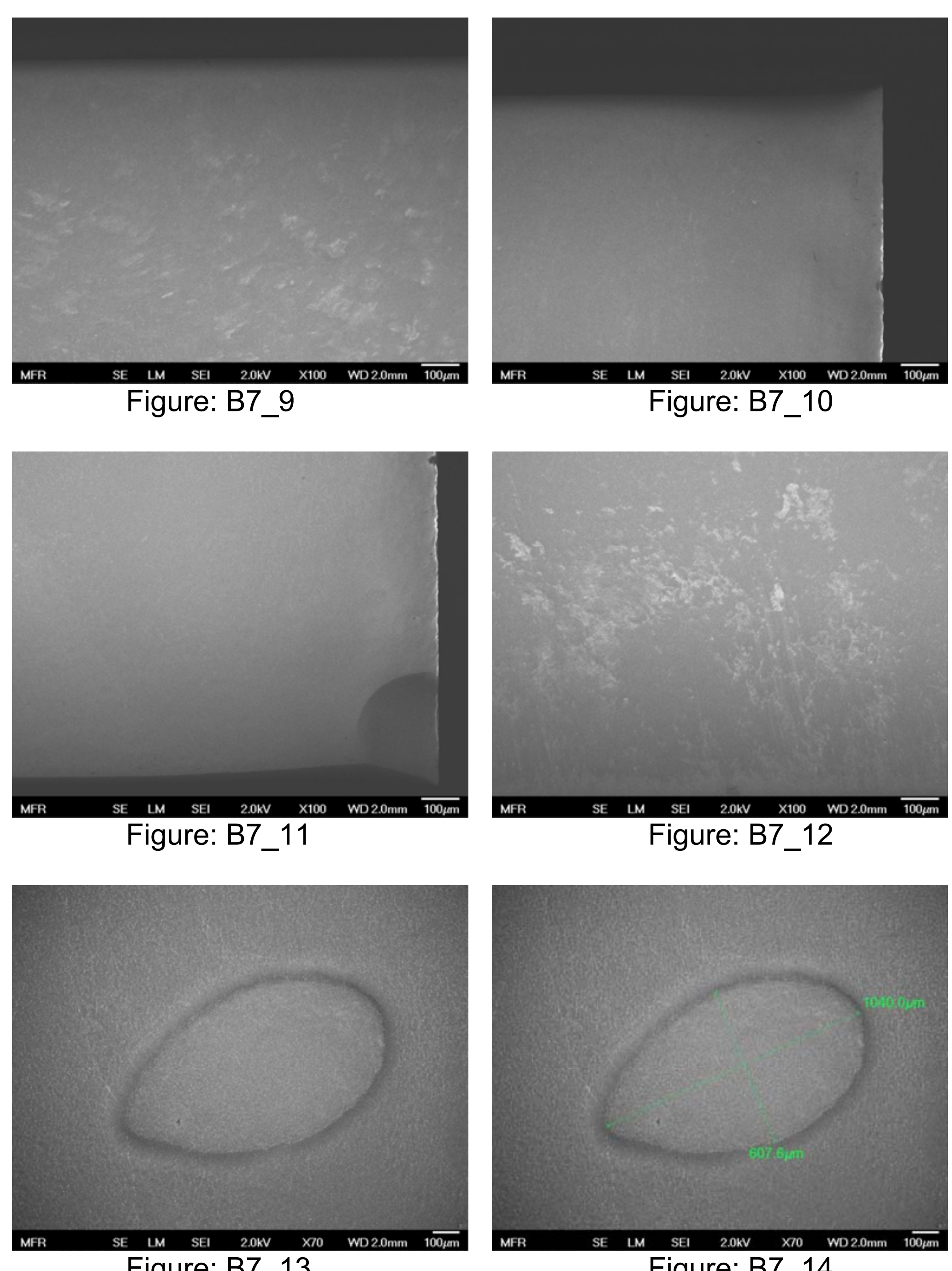

Figure: B7_9

Figure: B7_10

Figure: B7_11

Figure: B7_12

Figure: B7_13

Figure: B7_14

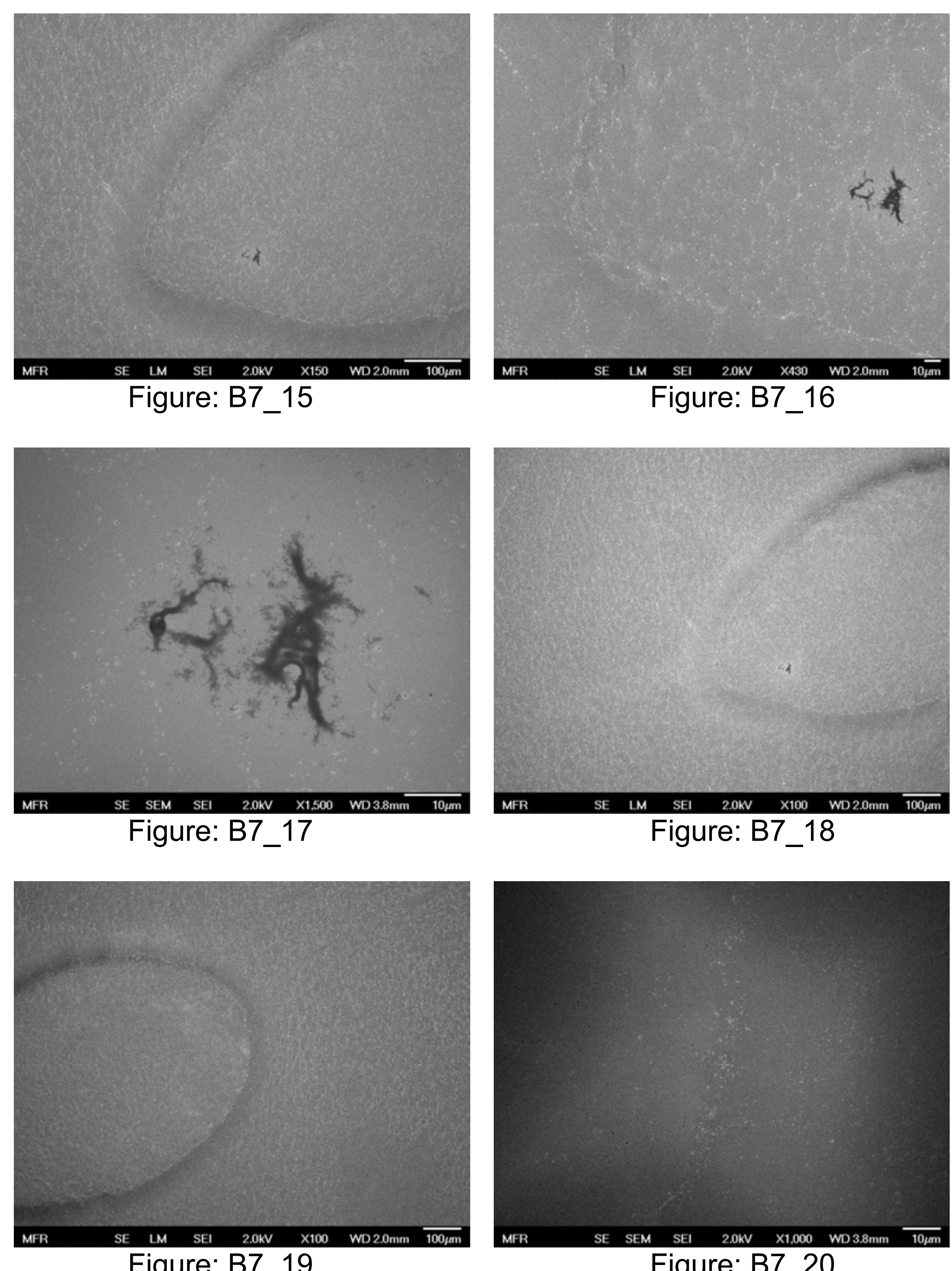

Figure: B7_15

Figure: B7_16

Figure: B7_17

Figure: B7_18

Figure: B7_19

Figure: B7_20

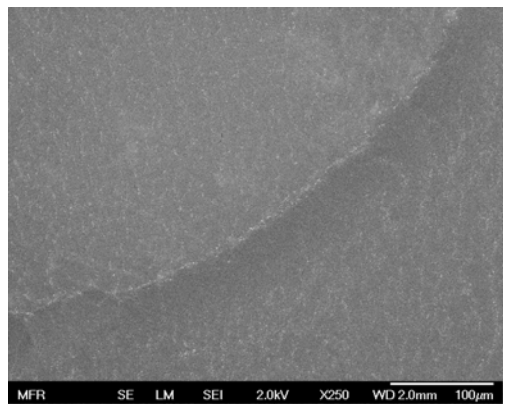

Figure: B7_21

Detector: B7, Side 4

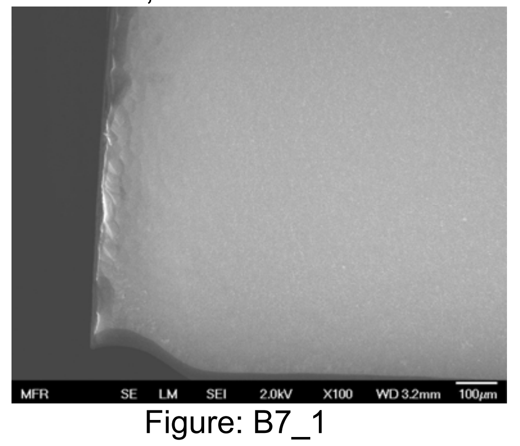

Figure: B7_1

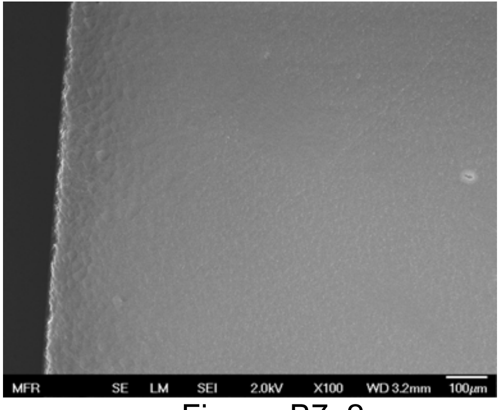

Figure: B7_2

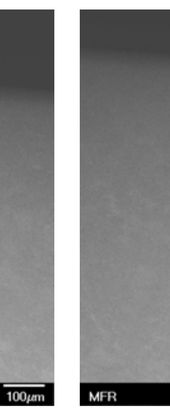

Figure: B7_3

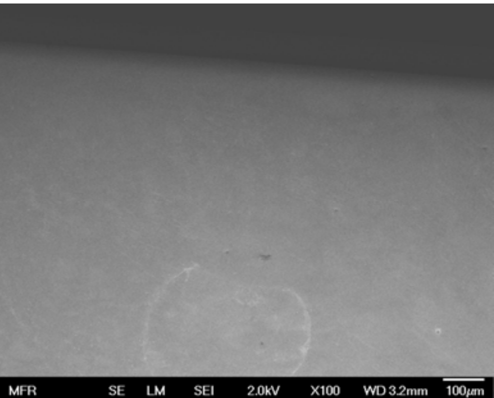

Figure: B7_4

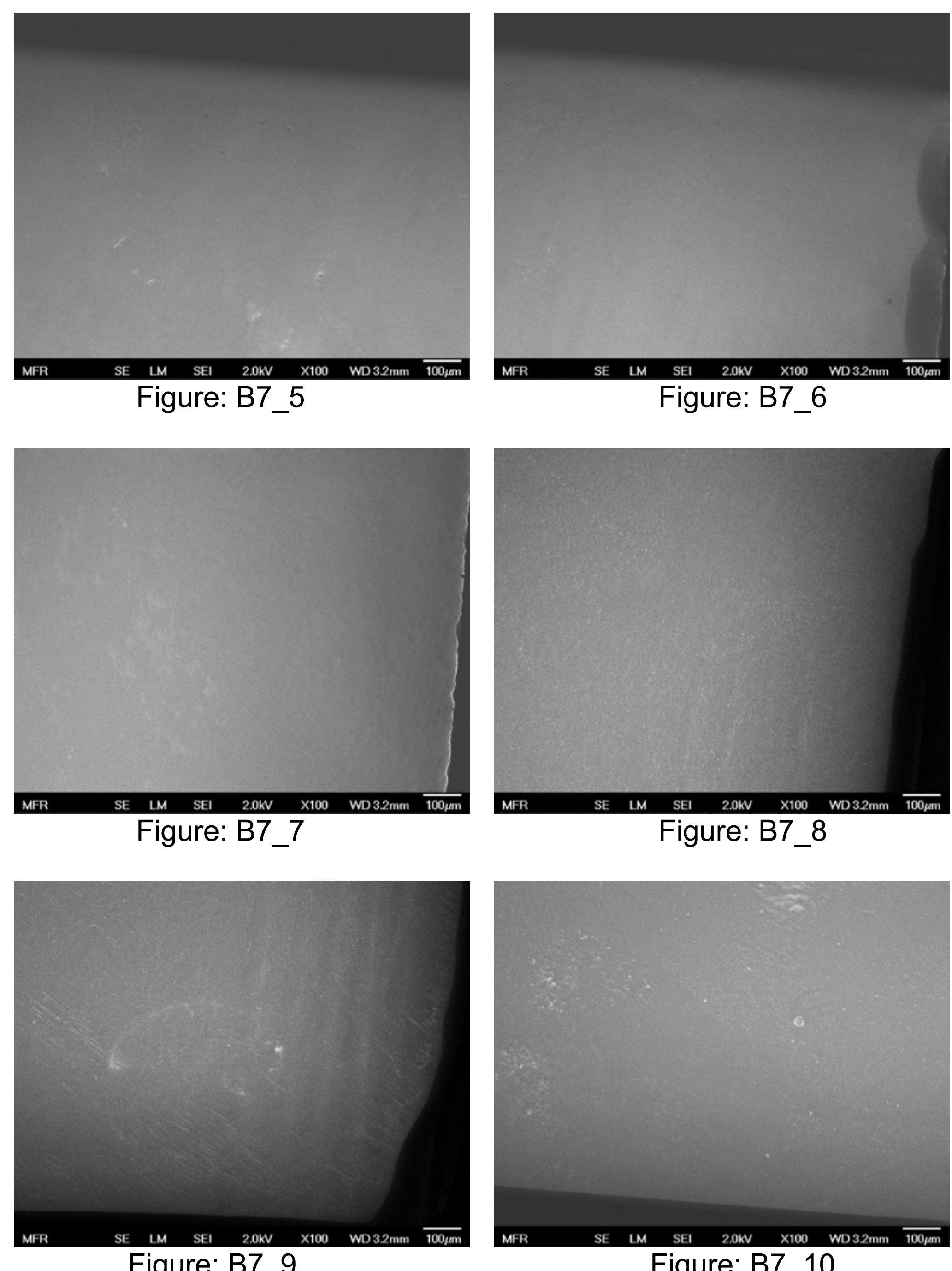

Figure: B7_5

Figure: B7_6

Figure: B7_7

Figure: B7_8

Figure: B7_9

Figure: B7_10

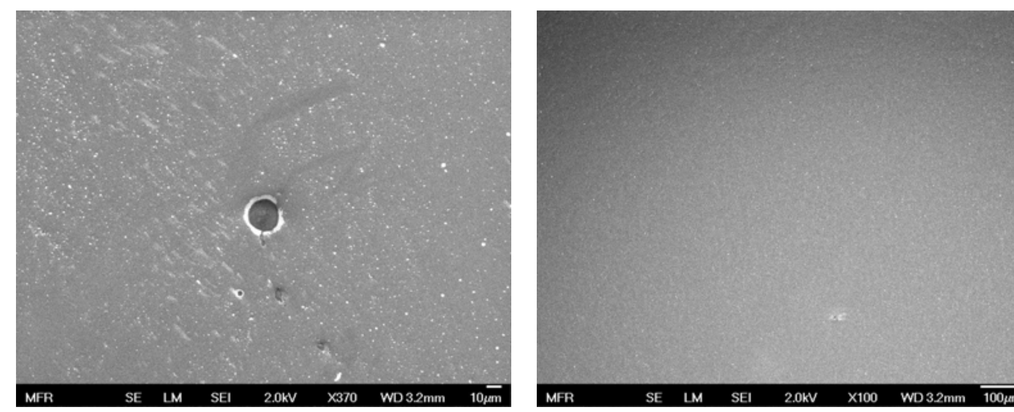

Figure: B7_11

Figure:B7_12

APPENDIX C

APPENDIX D

Structure defects

Result after the etching process of the germanium dummy, which is described in chapter 4.1: The Structure defects

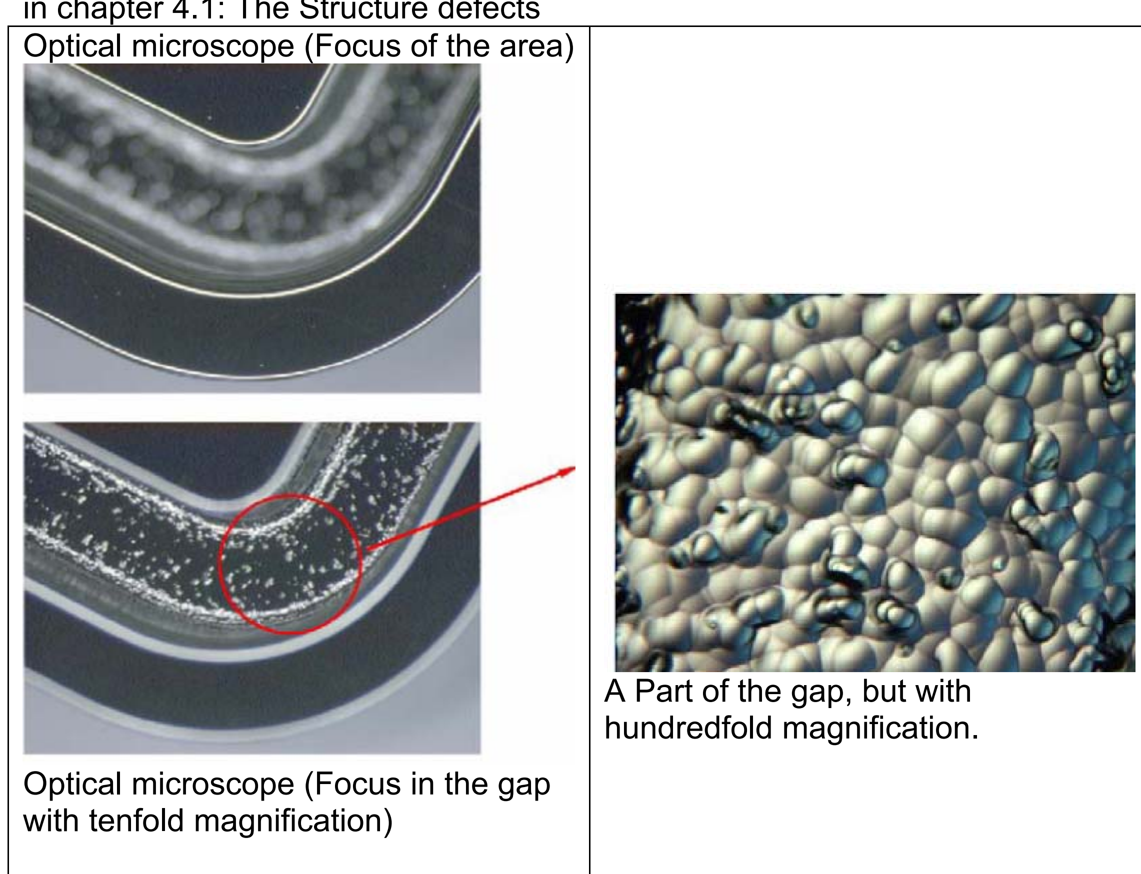

Optical microscope (Focus of the area)

Optical microscope (Focus in the gap with tenfold magnification)

A Part of the gap, but with hundredfold magnification.

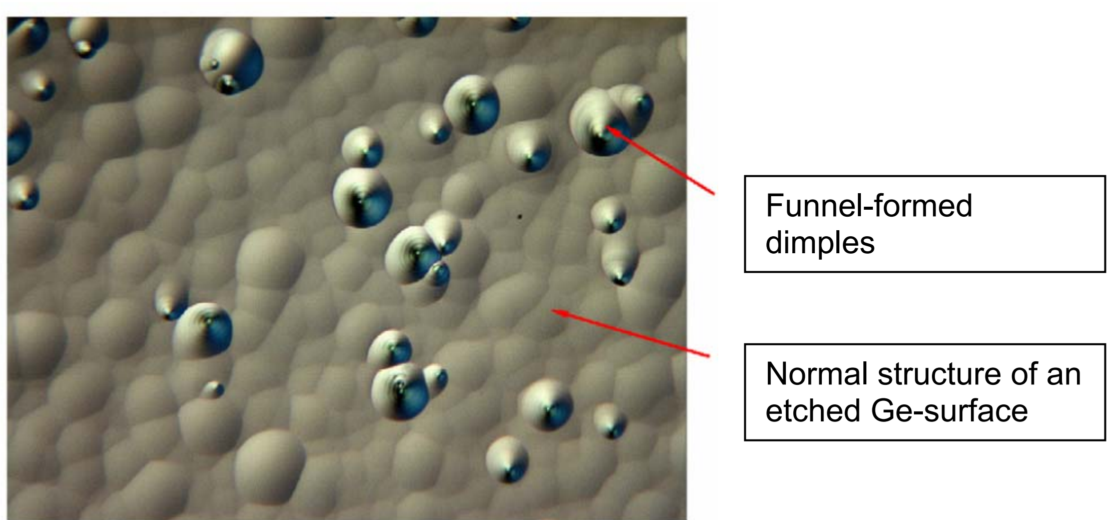

Part of the crystal surface with hundredfold magnification of an optical microscope.

APPENDIX E

Germanium crystal data

Umicore Electro-Optic Materials K67/9201
Olen, 09-DEC-2008

HIGH PURITY GERMANIUM, PHYSICAL DATA (1)

LOT.NUMBER	INTRI 5261
MELT NUMBER	CZ6 1897

1.GEOMETRY

CLASS	GKWA33
WEIGHT	91 G
LENGTH	33.2 mm
WIDTH	33.2 mm
THICKNESS	15.5 mm

2.ELECTRONIC PROPERTIES

MAJORITY CARRIER TYPE		P	
NET CARRIER CONCENTRATION	HEAD	0.35	10E10 cm-3
	TAIL	0.33	10E10 cm-3
HALL MOBILITY	HEAD	33.100	10E3 cm2/Vs
	TAIL	32.000	10E3 cm2/Vs
CU-CONCENTRATION	HEAD	0.00	

3.CRYSTALLOGRAPHIC PROPERTIES

DISLOCATION DENSITY	HEAD	18.83	10E2 cm-2
	TAIL	19.00	10E2 cm-2

(1)FOR MEASURING DETAILS CONSULT OUR SPECIFICATIONS ON HIGH PURITY GERMANIUM

BU.Ge
Q.A.7

9. Publications

München, den 25.09.08
Telefon: (089) 2195-3233
Aktenzeichen: 10 2008 037 359.1
Anmelder-Nr. 01078259
Gesellschaft für Schwerionenforschung mbH
Ihr Zeichen GSI08002PDE

Deutsches Patent- und Markenamt · 80297 München

Patentanwalt
Dipl.-Phys. Dr.rer.nat.
Jan Hendrik Nestler M.A.(SUNY)
Felix-Dahn-Str. 14
60431 Frankfurt

Bibliografie-Mitteilung

IPC-Hauptklasse		B23K 37/00
IPC-Nebenklasse		B23K 1/008 B23K 1/16
Anmeldetag		**12.08.2008**
Bezeichnung		Werkstückanordnung
Anmelder-Nr.	01078259	Gesellschaft für Schwerionenforschung mbH, 64291 Darmstadt, DE
Vertreter-Nr.	439185	Nestler, J., Dipl.-Phys.Univ. Dr.rer.nat. M.A.(SUNY), Pat.-Anw., 60431 Frankfurt
Erfinder		Engert, Tobias, 69518 Abtsteinach, DE; Gerl, Jürgen, Dr., 63128 Dietzenbach, DE; Kojouharo, Ivan, 55270 Zornheim, DE

Die Veröffentlichung der Anmeldung erfolgt voraussichtlich am **18.02.2010**

Sie unterbleibt, wenn die Anmeldung **vor Abschluss der technischen Vorbereitung für die Veröffentlichung** (8 Wochen vor dem vorgesehenen Veröffentlichungstag) zurückgenommen wird oder als zurückgenommen gilt (§ 32 Abs. 4 PatG).

Folgende angekreuzte Unterlagen sind innerhalb einer **Frist von ..... Monaten** .... -fach nachzureichen:

☐ Beschreibung (§ 6+10 PatV) ☐ Ansprüche (§ 6+9 PatV) ☐ Publikationsfähige Zeichnungen (§ 6+12 PatV)
ggf. mit der Erklärung der Übereinstimmung mit den bereits eingereichten Unterlagen (§ 15 Abs. 2 PatV)
☐ Zeichnung zur Zusammenfassung (§ 36 PatG, § 6 PatV)
☐ Prioritätsbeleg(e) fehlt/fehlen und ist/sind innerhalb der gesetzlichen Frist einzureichen (§ 41 Abs.1 PatG)
☐ Weitere Anforderungen: Siehe gesonderter Bescheid
☒ derzeit keine Anforderungen

Prüfungsstelle 45

Bitte Anmelder und Aktenzeichen bei allen Eingaben angeben!

Bitte beachten Sie die wichtigen Hinweise auf der Rückseite!

Dokumentenannahme und Nachtbriefkasten nur Zweibrückenstraße 12
Hauptgebäude: Zweibrückenstraße 12
Markenabteilungen: Cincinnatistr. 64, 81534 München
Hausadresse (für Fracht): Deutsches Patent- und Markenamt, Zweibrückenstraße 12, 80331 München
Telefon: (089) 2195-0
Telefax: (089) 2195-2221
Internet: http://www.dpma.de
Zahlungsempfänger: Bundeskasse Weiden, BBk München, Kto.Nr.: 700 010 54, BLZ: 700 000 00, BIC (SWIFT-Code): MARKDEF1700, IBAN: DE84 7000 0000 0070 0010 54
S-Bahnanschluss im Münchner Verkehrs- u. Tarifverbund (MVV): → Zweibrückenstr. 12 (Hauptgebäude): **S1 – S8 Haltestelle Isartor**; Schwere-Reiter-Straße 37; Cincinnatistr. 64

Lfd.Nr. 73
P2002

Empfangsbescheinigung

DEUTSCHES PATENT- UND MARKENAMT

(1) in der Anschrift Straße, Haus-Nr. und ggf. Postfach angeben

Sendungen des Deutschen Patent- und Markenamts sind zu richten an:
Dr. Jan Nestler
Patentanwalt
Felix-Dahn-Straße 14
60431 Frankfurt

Antrag auf Erteilung eines Patents — 1

Vordruck nicht für PCT-Verfahren verwenden s. Rückseite

☐ **TELEFAX** vorab am 11. August 2008

Aktenzeichen (wird vom Deutschen Patent- und Markenamt vergeben): 10 2008 037 359.1

(2) Zeichen des Anmelders/Vertreters (max. 20 Stellen): GSI08002PDE
Telefon des Anmelders/Vertreters: 069/95103479
Datum: 11. August 2008

(3) Der Empfänger in Feld (1) ist der — ggf. Nr. der Allgemeinen Vollmacht
☐ Anmelder ☐ Zustellungsbevollmächtigte ☒ Vertreter

(4) nur auszufüllen, wenn abweichend von Feld (1); Handelsregisternummer nur bei Firmen anzugeben

Anmelder (Name und Anschrift - kein Postfach! -)
Gesellschaft für Schwerionenforschung mbH
Planckstraße 1
64291 Darmstadt

Vertreter (Name und Anschrift)
Dr. Jan Nestler
Patentanwalt
Felix-Dahn-Straße 14
60431 Frankfurt

☒ Der Anmelder ist eingetragen im Handelsregister Nr. HRB 1528 beim Amtsgericht Darmstadt

(5) soweit bekannt
Anmelder-Nr.: —
Vertreter-Nr.: 439 185
Zustelladressen-Nr.: —
ABT / ERF

(6) s. auch Rückseite. IPC-Vorschlag ist unbedingt anzugeben, sofern bekannt

Bezeichnung der Erfindung
Werkstückanordnung

IPC-Vorschlag d. Anmelders

(7) Erläuterung u. Kostenhinweise auf der Rückseite

Sonstige Anträge

Aktenzeichen der Hauptanmeldung (des Hauptpatents)

☐ Die Anmeldung ist **Zusatz** zur Patentanmeldung (zum Patent) →
☒ **Prüfungsantrag** - Prüfung der Anmeldung mit Ermittlung der öffentlichen Druckschriften (§ 44 Patentgesetz)
☐ **Rechercheantrag** - Ermittlung der öffentlichen Druckschriften **ohne** Prüfung (§ 43 Patentgesetz)
☐ **Aussetzung** des Erteilungsbeschlusses auf ______ Monate (§ 49 Abs. 2 Patentgesetz)
(Max. 15 Mon. ab Anmelde- oder Prioritätstag)

(8) **Erklärungen**

Aktenzeichen der Stammanmeldung

☐ **Teilung/Ausscheidung** aus der Patentanmeldung →
☐ an **Lizenzvergabe** interessiert (unverbindlich)
☒ **Nachanmeldung im Ausland** beabsichtigt (unverbindlich)

(9) s. auch Rückseite
☐ Inländische **Priorität** (Datum, Aktenzeichen der Voranmeldung)
☐ Ausländische **Priorität** (Datum, Land, Aktenz. der Voranmeldung; vollständige Abschrift(en) der ausländischen Voranmeldung(en) beifügen)

(10) Erläuterung und Kostenhinweise s. Rückseite

Gebührenzahlung in Höhe von 410 EUR

☒ **Einzugsermächtigung** Vordruck (A 9507) *ist beigefügt*
☐ **Überweisung** *(nach Erhalt der Empfangsbescheinigung)*

Wird die Anmeldegebühr nicht innerhalb von 3 Monaten nach dem Tag des Eingangs der Anmeldung gezahlt, so gilt die Anmeldung als zurückgenommen!

(11) Anlagen 3 - 6 jeweils 3-fach; s. auch Rückseite

Anlagen

Nr.	Anzahl	Anlage
1		Vertretervollmacht
2	1	Erfinderbenennung (P 2792)
3	1	Zusammenfassung (ggf. mit Zeichnung Fig. 1)
4	30	Seite(n) Beschreibung (ggf. mit Bezugszeichenliste)
5	4	Seite(n) Patentansprüche
	15	Anzahl Patentansprüche
6	8	Blatt Zeichnungen
7		Abschrift(en) d. Voranmeld.
8		Zitierte Nichtpatentliteratur
9		Anzahl Datenträger
		☐ für Sequenzprotokoll nach § 11 Abs. 2 PatV
		☐ für umfangreiche Anmeldungsunterlagen nach § 6 Abs. 1 S. 2 PatV
10		

(12) Unterschrift(en)

Patentanwalt
(13) Funktion des Unterzeichners

Nur von der Dokumentenannahme auszufüllen:
Diese Patentanmeldung ist an dem durch Perforierung angegebenen Tag, bei Übermittlung durch Telefax an dem durch das Empfangsgerät aufgedruckten Datum beim Deutschen Patent- und Markenamt eingegangen. Sie hat das o.a. Aktenzeichen erhalten.
Dieses Aktenzeichen ist bei allen Eingaben anzugeben. Bei Zahlungen ist das vollständige Aktenzeichen und der Verwendungszweck in Form der Gebührennummer (s. Rückseite zu Feld (10)) zu vermerken.

☐ Bei Einzugsermächtigung: A 9507 bzw. Doppel an Referat 4.2.1 - Zahlungsverkehr - gesandt
☐ Die genannten Anlagen sind vollständig eingegangen.
☐ Folgende o.a. Anlagen fehlen.
Mit diesen Angaben ist keinerlei Aussage dazu verbunden, inwieweit die eingereichten Unterlagen den formellen und inhaltlichen Anmeldeerfordernissen entsprechen.

(Dienstsiegel) DEUTSCHES PATENT- UND MARKENAMT

Bitte beachten Sie die Hinweise auf der Rückseite der zurückgehaltenen Antragsdurchschrift

P 2007
3.07 EB

5

Zusammenfassung

Die Erfindung betrifft eine Werkstückanordnung (1, 15, 18, 43), bei der zwei Werkstücke (2, 3, 22, 23, 45. 46) mittels einer stoffschlüssigen Verbindungsnaht (4, 16, 19, 28, 47) miteinander verbunden sind. Dabei ist im
10
Bereich der stoffschlüssigen Verbindungsnaht (4, 16, 19, 28, 47) zumindest eine thermische Isolationseinrichtung (8, 9, 18, 21, 27, 48, 49) vorgesehen.

15 (Fig. 1)

Deutsches Patent- und Markenamt

München, den 17.06.2009
Telefon: (089) 2195-4564

Aktenzeichen: 10 2009 009 001.0-16

Anmelder-Nr. 18389848
GSI Helmholtzzentrum für Schwerionenforschung Gr

Ihr Zeichen GSI08004PDE

Deutsches Patent- und Markenamt · 80297 München

Herrn
Patentanwalt
Dr. Jan Nestler
Felix-Dahn-Str. 14
60431 Frankfurt

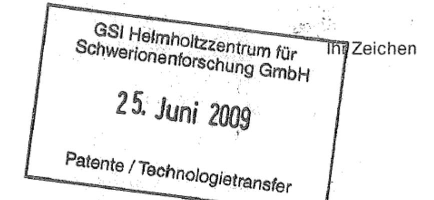

Bibliografie-Mitteilung

IPC-Hauptklasse	F28D 21/00
IPC-Nebenklasse	H01L 31/024 F25D 3/10 H05K 7/20
Anmeldetag	**14.02.2009**
Bezeichnung	Wärmeübergangsleiter
Anmelder-Nr. 18389848	GSI Helmholtzzentrum für Schwerionenforschung GmbH, 64291 Darmstadt, DE
Vertreter-Nr. 439185	Nestler, J., Dipl.-Phys.Univ. Dr.rer.nat. M.A.(SUNY), Pat.-Anw., 60431 Frankfurt
Erfinder	Engert, Tobias, 69518 Abtsteinach, DE; Kojouharov, Ivan, 55270 Zornheim, DE; Ge Jürgen, 63128 Dietzenbach, DE

Die Veröffentlichung der Anmeldung erfolgt voraussichtlich am **19.08.2010**

Sie unterbleibt, wenn die Anmeldung **vor Abschluss der technischen Vorbereitung für die Veröffentlichung** (8 Wochen vor dem vorgesehenen Veröffentlichungstag) zurückgenommen wird oder als zurückgenommen gilt (§ 32 Abs. 4 PatG).

Folgende angekreuzte Unterlagen sind innerhalb einer **Frist von ..... Monaten** .... -fach nachzureichen:

- ☐ Beschreibung (§ 6+10 PatV) ☐ Ansprüche (§ 6+9 PatV) ☐ Publikationsfähige Zeichnungen (§ 6+12 PatV)
  ggf. mit der Erklärung der Übereinstimmung mit den bereits eingereichten Unterlagen (§ 15 Abs. 2 PatV)
- ☐ Zeichnung zur Zusammenfassung (§ 36 PatG, § 6 PatV)
- ☐ Prioritätsbeleg(e) fehlt/fehlen und ist/sind innerhalb der gesetzlichen Frist einzureichen (§ 41 Abs.1 PatG)
- ☐ Weitere Anforderungen: Siehe gesonderter Bescheid
- ☒ derzeit keine f o r m a l e n Anforderungen

Prüfungsstelle für Klasse F28D

Bitte Anmelder und Aktenzeichen bei allen Eingaben angeben!

Bitte beachten Sie die wichtigen Hinweise auf der Rückseite!

Dokumentenannahme und Nachtbriefkasten nur Zweibrückenstraße 12
Hauptgebäude: Zweibrückenstraße 12
Markenabteilungen: Cincinnatistr. 64, 81534 München
Hausadresse (für Fracht): Deutsches Patent- und Markenamt, Zweibrückenstraße 12, 80331 München
Telefon: (089) 2195-0
Telefax: (089) 2195-2221
Internet: http://www.dpma.de
Zahlungsempfänger: Bundeskasse Weiden, BBk München, Kto.Nr.: 700 010 54, BLZ: 700 000 00, BIC (SWIFT-Code): MARKDEF, IBAN: DE84 7000 0000 0070 0C

S-Bahnanschluss im Münchner Verkehrs- u. Tarifverbund (MVV): → Zweibrückenstr. 12 (Hauptgebäude): **S1 – S8 Haltestelle Isartor**; Schwere-Reiter-Straße 37; Cincinnatistr. 64

Lfd.Nr. 164

P2002

Empfangsbescheinigung **DEUTSCHES PATENT- UND MARKENAMT**

Antrag auf Erteilung eines Patents 1

(1) in der Anschrift Straße, Haus-Nr. und ggf. Postfach angeben

Sendungen des Deutschen Patent- und Markenamts sind zu richten an:
Dr. Jan Nestler
Patentanwalt
Felix-Dahn-Straße 14
60431 Frankfurt

Vordruck nicht für PCT-Verfahren verwenden s. Rückseite

☐ TELEFAX vorab am

Aktenzeichen (wird vom Patent- und Markenamt vergeben)
10 2009 009 001.0

(2) Zeichen des Anmelders/Vertreters (max. 20 Stellen): GSI08004PDE
Telefon des Anmelders/Vertreters: 069/95103479
Datum: 13. Februar 2009

(3) Der Empfänger in Feld (1) ist der
☐ Anmelder ☐ Zustellungsbevollmächtigte ☐ Vertreter
ggf. Nr. der Allgemeinen Vollmacht

(4) nur auszufüllen, wenn abweichend von Feld (1); Handelsregisternummer bei Firmen angeben

Anmelder (Name und Anschrift - kein Postfach! -)
GSI Helmholtzzentrum
für Schwerionenforschung mbH
Planckstraße 1
64291 Darmstadt

Vertreter (Name und Anschrift)
Dr. Jan Nestler
Patentanwalt
Felix-Dahn-Straße 14
60431 Frankfurt

☐ Der Anmelder ist eingetragen im Handelsregister Nr. HRB 1528 beim Amtsgericht Darmstadt

(5) soweit bekannt

Anmelder-Nr.	Vertreter-Nr.	Zustelladressen-Nr.	ABT	ERF
	439 185		/	

(6) s. auch Rückseite; IPC-Vorschlag ist unbedingt anzugeben, sofern bekannt

Bezeichnung der Erfindung

Wärmeübergangsleiter

IPC-Vorschlag d. Anmelders

(7) Erläuterung u. Kostenhinweise auf der Rückseite

Sonstige Anträge

Aktenzeichen der Hauptanmeldung (des Hauptpatents)

☐ Die Anmeldung ist **Zusatz** zur Patentanmeldung (zum Patent) →
☒ **Prüfungsantrag** - Prüfung der Anmeldung **mit** Ermittlung der öffentlichen Druckschriften (§ 44 Patentgesetz)
☐ **Rechercheantrag** - Ermittlung der öffentlichen Druckschriften **ohne** Prüfung (§ 43 Patentgesetz)
☐ **Aussetzung** des Erteilungsbeschlusses auf ______ Monate (§ 49 Abs. 2 Patentgesetz)
(Max. 15 Mon. ab Anmelde- oder Prioritätstag)

(8)

Erklärungen

Aktenzeichen der Stammanmeldung

☐ **Teilung/Ausscheidung** aus der Patentanmeldung →
☐ an **Lizenzvergabe** interessiert (unverbindlich)
☐ **Nachanmeldung im Ausland** beabsichtigt (unverbindlich)

(9) s. auch Rückseite

☐ Inländische **Priorität** (Datum, Aktenzeichen der Voranmeldung)
☐ Ausländische **Priorität** (Datum, Land, Aktenz. der Voranmeldung; vollständige **Abschrift(en) der ausländischen Voranmeldung(en)** beifügen)

(10) Erläuterung und Kostenhinweise s. Rückseite

Gebührenzahlung in Höhe von 410 EUR

☐ **Einzugsermächtigung** **Vordruck (A 9507)** *ist beigefügt*
☐ **Überweisung** *(nach Erhalt der Empfangsbescheinigung)*

Wird die Anmeldegebühr nicht innerhalb von 3 Monaten nach dem Tag des Eingangs der Anmeldung gezahlt, so gilt die Anmeldung als zurückgenommen!

(11) Anlagen 3 - 6 jeweils 3-fach; s. auch Rückseite

Anlagen

Nr.	Anzahl	Anlage	Nr.	Anzahl	Anlage
1.		Vertretervollmacht	6	3	Blatt Zeichnungen
2.		Erfinderbenennung (P 2792)	7		Abschrift(en) d. Voranmeld.
3.	1	Zusammenfassung (ggf. mit Zeichnung Fig. 1)	8		Zitierte Nichtpatentliteratur
4.	21	Seite(n) Beschreibung (ggf. mit Bezugszeichenliste)	9		Anzahl Datenträger ☐ für Sequenzprotokoll nach § 11 Abs. 2 PatV ☐ für umfangreiche Anmeldungsunterlagen nach § 6 Abs. 1 S. 2 PatV
5.	3	Seite(n) Patentansprüche	10		
	12	Anzahl Patentansprüche			

(12) **Unterschrift(en)**

Patentanwalt

(13) Funktion des Unterzeichners

Nur von der Dokumentenannahme auszufüllen:
Diese Patentanmeldung ist an dem durch Perforierung angegebenen Tag, bei Übermittlung durch Telefax an dem vom Empfangsgerät aufgedruckten Datum beim Deutschen Patent- und Markenamt eingegangen. Sie hat das o.a. Aktenzeichen erhalten.
Dieses Aktenzeichen ist bei allen Eingaben anzugeben. Bei Zahlungen ist das vollständige Aktenzeichen ... Verwendungszweck in Form der Gebührennummer (s. Rückseite zu Feld (10)) zu vermerken.

☐ Bei Einzugsermächtigung: A 9507 bzw. Doppel an Referat 4.2.1. - Zahlungsverkehr - gesandt
☐ Die genannten Anlagen sind vollständig eingegangen.
☐ Folgende o.a. Anlagen fehlen:
Mit diesen Angaben ist keinerlei Aussage dazu verbunden, inwieweit die eingereichten Unterlagen den formellen und inhaltlichen Anmeldeerfordernissen entsprechen.

Bitte beachten Sie die Hinweise auf der Rückseite der zurückgehaltenen Antragsdurchschrift

DEUTSCHES PATENT- UND MARKENAMT 24

P 2007
3.07 EB

5

Zusammenfassung

Die Erfindung betrifft einen Wärmeübertragungsvorrichtung (1) zur Wärmeübertragung von einer Wärmequelle (20) zu einer Wärmesenke (16). Die Wärmeübertragungsvorrichtung (1) weist Kontakteinrichtungen (3) zur ther-
10 mischen Kontaktierung der Wärmeübertragungsvorrichtung (1) mit der Wärmequelle (20) sowie mit der Wärmesenke (16) auf. Ferner weist die Wärmeübertragungsvorrichtung (1) Wärmeleiteinrichtungen (2) zur Übertragung von thermischer Energie zwischen der Wärmequelle (20) und der Wärmesenke (16) auf. Die Wärmeleiteinrichtungen (2) und die Kontakteinrichtungen (3)
15 sind zumindest teilweise durch einen Ultraschallschweißvorgang miteinander verbunden.

(Fig. 1)

Deutsches Patent- und Markenamt

München, den 18. 11. 09
Telefon: (089) 2195-3314

Aktenzeichen: 10 2009 034 837.9 – 52

Anmelder-Nr. 18389848
GSI Helmholtzzentrum für Schwerionenforschung GmbH

Ihr Zeichen P 279

Deutsches Patent- und Markenamt · 80297 München

Frau
Dr. Dorothee Rück
c/o GSI Helmholtzzentrum für Schwerionenforschung GmbH
Planckstr. 1
64291 Darmstadt

GSI Helmholtzzentrum für Schwerionenforschung GmbH
20. Nov. 2009
Patente / Technologietransfer

Bibliografie-Mitteilung

IPC-Hauptklasse	G01D 11/24
IPC-Nebenklasse	G12B 9/02
Anmeldetag	**27.07.2009**
Bezeichnung	Gehäuse
Anmelder-Nr. 18389848	GSI Helmholtzzentrum für Schwerionenforschung GmbH, 64291 Darmstadt, DE
Erfinder	Engert, Tobias, 69518 Abtsteinach, DE; Kojouharov, Ivan, 55270 Zornheim, DE; Gerl, Jürgen, 63128 Dietzenbach, DE

Die Veröffentlichung der Anmeldung erfolgt voraussichtlich am **03.02.2011** ✓

Sie unterbleibt, wenn die Anmeldung **vor Abschluss der technischen Vorbereitung für die Veröffentlichung** (8 Wochen vor dem vorgesehenen Veröffentlichungstag) zurückgenommen wird oder als zurückgenommen gilt (§ 32 Abs. 4 PatG).

Folgende angekreuzte Unterlagen sind innerhalb einer **Frist von ..... Monaten** .... -fach nachzureichen:

☐ Beschreibung (§ 6+10 PatV) ☐ Ansprüche (§ 6+9 PatV) ☐ Publikationsfähige Zeichnungen (§ 6+12 PatV)
ggf. mit der Erklärung der Übereinstimmung mit den bereits eingereichten Unterlagen (§ 15 Abs. 2 PatV)
☐ Zeichnung zur Zusammenfassung (§ 36 PatG, § 6 PatV)
☐ Prioritätsbeleg(e) fehlt/fehlen und ist/sind innerhalb der gesetzlichen Frist einzureichen (§ 41 Abs.1 PatG)
☐ Weitere Anforderungen: Siehe gesonderter Bescheid
☒ derzeit keine f o r m a l e n Anforderungen

Prüfungsstelle ~~52~~ für Klasse G01D

Bitte Anmelder und Aktenzeichen bei allen Eingaben angeben!

Bitte beachten Sie die wichtigen Hinweise auf der Rückseite!

Dokumentenannahme und Nachtbriefkasten nur Zweibrückenstraße 12
Hauptgebäude: Zweibrückenstraße 12
Markenabteilungen: Cincinnatistr. 64, 81534 München
Hausadresse (für Fracht): Deutsches Patent- und Markenamt, Zweibrückenstraße 12, 80331 München
Telefon: (089) 2195-0
Telefax: (089) 2195-2221
Internet: http://www.dpma.de
Zahlungsempfänger: Bundeskasse Weiden, BBk München, Kto.Nr.: 700 010 54, BLZ: 700 000 00, BIC (SWIFT-Code): MARKDEF1700, IBAN: DE84 7000 0000 0070 0010 54
S-Bahnanschluss im Münchner Verkehrs- u. Tarifverbund (MVV): → Zweibrückenstr. 12 (Hauptgebäude): **S1 – S8 Haltestelle Isartor**; Schwere-Reiter-Straße 37; Cincinnatistr. 64

Lfd.Nr. 77
P2002

Empfangsbescheinigung **DEUTSCHES PATENT- UND MARKENAMT**

(1) In der Anschrift Straße, Haus-Nr. und ggf. Postfach angeben

Sendungen des Deutschen Patent- und Markenamts sind zu richten an:

Dr. Dorothee Rück
c/o GSI Helmholtzzentrum für
Schwerionenforschung GmbH
Planckstr. 1

D-64291 Darmstadt

GSI Helmholtzzentrum für Schwerionenforschung GmbH
-3. Aug. 2009
Patente / Technologietransfer

Vordruck nicht für PCT-Verfahren verwenden s. Rückseite

Antrag auf Erteilung eines Patents **1**

☐ **TELEFAX** vorab am

Aktenzeichen (wird vom Deutschen Patent- und Markenamt vergeben) **10 2009 034 837.9**

(2) Zeichen des Anmelders/Vertreters (max. 20 Stellen): P 279 | Telefon des Anmelders/Vertreters: 0 61 59 / 71 - 26 30 | Datum: 23.07.2009

(3) Der Empfänger in Feld (1) ist der ☐ Anmelder ☒ Zustellungsbevollmächtigte ☒ Vertreter | ggf. Nr. der Allgemeinen Vollmacht 4.3.5.-Nr. 608/07-Ang-AV

(4) nur auszufüllen, wenn abweichend von Feld (1). Handelsregisternummer nur bei Firmen anzugeben

Anmelder (Name und Anschrift - kein Postfach! -)
GSI Helmholtzzentrum für Schwerionenforschung GmbH
Planckstr. 1

D-64291 Darmstadt

Vertreter (Name und Anschrift)
siehe (1)

☒ Der Anmelder ist eingetragen im Handelsregister Nr. HRB 1528 beim Amtsgericht Darmstadt

(5) soweit bekannt

Anmelder-Nr.	Vertreter-Nr.	Zustelladressen-Nr.	ABT	ERF
			/	

(6) s. auch Rückseite. IPC-Vorschlag ist unbedingt anzugeben, sofern bekannt

Bezeichnung der Erfindung

Gehäuse

IPC-Vorschlag d. Anmelders

(7) Erläuterung u. Kostenhinweise auf der Rückseite

Sonstige Anträge | Aktenzeichen der Hauptanmeldung (des Hauptpatents)

☐ Die Anmeldung ist **Zusatz** zur Patentanmeldung (zum Patent) ➔
☒ **Prüfungsantrag** - Prüfung der Anmeldung **mit** Ermittlung der öffentlichen Druckschriften (§ 44 Patentgesetz)
☐ **Rechercheantrag** - Ermittlung der öffentlichen Druckschriften **ohne** Prüfung (§ 43 Patentgesetz)
☐ **Aussetzung** des Erteilungsbeschlusses auf ______ Monate (§ 49 Abs. 2 Patentgesetz)
(Max. 15 Mon. ab Anmelde- oder Prioritätstag)

(8) **Erklärungen** | Aktenzeichen der Stammanmeldung

☐ **Teilung/Ausscheidung** aus der Patentanmeldung ➔
☐ an **Lizenzvergabe** interessiert (unverbindlich)
☐ **Nachanmeldung im Ausland** beabsichtigt (unverbindlich)

(9) s. auch Rückseite

☐ Inländische **Priorität** (Datum, Aktenzeichen der Voranmeldung)
☐ Ausländische **Priorität** (Datum, Land, Aktenz. der Voranmeldung; vollständige Abschrift(en) der ausländischen Voranmeldung(en) beifügen)

(10) Erläuterung und Kostenhinweise s. Rückseite

Gebührenzahlung in Höhe von 410,00 EUR

☐ **Einzugsermächtigung** Vordruck (A 9507) *ist beigefügt*
☒ **Überweisung** *(nach Erhalt der Empfangsbescheinigung)*

Wird die Anmeldegebühr nicht innerhalb von 3 Monaten nach dem Tag des Eingangs der Anmeldung gezahlt, so gilt die Anmeldung als zurückgenommen!

(11) **Anlagen** (Anlagen 3. - 6. jeweils 3-fach; s. auch Rückseite)

1. 1 Vertretervollmacht
2. 1 Erfinderbenennung (P 2792)
3. 1 Zusammenfassung (ggf. mit Zeichnung Fig. 1)
4. 29 Seite(n) Beschreibung (ggf. mit Bezugszeichenliste)
5. 3 Seite(n) Patentansprüche; 13 Anzahl Patentansprüche
6. 5 Blatt Zeichnungen
7. ___ Abschrift(en) d. Voranmeld.
8. ___ Zitierte Nichtpatentliteratur
9. ___ Anzahl Datenträger
   ☐ für Sequenzprotokoll nach § 11 Abs. 2 PatV
   ☐ für umfangreiche Anmeldungsunterlagen nach § 6 Abs. 1 S. 2 PatV
10. ___

i.V. D. R.
(Dr. Dorothee Rück)
(12) Unterschrift(en)

Angestellte
(13) Funktion des Unterzeichners

Nur von der Dokumentenannahme auszufüllen:
Diese Patentanmeldung ist an dem durch Perforierung angegebenen Tag, bei Übermittlung durch Telefax an dem durch das Empfangsgerät aufgedruckten Datum beim Deutschen Patent- und Markenamt eingegangen. Sie hat das o.a. Aktenzeichen erhalten.
Dieses Aktenzeichen ist bei allen Eingaben anzugeben. Bei Zahlungen ist das vollständige Aktenzeichen und der Verwendungszweck in Form der Gebührennummer (s. Rückseite zu Feld (10)) zu vermerken.

☐ Bei Einzugsermächtigung: A 9507 bzw. Doppel an Referat 4.2.1. - Zahlungsverkehr - gesandt
☐ Die genannten Anlagen sind vollständig eingegangen.
☐ Folgende o.a. Anlagen fehlen:
Mit diesen Angaben ist keinerlei Aussage dazu verbunden, inwieweit die eingereichten Unterlagen den formellen und inhaltlichen Anmeldeerfordernissen entsprechen.

DEUTSCHES PATENT- UND MARKENAMT 52 Dienstsiegel

Bitte beachten Sie die Hinweise auf der Rückseite der zurückgehaltenen Antragsdurchschrift

P 2007
3.07 EB

5

Zusammenfassung

Die Erfindung betrifft ein Gehäuse (1) für unter Vakuum und/oder Schutzgas betriebene Geräte (6), das einen Gehäuseinnenraum (2) sowie einen Aufnahmebereich (9) zur Aufnahme eines Gettermaterials (7)

10 aufweist. Dabei ist die Verbindung zwischen dem Gehäuseinnenraum (2) und dem Aufnahmebereich (7) zur Aufnahme des Gettermaterials (9) als partikelundurchlässige Verbindung (43) ausgeführt.

15 (Fig. 1)

20

25

30

10. References

[BOD] H. Bodschwinna, *Moderne Methoden der Signalverarbeitung zur Welligkeitsmessung durch Abgrenzung des Welligkeitsanteils gegenüber Rauheit und Form, Chemnitz,* 29-31 Januar 1996, Tagungsband IX. Internationales Oberflächenkolloquium

[BSD] B. Schulz-Dobrick, Johannes Gutenberg-Universität Mainz, private communication 2009

[CAS] C.A.Siedlecki, Marchand, Biomat., 19, 1998, 441-454

[CTT] H.G. Thomas, Entwicklung eines Germanium-Cluster-Detektors für das Gamma-Spektrometer EUROBALL, Dr. Köster Verlag Berlin, Diss. 1995, ISBN 3-89574-113-2

[DIN1982] Norm DIN 4760 (Juni 1982). Gestaltabweichung. Begriffe. Ordnungssysteme.

[DIN 1998e] Norm DIN EN ISO 4287 (Oktober 1998e). Geometrische Produktspezifikation (GPS) – Oberflächenbeschaffenheit: Tastschnittverfahren, Benennungen, Definitionen und Kenngrößen der Oberflächenbeschaffenheit.

[DIN1990] Norm DIN EN ISO 4768 (Mai 1990). Ermittlung der Rauheitskenngrößen Ra, Rz, Rmax mit elektrischen Tastschnittgeräten. Begriffe und Messbedingungen.

[DUB] W.Beitz/K.-H.Grote: Dubbel, Taschenbuch für den Maschinenbau. 19 Auflage, 1997

[DPM] Deutsches Patent- und Markenamt, Kapsel für einen im Ultrahochvakuum arbeitenden Detektor, DE 4324709 A1, 26.01.1995

[EBE] J.Eberth und G.Hebbinghaus: EUROBALL Design Group Meeting, Communications, Simonskall, 9-10 Dez. 1988, Sonderdruck der KFA Jülich

[ENG] T.Engert, *Entwicklung von Fertigungsverfahren zur kompletten Bearbeitung von Germanium*, Diplomarbeit, Hochschule Darmstadt (2006)

[GER] J.Gerl, z.B: EUROBALL Design Group Meeting, Communications, Simonskall, 20-21 März 1992, Sonderdruck der KFA Jülich

[HAL] Halbleitertechnologie, O.V.: "Arten der Verunreinigung" URL: http://www.halbleiter.org/nasschemie/scheibenreinigung/, 12.12.2009

[HAM] Hammerschmidt/Eichner: Spanende Fertigung- und Prozesstechnik. Skript, Hochschule Darmstadt (2003)

[HER] H.-F. Hadamovsky: Werkstoffe der Halbleitertechnik, 2 Auflage, 1990, ISBN 3-342-00315-4

[HTA] H.Takano, J.R.Kenseth, S.S. Wong, J.C. O`Brien, M.D. Porter, Chem. Rev., 99(10),1999,2845-2890

[INU] Benutzerhandbuch: O.V.: Infinicon, Ultrarest UL 500

[JCB] J.C. Blakesley et al., NIM A 580, 774-777 (2007)

[JKO] J. Kojouharova, Study of operational characteristics of pixelated Germanium detectors, 11th National Congress on Theoretical and Applied Mechanics, 2-5 Sept. 2009, Borovets, Bulgaria

[KJK] K.J.Kim. AG.Fane, J.Member.Sci.,88,1994,103-114

[KNO] G.F.Knoll, *Radiation detection and measurement* Third edition, 1999. ISBN 0-471-07338-5

[KOJ] GeLab at GSI, I.Kojouharov, T.Engert, J.Gerl, Gamma Net, Padova, 10-11.05.2007

[KOV] K.O. Voss, Helmholtzzentrum für Schwerionenforschung GmbH, private communication 2009

[KRA] M.Krammer, Skript: Detektoren in der Hochenergiephysik, Halbleiterdetektoren (2005)

[KUT] D.Kutschin, z.B: EUROBALL Design Group Meeting, Communications, Simonskall, 20-21 März 1992, Sonderdruck der KFA Jülich

[LIE] R.M. Lieder et al., *Design of a Bismuth germanate anti-compton Spectrometer and Its Use in Nuclear Spectroscopy*, Nucl. Instr. and Meth. A220 (1984) 363-370

[LUT] Gerhard Lutz, *Semiconductor Radiation Detectors*, Device Physics, Springer-Verlag 1999, ISBN 3-540-64859-3

[MKR] M. Krause, Helmholtzzentrum für Schwerionenforschung GmbH, private communication 2009

[MSC] M. Schimek, Laser Zentrum Hannover e.V., Materials and Process Department, Hannover, private communication 2008

[NOL] P.Nolan et al., *The Performance of a Bismuth Germanate Escape Suppressed Spectrometer*, Nucl. Instr. and Meth. A236 (1985) 95-99

[ORT] EG&G, Modular Pulse-Processing Electronics and Semiconductor Radiation Detectors, Oak Ridge, 97/98

[OVP] O. Picht, Helmholtzzentrum für Schwerionenforschung GmbH, private communication 2009

[PAT] R.M. Patrikar, *Modelling and simulation of surface roughness,* Applied Surface Science, 2004, Nr. 1-4.

[PRO] Wikipedia, O.V.: "Profilometer". URL: http://de.wikipedia.org/wiki/Profilometer, [11.12.2009]

[RFR] L.Rossi, P.Fischer, T.Rohe, N.Wermes. Pixel detectors. Springer 2006, ISBN 3-540-28332-3

[RIS] S. Pietri, et al. NIM B 261, (2007) 1079

[RIW] H.J Wollersheim et al. NIM A 537, (2005) 637

[SEM] Th. Krings, SEMIKON Detector gmbH, Jülich, private communication 2009

[SNM] S.N.Magonov, M.H. Whangbo, Surface Analysis with STM and AFM, VCH Weinheim, 1996

[SSS] Schunk Sonosystems GmbH, O.V.:"Schunk Ultraschalltechnik". URL:http://www.sut.biz/en/sso/home, [10.10.2009]

[STP] St. Pätz, SAES Getters (Germany) GmbH, private communication 2009

[TNN] T.N.Ng et al., Applied Physics Letters 92, 213303 (2008)

[ULT] A. Wolff: Ultrasonic/Lasertec, 2009, Sonderausgabe der DMG

[UTZ] S. Utzelmann, z.B: EUROBALL Design Group Meeting, Communications, Simonskall, 20-21 März 1992, Sonderdruck der KFA Jülich